The Search for Gravitational Waves from the Coalescence of Black Hole Binary Systems in Data from the LIGO and Virgo Detectors Or: A Dark Walk through a Random Forest

Thesis by

Kari Alison Hodge

In Partial Fulfillment of the Requirements

for the Degree of

Doctor of Philosophy

California Institute of Technology

Pasadena, California

2014

(Defended 12 May 2014)

To my parents

Acknowledgments

First of all, I must thank my parents. You valued my education greatly and spent thousands of hours of your lives driving me to another city so that my primary education would be one that challenged me, gave me a problem-solving spirit, and encouraged creativity. Thank you for everything I learned from you directly as well, especially the life skills that are not taught in school. Thank you for helping me with my school projects, applying to colleges, and applying for financial aid. And lastly, thank you for encouraging me to not drop out as an sophomore at USC. I never would have taken my first physics class the next semester, switched my major, gotten a B.S. in physics, and certainly never would have found myself here today.

Secondly, I thank Alan Weinstein. After meeting with you as a prospective, I was infected with your enthusiasm and joined the LIGO data analysis group. Thank you for your guidance and your seemingly infinite knowledge of all aspects of LIGO. Thank you for believing in me even when you had to explain things that I probably should have known already. Thank you for your kindness and understanding of my need to do theater, and for coming to all of my performances. Thank you meeting with me weekly to discuss my thesis, even when it became apparent that I was going to be releasing a lot of stress through my eyeballs during these meetings. I could not have picked a better advisor. Thank you for taking me on as a student.

Thank you to my candidacy/defense committee — Yanbei Chen, Ken Libbrecht, and Sunil Golwala. And, of course, thank you to LIGO lab for funding me, allowing me to learn so much, and letting me travel to many conferences. Special thanks to everyone in the CBC and Detchar groups for embracing me and my work. A huge thank you to all the system administrators for the clusters (I think I used every single one!) — this thesis would have been impossible without you.

There are so many other people I want to thank, I cannot even conceive of putting them in some order.

To the physics graduate students in the entering class of 2007, especially Milivoje Lukic, Evan O'Connor, Brian Willet, Laura Book, Mhair Orchanian, Paula Popescu, and Kevin Engel — thank you for teaching me more physics than I could have learned alone. I truly enjoyed our time in the library doing homework problems and all the dinners out and boardgames. Extra thanks goes to Richard Norte and Jeff Kaplan who were my study partners and formidable Wii tennis opponents during the epic prep for our qualifying exams. Thank you for letting me into your home and letting me make espresso and chill on your balcony whenever I wanted. And Norte — thank you for always being up for an adventure and, lately, writing your own thesis in the library next to me — it really kept me on task. And thank you Henry Kozachkov for being a good friend

all these years.

And let me thank my fellow LIGO graduate students at Caltech. Stephen Privitera — sorry I got you involved in LIGO in the first place (just kidding, I know you love it) and thank you for helping me with the high-mass search and for letting me plan that crazy train adventure through Germany, Belgium, and the Netherlands (I'm sorry I almost got you stabbed). Leo Singer — your passion for astrophysics is truly inspiring. Jenne Driggers — thank you for being a super cool experimentalist and organizing that trip to the National Ignition Facility. David Yeaton-Massey — thank you for not running me over in the stairwell (I can't believe I'm making it through all these years in Bridge unscathed!). Eric Quintero — thanks for riding bikes with me in Boston. Drew Keppel — thank you for your help and for being such a role model. Lisa Goggin and Pinkesh Patel — thank you for showing me that finishing was possible.

I cannot forget to thank the other LIGO colleagues and collaborators I have had the pleasure of working with. Chad Hannah and Kipp Cannon — thank you for all your help with python and sqlite and for helping me install lalsuite countless times; you really helped launch my projects into action and taught me how to "fish". Tom Dent — thank you for being my partner in crime for the high-mass search and for making me think twice about several aspects of my own research; I really learned a lot from you. Collin Capano — thank you for all your pipedown help along the way and especially for writing dbinjfind, which was integral in the successful implementation of my random forest of bagged decison trees. Andrew Lundgren, Marco Cavaglia, and Duncan MacLeod — thank you for all your help with data quality and veto definer files. Jacob Slutsky — thank you for hanging out with me when I was a SciMon at Livingston and adventuring with me in other countries (especially because I know my lack of planning is not your style). And special thanks to all my AuxMVC collaborators — Ruslan Vaulin, Lindy Blackburn, Reed Essick, John J Oh, SangHoon Oh, Rahul Biswas, Kyungmin Kim, Young-Min Kim, EOL Bigot, Chang-Hwan Lee, Edwin Son, Xiaoge Wang, Junwei Cao, and Erik Katsavounidis. And thank you Sarah Caudill and Paul Baker for getting my crazy random forest of bagged decision trees into a published search; it was great working with you, and I learned a lot. Tristan Ursell and Colorado Reed — thank you for being my SURF students; it was a very educational experience for me too. And thank you to Rana Adhikari for ruling the bodega with an iron fist, such that 2nd floor Bridge has the best coffee on campus.

Thank you to everyone who helped me "Dance my PhD" — Anne Grauso, Morgan Gillio, Jared Frank, Samantha Jacober, Crystal Dilworth, David Brown, Dagny Fleischman, Willie Stanphill, Amit Lakhanpal, Doug Smith, Steve Collins, Klavdia Zemlianova, Yulan Lin, and Chandrea Patterson. And especially Alan Weinstein for your appearance as an electromagnetic glitch and for leading us in the LIGO dance at the end.

And of course, thank you to everyone in the LIGO-Virgo Collaboration who went dancing with me during our (inter)national conferences. It was such a joy to boogie with you all — especially Brennan Hughey, Chris Pankow, Lucia Santamaria, Nick Fotopoulos, Melissa Frei, Larry Price, and Jamie Rollins.

Thank you to my theater family at Caltech. You truly kept me happy and sane. Brian Brophy, Benjamin Sveinbjornsson, Crystal Dilworth, Meg Rosenberg, Miranda Stewart, Dave Seal, Christine Kennedy, and

Ann Lindsey — thank you! And most of all, Amit Lakhanpal — thank you for all our library time and for becoming one of my best and truest friends.

And thank you to my Orlando House/Phageling family for making me feel at home when I am with you.

Thank you to all my office mates through the years — Aidan Brooks, Matt Abernathy, Gabriele Vajente, Steven Privitera, Lucia Santamaria, Ajith Parameswaran, Peter Kalmus, Larry Price, Anand Sengupta, Steve Fairhurst, Lisa Goggin, Drew Keppel, and Diego Fazi. Thank you for all your great company, for the good conversation, and for putting up with my messy desk.

Lynnie Hedvig — thank you for always revitalizing me whenever we get to see each other. You'll always be my first "my". Elizabeth Forest — thank you for your beautiful mind and spirit. To be seen the way you see me, from a person as good as you, really gives me confidence. Nicole Pyburn (Valenzuela) — thank you for your unconditional love. Seren Rain Sehota — thank you for being a great roommate and for giving me word count motivations as I was embarking on this thesis. Shaun Maguire — thank you for being above-and-beyond supportive and always making the time to talk, despite how insanely busy you are. You have helped me in so many ways. Joshy Roche (and Frankie Staniszewski) — thank you for recognizing that this physics thing was totally right for me and for getting me pumped about it. Thank you for supporting me in those early years. Samantha Jacober — thank you for always making me feel at home, even before we lived together. Matt Gangi — thank you for your continued interest in my science, it is definitely re-energizing to have your perspective. Leah Yananton, Dawn Batson, Zorina Chen, Victoria Asher, Jenae Wilkens, Sara Drakely, Dieu Ha, Vi Ha, and Drew Denny — thank you for being amazing women and true sources of inspiration in my life.

Thank you so, so much to everyone who came to my defense — it was so meaningful to have all of your love and support. And thank you for clapping even though you weren't supposed to. You made it a memory I will always treasure.

Abstract

The LIGO and Virgo gravitational-wave observatories are complex and extremely sensitive strain detectors that can be used to search for a wide variety of gravitational waves from astrophysical and cosmological sources. In this thesis, I motivate the search for the gravitational wave signals from coalescing black hole binary systems with total mass between 25 and 100 $M_{\odot}$. The mechanisms for formation of such systems are not well-understood, and we do not have many observational constraints on the parameters that guide the formation scenarios. Detection of gravitational waves from such systems — or, in the absence of detection, the tightening of upper limits on the rate of such coalescences — will provide valuable information that can inform the astrophysics of the formation of these systems. I review the search for these systems and place upper limits on the rate of black hole binary coalescences with total mass between 25 and 100 $M_{\odot}$. I then show how the sensitivity of this search can be improved by up to 40% by the the application of the multivariate statistical classifier known as a random forest of bagged decision trees to more effectively discriminate between signal and non-Gaussian instrumental noise. I also discuss the use of this classifier in the search for the ringdown signal from the merger of two black holes with total mass between 50 and 450 $M_{\odot}$ and present upper limits. I also apply multivariate statistical classifiers to the problem of quantifying the non-Gaussianity of LIGO data. Despite these improvements, no gravitational-wave signals have been detected in LIGO data so far. However, the use of multivariate statistical classification can significantly improve the sensitivity of the Advanced LIGO detectors to such signals.

Preface

The work presented in this thesis was carried out within the LIGO Scientific Collaboration (LSC). The methods and results presented here are under review and are potentially subject to change. The opinions expressed here are those of the author and not necessarily those of the LSC. The author gratefully acknowledges the support of the United States National Science Foundation for the construction and operation of the LIGO Laboratory, which provided support for this work.

Contents

List of Figures

List of Tables

Chapter 1

The search for gravitational waves from the coalescence of black hole binary systems

Gravitational waves (GWs) are produced by anything with an accelerating mass quadrupole moment. Two compact objects, such as black holes or neutron stars, that are locked in orbit together are an example of such a system that would produce GWs in the frequency band accessible by current and near-future ground-based detectors like LIGO and Virgo. As they orbit one another, they produce GWs, which carry energy and angular momentum away from the system, thus causing them to spiral in towards one another and eventually merge; this process is called compact binary coalescence (CBC). As these gravitational waves propagate outward from the system, they stretch and squeeze spacetime in the plane perpendicular to the direction of propagation. LIGO and Virgo detectors use (very sophisticated) Michelson interferometers to detect the differential change in the length of two perpendicular arms.

In the ideal setting, where noise is Gaussian and stationary, the optimal detection statistic for detecting GW signals in LIGO-Virgo data are the signal-to-noise-ratio from a matched-filter analysis, which is described in Section 7.3.3. Matched-filter analysis requires that we have a bank of waveform examples (*templates*), which model the astrophysical signals we expect to be arriving at the detector. CBCs are unique among the potential sources of GWs in that the *inspiral* portion of their gravitational waveforms have been computed using both analytic and numerical methods. When the two objects in the binary are both black holes, the waveforms can be extended to the *merger* of the two black holes and the final black hole's *ring-down*; in this case the entire signal is known as the IMR waveform. The template that gives the largest matched-filter signal-to-noise ratio (SNR) also gives the component masses of the binary and their spin values, if any.

Unfortunately, interferometric gravitational wave detector noise is far from Gaussian or stationary. There are a lot of instrumental artifacts and environmental disturbances that also cause a large matched-filter SNR; these are known as *glitches* (see Section 4.1 for a thorough discussion of glitches). Higher mass systems

produce shorter waveforms in the detection band, and shorter templates are more prone to registering high SNRs from glitches, preventing the detection of higher mass systems (and even complicating the detection of lower-SNR signals from lower mass systems). This thesis focuses on reducing the effect of such glitches and other artifacts of the data on the ability of the LIGO detectors to detect GWs from high-mass CBCs optimally.

1.1 The motivation for the search for gravitational waves from black hole binary systems

Detecting the merger of two black holes, which can only be observed via the gravitational radiation emitted, will give us information about the physics of black holes. As black holes cannot be directly detected via observations in the electromagnetic spectrum, this is the only way to "see" them. Detecting their merger will confirm that these objects exist and are the objects described by General Relativity (GR), or provide direct evidence for physics beyond GR that may be required to explain the properties of such objects.

We can also verify the physics of GWs — that the emitted waves are what we expect based on the theory of GR, whose predictions are summarized in Section 2.2.1. The most interesting part of the detection will be the merger, when curved space smashes into curved space; this will give us insight into the strong-field, highly dynamical, and non-linear regime of GR, which has never been observed. Another test of GR is that of the no-hair theorem, which states that all stationary black hole solutions in GR can be described by only three parameters: the black hole's mass, electric charge, and angular momentum. By observing the ringdown of the final black hole after a merger, we can check that each quasi-normal mode of the ringdown is described by the same three parameters of BH perturbation theory [24] and confirm the no-hair theorem.

The merger of neutron star and black hole (NS+BH) and BH and solar mass BH systems is "under our lamppost" — the frequency content of their expected GWs during and near merger is in the sensitive band of the LIGO and Virgo detectors. Also, the amplitude of GWs emitted from a system scales with the system's mass; systems with tens of solar masses can be detected with advanced detectors across cosmological distances. Therefore, although we know, due to their pulsating radio signals, that there are NS+NS systems within advanced detectors' astrophysical reach, the first detection of GWs from the Advanced LIGO-Virgo detectors could come from a BH+BH merger.

Detecting the merger of NS+BH and BH+BH systems (together referred to as black hole binaries (BHBs)) will give us unique information about the nature and population of astrophysical black holes in the universe (how big they can be, how fast they can spin). Multiple detections will in turn give us information about the possible formation processes that lead to such systems, which can last many billions of years and are not yet fully understood. These processes are briefly discussed in Section 2.1.

1.2 Issues associated with the search for high-mass CBCs

The search for high-mass ($25 - 100 M_\odot$ total) CBCs complements the search for low-mass ($1 - 25 M_\odot$ total) CBCs. Numerous examples of NS+NS and low-mass NS+BH systems are known in our galaxy, and there are no known observations of BH+BH systems. This is one of the reasons that the low-mass search and the high-mass search are not combined into a single search. A second reason is that, as a practical matter, for low-mass systems, inspiral-only templates are sufficient, while IMR templates are required for high-mass binary signals. Third, higher mass templates are more likely to pick up glitches and assign these spurious events a large SNR, which can obscure signals from lower mass systems.

Figure 1.1 illustrates the effect of widening one's search space. The point where the background curves (blue, cyan, black, and green) intersect the x-axis is the SNR^2 of the loudest background event, below which signals are obscured. In the presence of Gaussian noise, searching over high-mass templates in addition to low-mass ones moves the background from the blue curve to the cyan one, which results in fewer observable low-mass signals (red), but enables the discovery of high-mass signals (magenta); see this by drawing a vertical line from the rightmost point of the blue/cyan curve to where it intersects with the red/magenta curves. In the presence of non-Gaussian noise, searching over low-mass templates results in the background curve picking up a non-Gaussian tail (compare the black curve to the blue curve). Searching over high-mass and low-mass templates in the presence of non-Gaussian noise also results in the background curve picking up a non-Gaussian tail, but in this case, the tail is much fatter and longer (compare the green curve to the cyan curve). This is because the high-mass templates are shorter and thus more likely to pick up non-Gaussian glitches, since they have similar timescales.

For these reasons, we search separately for low-mass and high-mass signals. This thesis will explore ways to reduce the extent of the non-Gaussian tail.

1.3 Mitigating the effect of glitches in the search for high-mass CBCs

This thesis focuses on mitigating the effects of glitches on the search for high-mass CBCs in LIGO-Virgo data. We perform several steps to reduce the number of glitches we have to sift through before finding a genuine GW. First, we carefully examine the quality of the data in each detector and do not analyze data if the detector is not functioning satisfactorily (see Chapter 4). Second, we enforce coincidence — a trigger must be seen by at least two detectors from the three: LIGO-Livingston, LIGO-Washington, and Virgo-Italy (see Section 7.3.4). Third, thresholding on the result of a χ^2 test, which measures how well the template matches the data in different frequency bands, allows the rejection of a large fraction of single-detector glitches (see Section 7.3.6). Ideally, we would also enforce coherence between the signals seen in the two or more detectors, and others are working on this tactic. However, most of our triggers are found in double coincidence, and a coherent step is only helpful when there are 3 or more detectors, to provide a constraint

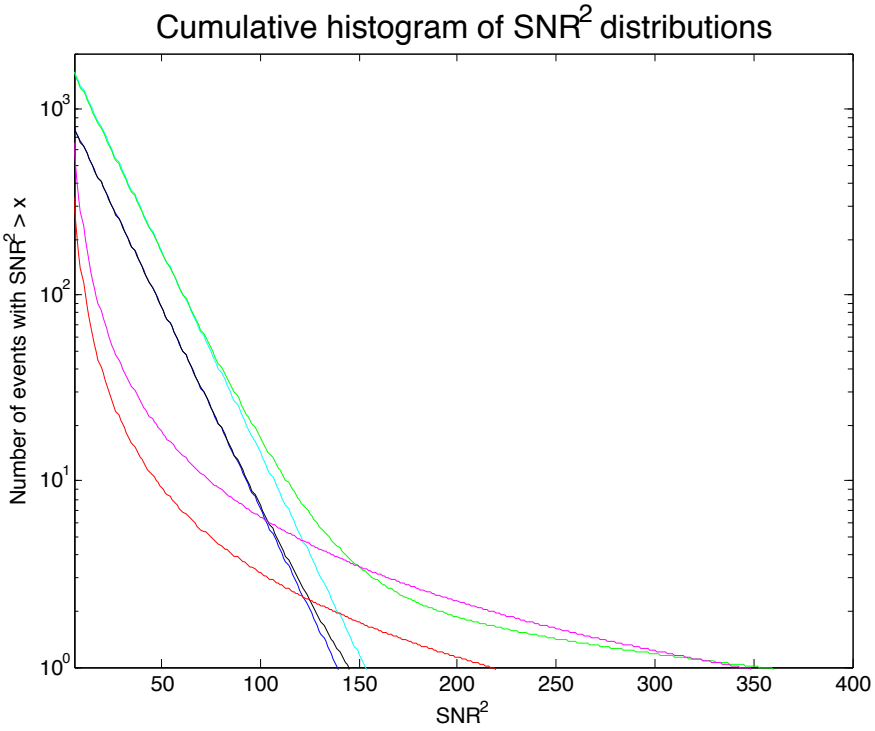

Figure 1.1: A cartoon plot representing the overlap of signal and background in different situations. Blue: Background triggers due to Gaussian noise, picked up by a search with low-mass templates. Cyan: Background triggers due to Gaussian noise, picked up by a search with low-mass and high-mass templates. Black: Background triggers due to Gaussian and non-Gaussian noise, picked up by a search with low-mass templates. Green: Background triggers due to Gaussian and non-Gaussian noise, picked up by a search with low-mass and high-mass templates. Red: Theoretical signal distribution for low-mass astrophysical signals. Magenta: Theoretical signal distribution for low-mass and high-mass astrophysical signals, assuming there are an equal number of each.

in the presence of the two polarizations of GWs (see Section 2.2.1). In the end, we are still left with a lot of glitches littering our lists of loudest candidate GW events produced by our detection pipeline.

This problem is worse for the types of signals we expect to be arriving from higher-mass compact binary systems, as the duration of their inspiral waveform is relatively shorter — closer to the timescale of glitches, i.e., on the order of a second or less. In the LIGO-Virgo searches for these coalescing compact binary systems (see Chapter 7 for a summary of the literature), we reweight the SNR by the χ^2, as glitches tend to have a worse/higher χ^2 than real GWs would. The distributions of this reweighted SNR are a lot closer to the Gaussian limit, especially for lower mass systems ($1 - 25M_\odot$ total); however, there is room for much improvement in the search for gravitational waves from higher mass systems ($25 - 100M_\odot$ total).

By combining SNR and χ^2 in this way, we are able to create a detection statistic that better separates our background events from our simulated signal events than the theoretical ideal, the matched-filter SNR, alone. However, the matched-filter outputs more than just SNR and χ^2; we can also easily examine the templates found in the different detectors for closeness. For example, if there are signals at two detectors at the exact

same time, but the template matched in one detector is for a neutron star and a 25 solar mass black hole and the template matched in the other detector is for two $25M_{\odot}$ black holes, one can surmise that the two signals are really glitches that occurred at the same time due to unlucky coincidence.

The search can surely be improved by folding the template parameters and the time difference between the signal arrivals at the different detectors into the detection statistic. However, this proves to be quite challenging to do analytically, as humans can only really process two-dimensional correlations at once, maybe three. Moreover, in a single dimension, the distribution of values overlaps significantly between our signal distribution and background distribution; see the red versus black distributions in the histograms in Section 8.3.1.4. We could use numerical solutions, for example, a series of two dimensional likelihood calculations, but this is not computationally feasible for the hundreds of thousands of coincident events produced by the LIGO-Virgo system of detectors.

Multivariate statistical classification is the perfect tool to incorporate all the information from a matched-filter analysis into a single detection statistic. Section 5.3 will describe the multivariate method used, and Section 8.3.1.6 quantifies how it improves the search.

It can also be used to identify times when the detector is likely to be especially glitchy, without looking at the GW channel itself. The efforts in this realm are discussed in Chapter 6.

Chapter 2

The physics and astrophysics of gravitational waves from compact binary coalescences with total mass of $25 - 100\ \mathrm{M}_{\odot}$

2.1 Astrophysics of compact binaries with two black holes or one black hole and one neutron star

The likelihood of detecting coalescing BH+BH or BH+NS systems necessarily depends on the number of such binaries within our detection volume and the timescales at which they will merge. Since such systems have never been directly observed (in our Galaxy or extragalactically), the rate for such detections with LIGO is extremely uncertain. These rates are based largely on models attempting to synthesize the population of compact binaries in Milky Way-like galaxies, via two formation scenarios: Isolated Binary Evolution (IBE) and Dynamical-Formation Scenarios. These processes and their expected rates will be briefly discussed in the following subsections.

The LIGO-Virgo Collaboration (LVC) has agreed on a set of astrophysical predictions of how many events LIGO will see, summarized in Table 2.1 [21]. Please note that because many configurations of numerical simulations of IBE do not produce black holes much more massive than $10\ M_{\odot}$ (as explained in Section 2.1.2), the estimates for BH+BH merger are for two $10\ M_{\odot}$ black holes, which is actually searched for with the LIGO low-mass search; our high-mass search begins at a total mass of $25\ M_{\odot}$. The estimates for an intermediate mass ratio inspiral (IMRI) with an intermediate mass black hole (IMBH) take into consideration many Dynamical-Formation Scenarios, but focus on a stellar mass object (NS or BH) into an IMBH between 50 and $350\ M_{\odot}$. (Note that the literature is not consistent on the mass range defined by IMBH). There are regions of the high-mass search that are ignored by this table (e.g. a $25\ M_{\odot}$ on $25\ M_{\odot}$ system). Nonetheless, Table 2.1 is presented for as an "official" set of expectations by the LVC.

Black holes with masses in the ranges considered in our search for high-mass CBCs are predicted via computer simulations, see Figure 2.1 [20]. But, as will become clear in the following sections, there is a lot of uncertainty in the ways such systems can evolve, how many there are, and what masses they can have. In the future, as the LVC makes (or doesn't make) detections of CBCs, we can constrain the astrophysical models of stellar and galactic evolution.

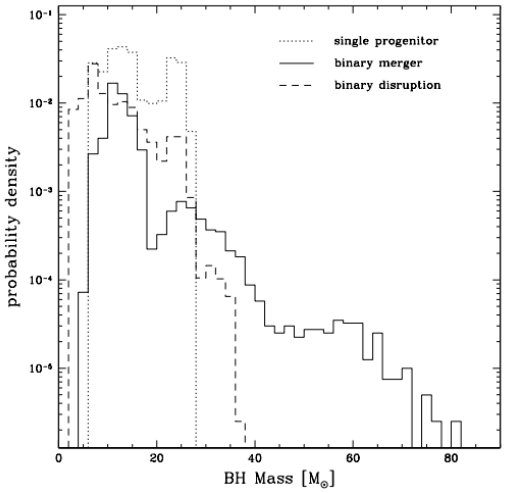

Figure 2.1: The mass distributions of various kinds of single BHs at 11 Myr based on simulations using Reference [1]'s standard model (A). The dotted line indicates BHs evolved from primordial single stars; the dashed line shows single BHs from disrupted binaries; and the solid line shows single BHs that are remnants of merged binaries. The bin width is 2.0 $M_{\odot}$and the counts are normalized to the total number of BHs [1].

2.1.1 Isolated binary evolution

In isolated binary evolution (IBE), two massive stars form from a common progenitor gas cloud and form a binary. After some time, one star undergoes core collapse supernova and turns into a NS or a BH, but in rare cases (of interest here), the mass loss in the supernova is low enough that the binary survives the event. Some time later, the same thing happens to the other star, leaving a double compact object (NS+NS, NS+BH, or BH+BH) which will eventually become a coalescing binary system [25]. During the evolution of the system, there are many paths that can be taken that do not lead to the formation of the a CBC. For example, in a simple model where two stars are in a circular orbit and one goes supernova, but does not happen to receive a kick, the stars only remain bound if the mass loss from the supernova is less than half of the original total mass [26]. Moreover, even if a BHB does form, if there is no common envelope phase during the supernova, the resulting compact objects will likely be too far apart to merge within the age of the universe [27].

The common envelope phase(s) are important in that they decrease the orbital separation of the binary, but they can also inhibit the production of a number of BHB systems. The common envelope phase can result in the two stars merging via dynamical friction rather than via gravitational wave emission. This process especially inhibits the production of close high-mass BH+BH binaries when the donor star is evolving

Table 2.1: Detection rates for compact binary coalescence sources, from Reference [20], an extensive literature search. Please refer to Reference [20] for details on each estimate. The Initial LIGO rates are based on a horizon distance of 33 Mpc for an optimally oriented 1.4+1.4 $M_\odot$ NS+NS system, 70 Mpc for an optimally oriented 1.4+10 $M_\odot$ NS+BH system, and 161 Mpc for an optimally oriented 10+10 $M_\odot$ BH+BH system. These horizon distances are 445, 927, and 2187 Mpc, respectively, for Advanced LIGO [20]. The intermediate mass ratio inspiral (IMRI) is taken to be a solar mass object spiraling into an intermediate mass black hole (IMBH) having a mass between 50 and 350 $M_\odot$. The rates for these systems are take from Reference [21]'s considerations on 3-body hardening in globular clusters. The rates for IMBH+IMBH ringdown signals are taken from Reference [22]'s considerations of N-body interactions in young star clusters.

IFO	Source	$\dot{N}_{\rm low}$ $\rm yr^{-1}$	$\dot{N}_{\rm re}$ $\rm yr^{-1}$	$\dot{N}_{\rm high}$ $\rm yr^{-1}$	$\dot{N}_{\rm max}$ $\rm yr^{-1}$
Initial	NS-NS	2×10^{-4}	0.02	0.2	0.6
	NS-BH	7×10^{-5}	0.004	0.1	
	BH-BH	2×10^{-4}	0.007	0.5	
	IMRI into IMBH			< 0.001	0.01
	IMBH-IMBH			10^{-4}	10^{-3}
Advanced	NS-NS	0.4	40	400	1000
	NS-BH	0.2	10	300	
	BH-BH	0.4	20	1000	
	IMRI into IMBH			10	300
	IMBH-IMBH			0.1	1

through the Hertzsprung Gap (increasing in radius). If there were no common envelope evolution during the radius increase, there would be hundreds of times more possible detections [28]. In Figure 2.2, the difference between Model B (bottom 2 panels), in which the progenitor stars merge if the common envelope phase is initiated by a Herzsprung gap star, and Model A (top two panels), in which progenitor stars are allowed to remain distinct and can continue evolving into a double compact object, is shown; the result is that Model B has many fewer resultant double compact objects, which also have a much lower chirp mass (see Equation (2.14)) [2]. If the stars can evolve through the Hertzsprung Gap before the common envelope phase, their centers can be further apart. This is important, because if the stars start off too close together, they can end up merging via tidal effects before turning into compact objects [27].

If the progenitor stars are massive enough, a supernova is not needed to produce a compact object. At around and above 100 $M_\odot$, the star's core can be so massive that it collapses without a supernova explosion [27]. This allows the resultant BH to retain most of the mass of its parent star.

The spins of the compact-objects-produced IBE scenarios tend to be aligned, since their massive progenitor stars probably had their spins aligned with the orbital axis (since they were born from the same gas cloud). Even if fragmentation of the gas cloud occurred [29], strong torques along the orbital axis encourage spin-orbital alignment [27]. If one of the black holes received a kick from a supernova, the spins could be misaligned, but this would be rare, since kicks tend to disrupt the binary. Detection of GWs from these systems will allow us to determine the masses and spins of the system producing the GWs, and give us insight into the way the BHB was formed. For example, since core-collapse (with no supernova) produces BHs with no mass (and angular momentum) loss, these BHs will be spinning very rapidly.

Of course, the predicted masses and spins of the BHB systems are very sensitive to the computer simulations' inputs and code itself. The methods for these simulations are introduced in the following section.

2.1.2 Population synthesis

The stellar and binary populations resulting from IBE are often estimated via population synthesis, the umbrella term for a family of computer simulation methods; the results of which are useful for the LVC because they estimate how many pairs of zero-age main sequence stars turn into compact binaries.

For IBE, a single simulation creates a model for primordial stars, sets up rules for the stars' evolutions, and then sets the model to evolving. Of course, there are a lot of assumptions/choices one must make for the initial conditions that are entered into the simulation. In practice, a distribution of reasonable ranges for the flexible parameters is chosen and a Monte Carlo is done over the parameter space; this results in many possible futures for a set of primordial stars, but only those that are consistent with astrophysical observations are considered in the end. Because of the dependence on sanity checking end results against astrophysical observations, which historically have been dominated by galactic NS+NS systems, most past results have only been valid for Milky Way-like galaxies (i.e. spiral galaxies). The results quoted in [21] are from simulations done only for Milky Way-like galaxies. Unfortunately, spiral galaxies just don't produce that many BH+BH systems because the stars forming the progenitors are not sufficiently massive, but the initial mass function for elliptical galaxies is much shallower, allowing for a greater proportion of high mass zero age main sequence stars [30].

Another key peculiarity about the simulations used to predict BH+BH mergers in [21] is that the metallicity of stars is usually assumed to be solar metallicity [31]. Metallicity refers to the atomic content of stars. There are many ways of measuring metallicity; one way is Z, the fraction of the star's chemical composition that is not hydrogen and helium. Our sun, a Population I star, has $Z = 0.02$ [32]. Though this is a relatively high metallicity itself, high-metallicity stars are generally categorized by having a metallicity greater than that of our sun. High-metallicity stars are second generation stars (Population I) — they are made of the recycled material from the supernova of their parent star [33]. High-metallicity stars tend to be lighter than low-metallicity stars because of stellar wind effects — photons ejected by the star hit the electron cloud of the metal atoms in the outer layer of the star and push them out [34]. In contrast, low-metallicity stars' outer layers are more transparent to photons and therefore are not subject to significant mass loss before they have the opportunity to undergo core collapse and potentially turn into a black hole. This effect is twofold relevant to the search for high-mass CBCs: first, the mass of the final black holes can be larger, thus increasing the distance to which we are sensitive to these systems; second, the higher masses make the likelihood of a large natal kick much lower, so the black hole is more likely to stay in the binary. The effect of metallicity on the number and mass distributions of resultant double compact objects in population synthesis is shown in Figure 2.2 [2]. Note that only in the second panel (low rate of common envelope merger and low metallicity) are there a significant number of high mass BH+BH systems. In reality, stars will probably have a range of

metallicities between these values [35].

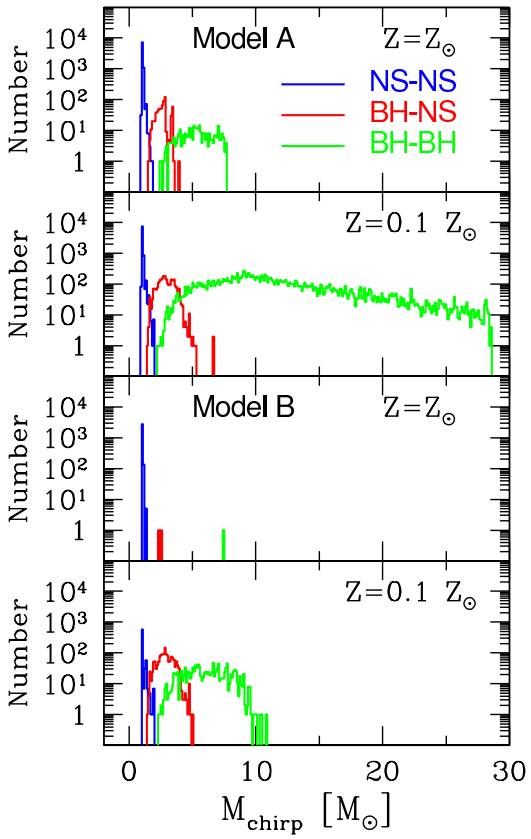

Figure 2.2: Histograms of number versus chirp mass for 4 different Population Synthesis scenarios [2]. The top two panels are for simulations of category A, in which progenitor stars are allowed to remain distinct and can continue evolving into a double compact object even if the donor star is evolving through the Hertzsprung gap during the common envelope phase; the bottom two are for category B, in which the progenitor stars merge if the common envelope phase is initiated by a Herzsprung gap star. Note that for both A and B, both the number of, and the maximum chirp mass (which, as we will see in Section 2.2.1, is the relevant combination of component masses used for describing CBCs) increase for the systems with 10 percent solar metallicity (second and fourth panels) [2].

2.1.3 Dynamical formation scenarios

Interactions between black holes in dense cluster environments can also lead to close BH+BH systems [36]. There are three main dynamical formation scenarios that can lead to a high-mass black hole binary system: 1) N-body interactions in globular clusters, 2) 2-body scattering in Galactic nuclei, 3) 3-body interactions involving black holes in galactic nuclei [21]. The theory behind such interactions and the observational evidence constraining them is much weaker than for IBE, but they can produce more black holes in the mass range relevant to this thesis, and the detection of such systems can inform the astrophysics [37].

2.1.3.1 Globular clusters

Globular clusters are very tightly bound by gravity, which gives them their spherical shapes and relatively high stellar densities toward their centers (mass segregation). In the dense environment, high-mass stars quickly evolve via supernova into black holes. These massive black holes fall further toward the center, where they meet with other black holes, which will quickly break up any remaining star-BH binaries. During this interaction, the BHs acquire kinetic energy and can be ejected from the cluster as either single BHs or binaries. This entire process is known as segregation, decoupling, and evaporation [37]. These binaries can merge much more quickly than those produced by IBE, since the interactions with the other nearby objects cause the binary to "harden" (i.e. for the orbital separation to decrease) [27].

Since BH+BH binaries produced from dynamical cluster evaporation do not rely on supernova kicks, common envelopes, or mass transfer to bring them close enough to merge in a Hubble time, their masses can be higher, see Figure 2.3 [3]. Their spins and orbital angular momenta are not aligned in any way because interactions tilt the orbital plane [27].

Future gravitational wave observations will provide very useful astrophysical information to this field by more tightly constraining g_{cl} (the fraction of stars formed in clusters) and g_{evap} (the fraction of cluster-forming mass with birth conditions that could lead to segregation, decoupling, and evaporation). Weak observational constraints combined with numerical simulations yield $g_{cl}g_{evap} = 5 \times 10^{-2}$, leading to a plausible but optimistic rate listed as $\dot{N}_{high}$ of IMBH+IMBH mergers in Table 2.1.

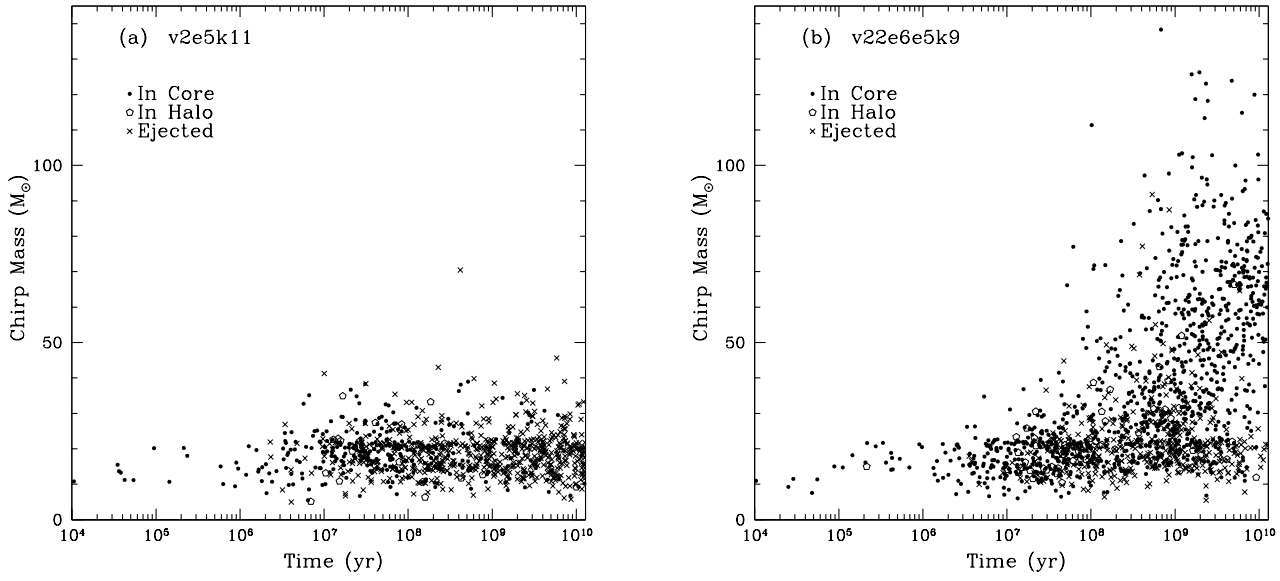

Figure 2.3: A comparison of two numerical simulations of BH pair formation in globular clusters. The left panel (a) shows the least efficient (out of 46 simulations) cluster, in terms of producing large BHs and BH+BH binaries. The right panel (b) does not reach equipartition (when the rate of BH interactions with other stars in the cluster is less than or equal to the rate of BHs with other BHs) before a Hubble time; therefore, there are many more BHs in the cluster — allowing the formation of many more binaries. The x-axis is time since the beginning of the simulation (11 Myr after the Big Bang) [3].

2.1.3.2 Galactic nuclei

A galactic nucleus with a supermassive black hole and many stellar-mass black holes will have steep density cusps, which allow the formation of tight BH+BH binaries directly via 2-body scattering. In this scenario, an encounter between two BHs that would initially be hyperbolic, can lead to capture via energy loss due to gravitational radiation (Bremsstrahlung) during the point when the two BHs are closest together. These binaries tend to be eccentric and coalesce on a timescale of hours; in fact, they are still eccentric when they enter the LIGO band [38].

In the nuclear clusters of small galaxies without a supermassive black hole, 3-body interactions cause wide BH+BH binaries to tighten more quickly than they would in an isolated scenario, allowing the radiation reaction to lead them into inspiral. Similar to what has been observed in triple star systems, the two most massive objects form a binary; the third object orbits the binary and is close and massive enough to interact with it and affect the eccentricity of the binary. The eccentricity oscillates (the oscillations are referred to as Kozai cycles), which causes the binary's orbit to harden more quickly than if it were isolated — an eccentric binary will tend to circularize as the orbital separation decreases, which in turn decreases the rate of hardening [27].

There are no established predictions for the number of BH+BH or BH+NS systems (with total mass between 25 and 100 $M_{\odot}$) from 2-body scattering or N-body interactions in globular clusters. If the BHs are approximately of solar mass, Reference [39] predicts a "few $\times$ 10^{-2}" mergers per nuclear cluster per Myr. Reference [27] predicts that all dynamical formation scenarios could produce 10 BH+BH mergers (with total mass around and above 100 $M_{\odot}$) per cubic Mpc per Myr. Such mergers would not have spins aligned with their orbits, because orbital tilting is produced during the cycles [27].

2.1.4 Observational evidence from low-metallicity galaxies

There have recently been observed two extragalactic X-ray binaries in low-metallicity environments: IC10 X-1 and NGC300 X-1. Each system is thought to consist of a BH with mass $\sim$ 20 - 30 $M_{\odot}$ accreting from a massive Wolf-Rayet (WR) star companion with mass $\gtrsim$ 20 $M_{\odot}$. Models predict that these systems will evolve into BH+BH binaries with chirp masses of about 15 $M_{\odot}$ within 3 Gyr. Extrapolating from the fact that there are 2 of these systems within 2 Mpc, we estimate a detection rate of R = $3.4^{+8.3}_{-2.9}$ detections per year at the 99 percent confidence level, for initial LIGO [40]. That no such signals were found in initial LIGO/Virgo data allows us to rule out the upper end of this predicted rate.

Measuring the rates via future GW observations will allow us to tune the knobs of the population synthesis models, have a better understanding of low versus high metallicity environments, and gain a deeper analytical understanding of the different stages of stellar evolution [40].

2.2 The physics of gravitational waves from compact binary coalescences

2.2.1 The mathematical formulation of gravitational waves

Gravitational waves are a theoretical consequence of Einstein's theory of General Relativity. The fundamental equations of this theory, relating the curvature of spacetime to matter/energy are

$$G_{\alpha\beta} = \frac{8\pi G}{c^4} T_{\alpha\beta}, \tag{2.1}$$

where $G_{\alpha\beta}$, a function of the spacetime metric g_{ab} and its derivatives, is the Einstein tensor describing the curvature of spacetime and $T_{\alpha\beta}$ is the stress-energy tensor. G and c are the gravitational constant and the speed of light, respectively. α and β run over time and three spatial coordinates. The theory and formalism used in this section follow those of the book "Gravitational-Wave Physics and Astronomy: An Introduction to Theory, Experiment and Data Analysis" by Jolien D.E. Creighton and Warren G. Anderson.

In *linearized gravity*, the general spacetime metric can be expressed as the flat Minkowski metric $\eta_{\alpha\beta}$ plus some perturbation $h_{\alpha\beta}$:

$$g_{\alpha\beta} = \eta_{\alpha\beta} + h_{\alpha\beta}. \tag{2.2}$$

It is useful to use the trace-reversed metric perturbation instead, which is given by

$$\overline{h}_{\alpha\beta} = h_{\alpha\beta} - \frac{1}{2}\eta_{\alpha\beta}. \tag{2.3}$$

Then, in the Lorenz gauge (where the divergence of the trace-reversed metric is zero), the linearized Einstein equations become

$$\Box\overline{h}_{\alpha\beta} = \frac{8\pi G}{c^4} T_{\alpha\beta}, \tag{2.4}$$

where $\Box$ is the d'Alembert operator [41], which is the Laplacian generalized to 4-dimensional flat (Minkowski) spacetime.

In a vacuum, this becomes

$$\Box\overline{h}_{\alpha\beta} = 0, \tag{2.5}$$

which we recognize as a wave equation. We can choose a plane-wave solution traveling in the z direction. By combining Equation (2.5) and Equation (2.3), we see that the non-vanishing parts of the trace-reversed metric are $\overline{h}_{xx}$, $\overline{h}_{xy}$, $\overline{h}_{yx}$, and $\overline{h}_{yy}$, which are all functions of $(t - z/c)$. This corresponds to a metric perturbation traveling at the speed of light along the z axis [41].

Independent of gauge, there are two independent functions of $(t - z/c)$ that come out of these equations. These will be called h_+ and $h_\times$ and are the two polarizations of these transverse waves (the so-called

gravitational waves referred to in this thesis) [41].

The energy carried by these waves is

$$T_{tt}^{GW} = \frac{c^4}{16\pi G}\langle \dot{h_+}^2 + \dot{h_\times}^2 \rangle \ \propto \omega^2, \tag{2.6}$$

where T_{tt}^{GW} is the time-time component of the stress-energy tensor associated with the GW and ω is the angular frequency of the wave [41].

In the transverse traceless gauge (denoted ^{TT}), the form of the metric perturbation both far (characteristic size of the source $\ll$ GW wavelength $\ll$ distance to the source r) from and near (GW wavelength $\gg$ distance to the source $r \gg$ characteristic size of the source) to the source is, under the *quadrupole approximation*,

$$h_{ij}^{TT} \simeq \frac{2G}{c^4 r}\ddot{I}^{TT}(t - r/c), \tag{2.7}$$

where r is the distance to the source and I_{ij}^{TT} is the quadrupole tensor of the source in the transverse traceless gauge, given by

$$I_{ij}^{TT} = \int \left(||\overrightarrow{x}||^2 \delta_{ij} - x_i x_j \right) \rho(\overrightarrow{x}) d^3\overrightarrow{x}. \tag{2.8}$$

Note that in this gauge, $h_\times$=h_{xy} and h_+=h_{xx}. In the quadrupole approximation, higher moments of inertia are ignored because the quadrupole moment dominates [41].

For an orbiting compact binary system, under the quadrupole approximation, the form of the two polarizations of the metric perturbation looks like this far from the source:

$$h_+(t(\beta)) = -\frac{2G\mu}{c^2 r}(1 + \cos^2 \iota)\beta^2 \cos 2\phi(\beta), \tag{2.9}$$

$$h_\times(t(\beta)) = -\frac{4G\mu}{c^2 r}\cos \iota \beta^2 \sin 2\phi(\beta), \tag{2.10}$$

where μ is the reduced mass $\mu = m_1 m_2/(m_1 + m_2)$, ι is the inclination angle from the observer to the source, $\phi(\beta)$ tracks the orbital phase, and β is the characteristic velocity of the center of mass system divided by the speed of light (v/c), which can be used as a proxy for the orbital frequency, ω, or orbital separation, a, thanks to Kepler's law,

$$\beta = \frac{\sqrt[3]{GM\omega}}{c} = \sqrt{\frac{GM}{ac^2}}. \tag{2.11}$$

From Equation (2.5) and Equation (2.11), one can see that as the orbit gets smaller, the frequency of the gravitational wave increases, as does its amplitude; this is known as a chirp signal [41].

Using the quasi-Newtonian formalism (note that Newton's laws say the binary orbit is stable, but in the literature this is nonetheless sometimes referred to as Newtonian), which is applicable when the orbit is not yet relativistic, the GW frequency

$$f = 2f_{orb} = \omega/\pi \tag{2.12}$$

evolves like

$$\frac{df}{dt} = \frac{96}{5}\pi^{8/3}\frac{G\mathcal{M}}{c^3}^{5/3} f^{11/3}, \tag{2.13}$$

where

$$\mathcal{M} = (m_1 m_2)^{3/5}(m_1 + m_2)^{-1/5} \tag{2.14}$$

is known as the *chirp mass*. This quantity is important because the lowest-order (in β) term in the CBC waveform depends only on the chirp mass, not the mass ratio. The chirp mass can also be expressed as

$$\mathcal{M} = M_{\text{total}}\eta^{3/5}, \tag{2.15}$$

where $M_{\text{total}} = m_1 + m_2$, and

$$\eta = \frac{m_1 m_2}{M_{\text{total}}^2}. \tag{2.16}$$

If we integrate Equation (2.13) from an arbitrary time to the time of coalescence, t_c, we get

$$h_+(t) = -\frac{2G\mathcal{M}}{c^2 r}\frac{(1+\cos^2\iota)}{2}\left(\frac{c^3(t_c-t)}{5G\mathcal{M}}\right)^{-1/4}\cos\left[2\phi_c - 2\left(\frac{c^3(t_c-t)}{5G\mathcal{M}}\right)^{5/8}\right] \tag{2.17}$$

$$h_\times(t) = -\frac{2G\mathcal{M}}{c^2 r}\cos\iota\left(\frac{c^3(t_c-t)}{5G\mathcal{M}}\right)^{-1/4}\sin\left[2\phi_c - 2\left(\frac{c^3(t_c-t)}{5G\mathcal{M}}\right)^{5/8}\right] \tag{2.18}$$

as the representations of the inspiral portion of the waveform in the time domain; note that h_+ and $h_\times$ are unitless and represent a *strain*. The effect of the different polarizations can be illustrated by imagining a ring of particles in the plane perpendicular to the direction of propagation. The h_+ polarization will alternately stretch the circle in the x-direction (while squeezing it in the y-direction), then stretch the circle in the y-direction (while squeezing it in the x-direction). The $h_\times$ polarization has the same effect on the circle, but rotated by $\pi/2$; see Figure 2.4. The polarization content of GWs reaching an observer depends solely on the inclination angle ι. If $\iota = 0$, the plane of the binary orbit is face-on to the observer, and the GW has equal amounts of h_+ and $h_\times$ (circular polarization). If $\iota = \pi/2$, the plane of the binary orbit is edge-on to the observer, and the GW is only h_+ (linear polarization).

In the frequency domain, which is used for LIGO/Virgo data analysis, the leading post-Newtonian (PN) order term of the chirp waveform looks like

$$\tilde{h}(f) = \int_{-\infty}^{\infty} e^{-2\pi i f t}(h_+ + i h_\times)dt = \mathcal{A}f^{-7/6}e^{i\psi(f)+i\pi/4}, \tag{2.19}$$

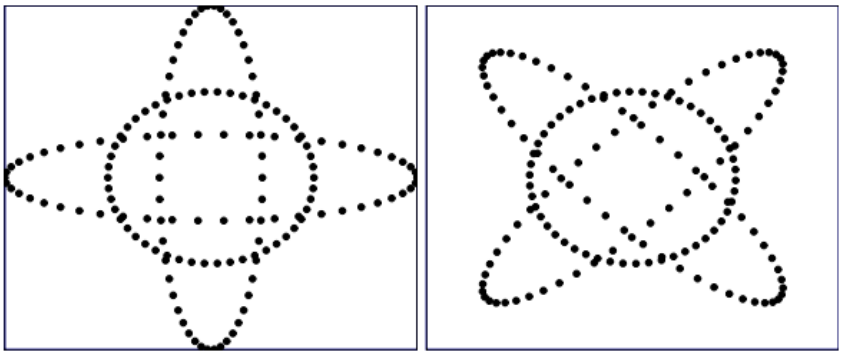

Figure 2.4: The effect of gravitational waves on a circle of particles in a plane perpendicular to the direction of propagation. The left panel shows a purely plus-polarized GW. During a full period of the GW, the particles go from circle to horizontal ellipse to circle to vertical ellipse back to circle. The right panel shows a purely cross-polarized GW.

where $\Psi(f)$ describes the phase evolution and

$$\mathcal{A} = \frac{\mathcal{C}}{r\pi^{2/3}}\sqrt{\frac{5}{24}}\mathcal{M}^{5/6}, \tag{2.20}$$

where $\mathcal{C}$ is a function of the antenna pattern of the detector (see Figure 3.11) and inclination angle ι. r is the distance to the source and $\mathcal{M}$ is the chirp mass. Note that Equation (2.19) uses the stationary phase approximation (that the frequency of the wave changes slowly during the inspiral) [41]; the full waveform can be found in [42].

PN theory uses Taylor expansions in β to calculate waveforms that are accurate up to the final stages of the inspiral and, notably, can be used in the generic case where both compact objects are spinning in any direction. Inspiral-only waveforms have been calculated up to corrections β^7 (this is known in the literature as the parametrized post-Newtonian (PPN) order 3.5). However, near merger, the PPN expansion breaks down and other methods are required because as the two bodies get closer together, higher order radiative effects and non-linear dynamics significantly alter the waveform. NR is needed to calculate the waveform for these last few inspiral cycles and merger. See Reference [43] for an overview of NR methods for NS+BH systems. There have been many NR simulations done for non-spinning (see Figure 2.5) and aligned spin systems, but current progress is being made on a full catalog of non-aligned spin waveforms, which look significantly different due to precession effects (see Figure 2.6). After the merger, in the case of 2 black holes, the ringdown is described analytically as a superposition of quasinormal modes [44].

The following two subsections describe the two methods used to compute the full IMR waveforms used in this thesis; a more in-depth comparison of PN templates can be found in [45] and full IMR waveforms in [44] and [46]. The waveforms used in this thesis are both for nonspinning and aligned spin systems, which is reasonable but not complete — as seen in Section 2.1, IBE tends to produce binaries with aligned spin, but there is no reason to suspect this for dynamical formation scenarios. The waveforms for non-aligned spin

systems look significantly different because the spin-orbit coupling of non-aligned spins causes the plane of the orbit to precess, which causes amplitude and phase fluctuations in the waveform seen in the detector [47]; see Section 3.2 for a discussion of a detector's response to a passing GW.

The waveform for a specific system can look significantly different depending on the waveform family used to parametrize it. Table 2.2 and Table 2.3 show how even the number of cycles differ for the different families.

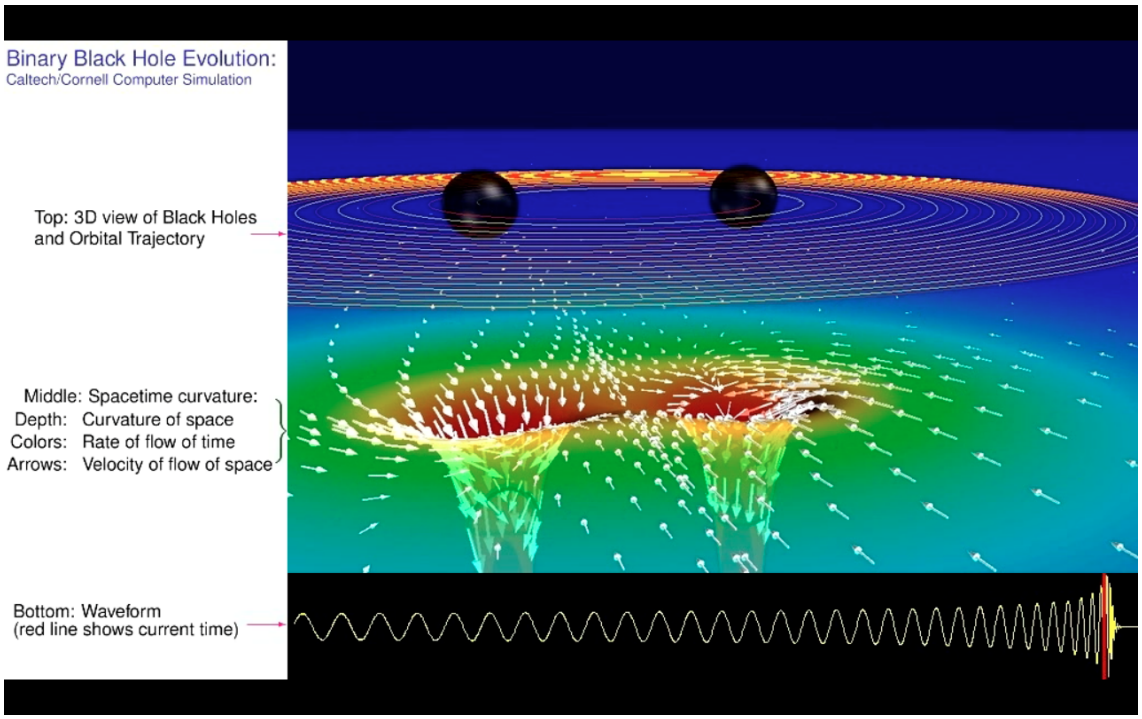

Figure 2.5: A screenshot from a Caltech-Cornell NR simulation of two equal-mass nonspinning black holes. Visit for the full movie and more animated simulations.

2.2.1.1 Effective-one-body + numerical relativity (EOBNR) waveforms

The EOBNR waveforms combine the effective-one-body (EOBNR) formalism with NR results. effective-one-body (EOB) methods map the dynamics onto a test particle in an external effective metric. Though the EOB equations can be expressed analytically, what is done in practice is a non-perturbative resummation of the PN expansion of the equations of motion [48]. For a single system, EOB waveforms are calculated for each leading l, m mode (using spherical harmonic notation), but still have a few tunable parameters. Each waveform is calculated separately in two parts: the *inspiral-plunge* and the *merger-ringdown*. For the systems whose waveforms have been calculated with NR, Buonanno et al. calibrate the inspiral-plunge EOB waveforms against the NR waveforms and set the tunable parameters to achieve the greatest amplitude and phase consistency between the two [49]. The inspiral-plunge waveform is then stitched to the merger-ringdown waveform, which is a sum of 8 quasinormal modes. The tuned EOBNR waveforms used in the

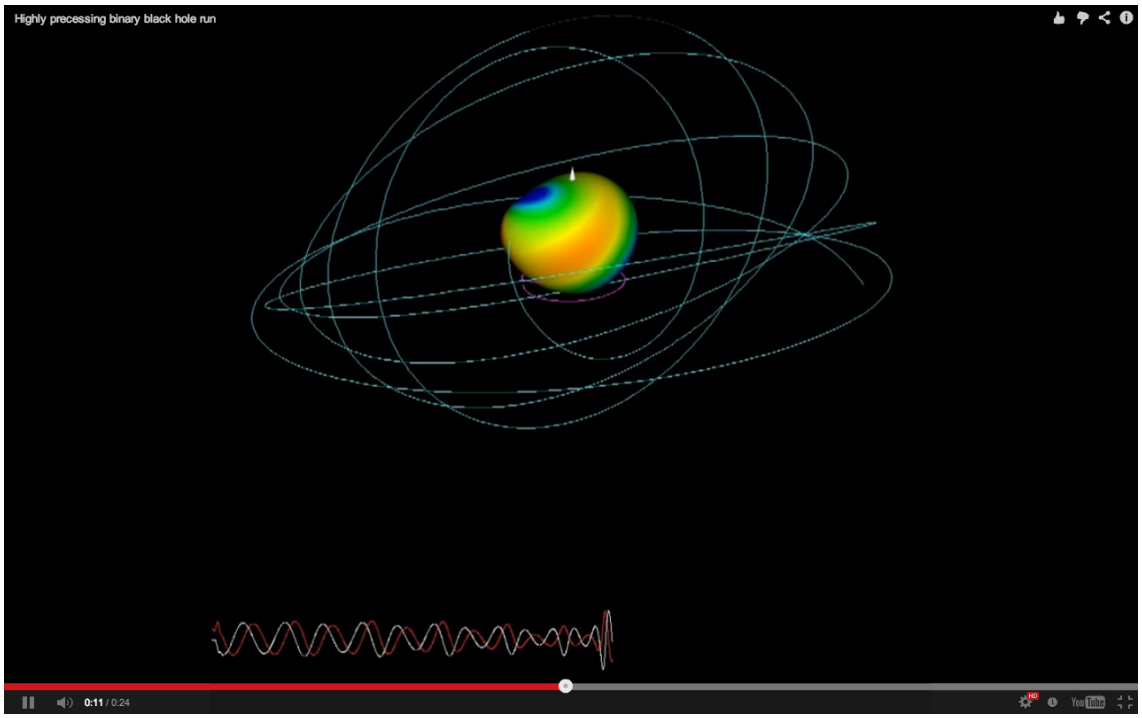

Figure 2.6: A screenshot, at merger, from a NR simulation of two black holes with a mass ratio of 6:1 and non-aligned spins of .91 and .3, respectively. Note the amplitude and phase modulation, which is due to the precession of the orbital plane resulting from the spin-orbit coupling of the non-aligned spins. Visit http://www.black-holes.org/explore2.html for the full movie and more animated simulations.

search for high-mass CBCs have been tuned using NR for mass ratios m_1/m_2 = 1, 2, 3, 4 ,6 and total masses $M = 20 - 200 M_\odot$ [49].

There are two different versions of EOBNR waveforms used in this thesis. EOBNRv1 is used, for historical reasons, to create the template banks as discussed in Section 7.3.2. EOBNRv2 is used to create the simulated signals we use to test the sensitivity of our pipeline and create upper limits. Though the EOBNR approach works for waveforms from systems where the compact objects are spinning, the code was not reviewed in time for it to be included in the search described in this thesis. Figure 2.7 and Figure 2.8 show the EOBNRv2 waveforms for the equal-mass case, as compared to the waveforms discussed in the following section. Although EOBNRv2 waveforms were only tested for mass ratios up to 6, they should be valid in the limit of large mass ratios, as they are created on the model of a test particle orbiting an effective potential; Figure 2.9 and Figure 2.10 show these EOBNRv2 waveforms for the asymmetric mass ratios on the template bank for the highmass search (25 - 100 $M_\odot$).

The EOBNR waveforms are created in the time domain and are fast-Fourier transformed (FFTed) before they are used in the analysis. The FFT waveform multiplied by the square root of the frequency can be laid atop the strain amplitude sensitivity of the detectors, allowing us to easily visualize our ability to detect a particular signal. The strain amplitude sensitivity of the detectors is a result of design choices and known and unknown noise sources, which will be described in Section 3.4.

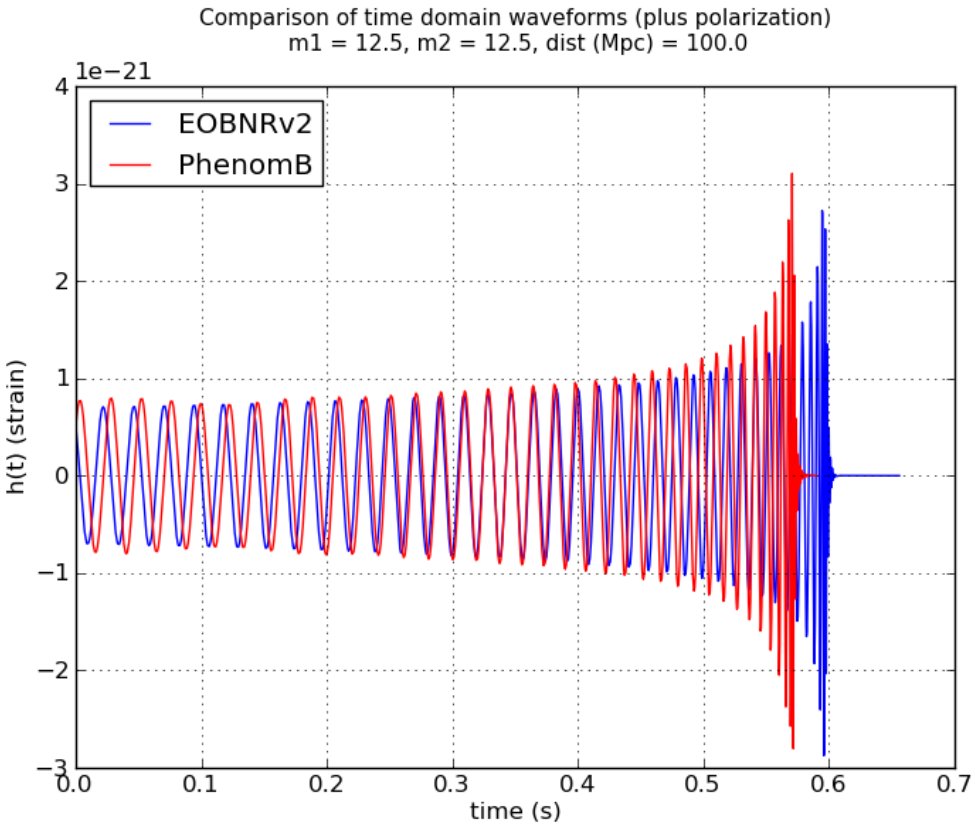

Figure 2.7: Time-domain waveforms for a 12.5 $M_{\odot}$+ 12.5 $M_{\odot}$system.

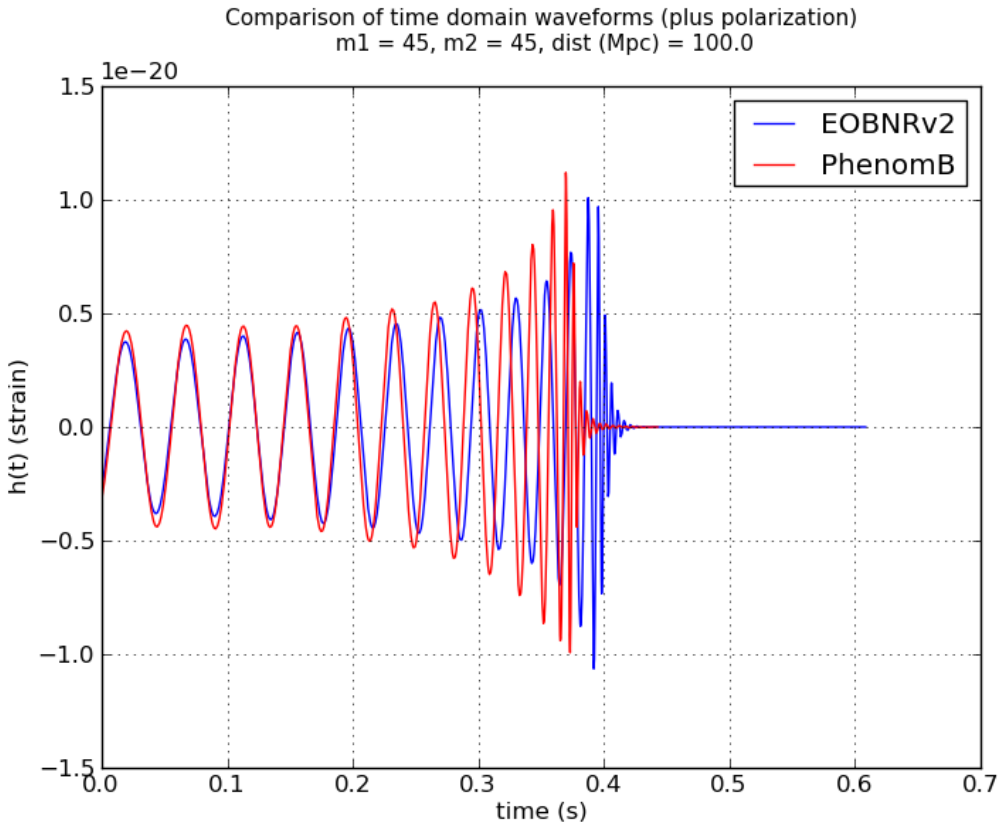

Figure 2.8: Time-domain waveforms for a 45 $M_{\odot}$+ 45 $M_{\odot}$system.

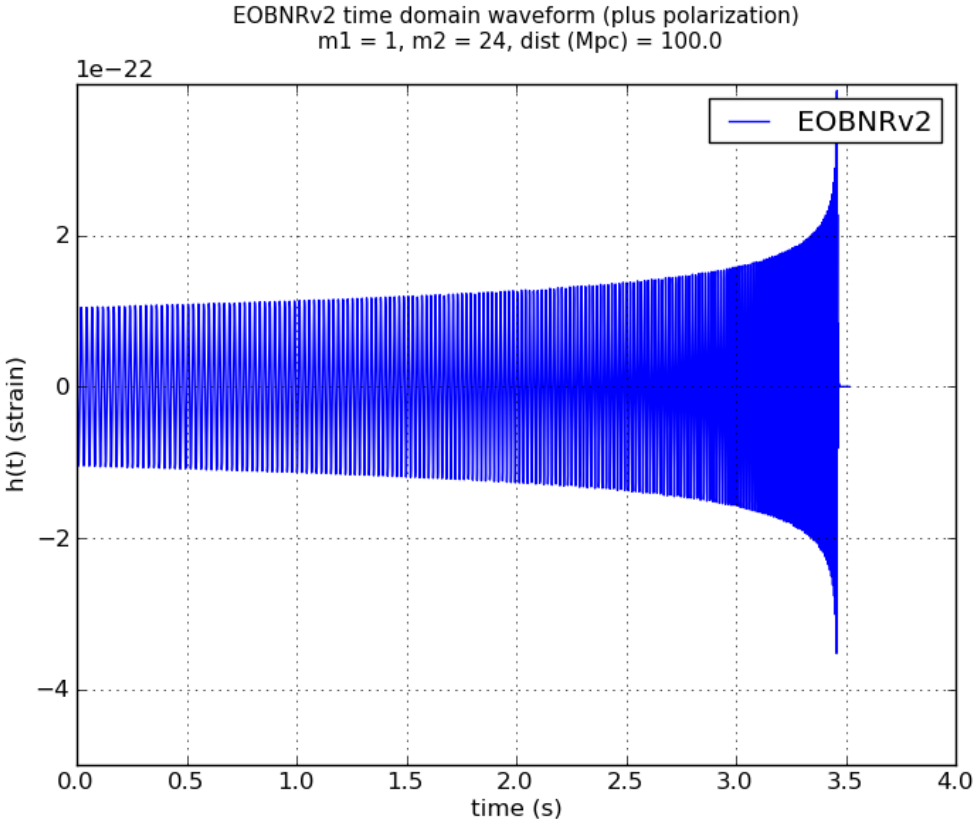

Figure 2.9: An EOBNRv2 time-domain waveform for a 1 $M_{\odot}$+ 24 $M_{\odot}$system. Note that the merger and ringdown are present even though not visible due to the scale of the plot. The IMRPhenomB waveform is not plotted, as it is not valid for this mass ratio.

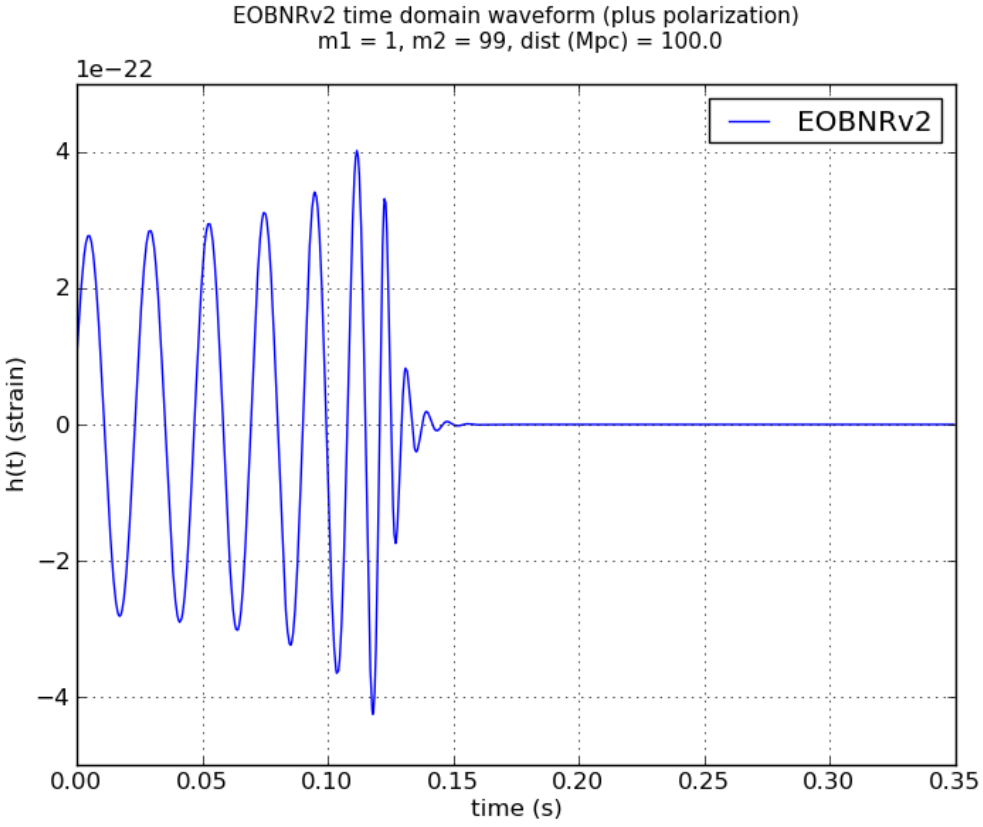

Figure 2.10: An EOBNRv2 time-domain waveform for a 1 $M_{\odot}$+ 99 $M_{\odot}$system. The IMRPhenomB waveform is not plotted, as it is not valid for this mass ratio.

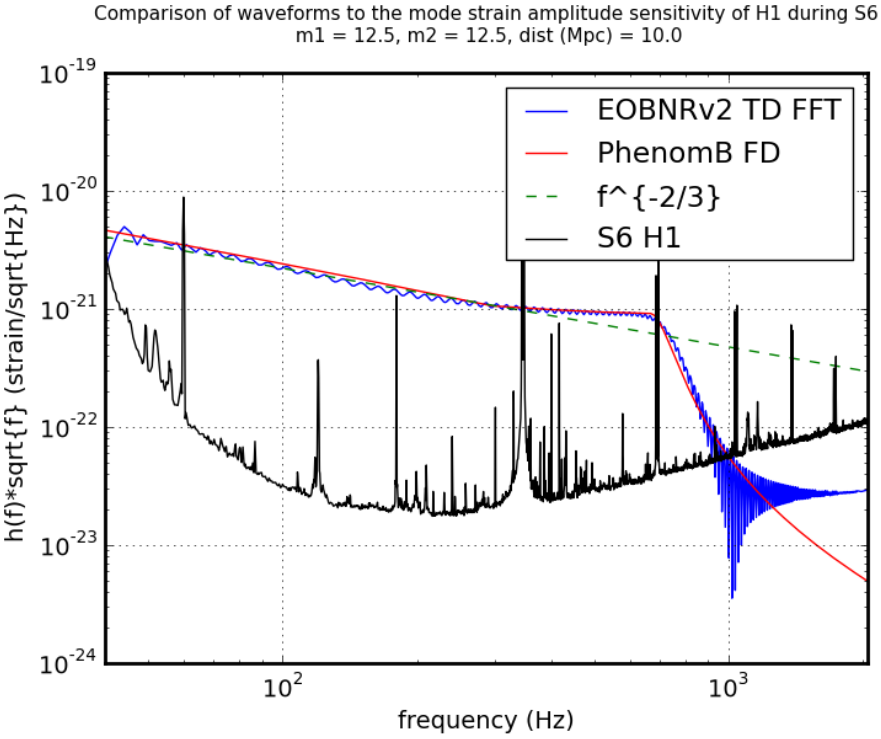

Figure 2.11: Waveforms for a 12.5 $M_{\odot}$+ 12.5 $M_{\odot}$ system in the frequency domain, compared to the mode of H1's noise amplitude spectral density during S6 [4]. The EOBNR waveform was originally in the time domain, and was fast Fourier transformed into the frequency domain, resulting in non-physical wiggles. The green dashed curve indicates the frequency journey of an inspiral-only waveform, whose amplitude has been set by the IMRPhenomB waveform. Merger is short and has an undefined duration. The Fourier transform of a ringdown is the imaginary part of a Lorentzian, and can be seen in this plot beginning when the blue or red curve deviates (has a less steep slope) from the green dashed curve and continuing through the steeper negative slope towards the right of the plot, remembering that the wiggles on the blue curve are non-physical.

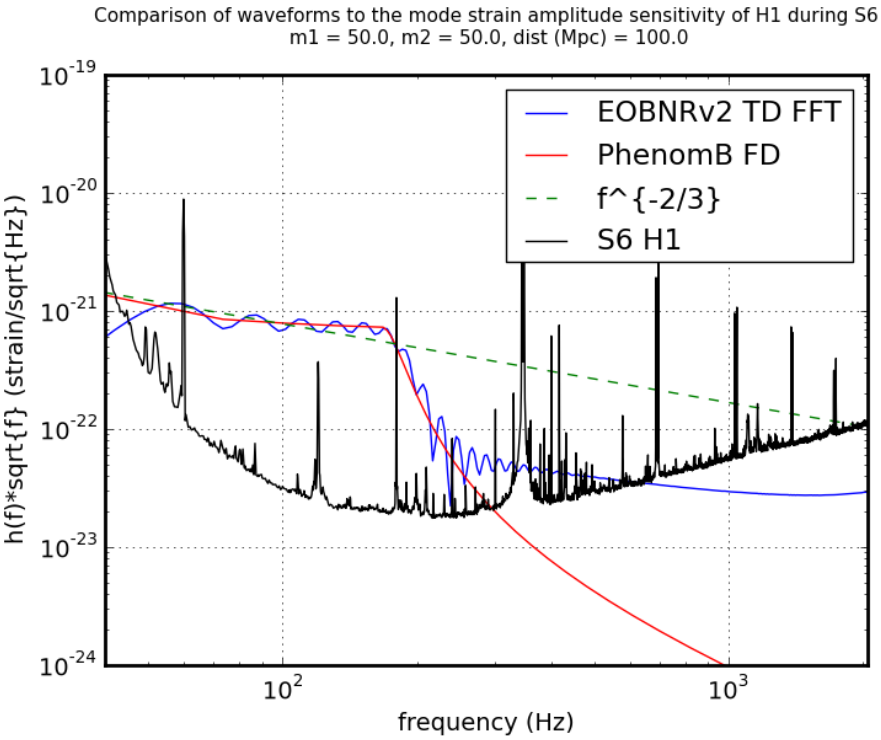

Figure 2.12: Waveforms for a 50 $M_{\odot}$+ 50 $M_{\odot}$ system in the frequency domain, compared to the mode of H1's noise amplitude spectral density during S6 [4]. The EOBNR waveform was originally in the time domain, and was fast Fourier transformed into the frequency domain, resulting in non-physical wiggles throughout the waveform, since the waveform has a finite duration. The green dashed curve indicates the frequency journey of an inspiral-only waveform, whose amplitude has been set by the IMRPhenomB waveform. Merger is short and has an undefined duration. The Fourier transform of a ringdown is the imaginary part of a Lorentzian, and can be seen in this plot beginning when the blue or red curve deviates (has a less steep slope) from the green dashed curve and continuing through the steeper negative slope towards the right of the plot, remembering that the wiggles on the blue curve are non-physical.

2.2.1.2 Phenomenological waveforms including spin

Phenomenological waveforms start with an analytical PN inspiral, which is stitched to a merger-ringdown signal with parameters tuned using NR methods. As such, the waveform can be expressed by the following equation:

$$A(f) \equiv C f_1^{-7/6} \begin{cases} f'^{-7/6}(1 + \Sigma_{i=2}^{3} \alpha_i v^i) & \text{if } f < f_1 \\ w_m f'^{-2/3}(1 + \Sigma_{i=1}^{2} \epsilon_i v^i) & \text{if } f_1 \leqslant f < f_2 \\ w_r \mathcal{L}(f, f_2, \sigma) & \text{if } f_2 \leqslant f < f_3, \end{cases} \tag{2.21}$$

where C is a numerical constant depending on sky-location, orientation, and masses; and $f' = f/f_1$. The inspiral phase ends at f_1, the merger phase is between f_1 and f_2, and the ringdown phase is between f_2 and f_3. According to post-Newtonian formalism, $v = (\pi M_{\text{total}} f)^{1/3}$ can be compared to β in Equation (2.11), except with $G = c = 1$, and f being the GW frequency rather than the orbital frequency. $\mathcal{L}$ is a Lorentzian centered around f_2 with width σ [50]. The α_i and ϵ_i are tunable parameters, constructed as functions of the mass ratio and an optional combined spin parameter [50], given by

$$\chi = \left(1 + \frac{m_1 - m_2}{M}\right) \frac{\chi_1}{2} + \left(1 + \frac{m_2 - m_1}{M}\right) \frac{\chi_2}{2}, \tag{2.22}$$

where $\chi_i = S_i/{m_i}^2$ is the dimensionless spin of black hole i, projected onto the orbital angular momentum.

The full waveforms have been calibrated against NR for $|\chi| \leqslant 0.85$, and mass ratios between 1 and 4 and are recommended for mass ratios only up to 10 [50]; the inspiral portion of the waveform has also been checked to be consistent in the extreme mass ratio limit [50]. To match what we expect astrophysically, we would like to trust these up to mass ratios of 20; efforts in numerical and analytical relativity are currently underway to reach this goal.

This family of phenomenological waveforms was created in the frequency domain. Examples are shown in Figure 2.11, for an equal-mass system with a total mass of 25 $M_\odot$, and in Figure 2.12 for an equal-mass system with a total mass of 100 $M_\odot$. Note that the distance of the system in Figure 2.11 is at 10 Mpc, but 100 Mpc in Figure 2.12. As the IMRPhenomB waveforms are created in the frequency domain, they do not have the same non-physical wiggles as the EOBNR waveforms in Figure 2.11 and Figure 2.12.

This thesis uses two sets of phenomenological waveforms — a nonspinning set and a set with aligned or anti-aligned spins (the waveform gets much more complicated when the precession effects are included, causing a vast increase in the parameter space needed to be searched over). Systems with aligned spins will always have $\chi > 0$ and will produce longer waveforms in LIGO's sensitive band than systems with the same mass and $\chi \leqslant 0$; see, for example, the equal-mass system in Figure 2.13. Systems with anti-aligned spins can have a range values of the combined spin parameter; Figure 2.14 shows the case of an equal-mass system with anti-aligned spins of equal magnitude — by Equation (2.22), this system has $\chi = 0$. For a

system with a component mass ratio of 1:4 and a total mass of 50 $M_{\odot}$, Figure 2.15 depicts the $\chi = 0$ (non-spinning) and $\chi = .5$ (aligned spin) case. Figure 2.16 shows the anti-aligned spin cases for the same system ($\chi_{1,2} = \pm 0.5$); if the more massive component has the positive dimensionless spin parameter, the combined spin parameter is positive (likewise, if the more massive component has a negative dimensionless spin parameter, the combined spin parameter is negative). As is seen in Figure 2.15 and Figure 2.16, as the combined spin parameter increases, so does the length of the waveform in LIGO's sensitive band.

The $\chi = 0$ IMRPhenomB waveforms are also compared to their EOBNRv2 counterparts in Figure 2.7 and Figure 2.8. Although the two models used in the analysis described in this thesis are supposed to be similar, they differ in end time and phase evolution, which can make a big difference; therefore, it is important to use both — until we detect GWs, we do not know which one better matches reality. The IMRPhenomB waveforms, which are used in this thesis to assess our sensitivity, are not used in the official rate upper limit calculation as they are not trusted above a mass ratio of 10.

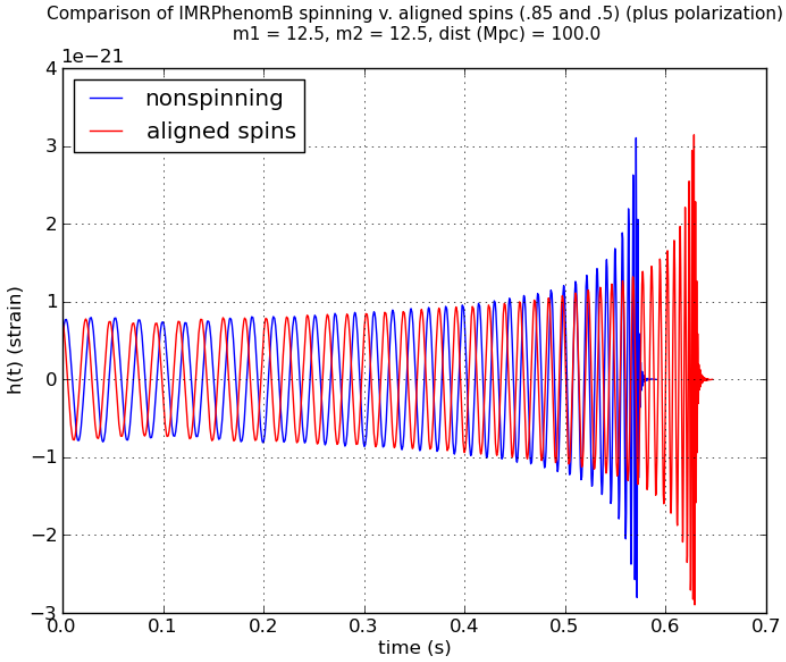

Figure 2.13: Time-domain waveforms for a 12.5 $M_{\odot}$+ 12.5 $M_{\odot}$system. Blue: neither black hole is spinning. Red: dimensionless spins are aligned but unequal in magnitude ($\chi_1 = 0.85$, $\chi_2 = 0.5$), giving a combined spin parameter of $\chi = 0.675$.

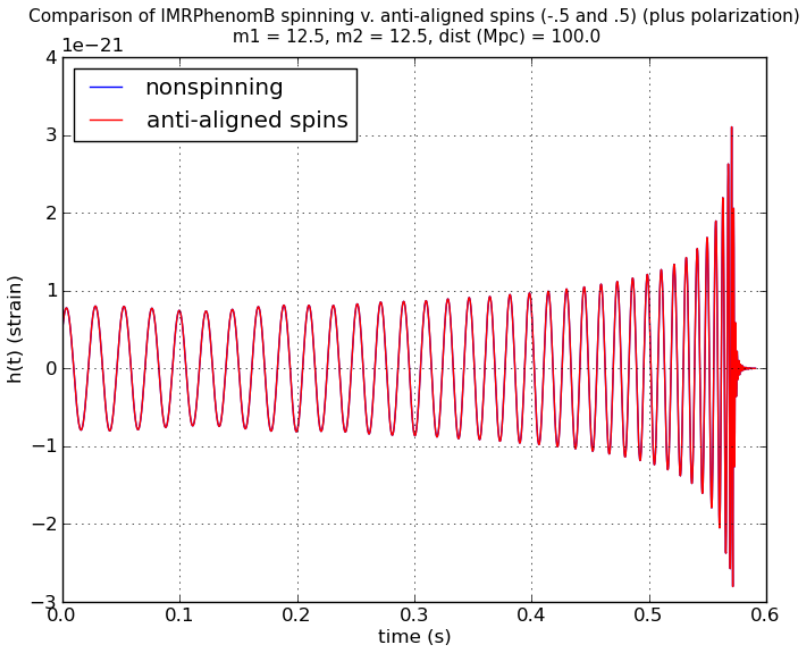

Figure 2.14: Time-domain waveforms for a 12.5 $M_{\odot}$+ 12.5 $M_{\odot}$system. Blue: neither black hole is spinning. Red: dimensionless spins are anti-aligned, and equal in magnitude ($\chi_{1,2} = 0.5$). The red and blue curves lie atop one another, as is expected — the combined spin parameter $\chi = 0$ for both systems.

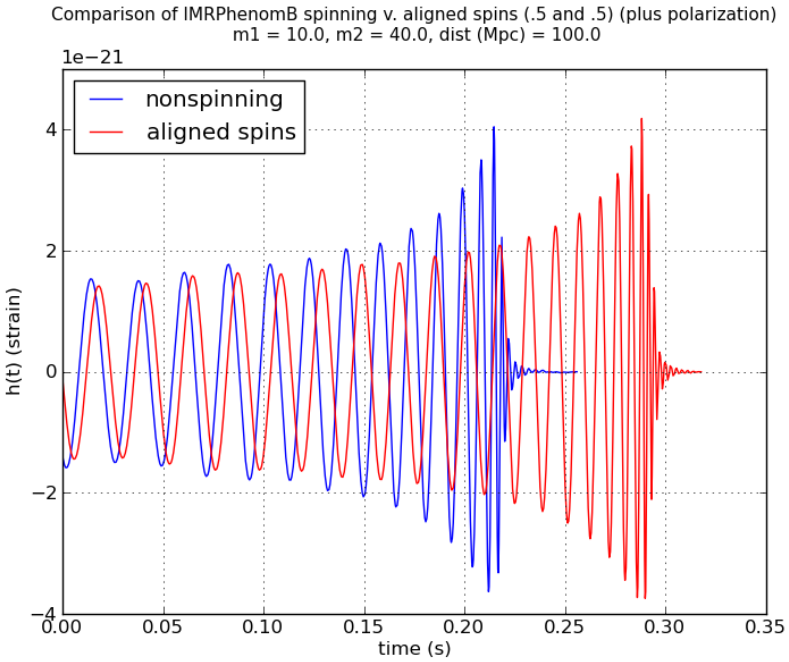

Figure 2.15: Time-domain waveforms for a 10 $M_{\odot}$+ 40 $M_{\odot}$system. Blue: neither black hole is spinning ($\chi = 0$). Red: dimensionless spins are aligned and equal in magnitude, with $\chi = 0.5$.

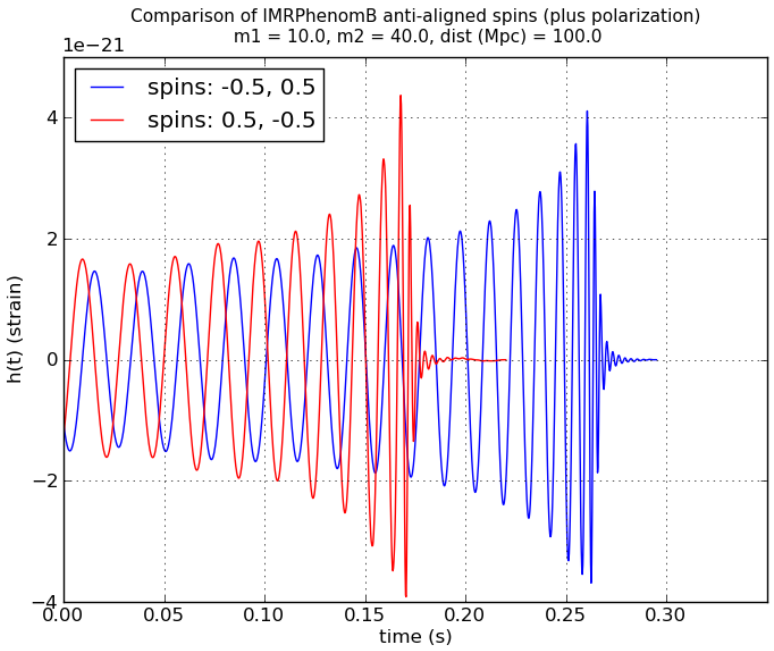

Figure 2.16: Time-domain waveforms for a 10 $M_\odot$+ 40 $M_\odot$system. Both waveforms are from systems with component black holes having anti-aligned spins. Blue: a 10 $M_\odot$ black hole with $\chi_1 = -0.5$ with a 40 $M_\odot$ black hole with $\chi_2 = 0.5$, giving a combined spin parameter of $\chi = 0.3$. Red: a 10 $M_\odot$ black hole with $\chi_1 = 0.5$ with a 40 $M_\odot$ black hole with $\chi_2 = -0.5$, giving a combined spin parameter of $\chi = -0.3$.

Table 2.2: The number of full cycles in LIGO's band for various non-spinning waveforms at the corners of our search space. The starting frequency is of 40 Hz for the LIGO detectors. Cycles are listed for the inspiral-only portion of the waveform (TaylorT3 at 2 PPN), the full IMR waveform in the EOBNRv2 implementation, and the full IMR waveform in the IMRPhenomB implementation.

Component masses	inspiral-only (PPN)	EOBNRv2	IMRPhenomB
12.5 $M_\odot$+ 12.5 $M_\odot$	36	46	48
24 $M_\odot$+ 1 $M_\odot$	219	204	231
99 $M_\odot$+ 1 $M_\odot$	0	12	38
50 $M_\odot$+ 50 $M_\odot$	0	12	2

Table 2.3: High frequency cutoff, duration, and number of cycles in the detector's band of the different waveforms. The PPN inspiral column is taken from the 2nd PPN order of the inspiral (parametrized by the TaylorT4 family), which is taken to end at the innermost stable circular orbit. Because of design differences between the detectors, LIGO has a low frequency cutoff of 40 Hz while Virgo has a low frequency cutoff of 30 Hz.

Component masses	high frequency cutoff	LIGO: duration (number of cycles) in PPN inspiral	Virgo: duration (number of cycles) in PPN inspiral
12.5 $M_\odot$+ 12.5 $M_\odot$	175 Hz	.6 s (36.1)	1.4 s (61.8)
24 $M_\odot$+ 1 $M_\odot$	157 Hz	3.8 s (219)	8.5 s (380)
99 $M_\odot$+ 1 $M_\odot$	38 Hz	0.6 (0)	1.7 s (46.8)
50 $M_\odot$+ 50 $M_\odot$	44 Hz	.003 s (.5)	.009 s (2.6)

2.2.2 The sensitivity of the detectors to compact binary coalescences

The data used in this thesis were taken from LIGO's 6^{th} science run (S6) and Virgo's 2^{nd} and 3^{rd} science runs (VSR2 and VSR3). By this time, the performance of the detectors was near optimal, given the design of the instruments.

The performance of a LIGO or Virgo detector, in terms of CBC searches, is defined by the horizon distance, which is the distance out to which it can see an optimally oriented binary ($\iota = 0$) with an average SNR of ρ=8, given by

$$\langle \rho \rangle = \sqrt{4 \int_{f_{low}}^{f^{high}} \frac{|\tilde{h}(f)|^2}{S_n(f)} df}, \tag{2.23}$$

where f_{low} is the low-frequency cutoff determined by the detector, 40 Hz for LIGO detectors during S6 and 30 Hz for Virgo during VSR2 and VSR3; f_{high} is determined by the sampling rate of the data, whose Nyquist frequency is 1024 Hz, and the expected waveform, $\tilde{h}(f)$; and $S_n(f)$ is the power spectral density of the detector, which is a measure of the mean square noise fluctuations [4]. It is the square of the strain amplitude sensitivity, shown for the different detectors in Figure 2.17 and Figure 2.18.

By inserting Equation (2.19) and Equation (2.20) into Equation (2.23), setting $\langle \rho \rangle = 8$ (a good approximation to the single-detector SNR threshold for confident detection), we can solve for $r = D$, the horizon distance (for an inspiral only waveform, under the quadrupole approximation):

$$D = \frac{1}{8} \left(\frac{5\pi}{24c^3} \right)^{1/2} (G\mathcal{M})^{5/6} \pi^{-7/6} \sqrt{4 \int_{f_{low}}^{f_{high}} \frac{f^{-7/3}}{S_n(f)} df}, \tag{2.24}$$

which shows how the sensitivity is dependent on the chirp mass $\mathcal{M}$ of the system. However, it is important to note that this calculation has only taken the inspiral portion of the waveform into consideration. The merger and ringdown can comprise a significant fraction of the power output of a GW for high-mass systems; see how much higher above the noise the merger and ringdown are for the 100 total $M_\odot$ system in Figure 2.12 as compared to the 25 total $M_\odot$ system in Figure 2.11. But it is difficult to show the horizon distance analytically for IMR waveforms because they have complicated parameterizations, numerical solutions to differential equations, or numerical solutions to the full GR equations. Figure 2.19 uses full IMR waveforms and a numerical analysis to illustrate how the detectors are sensitive to higher mass systems to larger distances [4].

The sensitivity of a detector is related to the horizon distance by

$$\text{sensitivity (range)} = D/2.26, \tag{2.25}$$

since the horizon distance was calculated for a binary with optimal orientation and sky location. The factor of 2.26 comes from integrating over sky location and inclination angles that would give an SNR of 8 (see

Section 3.2 for the definition of these angles with respect to a detector).

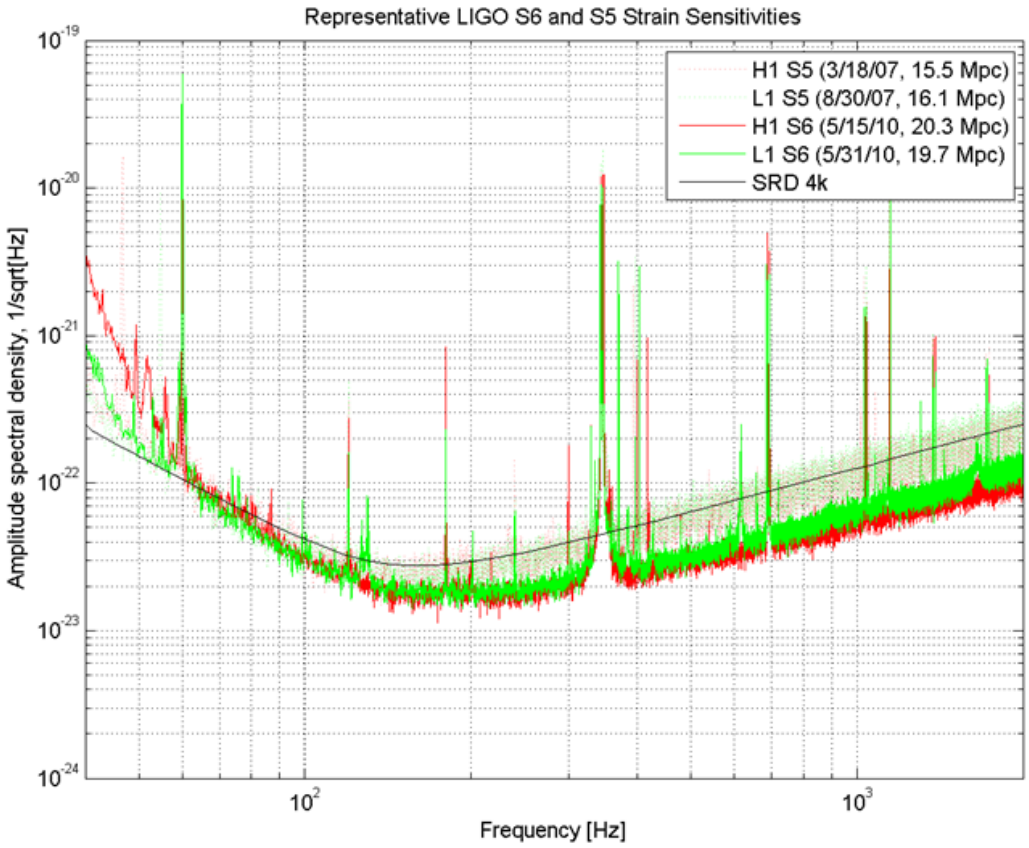

Figure 2.17: Representative curves for the strain amplitude sensitivity for LIGO Livingston (L1), in solid red, and LIGO Hanford (H1), in green, during S6 as compared to S5 (dotted lines). Note that S6 performance exceeded the Science Requirements Document (SRD) for Initial LIGO, due to enhancements made between S5 and S6. The distances in the legend are the horizon distance for an optimally oriented NS+NS inspiral. Image courtesy of John Zweizig.

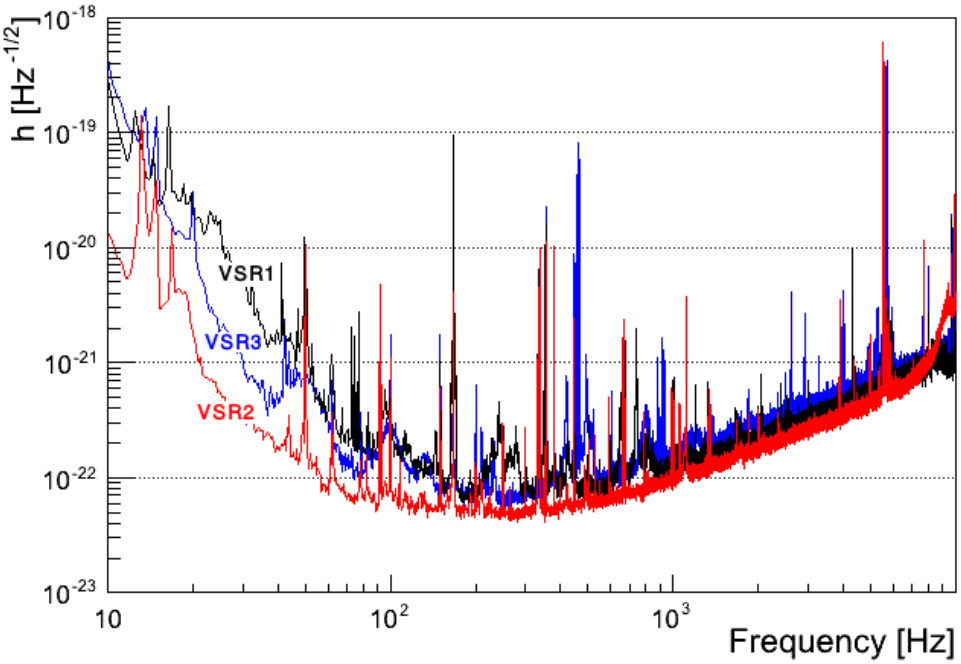

Figure 2.18: Representative curves for the strain amplitude sensitivity for Virgo during Virgo science run (VSR) 1, 2, and 3 [5]. Note that VSR1 was during S5, while VSR2 and VSR3 were during S6.

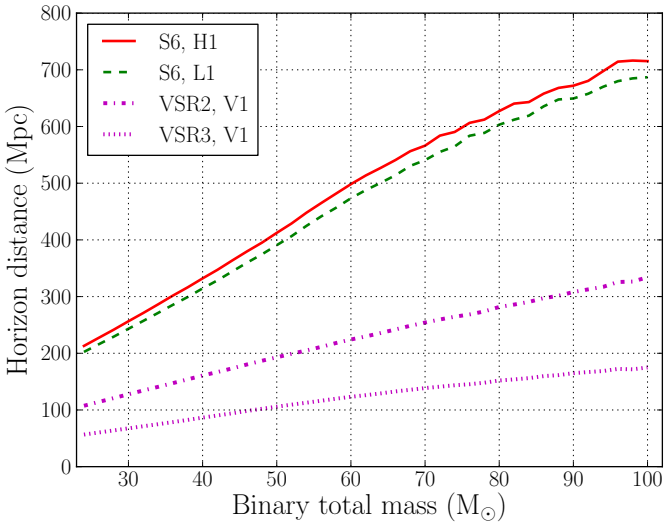

Figure 2.19: Horizon distances for non-spinning equal-mass IMR signals in the LIGO and Virgo detectors, using EOBNRv2 waveforms, which are explained in Section 2.2.1.1 as the signal model, averaged over periods of data when the detector sensitivities were near optimal for S6 and VSR2/3, respectively [4]. Note that above 100 $M_{\odot}$, the horizon distance drops abruptly, as the number of cycles in the detectors' sensitive bands go to zero (see Table 2.2).

Chapter 3

Ground-based interferometric GW detection

Initial LIGO and Virgo (V1) operated between 1999 and 2010 and collected data in a series of observational science runs, delimited by commissioning breaks and hardware upgrades. Initial LIGO science data sets are labeled science run 1 (S1), S2, S3, S4, S5, and S6; initial Virgo's are labeled VSR1, VSR2, and VSR3. From S1 to S5, there were three LIGO detectors, a 4-kilometer arm detector in Livingston (L1) (see Figure 3.1), a 4-kilometer arm detector in Hanford (H1), and a 2-kilometer arm detector (H2) sharing the same vacuum system as H1 (see Figure 3.2). H1 and L1 were upgraded for S6 [51], also known as *enhanced LIGO*, to include DC readout [10], a higher powered laser, a substantially upgraded thermal compensation system (TCS) [52] [53], and, most notably, improved sensitivity with respect to S5 for signals above 300 Hz [54]; H2 was not in use during S6. S5 (during which LIGO reached its design sensitivity [42]) and S6 have the longest stretches of science data for LIGO detectors. Some of the many papers published on the search for CBCs from this data (and in some cases Virgo data) are References [55], [56], [23], [57], [58], and [17]. No GWs were found, but this was not unexpected.

Currently, the H1 and L1 detectors are being replaced by their advanced versions, as is Virgo (the sites and vacuum enclosures remain the same, but the detectors themselves are completely redesigned) [59]. We can also look forward to LIGO-India, which will employ the base hardware from H2, and Japan's Kamioka Gravitational Wave Detector (KAGRA) [60], which will be underground and have cryogenically cooled test masses.

This thesis is based mainly on the data during LIGO's S6 and Virgo's VSR2 and VSR3 data sets. In the following sections I will explain the basic elements of the detectors that are required to understand the results presented in this thesis.

Figure 3.1: An arial view of LIGO Livingston (L1) showing the full y-arm, part of the x-arm and the exterior building around the control room and laser and vacuum equipment area. Image taken from www.ligo.org.

Figure 3.2: An arial view of LIGO Hanford (H1 and H2) showing the full y-arm, part of the x-arm and the exterior building around the control room and laser and vacuum equipment area. Image taken from www.ligo.org.

3.1 The operating principles of ground-based interferometric GW detectors

As hinted at in Section 2.2.1, in order to detect GWs you need an instrument that measures differential strain. Strain is equal to the change in length over length,

$$h = \delta L / L, \tag{3.1}$$

where L is the length of your measuring device. A gravitational wave from a 50+50 $M_{\odot}$ system at 100 Mpc will impart a strain on the order of 10^{-20} around merger (see Figure 2.12, noting that the y-axis is the strain scaled by the square root of the x-axis). Therefore, we need an instrument that can measure very small ratios of change in length to length.

The designers of the LIGO and Virgo detectors chose a Michelson interferometer as the basic structure for the instrument, since it can measure small length changes δL to very high precision. In a classic Michelson, coherent incident light is directed at a beam splitter, which sends half of the light down the x-axis and half of the light down the y-axis. There are mirrors at the end of each arm that send the light back toward the beam splitter (see Figure 3.3); depending on the difference in arm lengths, when this light recombines it will either head back toward the laser (symmetric port) or toward a photodetector (anti-symmetric port). If the arms are exactly the same length, no light hits the photodetector and thus the anti-symmetric port has earned the nickname "the dark port". If a GW passes through the detector, it changes the relative positions of the mirrors, allowing a pattern of light to reach the anti-symmetric port's photodetector — this can be calibrated into the likely GW strain signal.

In reality, the LIGO and Virgo detectors are much more than Michelsons. The full optical configuration is sometimes referred to as a power-recycled Fabry-Perot Michelson interferometer (PRFPMI) [61]. Fabry-Perot and power-recycling optical cavities increase the laser power in the arms, effectively increasing L because the light bounces back and forth hundreds of times before exiting to the anti-symmetric port, thus improving the sensitivity at relevant frequencies by two orders of magnitude [62]. However, this signal is still very tiny — only quadratically proportional to the small GW signal we are trying to detect. Therefore, LIGO detectors employ either *heterodyne detection* (S1 - S5) or a specialized form of *homodyne detection* (S6) known as *DC readout*. DC readout adds a local oscillator field at the same frequency as the input laser. When a GW signal modulates the phase of the input laser, it will interfere with the local oscillator to produce power variations on the anti-symmetric port's photodetector that are linearly proportional to the GW signal [10]. Homodyne detection benefits from a local oscillator field that has been filtered by the Fabry-Perot arms, and an output mode cleaner (between the beam splitter and the anti-symmetric port) which removes "junk" light that may be resonating in the power-recycling cavity [10]. Virgo does the same thing [63].

Since the detectors are measuring extremely tiny distances with lasers, it is important that the laser light

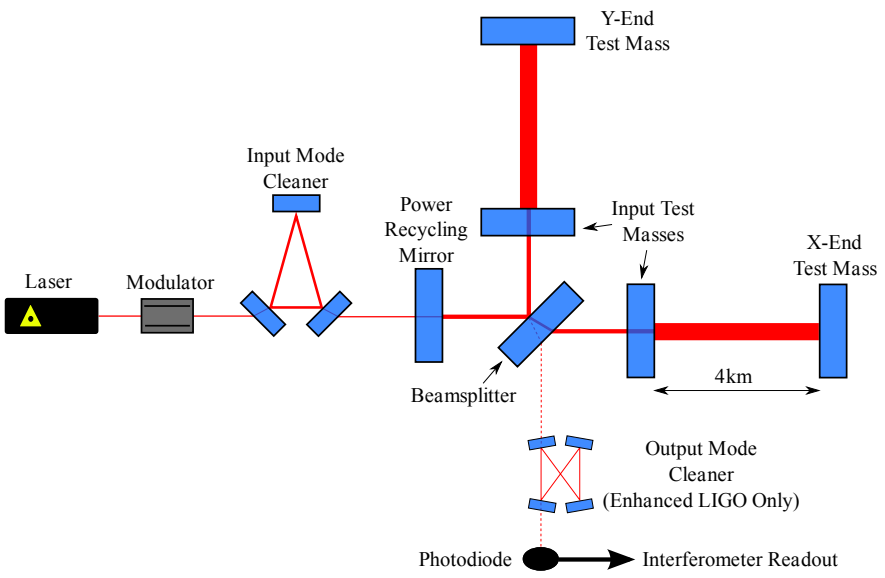

Figure 3.3: A basic illustration of a LIGO detector and its main components during S6 [6].

is extremely stable and that scattering is minimized. The beam path and optical components are enclosed in a vacuum (10^{-9} - 10^{-8} torr for LIGO detectors) [62] so that the laser beam experiences minimal random phase fluctuations due to residual gas fluctuations in the beampipe. Also, high vacuum ensures the mirrors do not get dusty; dust not only causes scatter but also causes the optics to heat up unevenly [64]. The mirrors, often referred to as test masses, are coated with dielectric and polished to have very low absorption (a few parts-per-million (ppm)) and scattering ($60 - 70$ ppm)) [62]. Scattering not only leads to loss in laser power where it is needed, but to photons with the wrong frequency sneaking into the anti-symmetric port's photodiode.

In order for Earthly motions to not influence the test masses and mimic GWs, seismic isolation systems are used. For Initial LIGO, a passive form of isolation for components inside the vacuum is achieved by a stack of masses and springs, providing vertical isolation at frequencies above a few Hz. This is essentially a cascade of harmonic oscillators [65], which are natural passive mechanical low-pass filters. In addition, the mirrors are suspended with thin wires as pendula, which further provide passive isolation in the horizontal (beam path) direction from seismic noise as well as thermal noise coming from the passive isolation stack [65].

There are also active isolation measures taken to isolate motions in the direction of the laser beam [66]. Because Livingston experiences more seismic disturbance than Hanford (logging and other anthropogenic activity prevented science data from being taken for most of the daytime hours prior to S4 [67] [68]), hydraulic external pre-isolators (HEPI) that were planned as an upgrade for Advanced LIGO were added to L1 between S3 and S4 to actively suppress vibrations [9]. In the middle of S6, the performance of HEPI was greatly improved by adding feed-forward control; this can be seen by contrasting the sporadicity of the green dots in Figure 3.4 from about 80 days to 156 days to the density of green dots from 156 days onward, indicating that the detector was able to stay in lock for longer [6]. The feed-forward system "damps low-frequency

noise by using signals from the onsite seismometers to control movement of the vacuum chambers for the end test masses" [66]. Hanford has been using a piezoelectric pre-isolation (PEPI) system since S2, but will be upgraded to HEPI for Advanced LIGO [66].

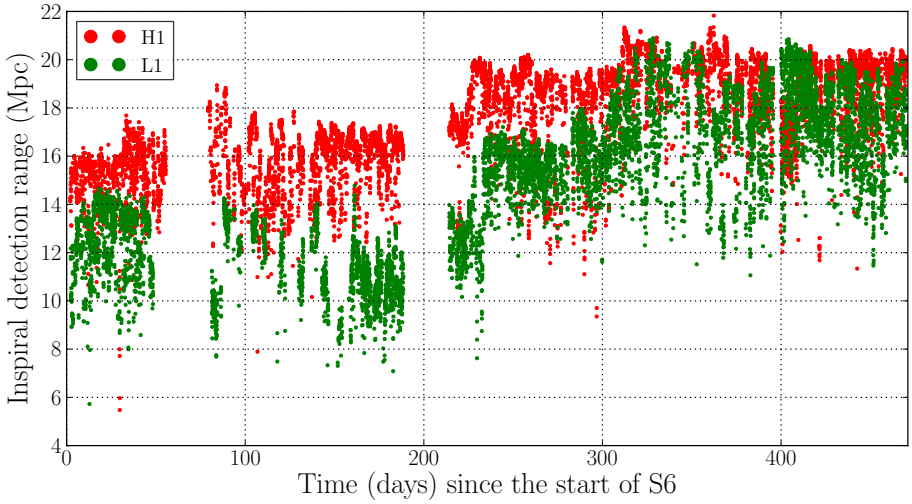

Figure 3.4: The range (See Equation (2.25) to which the LIGO detectors are sensitive to a binary neutron star inspiral signal, shown to illustrate the changing sensitivity as various hardware or software upgrades are made throughout the course of the run [6].

A very important part of the detectors' proper function are *servos*, also known as control loops. These stabilize the laser amplitude and frequency at the pre-stabilized laser table (PSL), damp the pendulum motion of the suspended optics, control the lengths of various cavities and the angular positions of the optics, and more. For example, the lengths of the two Fabry-Perot cavities in the arms and the power-recycling cavity are kept at an integer number of wavelengths so that new light that enters interferes constructively with the light already resonant in the cavities. There is also a servo that controls the Michelson phase so that the anti-symmetric port stays at the dark fringe [62]. The detector strain signal is derived from the sensing and actuation signals of the differential arm motion control loop — see Section 3.3 below.

Virgo detectors operate in a similar fashion; see Reference [63].

3.1.1 Subsystems of the LIGO interferometers

The LIGO and Virgo detectors can be thought of as the assemblage of many subsystems. Not only does each subsystem have a valuable role in the operation of the detector, they also provide key information in data quality and detector characterization studies (see Chapter 4). For enhanced LIGO, the subsystems are listed below:

- PSL: The pre-stabilized laser subsystem ensures that the laser entering the vacuum system has a stable frequency and intensity. Additional intensity stabilization at the laser's fundamental mode is provided by a mode cleaner (the pre-mode cleaner) [69].

- IO: The input optics subsystem shares an optical table with the PSL subsystem. This subsystem's components (see Figure 3.5) are responsible for additional mode matching and controlling the power and frequency of the laser that enters the interferometer. It uses an electro-optic modulator to phase modulate the beam to produce radio frequency (RF) sidebands, which are sent into the interferometer and to the length and alignment control subsystems [7]. The input mode cleaner is used to further stabilize the laser frequency, and further define the transverse mode of the beam before entering the main interferometer. Moreover, the Faraday isolator prevents light from back-scattering into the PSL subsystem. The mode matching telescope widens the diameter of the laser while further stabilizing the frequency and isolating the TEM_{00} mode that will be resonant between the ITMs and ETMs [7].

- COC: The core optics components subsystem consist of the two input test masses, the two end test masses, the beam splitter, and the recycling mirror [69]. The optics are made from fused silica and have specialized reflective and anti-reflective coatings applied [70].

- COS: The core optics support subsystem generates optical pick-off beams from each of the core optics and takes them outside of the vacuum so they can be used by the LSC and ASC subsystems [71].

- SUS: The suspensions subsystem controls the position of the suspended optics (input test masses, end test masses, and mode cleaner optics). These optics are suspended via a single wire that loops around the barrel of the mirror. The optics have four magnets glued to them. These magnets are used in conjunction with optical sensor and electro-magnetic (OSEM) actuators to adjust the angular and horizontal positions of the mirrors. Once the interferometer is in lock, SUS is only used to damp pendulum motion of the optics; length control is left to the LSC subsystem, and angular control is left to the ASC subsystem [8].

- LSC: The length-sensing and control subsystem receives length-sensing information from the photodiodes and sends them to the actuators (OSEMs) on the suspensions, which adjust the longitudinal distances between the input and end test masses (ITMs and ETMs) such that the fundamental mode fulfills the required interference conditions. The common arm (CARM) signal is fed back to the ETMs at low frequency and to the frequency stabilization servo at high frequencies. Servo filters process these signals to keep stable feedback control of the loop [72]. This is the subsystem that measures and controls DARM (the error signal that is converted into a GW signal; see the following section). This subsystem operates at 16348 samples/second [8].

- ASC: The alignment-sensing and control subsystem has two main parts: 1) the initial alignment-sensing (IAS) of the *optics* to configure them such that lock is possible by interfacing with the COC, COS, SUS, SEI, and IOO subsystems; 2) ASC of the *cavities* via wavefront sensors and OSEM actuation [73]. This second part (sometimes referred to as angular-sensing and control) tracks and fixes the pitch and yaw of 8 mirrors (beam splitter, ETMX, ETMY, ITMX, ITMY, two mode matching

telescopes, and recycling mirror) such that there is maximal power buildup in the Fabry-Perot cavities. Wavefront sensors, quadrant photodiodes, and a camera are used to examine the laser light and its sidebands. See Figure 3.6 for the locations of these components. This information is fed into a control loop that controls the mirrors' positions via the OSEMs. Wavefront sensors are quadrant photodiodes equipped with RF electronics; they use the Pound-Drever-Hall method to produce error signals for the control loop. Each wavefront sensor produces two channels — the in-phase and quad-phase demodulation of the input beam with the RF sidebands. The ASC subsystem operates at 2048 samples/second [8].

- PEM: The physical environmental monitors subsystem is composed of numerous seismometers, magnetometers, accelerometers, weather stations, mains voltage monitors, temperature sensors, and an AOR radio receiver distributed throughout each LIGO site. See Figure 3.7 for the locations of these monitors [74]. Most of these sensors are passively recording information about the state of the environment, and are used later to assess data quality. The seismometer information, however, is used in the seismic isolation subsystem.

- SEI: The seismic isolation subsystem uses information from the network of seismometers to actively subtract seismic noise from the tables holding the optics. Figure 3.8 shows a seismic isolation configuration. The configuration includes four passive isolation stacks for each core optic, but these are not controlled by a servo. In S6, the active isolation comes from the sensor and actuator (hydraulic external pre-isolator for L1 and piezoelectric pre-isolator for H1). The control loop in L1 began using Weiner feed-forward filtering in the middle of S6 [9].

- OMC: The output mode cleaner subsystem was added during S6 to support the new DC readout plan. This subsystem removes any spurious higher-order modes that have arisen while the laser is in the interferometer arms. The OMC also removes the RF sidebands, as they are no longer necessary (and, in fact, add extra noise) for DC readout using homodyne detection. The subsystem includes several optics for beam alignment and purification, as well as photodiodes for readout; see Figure 3.9 for the locations of these components. One of the optics is outfitted with a piezoelectric actuator (for fast position correction) and another with a thermal actuator (for slow position correction). The OMC has its own vacuum and seismic isolation system, consisting of two active pendula mounted on an active isolator [10].

- TCS: The thermal compensation system, upgraded during S6, corrects for under- or over-heating of the ITMs so that their effective radius of curvature is close to the design value (otherwise the light coming back through the ITMs will not be reflected by the recycling mirror, leading to a loss of laser power). The subsystem includes optics, a camera for each ITM, an optical imaging system, a servo, and a CO_2 laser for applying the heat [52].

- CDS: The control and data system provides the closed loop control of the instruments' servos. It is responsible for monitoring and control of the vacuum system, providing diagnostics to monitor interferometer performance, collaborate with the PSL, ASC, SUS, LSC, and SEI subsystems. It is also responsible for bringing the interferometer into "lock" [69].

- DAQ: The data acquisition subsystem records both digital and analog information from all the subsystems' various sensors. The amount of data can be up to 5 Mbytes per second during S6 (this number will increase by an order of magnitude for Advanced LIGO) [69].

These subsystems are responsible for getting the detector into lock (i.e., the fundamental mode of the laser is resonant in the Fabry-Perot cavities, and the mirror positions are stable), keeping the detector under length and alignment control at its design configuration, and recording information from the various components of the detector. Each time-varying piece of information is recorded in a data channel. Data channels are described in the following subsection.

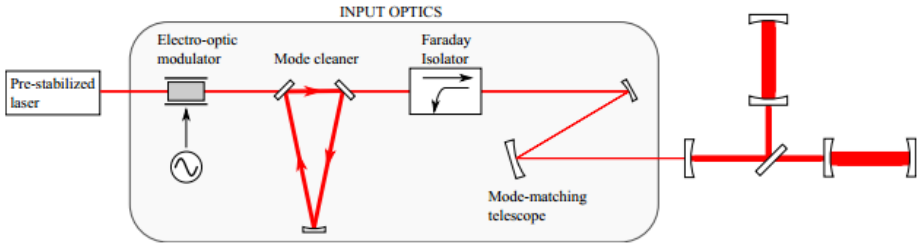

Figure 3.5: An illustration of the input optics subsystem for LIGO during S6 (enhanced LIGO). The electro-optic modulator produces the RF sidebands that are used by other subsystems; this is the last component that is outside the vacuum. The mode cleaner suppresses laser light that is not in the TEM_{00} mode, provides frequency stabilization, and passively reduces beam jitter above 10 Hz. The Faraday isolator prevents back-propagation of the laser and provides access to the symmetric port beam for length and alignment-sensing [7].

3.1.2 Data channels

In the language used by the LVC, data channels refer to streams of digital numbers, sampled at several fixed frequencies, from different components of the detectors. In general, these are time-series taken by measurement devices or used by servos at various sampling rates.

The main output of an interferometric gravitational wave detector is, of course, the signal measured by the photodetector at the anti-symmetric port; this differential arm length (DARM) information is recorded in the *GW channel*. But the GW channel is just one of the tens of thousands of channels located on and around the detectors. The other channels are known as *auxiliary channels*. In addition to being used by the subsystems listed in the previous section, they monitor two main sources of noise: instrumental and environmental. Many of the instrumental channels record information from the servos controlling the laser and the position

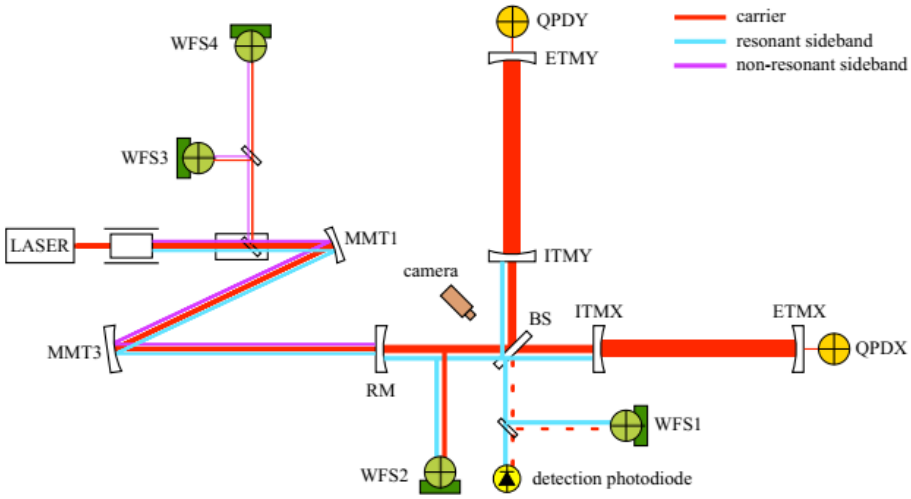

Figure 3.6: An illustration of the angular-sensing and control subsystem for LIGO during S6 (enhanced LIGO). The QPDs (quadrant photodiodes) sense the alignment of the light transmitted to the ETMs (end test masses). The WFSs (wavefront sensors) sense the angular alignment of the input beams with respect to their resonant cavity modes. The camera senses the beam position incident on the BS (beam splitter). The positions of the ETMs, BS, ITMs (input test masses), RM (recycling mirror), and MMTs (mode matching telescopes) are adjusted with OSEMs via a servo using the information from the QPDs and WFSs. [8]

and alignment of the optics [75]. Figure 3.10 shows some of the devices used for recording information from the optics. In addition to instrumental channels, there are physical environmental monitor (PEM) channels that collect data from numerous places along the detector, recording seismic, acoustic, electromagnetic, etc. information [75] (see Figure 3.7).

These channels can be monitored to inform scientists when an individual subsystem or the detector as a whole is functioning properly or not. When they are not, or when a short-duration instrumental or environmental disturbance occurs, a signal can be seen in the GW channel that is not due to a GW; for example, seismic motion moves the mirrors and scattered light can hit the photodetector. Thus, the auxiliary channels can be used to veto data that is untrustworthy [76] (as discussed in Chapter 4) or to create a ranking system that indicates the level of trustworthiness of the data (see Chapter 6). Table 3.1 lists some of the most important channels used in the detector characterization and data-quality studies described in detail in Section 4.1.3.

3.2 Antenna response of detector to GW signals

The strain seen by an interferometric GW detector depends on the orientation of the detector with respect to the source as well as the polarization of the incoming GWs. The following equation projects the effect of the different polarizations onto the plane of the detector:

$$h(t+t_0) = F_+(\theta,\phi,\psi,t+t_0)h_+(\iota,\Sigma,t+t_c) + F_\times(\theta,\phi,\psi,t+t_0)h_\times(\iota,\Sigma,t+t_c), \tag{3.2}$$

Table 3.1: A non-comprehensive list of various auxiliary channels recorded by components in the LIGO detectors

Channel name	Description
LSC-{MICH,PRC,DARM,CARM}_CTRL	16384-Hz channels recording the information used to control the Michelson, power-recycling cavity, and differential and common arm length degrees of freedom.
LSC-DARM_ERR	A 16384-Hz channel recording the error signal for the control loop associated with the GW signal and described in Section 3.3.
LSC-REFL_{I,Q}	8192- (in-phase) and 4096- (quad-phase) Hz channels monitoring the light coming back through the symmetric port, measured by RF photodiodes in the Faraday isolator. See Figure 3.10.
ASC-{E,I}TM{X,Y}_{P,Y}	512-Hz angular torque feedback control signals for pitch and yaw of the X and Y ETMs and ITMs.
ASC-QPD{X,Y}_{P,Y}	256-Hz channels measuring the beam position on the X and Y ETMs.
ASC-WFS{1,2,3,4}_{Q,I}_{P,Y}	512-Hz channels measuring the in-phase and quadrature readout of the alignment of the beam with respect to detector's cavities. How the WFSs align to the different optical cavities is beyond the scope of this thesis.
OMC-QPD{1,2,3,4}_{P,Y,SUM}_OUT_DAQ	4096-Hz (for QPD{1,2} and 2048-Hz (for QPD{3,4}) channels measuring the pitch, yaw, and sum motion of the OMC mirrors. The pitch, yaw, and sum can be derived from the four quadrants of the photodiode: PITCH = (UL+UR)-(LL+LR), YAW = (UL+LL)-(UR+LR), SUM = (UL+UR+LL+LR); where the quadrants are labeled by upper, lower, left, and right.
PEM-E{X,Y}_SEIS{X,Y,Z}	256-Hz channels recording seismic activity in the X,Y, and Z directions at the X and Y end stations.
PEM-LVEA_MAG{X,Y,Z}	2048-Hz channels recording magnetic fields in the X, Y, and Z directions in the laser and vacuum enclosure area at the vertex of the interferometer.
PEM-RADIO_LVEA	2048-Hz channels recording information from a radio receiver in the laser and vacuum enclosure area at the vertex of the interferometer.
PEM-{PSL1,BSC1,BSC3,HAM3,HAM6,LVEA,ISCT}_MIC	2048-Hz channels recording audio noise in various places around the detector; see Figure 3.7 for their locations, but the areas on the detector are labeled in Figure 3.10.
SEI-{ITMX,ITMY,ETMX,ETMY,BS,RM}_{X,Y,Z}	256-Hz channels recording seismic activity in the X, Y, and Z directions from seismometers near various optics inside the vacuum system .
SEI-OUT_{X,Y}	256-Hz channels recording the output of the control system for active seismic isolation in the X and Y direction.
SUS-{ITMX,ITMY,ETMX,ETMY,BS,RM}_SUS{PITCH,YAW}_IN	64-Hz channels recording the pitch and yaw of various optics.
SUS-{ITMX,ITMY,ETMX,ETMY,BS,RM}_OPLEV_{P,Y}ERROR	512-Hz channels containing the error signal for the SUS control system for the pitch and yaw of various optics.
SUS-{ITMX,ITMY,ETMX,ETMY}_{LL,LR,UL,UR}COIL_OUTPUT	16 Hz channels containing the values of the currents in the coils used to control mirror positions.

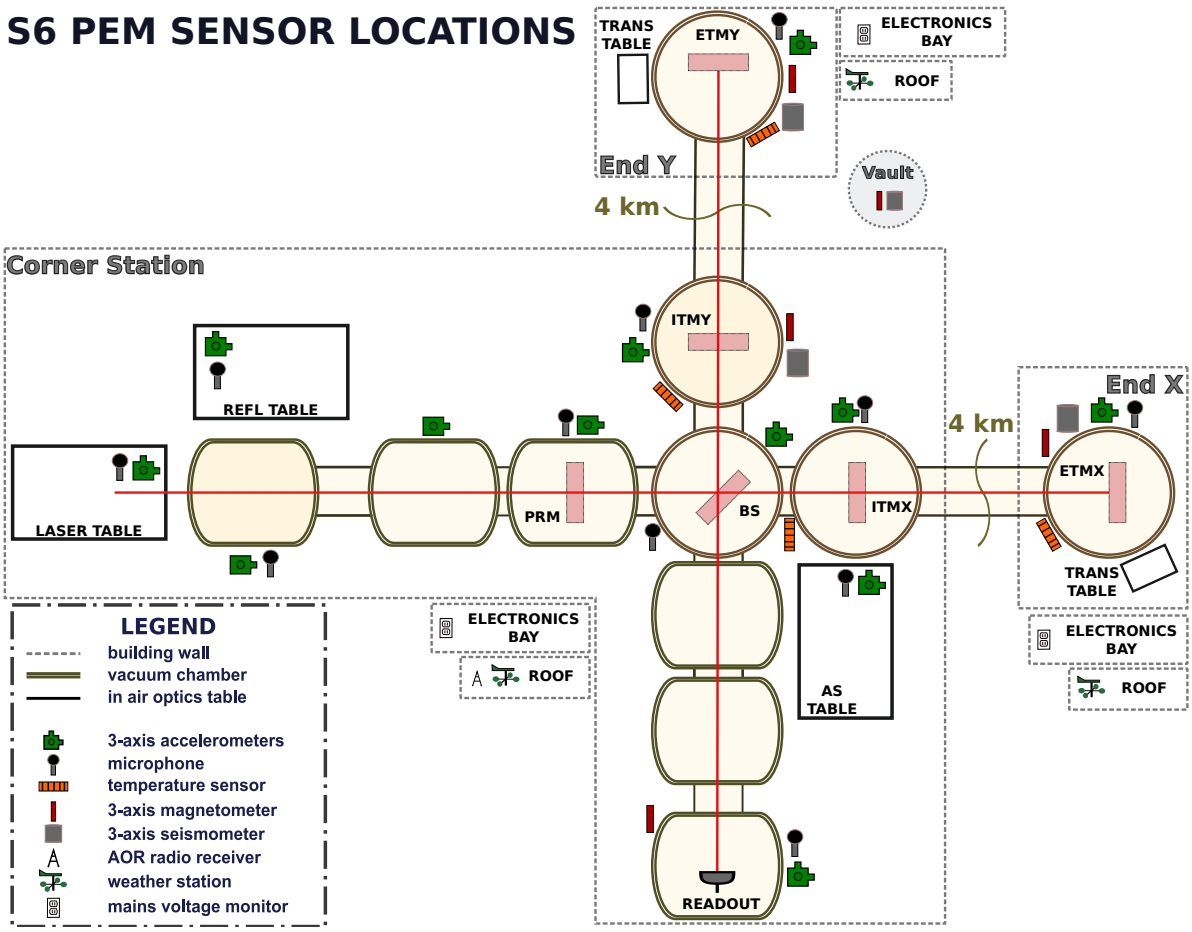

Figure 3.7: A diagram depicting the locations of physical environmental sensor locations at L1. Figure courtesy of Annamaria Effler.

where F_+ and $F_\times$ are the antenna pattern factors of a specific detector. They depend on time since the detectors are on the Earth, which is rotating with respect to celestial coordinates. t_0 is the average time the coalescing signal reaches the rotating detector and t_c is the time the system coalesces at the center of the Earth (a fiducial location common to all detectors, making $t_0 - t_c$ the propagation time from the detector to the center of the Earth. Σ contains all the other parameters in the waveform (see, for example, Equation (2.16)). In order to define the angles, we must set up three coordinate systems — see Figure 3.11. The inclination angle ι is the polar angle between the source frame's z-axis (for CBCs, this is the direction of the orbital angular momentum) and the detector's z'-axis (roughly, the local zenith). The polarization angle ψ is the azimuthal angle from the detector's x'-axis to the GW's x"-axis. (Note that the terminology is a bit confusing here — the inclination angle determines the polarization content of the GW, while the polarization angle determines the angle between the stretch-squeeze in the h_+ wave and the axes of the arms of the detector). θ is the polar angle between the detector's z'-axis and the GW's z"-axis (the direction of propagation of the GW). ϕ is the azimuthal angle between the x'-axis and the projection of the z"-axis onto the x'-y' plane.

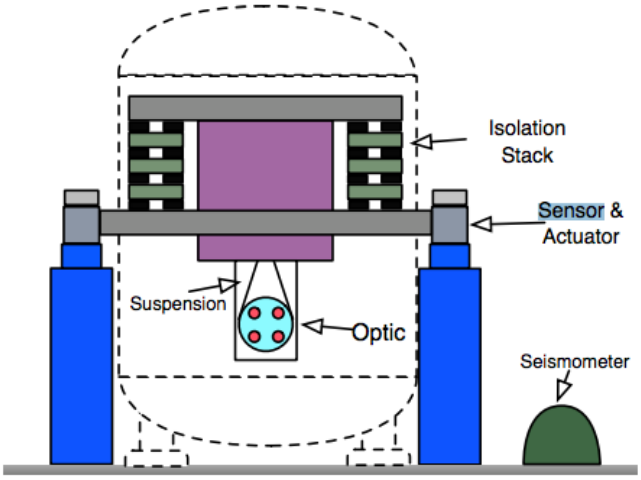

Figure 3.8: A representation of the seismic isolation stack for one of the suspended optics. Inside the dashed line is the vacuum system. The isolation stack provides passive isolation and the sensor and actuator are used to provide active seismic isolation in the x- and y-directions [9].

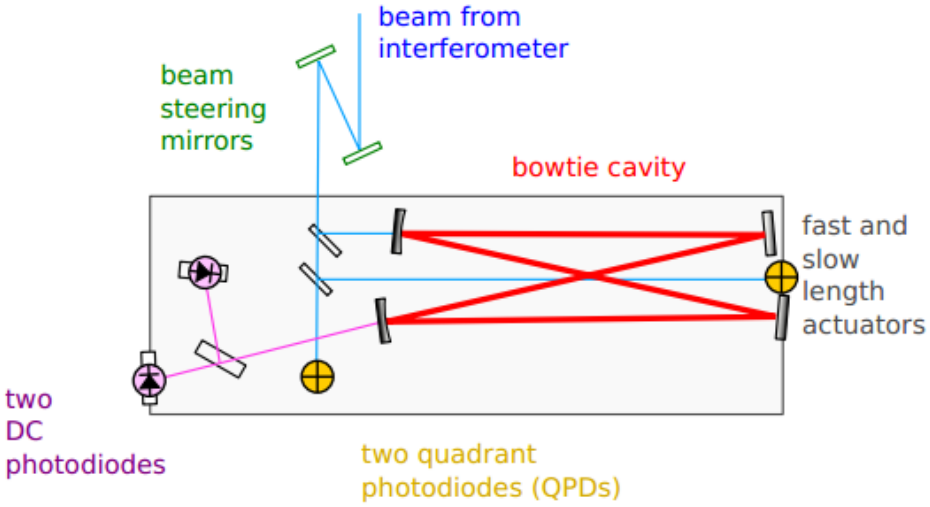

Figure 3.9: A representation of the output mode cleaner optical setup [10].

Using these definitions, the antenna pattern factors can be expressed as [42]:

$$F_+ = \frac{1}{2}(1+\cos^2\theta)\cos 2\varphi\cos 2\psi - \cos\theta\sin 2\varphi\sin 2\psi \tag{3.3}$$

and

$$F_\times = \frac{1}{2}(1+\cos^2\theta)\cos 2\varphi\sin 2\psi + \cos\theta\sin 2\varphi\cos 2\psi. \tag{3.4}$$

We can average over all polarization angles, since these should be independent of the direction of arrival,

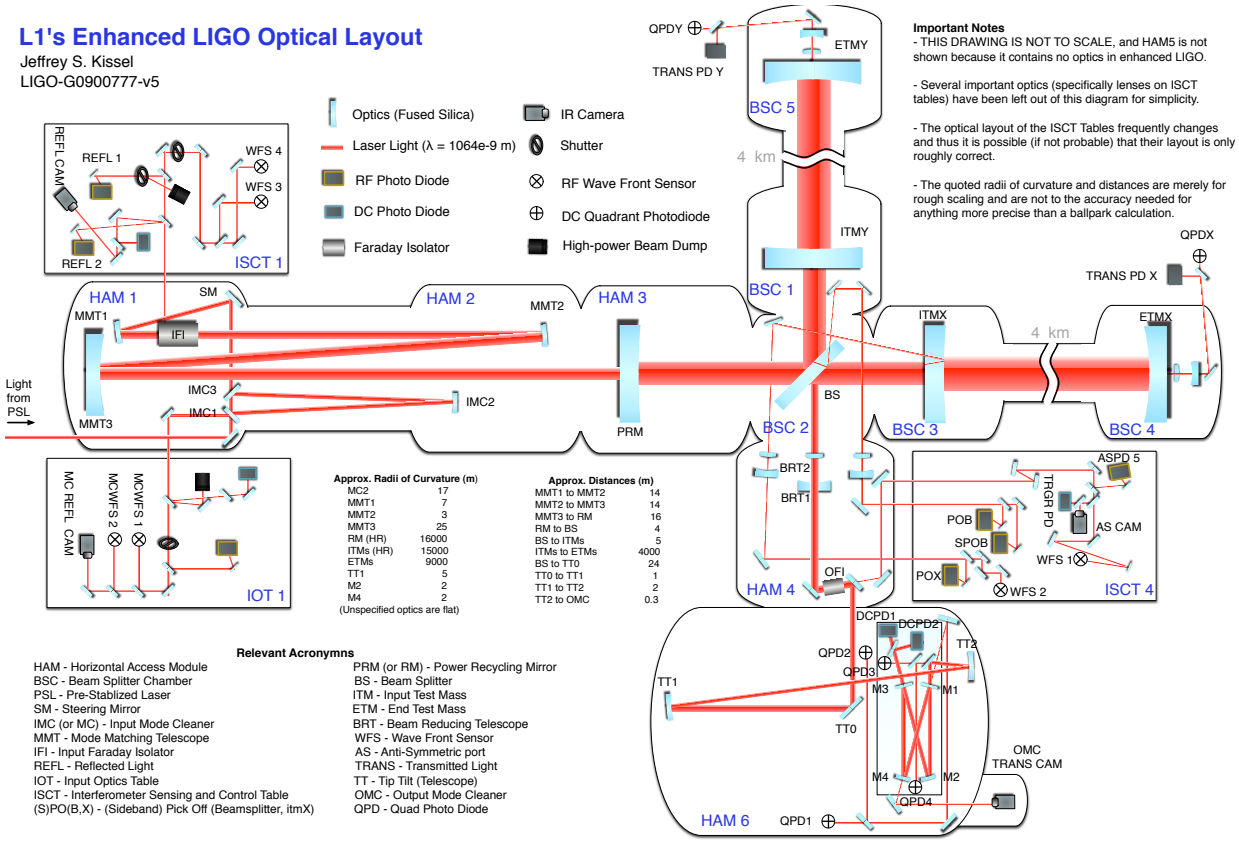

Figure 3.10: A diagram depicting the locations of various optical components and the auxiliary channels recording information from/about them. Figure courtesy of Jeff Kissel.

and calculate the mean square response of the detector as

$$\overline{F}^2 = \int F_+^2 d\psi = \frac{1}{4}(1+\cos^2\theta)^2\cos^2 2\varphi + \cos^2\theta \sin^2 2\varphi \tag{3.5}$$

$$= F_+^2(\theta,\varphi,\psi=0) + F_\times^2(\theta,\varphi,\psi=0), \tag{3.6}$$

which is visualized in Figure 3.12.

3.3 Calibration

The formulas and theory in this section are from Reference [77] and conversations with Alan Weinstein.

For LIGO detectors, calibration is the process of converting one (or more) of the data channels of the LIGO detector into GW strain. In other words, it takes the channels LSC-DARM_ERR and LSC-DARM_CTRL (see Table 3.1) and turns them into $h(t)$. In S6, DARM_ERR is constructed via DC readout; but in S5 it was derived from LSC-AS_Q (see Table 4.1).

Calibration involves understanding the frequency-dependent amplitude and phase response of each ele-

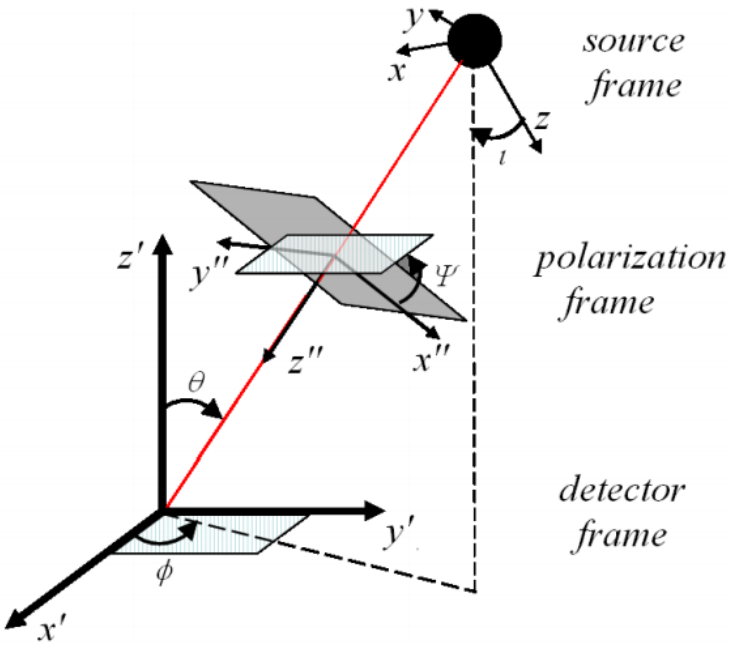

Figure 3.11: The relevant angles for the calculation of the strain seen by an interferometric GW detector. The x'-y'-z' frame is that of the detector, the x-y-z frame is that of the source, and the x"-y"-z" frame is that of the GWs. ψ is the polarization angle. The z-axis is defined by aligning it with the orbital angular momentum of the binary system. The z"-axis is defined by the direction from the source to the detector; the x"- and y"-axes are defined by the stretching and squeezing directions of h_+ in the GW frame (see Figure 2.4). The x'- and y'-axes are defined by the arms of the detector; we then use the right hand rule to define the z'-axis [11].

ment in the DARM control loop shown in Figure 3.13. The incoming GW signal, i.e., the ΔL_{ext} input in the control loop, and the corresponding motion of the mirrors are analog; but the readout, e_D, is measured in digital counts proportional to mirror displacement. In the context of control loops, e_D is the control loop error signal, often referred to as DARM_ERR, or the *GW channel*. Because C, D, and A are functions of frequency (and $\gamma(t)$ is a slowly changing function of time due to the optical gain changing from laser power fluctuations or mirror misalignments), as we travel through the control system, we multiply their effects as follows:

$$e_D = \gamma(t)C(f)\Delta L_{\text{ext}} - \gamma(t)C(f)A(f)D(f)e_D, \tag{3.7}$$

where $\gamma(t)C(f)$ is the length-sensing function, $A(f)$ is the actuation function describing how the test masses respond to the influence of the control loop, and $D(f)$ is the set of digital filters, which are implemented into the LIGO control system in order to transform the error signal into a control signal, like

$$D(f)e_D = s_D, \tag{3.8}$$

where $s_D(f)$ is the *digital control signal*. $s_D(f)$ is one of our data channels, DARM_CTRL (see Sec-

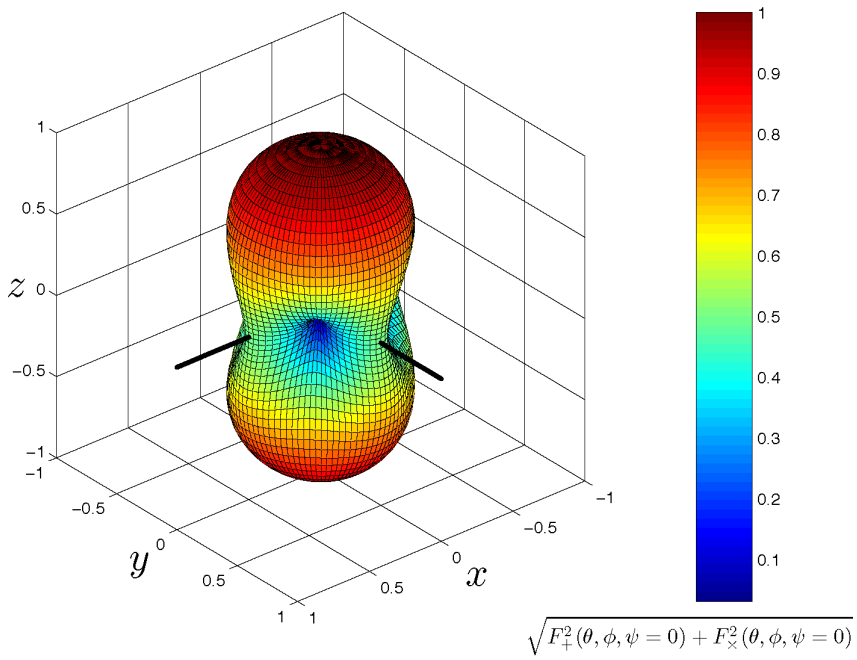

Figure 3.12: The root mean square antenna pattern of a LIGO detector whose x- and y-arms are represented by the black bars to circularly polarized GWs [12].

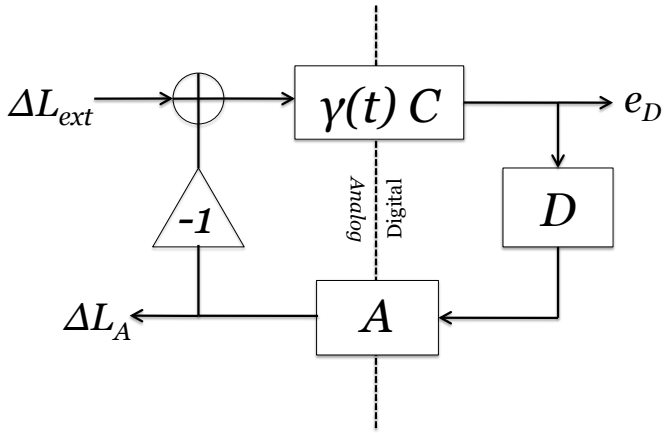

Figure 3.13: The control loop for LIGO interferometers. ΔL_{ext} is the motion of the mirrors caused by GWs or a local disturbance, $\gamma(t)C(f)$ is the length-sensing function, e_D is digital error signal, $D(f)$ is the set of digital filters on e_D in order to feed it into is the actuation function $A(f)$ that calculates the ΔL_A in an attempt to cancel the ΔL_{ext}.

tion 3.1.2), and is designed to keep DARM_ERR close to zero. Similarly, the actuation function can be expressed as

$$A(f)s_D(f) = \Delta L_A, \tag{3.9}$$

where ΔL_A is corrective displacement on the mirrors exerted by the control loop.

The control loop can also be expressed by the following equation, derived from Equation (3.7):

$$e_D = \frac{\gamma(t)C\Delta L_{\text{ext}}}{1+\gamma(t)CAD} = \frac{\gamma(t)C\Delta L_{\text{ext}}}{1+G}, \tag{3.10}$$

where $G = \gamma(t)CAD$ is known as the *open loop transfer* and can be split into two parts

$$G = \gamma(t)G_0(f), \tag{3.11}$$

where $G_0(f) = CAD$ is known as the *nominal open loop transfer function*. $G_0(f)$ is measured experimentally by sweeping through all frequencies in a procedure known as *swept sine calibration* to give us $G_0(f)$ at snapshots of time.

There are three inherent problems with this approach alone. Firstly, in between swept sine shapshots, which are only taken a few times during each science run, there can be time variation of $G(f,t)$. We try to capture this time variation with $\gamma(t)$, using permanent calibration lines at well-chosen frequencies around 50, 400, and 1100 Hz; the statistical error on this procedure is captured by measuring $\gamma(t)$ every second and computing the standard deviation. Secondly, the swept sine procedure itself also has statistical error, measured by repeating the measurement. Thirdly, there is a systematic error which is estimated by comparing a detailed theoretical model of G to our measurements.

The goal is, of course, to translate any given e_D at a snapshot of time into the corresponding GW strain, causing the mirror motion $\Delta L_{\text{ext}}(f)$, which requires learning the form of the response function R_L,

$$\Delta L_{\text{ext}}(f) = R_L(f)e_D(f), \tag{3.12}$$

where R_L is given by

$$R_L(f,t) = \frac{1+\gamma(t)G_0(f)}{\gamma(t)C(f)}. \tag{3.13}$$

A simple convolution uses the response function and the error signal to calculate the gravitational wave strain in the time domain:

$$h(t) = \frac{1}{L}\int R_L(t-t')e_D(t')dt', \tag{3.14}$$

where $R_L(t)$ are digital finite impulse response (FIR) filters calculated from $R_L(f)$.

As the open loop gain is known by measurement, all that remains to get a full model of the amplitude and phase of $R_L(f,t)$ is to find $\gamma(t)C$. We know $\gamma(t)$ by measurement, but in order to model $C(f)$ we must extract its contribution from $G_0(f) = CAD$. We know D exactly by construction; we know the functional form of the frequency response of both C (cavity pole) and A (damped, driven pendulum) by theory.

The cavity pole response function can be calculated from the knowledge that a change in the length of the

Fabry-Perot cavity will cause the phase of the laser light exiting the cavity to be different than when it entered the cavity. The transfer function (on resonance) between the cavity length and the change in phase is:

$$H_{\rm FP}(f) = \frac{2\pi}{\lambda}\frac{1}{r_c}\frac{r_e(1-r_i^2)}{1-r_i r_e}\frac{\sin(2\pi f L/c)}{2\pi f L/c}\frac{e^{-2\pi i f L/c}}{1-r_i r_e e^{-4\pi i f L/c}}, \tag{3.15}$$

where $r_c = (r_e - r_i)/(1 - r_i r_e)$ is the reflectivity of the Fabry-Perot cavity on resonance and $r_e \cong 1$ and $r_i = \sqrt{1-0.3}$ are the reflectivity of the end and initial test masses, respectively. L is the length of the cavity and c is the speed of light. The frequency dependence of this transfer function can be expressed as a simple cavity pole response,

$$\frac{1}{1+i\frac{f}{f_{\rm pole}}}, \tag{3.16}$$

where f is the frequency of the $\Delta L_{\rm ext}$ signal, and $f_{\rm pole} = c(1 - r_i r_e)/2\pi L(1 + r_i r_e)$ is approximately 90 Hz for initial and enhanced LIGO detectors. This cavity pole transfer function is defined as the ratio of Equation (3.15) at $f \ll c/2L$ to it at $f = 0$.

The damped, driven pendulum equation can be expressed as a force-to-displacement transfer function for the center of mass of the optic:

$$P \propto \frac{1}{f_0^2 + i\frac{f_0}{Q}f - f^2}, \tag{3.17}$$

where f_0 is the natural frequency of the pendulum (nominally 0.74 Hz), Q is the quality factor of the pendulum (10 for H1 and 100 for L1), and f is the driving frequency [77].

The challenge is to separate amplitudes of the transfer functions C and A. The separation of these constants is accomplished with the *free-swinging Michelson* technique, in which the interferometer is not under control of the control loop, the arms are not locked, and the light in the cavities is not at resonance. In this configuration, the input test mass mirrors are moved with the actuation coils and then let go, allowing them to swing through the Michelson fringe, which we know is exactly one wavelength of our laser (1064 nanometers). A separate procedure transfers this normalization of the calibration coefficients from the input test masses to the end test masses by locking the arms. By also looking at e_D as this happens, we can figure out the amplitude of the actuation function A; from this the amplitude of the length-sensing function C can be extracted as well.

Calibration is important because it is the largest known source of systematic error in the analysis described in this thesis, as well as most analyses of LIGO data. The calibration systematic error is due to the uncertainty in the amplitude and phase of the response function as a function of frequency of $L_{\rm ext}$. The full error analysis can be found in Reference [77]. For the high-mass search, the other significant source of systematic errors are from our uncertainty in our waveform models (not as quantifiable) and the Monte Carlo errors on the software injections used to evaluate the efficiency of our pipeline (easily quantifiable).

3.3.1 Hardware injections

We can use the control loop described above to make the detectors behave approximately as they would in the presence GWs. To perform one of these so-called *hardware injections*, we first calculate the detector strain $h(t)$ that would be produced by a particular astrophysical source. Using a transfer function from strain to mirror force coil voltage counts (for $f \gg f_0$):

$$T(f) = \frac{L}{C}\frac{f^2}{f_0^2}, \tag{3.18}$$

where L is the length of the interferometer's arm, C is the calibration point in nm/count, and f_0 is the pendulum frequency of the end test mass (0.74 Hz); we can transform $h(t)$ into $v(t)$. When $v(t)$ is injected into the control loop, an end test mass moves in approximately the way the astrophysical signal would cause it to. Hardware injections are used to test our understanding of calibration, search algorithms (for example, the one described in Chapter 7), and veto safety (see Section 4.2.1.5) [78].

An example of a hardware injection of a high-mass signal can be seen as a spectrogram in Figure 3.14 and as a time-series in Figure 3.15.

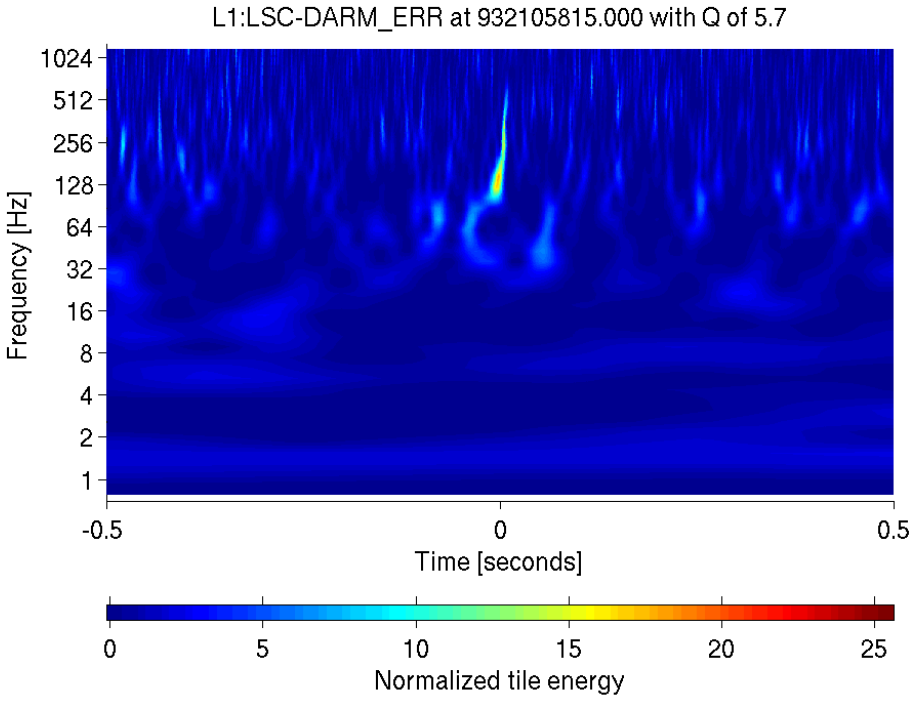

Figure 3.14: A whitened time-frequency spectrogram illustrating a GW signal from a $18.901 + 15.910$ $M_\odot$ system, at a distance of 19.557 Mpc, as seen in L1's GW channel. This signal was produced via a hardware injection.

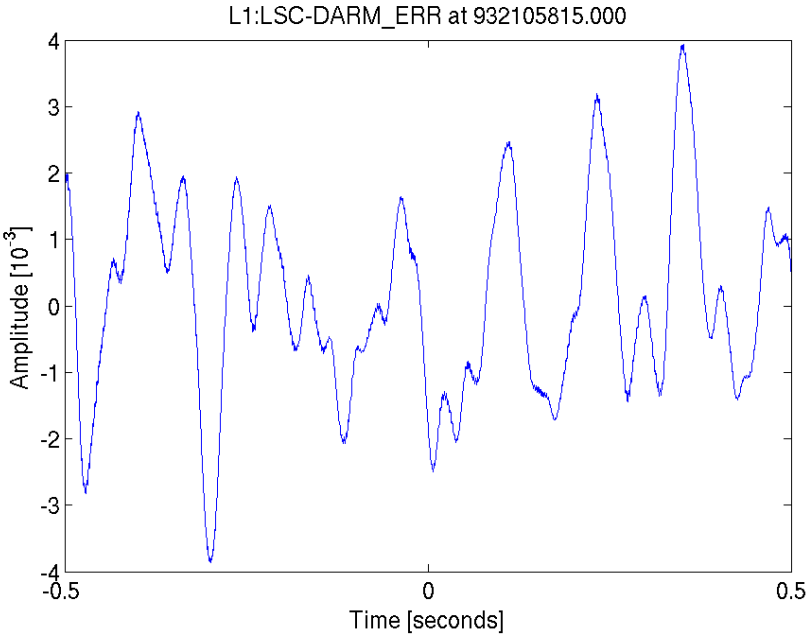

Figure 3.15: A raw timeseries illustrating a GW signal from a $18.901 + 15.910\ M_{\odot}$ system, at a distance of 19.557 Mpc, as seen in in L1's GW channel. Note, however, that the signal (the injected CBC chirp waveform) is lost in the much larger low frequency noise. This signal was produced via a hardware injection.

3.4 LIGO and Virgo detectors' noise

The sensitivity of interferometric GW detectors is strongly frequency-dependent due to design choices and the physical limitations of the various components of the detectors. Depending on the noise spectra, a detector is more or less sensitive to different astrophysical sources. Measured noise spectra can be seen for LIGO and Virgo in Figure 2.17 and Figure 2.18, respectively. For initial LIGO, the theoretical forms of these noise sources are shown in Figure 3.16; experimentally-derived noise curves for one of the LIGO detectors during S6 are shown in Figure 3.17. These figures, sometimes referred to as the "noise budget", are created by back-referencing the noise (which can come in a variety of units) from various sources via mathematical models used to calculate the strain equivalent noise. In other words, not all noise sources manifest as strain noise (moving the mirrors, or changing the frequency of the laser such that it appears that the mirrors have moved), but can be translated into displacement/strain noise by using a transfer function.

The main sources of noise are described in the following list, following Reference [13]:

- *Seismic* noise is due to the motion of the Earth from across the world (Earthquakes, .01 - 1 Hz), to ocean waves shaking the continental plate that LIGO sits on (microseismic, $\sim$ 1/6 Hz), to wind and human-produced noise (anthropogenic, 1 - 30 Hz). The shape of curve is due to the noise at the test mass, after filtering by the mirror suspension and seismic isolation system (see Figure 3.8), which consists of the active HEPI system (in L1 only), the passive three-stage seismic isolation system and the actively

damped single-pendulum system, each of which adds a $1/f^2$ reduction in the noise. Accounting for the ground motion, which already decreases as a function of frequency, the seismic noise curve falls rapidly above 10 Hz (more steeply than f^{-10}.

- *Thermal* noise is present in any damped mechanical system, as described by the the Fluctuation-Dissipation Theorem, which states that the damping (dissipation of thermal energy) comes along with Brownian motion in the system's modes of oscillation [79]. This is relevant to the pendulum-suspended mirrors (whose fundamental mode peaks at 0.74 Hz), the violin modes of the suspension wires (multiple peaks clustering at 340 Hz and harmonics), and the drum mode of the test masses themselves (above 10 kHz). In the pendulum, the noise falls as $1/f^2$ above the pendulum frequency (0.74 Hz) and below the the violin mode resonances (which are not shown in Figure 3.16, but can be seen in Figure 3.17). In the test masses, this noise falls as $1/\sqrt{f}$ assuming a constant (independent of frequency) mechanical loss of the mirror material, causing the noise to leak outside of the drum mode peak.

- *Radiation pressure* and *shot noise* are two sides of the coin of quantum laser noise. The shot noise is due to quantum fluctuations in the number of photons reaching the anti-symmetric port's photodiode. It rises linearly with frequency due to the cavity pole transfer function (take the magnitude of Equation (3.16)) that transforms a phase shift in the light to a GW signal. Shot noise can be lowered by increasing the power of the laser or including a power-recycling cavity. However, doing so increases radiation pressure noise because there are more photons pushing on the mirrors, and therefore more quantum fluctuations in the number of photons. The radiation pressure noise theoretically falls as $1/f^2$, because it is just "white" force noise transformed into displacement noise as in Equation (3.17). The radiation pressure noise increases with the intensity of the laser. The origin of these has been shown to be the quantum noise of the vacuum entering the anti-symmetric port [80]. Shot noise dominates the GW noise spectrum in initial LIGO from 250 Hz to 8 kHz, as is evident in Figure 3.17. Radiation pressure noise has not been observed in LIGO; it lies below other noise sources at low frequencies, as illustrated in Figure 3.16 and Figure 3.17. In Advanced LIGO, radiation pressure noise will be the dominant noise source between about 10 and 40 Hz [59].

- *Residual gas* noise is due to gas molecules that were not eliminated during the vacuum pumping of the instrument's interior. This gas produces several sources of noise. First, there will be a non-unit and fluctuating index of refraction in the beam tubes, causing phase fluctuations on the laser light (sensing noise), which we interpret as GW strain. In addition, the residual gas will randomly kick the mirrors, causing displacement noise; this is negligible in initial LIGO. In addition, dust particles deposited on the mirrors produce scattering centers; the scattered light finds its way back to our detection photodiode, producing glitches.

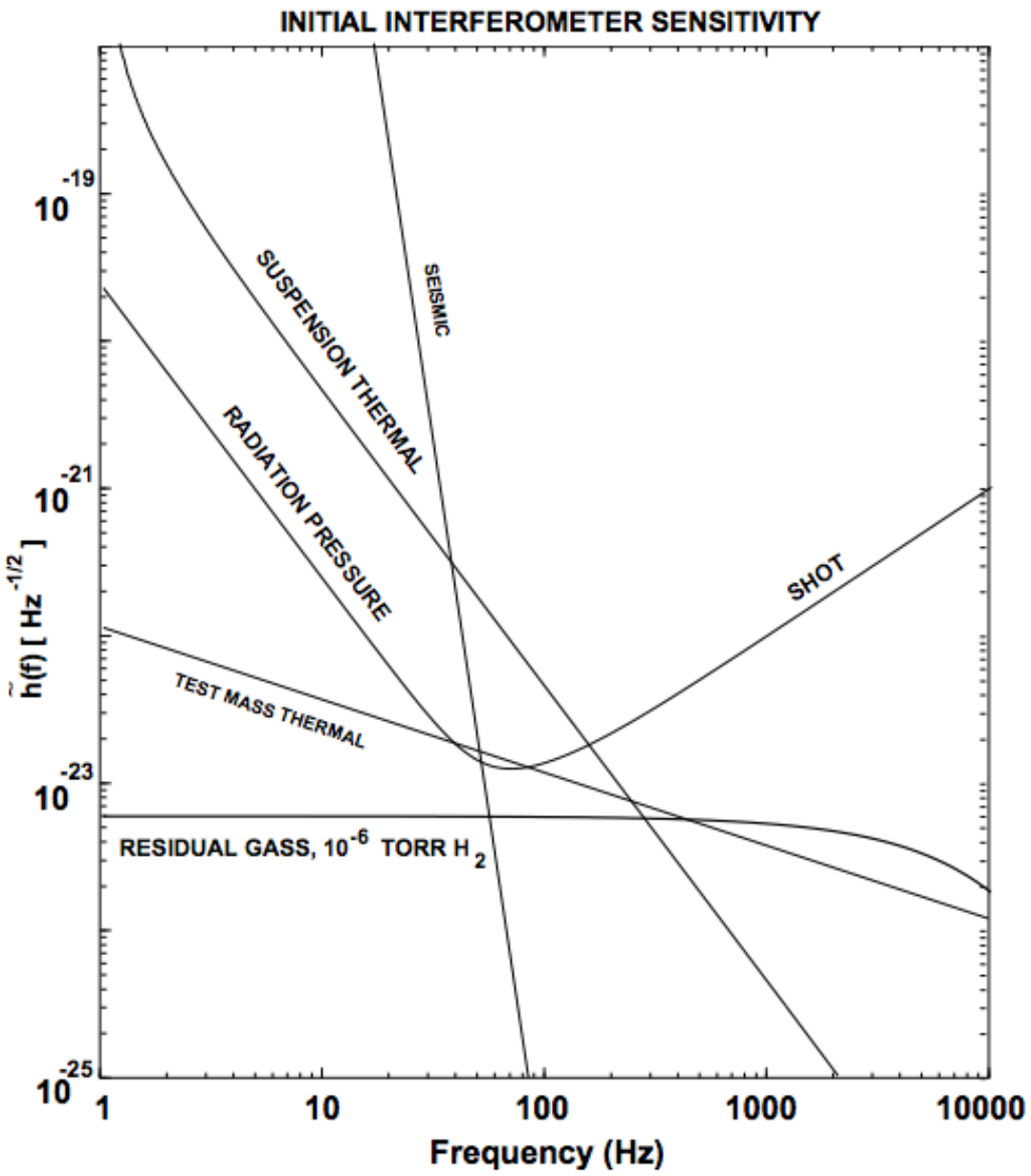

Figure 3.16: The theoretical noise sources limiting initial LIGO strain sensitivity. See Section 3.4 for a detailed description of each contribution to the noise [13].

3.4.1 Gaussian versus non-Gaussian noise

The noise curves presented in the previous section are the result of time-averaging the noise and do not represent the non-stationarity of the noise at either long or short timescales. The long-timescale non-stationarity is evident in the binary neutron star range as a function of time, Figure 3.4. The main sources of short-timescale non-stationarity are laser intensity fluctuations and alignment issues, which generally manifest as low-frequency non-Gaussian noise. On the other hand, the quantum noise at higher frequencies tends

to be more Gaussian. Here, we distinguish between two types of non-Gaussianity. The first are excursions

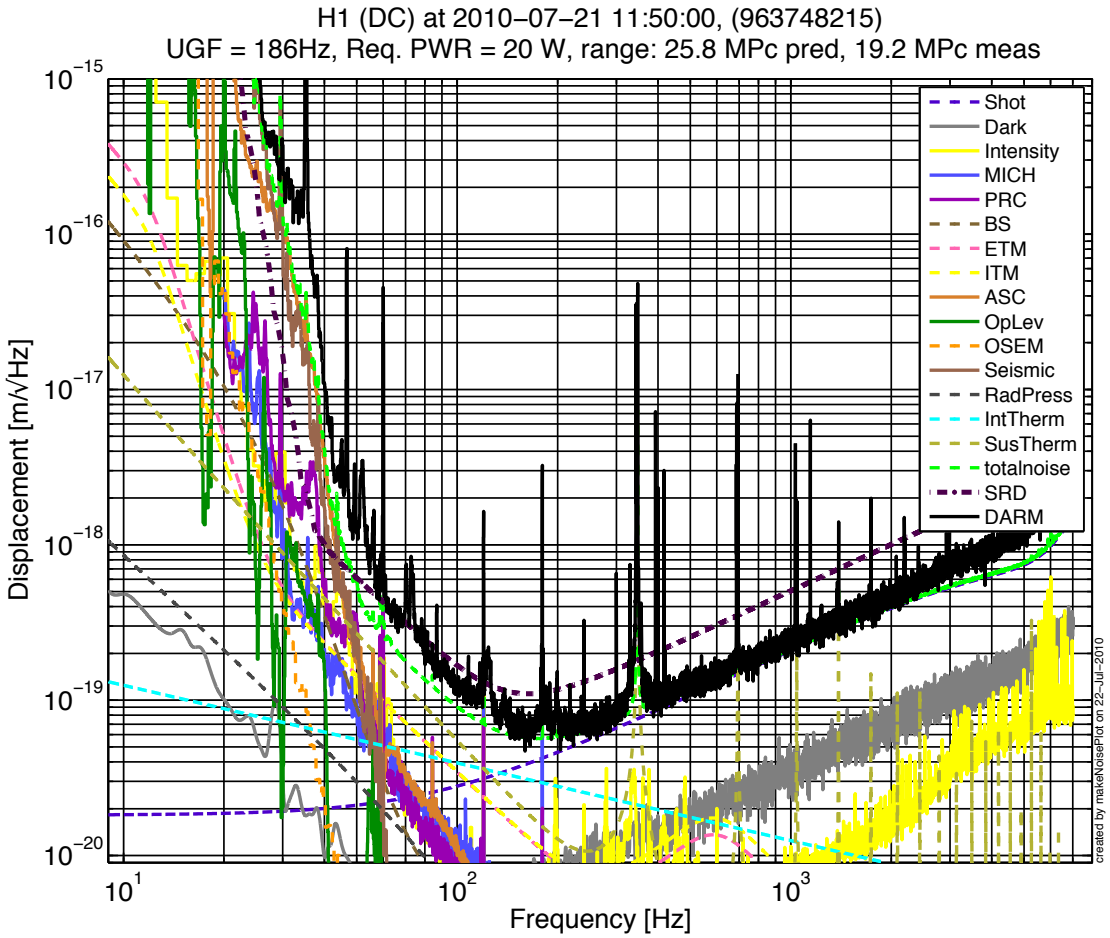

Figure 3.17: The noise budget for H1 during S6. The shot noise is due to the Poisson fluctuations in the laser light hitting the anti-symmetric port's sensing photodiode. The dark noise is the noise that is measured on the photodetector when the laser is turned off; it is due only to the electronics themselves. The intensity noise is due the fluctuations in the laser intensity, whose power emitted is nominally 20 W. The MICH noise is from the control signal that keeps the anti-symmetric port dark. Similarly, the PRC noise is from the control signal that keeps the laser resonant in the power-recycling cavity. The BS (beam splitter), ETM (end test masses), ITM (input test masses) and ASC (angular-sensing and control) noise is residual noise from control systems that monitor and control the mirrors' positions and orientations. The OpLev noise is from the optical lever servo, which senses and controls the mirror angular positions (pitch and yaw). The OSEM noise is from the optical shadow sensor and magnetic actuator, which locally damp the pendulum motion of the mirrors. The seismic noise is due to a variety of sources that produce displacement noise at the mirrors (ITMs and ETMs). The IntTherm noise is the thermal noise internal to the test masses themselves. The SusTherm is the thermal noise in the suspension wires at the violin mode frequencies of $\tilde{3}40$ Hz and harmonics; it also includes the pendulum mode at 0.74 Hz (off the scale of this plot) and $1/f^2$ falloff. The totalnoise curve is the sum of all the listed noise sources (which were already transformed into displacement noise), added in quadrature. The DARM curve is the total noise measured at the anti-symmetric port; the gap between the DARM curve and the total noise curve, especially noticeable below 60 Hz, is not quantitatively understood. The SRD is the strain sensitivity goal listed in the science requirements document [14], presented to the National Science Foundation in 1995.

of 3 to 5 σ from the mean. These alone are not problematic, because they are rarely found in coincidence between detectors. The second are the extremely non-Gaussian excursions of many more σ from the mean; these are the glitches that really limit our sensitivity because they need only be found in coincidence with a 3 σ excursion in another detector. The next chapter goes into the causes of several types of glitches, as well as methods used to veto them.

Chapter 4

Glitches, their effect on data quality, and the need for vetoes

As discussed briefly in Section 1.3, glitches are a problem for the high-mass search because they cause events with a large signal-to-noise-ratio to be found by the matched-filter algorithm. These events not only obscure potential astrophysical GW events, but also would lower our detection confidence in a true event. Of course, the effect is not limited to the high-mass search; glitches present problems for every search done by LIGO and Virgo. This chapter discusses glitches and glitch-finding algorithms in general, gives specific examples of glitches in LIGO S6 data, and explains the traditional methods of mitigating the effect of glitches on a search like the high-mass search. There are two main titles given to research in this realm — *data quality* and *detector characterization*. Although much of their work overlaps, they can be distinguished by the direction the information learned travels — data-quality information tends to go downstream to astrophysical search pipelines, while detector characterization information tends to go upstream to detector commissioners.

4.1 Glitches and glitch-finding algorithms

Glitches are short duration events recorded by the GW channel that can be attributed to an environmental or instrumental disturbance and, as such, we are confident they are not GWs. For the high-mass search, for example, glitches are spurious events that are picked up by the matched-filter algorithm, which compares the data in the GW channel to short-duration templates that model waveforms from high mass binary black hole coalescence. Therefore, glitches with duration and frequency content comparable to the the waveforms listed in Table 2.3 cause the most difficulty for the high-mass search, because the high-mass templates are so short that a χ^2 test does not work well (see Section 7.3.6 for an in-depth discussion of this test).

Glitches can be identified with various algorithms. Two such algorithms were used in this thesis; they are described in the following subsections. The shared goal of these algorithms is to do a fast transform in a wavelet basis that is essentially performing a matched-filter for shapes that look like glitches. These glitches can be found not only in the GW channel, but also in the auxiliary channels; Figure 4.1 shows a glitch in

one of the auxiliary channels. Like many glitches it can be characterized as a ringdown — an abrupt change followed by a decay described by normal modes.

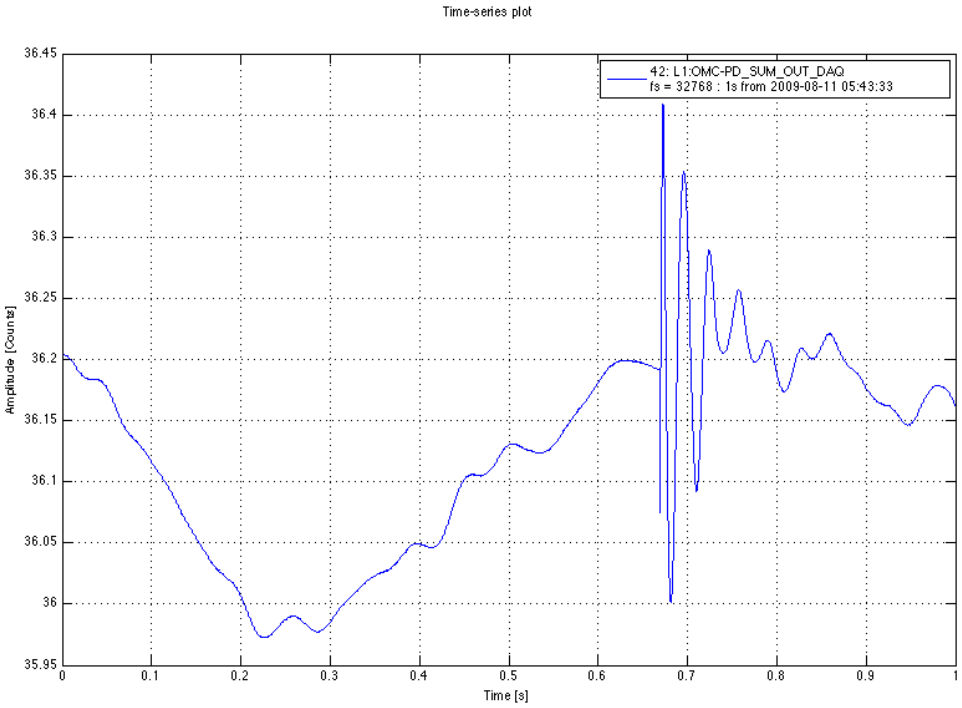

Figure 4.1: An extremely loud glitch seen in an auxiliary channel recording the sum of the photodetectors in the output mode cleaner. Image courtesy of the Detector Characterization group Wiki page https://wiki.ligo.org/DetChar/OMCSpikeGlitches. Note the characteristic ringdown shape.

4.1.1 KleineWelle as a glitch-finding algorithm

In a general sense, glitches manifest as excess energy in a time-series. KleineWelle (German for "little wave", or wavelet) uses the dyadic wavelet transform [81], a multiresolution technique that looks for excess energy in the time-scale space [82]. Dyadic, here, means that the wavelet coefficients are calculated for size scales (time-scales, for us) that vary by powers of two. KleineWelle is useful because it is able to identify and characterize transients in any time-series, such as those from the LIGO detectors' data acquisition systems. A wavelet transform, as opposed to a Fourier transform, is designed to look for small bumps in the data. A wavelet transform, much like a Fourier or Laplace transform, can be expressed as an integral

$$W_g(u,s) = \int_{-\infty}^{\infty} g(t) \frac{1}{\sqrt{s}} \Psi^* \left(\frac{t-u}{s} \right) dt, \tag{4.1}$$

where $g(t)$ is the time series; s defines the scale; Ψ is the wavelet, which is a function of $\frac{t-u}{s}$, where u is a generic time variable with the same range as t. Depending on the scale, we have good time resolution at the

expense of frequency resolution (small scale) or good frequency resolution at the expense of time resolution (large scale) [82]. In other words, at large frequencies, we have poor frequency resolution and good time resolution — see Figure 4.2. Many wavelets can be used; the one currently employed by most LIGO analyses is the Haar wavelet, which can be seen in Figure 4.3.

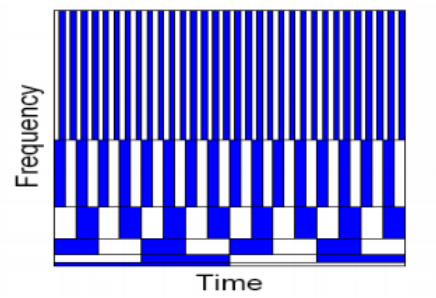

Figure 4.2: The tiling of time-frequency space for the KleineWelle algorithm. The central frequencies of each tile are related by powers of 2. Scale refers to the tile width on the time-axis. The tiles at high frequencies have small scale and poor frequency resolution. The tiles at low frequencies have high scale and poor time resolution [15].

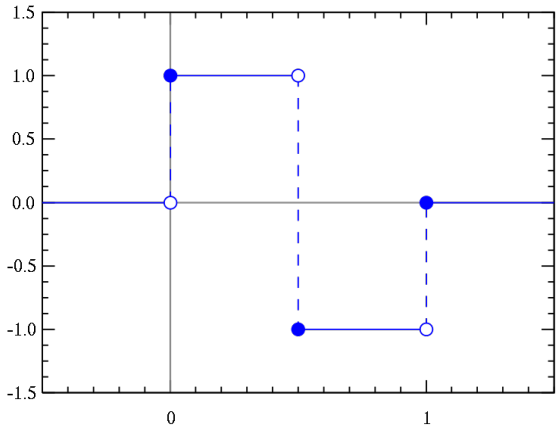

Figure 4.3: A plot of the Haar wavelet. As the scale increases, the wavelet widens. Image courtesy of Wikipedia.

In the case of discrete data (data channels from the LIGO data acquisition system are typically sampled at rates that are powers of two (see, for example, the channels' rates in Table 3.1) we can, instead of computing the integral, use high and low pass filters. See Reference [83] for a discussion of the general computational application of Haar wavelets.

We can define normalized tile energies (sometimes referred to as pixel energies), for each tile in the time-frequency plane:

$$E_j = Y_j^2/\sigma_j^2, \tag{4.2}$$

where the Y_j are the discretized versions of the wavelet coefficients $W_g(u,s)$. For sufficiently large j (scale$=2^j$), the Y_j are Gaussian distributed with a mean 0 and standard deviation σ_j. Thus, the E_j are χ^2-distributed with one degree of freedom. However, it is sometimes useful to define the normalized energy of a cluster of tiles, which is simply the sum of the normalized tile energies of adjacent P tiles that lie above a user-defined threshold; in Gaussian noise, this normalized cluster energy E is chi-squared distributed with P degrees of freedom. The KleineWelle analysis produces several pieces of useful information about any glitches they find, including:

- The *significance* of the cluster, given by $S = -ln \int_{E_{cluster}}^{\infty} \chi^2_P(E)dE$;
- The central frequency of the glitch;
- The number of wavelet coefficients clustered to form the glitch (a measure of time-frequency volume);
- The start and end time of the glitch, which combine to give the glitch duration and/or the central time of the glitch.

Events which have a significance above a nominal threshold are saved along with these pieces of information. The glitches found by the KleineWelle analysis are used in several parts of this thesis.

4.1.2 Omega as a glitch-finding algorithm

Even if different glitch-finding algorithms find the same glitches, their time-frequency reconstruction might not be consistent. LIGO glitch-finding studies also include an analysis known as Omega. Omega tends to have better sensitivity at low frequencies than KleineWelle [84], which is important for detecting glitches that are confused for higher mass systems. The Omega algorithm transforms a time-series $g(t)$ into a set of three-dimensional tiles in the the time-frequency-quality factor space by using the so-called Q transform [85]

$$\mathcal{G}(\tau, f, Q) = \int_{-\infty}^{\infty} g(t)w(t-\tau, f, Q)e^{-2\pi i f t}dt, \tag{4.3}$$

where w is a time-domain window with center τ and duration inversely proportional to the central frequency f [81], and Q is the quality factor (the central frequency divided by the bandwidth) [85] [16]. Like our implementation of the KleineWelle algorithm, we tile the time-frequency space linearly in time and logarithmically in frequency; unlike our implementation of the KleineWelle algorithm, the central frequencies of the tiles are not required to vary by powers of 2. Additionally, for the Omega algorithm, we tile Q logarithmically — see Figure 4.4 [16].

If we choose our window w to be a Gaussian, the integrand in Equation (4.3) becomes the multiplication of the data $g(t)$ with a sine-Gaussian — a sine-Gaussian is a nice approximation to a ringdown that differs (conveniently) in that it does not have an abrupt start:

$$\mathcal{G}(\tau, f, Q) = \int_{-\infty}^{\infty} g(t)e^{-(2\pi f(t-\tau)/Q)^2}e^{-2\pi i f t}dt. \tag{4.4}$$

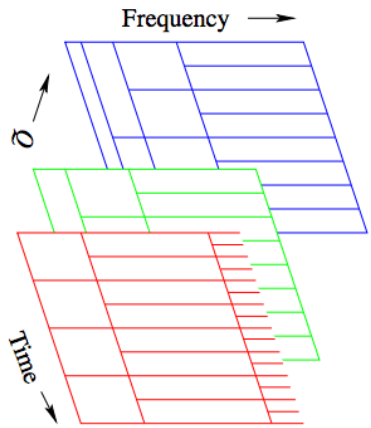

Figure 4.4: The tiling of time-frequency-Q space in the Omega glitch-finding algorithm. The tiles are spaced linearly in time and logarithmically in frequency and Q [16].

Like with KleineWelle, we can calculate normalized tile energies. Here, though, they are defined as

$$Z = |\mathcal{G}|^2 / \left\langle |\mathcal{G}|^2 \right\rangle_\tau = |\mathcal{G}|^2 / \sigma^2_{\mathcal{G}}, \tag{4.5}$$

where the denominator is the mean tile energy for the tile with central time τ [86] (calculated with outliers removed) [16]. If the time-series contained ideal white noise, the normalized tile energies are exponentially distributed [86] (probability$(Z' > Z) = e^{-Z}$). Adjacent tiles with energies above a given threshold can be clustered, and the total energy of the cluster is the sum of the individual tile energies. The normalized cluster energy E is χ^2 distributed with $2P$ degrees of freedom, if P adjacent tiles have been clustered [16].

As with the KleineWelle analysis, we can save the following information about a glitch found with the Omega algorithm:

- The *significance* of the cluster, given by probability$(E' > E) = \Gamma(P, E)/\Gamma(P)$, where the Γ are upper incomplete gamma functions [16];
- The significance and SNR of individual tiles — Z and $\sqrt{Z-1}$, respectively;
- The central frequency of the glitch;
- The number of tiles clustered to form the glitch, taking into account that some tiles overlap;
- The start and end time of the glitch, which combine to give the glitch duration and/or the central time of the glitch.

Of course, our data are discrete, so we actually compute the discrete Q transform,

$$X[n, l, Q] = \sum_{m=0}^{M-1} G[m] W[m - n, l, Q] e^{-i2\pi ml/M}. \tag{4.6}$$

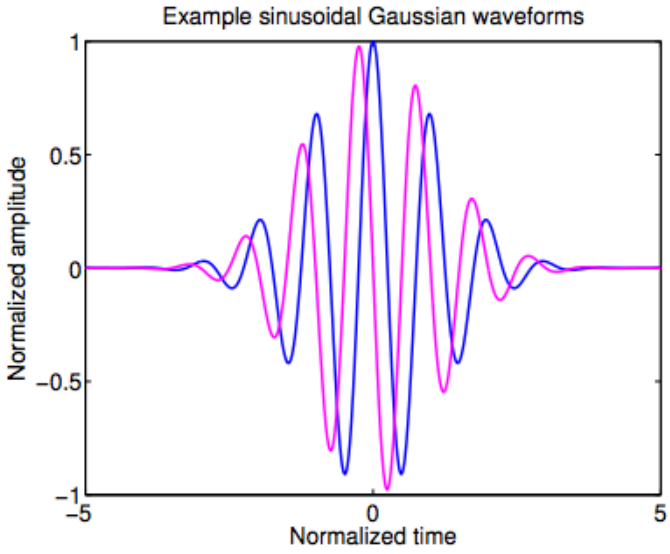

Figure 4.5: Time-domain representations of the sine-Gaussian waveform. These have a central frequency of 1 Hz and $Q = 10$. The blue curve is symmetric about $t = 0$ ("even"), while the magenta is "odd", corresponding to the real and imaginary parts of Equation (4.4) [16].

Here, we must assume that the timeseries $G[m]$ is periodic with period M, even though this is not truly the case. W is a set of wavelets centered on time indices $m - n$ that are integer multiples of M. The windows are proportional in length to Q and inversely proportional to l, the frequency index [81]. Computing this in the frequency domain is convenient because then we only have to Fourier transform the data once. In the frequency domain, Equation (4.6) becomes

$$X[n, l, Q] = \frac{1}{M} \sum_{k=0}^{M-1} \tilde{g}[k + l]\tilde{w}^*[k, l, Q]e^{+2\pi ink/M}, \tag{4.7}$$

where $\tilde{g}[k] = \Sigma_{m=0}^{M-1} g[n]e^{-2\pi mk/M}$ is the Fourier transform of the original time series. The $\tilde{w}$ used in practice is not a Gaussian, but the bisquare (or Connes) window:

$$\tilde{w}(f) = \begin{cases} A(1 - (f/\Delta f)^2)^2 & |f| < \Delta f, \\ 0 & \text{otherwise}, \end{cases} \tag{4.8}$$

where A is normalization constant picked such that if a signal overlaps more than one tile, the sum of the total energy is the same as if it were localized to one tile [16].

4.1.3 Detector characterization and glitch examples

Detector characterization is the process of looking at the auxiliary channels in conjunction with the GW channel — with the goal of identifying not only the times when the detector is not functioning properly, but

also the causes of the problems so that they might be fixed. Often, the problems cannot be mitigated during the course of a science run, in which case the "bad" data are vetoed. Section 4.2 is devoted to the vetoing procedure. The immediately following subsections illustrate the work done by the Detector Characterization group by presenting the stories of several families of glitches.

4.1.3.1 Grid glitches

Grid glitches (only found in H1) are characterized by a distinctive shape in a plot produced by the Omega analysis (see Section 4.1.2) of the GW channel, as seen in Figure 4.6. The grid structure on the plot is an artifact of the time-frequency tiling of the Omega algorithm's implementation (see Figure 4.4), but it also a clue as to the possible source of the glitches, as it indicates a stochastic and broad-band noise. Coincident with periods of grid glitches are times of abnormal readings in the quadrant photodiodes in the output mode cleaner (see Figure 3.3 for the locations of these photodiodes, and Figure 4.7 and Figure 4.8 for the Omega analysis on these photodiodes).

In the end, it was found to be an electronics glitch somewhere near the output mode cleaner, and a resoldering of the piezoelectric tower's power supply eliminated grid glitches in the future.

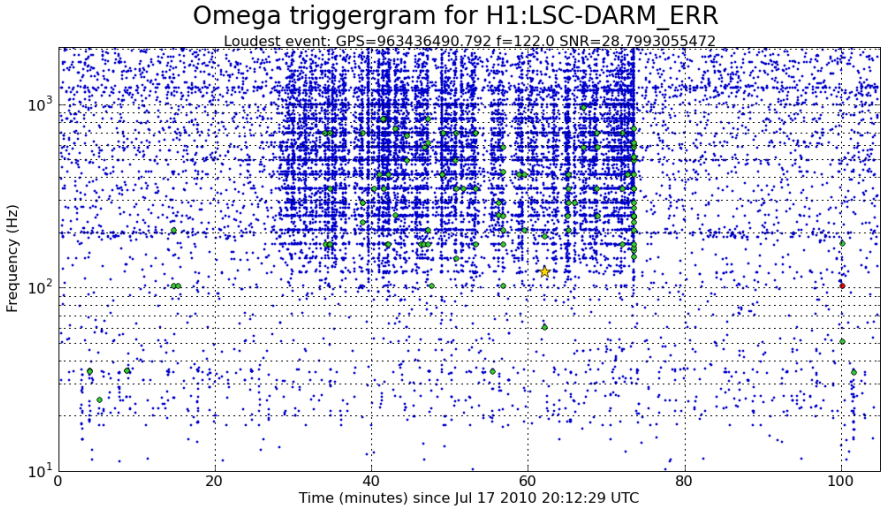

Figure 4.6: An Omega-gram indicates the time-frequency tiles with excess power in the GW channel; the pattern is characteristic of the grid glitches described in Section 4.1.3.1. Each blue dot is an event found with SNR > 5, each green dot is an event found with SNR > 10, and each red dot is an event found with SNR > 20. Image courtesy of the Detector Characterization group Wiki page https://wiki.ligo.org/DetChar/H1GridGlitches.

4.1.3.2 Flip glitches

The flip glitch was given its name because of the distinctive shape of the glitch in the GW channel in time-frequency space. For example, see Figure 4.9, which was also created with the Omega algorithm. Although

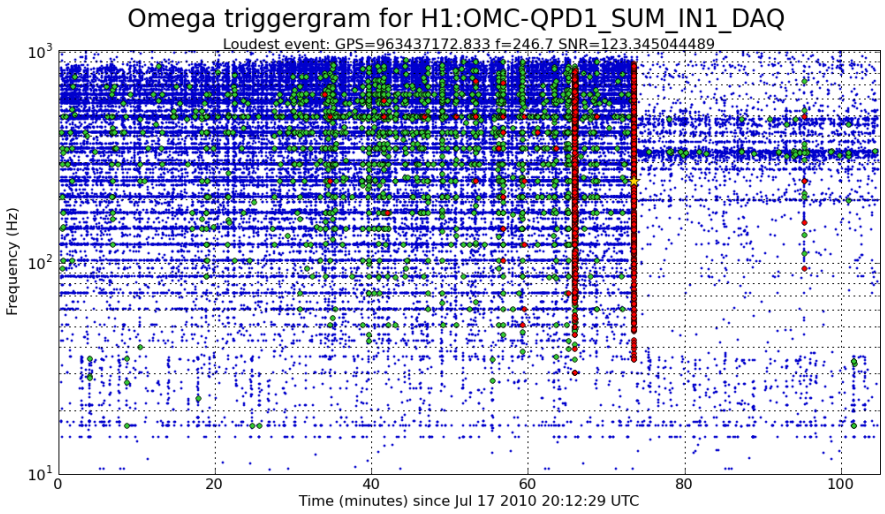

Figure 4.7: An Omega-gram indicates the time-frequency tiles with excess power in the output mode cleaner's QPD1_SUM channel, at the same time as the grid glitches seen in Figure 4.6. Each blue dot is an event found with SNR $>$ 5, each green dot is an event found with SNR $>$ 10, and each red dot is an event found with SNR $>$ 20. Image courtesy of the Detector Characterization group Wiki page https://wiki.ligo.org/DetChar/H1GridGlitches.

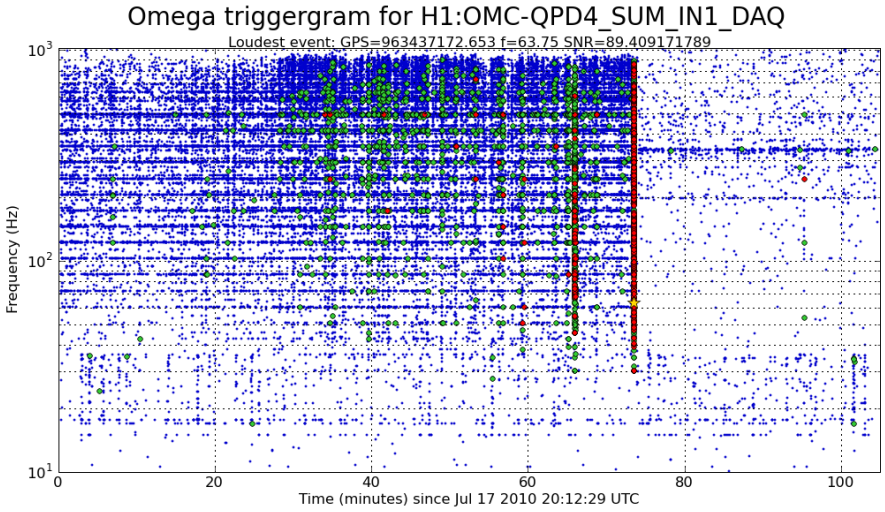

Figure 4.8: An Omega-gram indicates the time-frequency tiles with excess power in the output mode cleaner's QPD4_SUM channel, at the same time as the grid glitches seen in Figure 4.6. Each blue dot is an event found with SNR $>$ 5, each green dot is an event found with SNR $>$ 10, and each red dot is an event found with SNR $>$ 20. Image courtesy of the Detector Characterization group Wiki page https://wiki.ligo.org/DetChar/H1GridGlitches.

members of the flip glitch family share the same shape in the GW channel, they do not have a consistent correlation to the same auxiliary channels. Sometimes they are accompanied by a glitch in an auxiliary channel sensor in the output mode cleaner (shown in Figure 3.10), but other times the output mode cleaner auxiliary channels are clean and the auxiliary channels measuring the Michelson or power-recycling cavity

degrees of freedom show excess power. As explained in the following chapter, since we are only allowed to look at auxiliary channels when removing glitchy data from the analysis for fear of vetoing an astrophysical GW burst signal, it is difficult to veto glitches like this where the only identifying features are in the GW channel.

The output mode cleaner caused problems unique to S6. Unlike glitches from environmental or instrumental sources outside of the OMC, glitches originating in the OMC are not always recorded by multiple auxiliary channels. Since the photodetector used to record GW data are on the same optical table as the OMC subsystem, some glitches in the OMC will only be recorded in the GW channel.

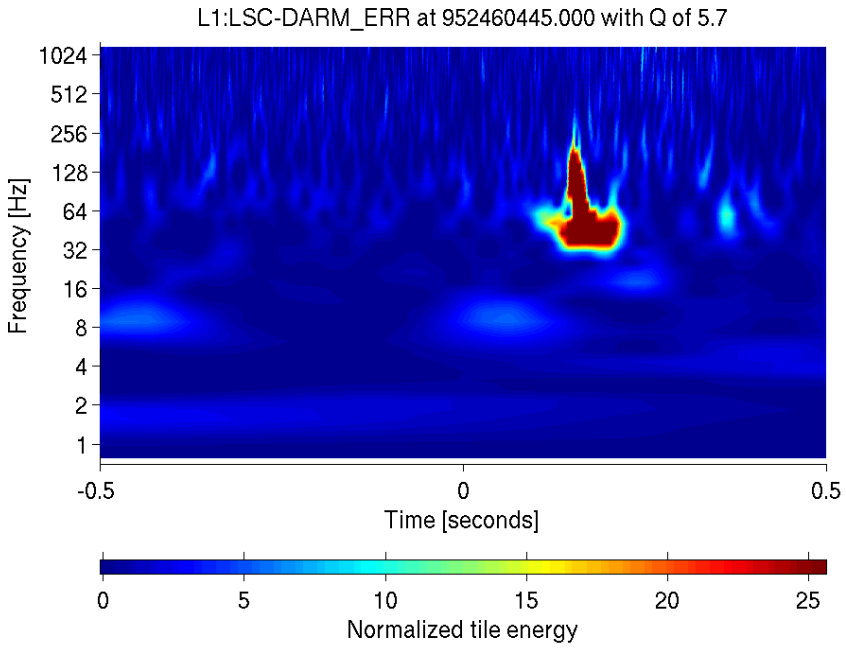

Figure 4.9: This is a Q-scan, also produced by the Omega algorithm. In this plot, the sine-Gaussian decomposition has been whitened and smoothed to emphasize the kinds of glitches seen in LIGO data. Shown here is a Q-scan illustrating a particularly loud example of a flip glitch seen in the GW channel. Figure courtesy of the Detector Characterization group Wiki page https://wiki.ligo.org/DetChar/CurrentGlitchesL1Flip.

4.1.3.3 Upconversion noise

There are many sources of seismic noise, from distant Earthquakes producing noise in the .01 - 1 Hz band to anthropogenic sources producing noise in the 10-30 Hz band. Although the low-frequency cutoff is 40 Hz for LIGO detectors, seismic noise sources still have a considerable effect due to upconversion. The upconversion is thought to be the result of the seismic motion moving electromagnetic components, which causes a Barkhausen effect (discontinuous jumps in flux density of a ferromagnet despite a continuous change of the external magnetic field [87]) in the magnets glued to the mirrors to control their position and angular degrees of freedom [85].

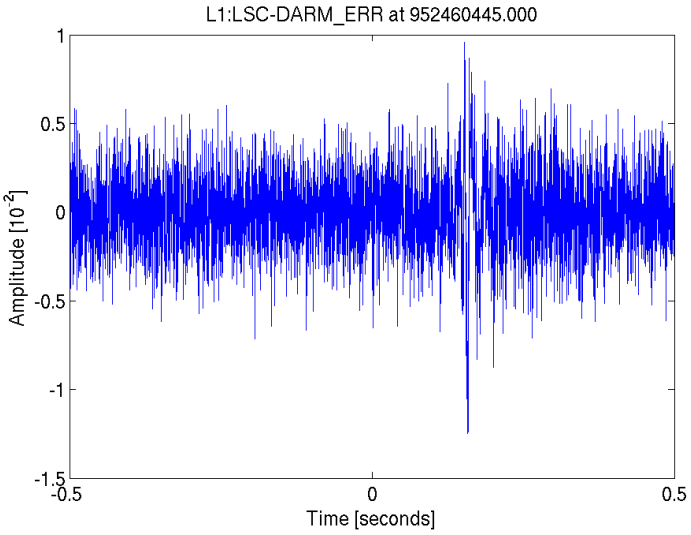

Figure 4.10: The whitened time-domain signal of the flip glitch shown in Figure 4.9. Although not evident at fist glance, a ringdown shape can be seen starting at 0.2 s.

Seismometers are good at measuring the absolute level of seismic activity in their sensitive band. However, upconversion noise is due to spikes above baseline activity; this means that it is difficult to look at their readout and deduce if upconversion noise is a problem at that time. Section 4.2.1.2 describes a method used to veto glitches of this sort.

4.1.3.4 Spike Glitches

Occasionally, there are common and loud glitches for which no explanation can be found. The spike glitch, found only in L1, falls into this category. When the glitch is very loud, as seen in the GW channel, a spike shape is seen in the channel monitoring the sum of the photodiodes in the output mode cleaner (see Figure 4.1 and Figure 4.11). However, this channel is sensitive to GWs, and thus should not be used to identify glitchy times. No other channel or combination of channels could be found to have correlations with spike glitches. During a few particularly bad weeks of data, a veto was created using a matched-filter for this shape in the GW channel, despite this being a potentially dangerous (GW self-veto) procedure (see Section 4.2.1.2).

4.2 The need for vetoes

After the interferometers lock and the laser light becomes resonant in the arms, the detectors can start taking Science Data. But in all searches for GWs in LIGO-Virgo data, it is necessary to first check the quality of the Science Data before beginning the data analysis procedure. Poor data quality manifests itself as either a higher level of noise (an upward shift of the amplitude spectral density curve in Figure 2.11 for example), or

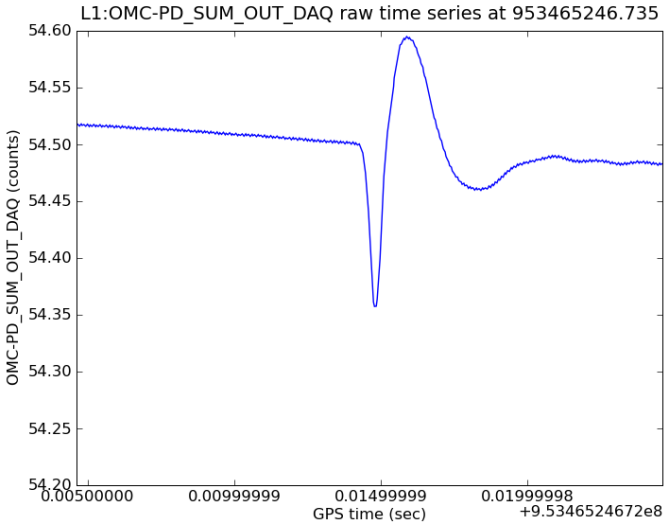

Figure 4.11: The characteristic spike shape of the spike glitch, seen in the output mode cleaner photodiode sum channel. Image courtesy of the Detector Characterization group Wiki page https://wiki.ligo.org/DetChar/OMCSpikeGlitches.

a greater occurrence of glitches, which are defined in Section 4.1. In the high-mass search, poor data quality leads to false alarms, which obscure potential GW signals. In order to mitigate this, we veto segments of data or just the events that occur during certain segments, where an *event* is something that is found by the matched-filter pipeline with an SNR greater than some pre-defined threshold (see Section 7.3.3).

Of course, it would be counter-productive to remove all events in the GW channel, as a true GW signal might be discarded. Fortunately, the sensors and monitors in and around the detectors will also witness glitches that show up in the GW channel, since a disturbance will couple to both the GW channel and the witness channel; the output of these sensors and monitors can be used to create the vetoes that define the segments of data to be removed or flagged — these segments labeled with *data-quality flags*.

Traditional vetoes employ a subset of the full list of auxiliary channels (see Section 3.1.2 for examples of these), making sure to never use a channel that is sensitive to actual GWs; this subset is known as the *safe channel list*. There are channels that are *a priori* deemed unsafe, because the GW channel is known to couple into these channels directly; see Table 4.1 for a list of *a priori* unsafe channels. There are also channels that, due to imperfections in the controls or nonlinearities in the system, will be sensitive to a large enough GW.

Rather than directly determining the safety of these channels, we perform a statistical analysis of the safety of data-quality flags that have been based on the channels; see Section 4.2.1 for a discussion of data-quality flag creation. To determine the safety of the flags, we first inject signals into the control loop (discussed in Section 3.3) that move the end test masses in the way we expect a true GW to do. These *hardware injections* are done hundreds of times during the course of a science run to build up statistics. If the data-quality flag vetoes more hardware injections than would be predicted by random chance, such vetoes are deemed unsafe;

see Section 4.2.1.5 for a full description of the safety analysis. Because of differences between the detectors, and even within a single detector over the course of a science run due to hardware/software commissioning, the full list of unsafe channels can vary between H1 and L1, as well as within H1 or L1 during a science run.

4.2.1 Vetoes/flags for the high-mass search

In order to create the data-quality flags used as vetoes, we first use general information contained in the auxiliary channels' data streams as well as algorithms to identify glitches in the GW and auxiliary channels; both KW (see Section 4.1.1), and Omega (see Section 4.1.2), are used. Next, we perform statistical analyses to quantify the correlation between glitches or generic heightened noise in the safe channels (those known to not contain GW channel information) and glitches in the GW channel. Then we identify the central time and duration (in many cases a padding is added before and/or after a glitch in an auxiliary channel) of the data to veto/flag. Each data-quality flag is then tested for safety, as explained in Section 4.2.1.5. Different methods are used for different types of vetoes; these are described in the following subsections.

As there are different levels of coupling between the GW channel and any given auxiliary channel, as well as different levels of confidence in the persistence of the coupling, there are different categories of vetoes/flags. The terms veto and flag are sometimes used interchangeably because some of the data-quality flags are used to veto segments of data prior to the high-mass analysis, some are used to veto individual events produced by the high-mass analysis pipeline, and some are used simply to provide information about a segment of data and are not used to veto anything. For the S6 high-mass search, astrophysical upper limits are calculated with Category 4 vetoes applied, but GWs are searched for in data with only Category 3 vetoes applied. Category 1 time is removed prior to the start of the analysis. In general, Category N Time means the time remaining after Category 1 - N vetoes are applied. The veto structure is explained in the following list, and the amount of data left after each category's vetoes have been applied is in Table 7.1.

- Category 1 vetoes flag times when the detector was not taking data in the design configuration [76]. Examples include: when Science Mode was turned on accidentally when the detector was not in lock, when the calibration of γ was bad (see Section 3.3), when the temperature in the laser and vacuum equipment area was uncontrolled, when the GW channel photodiode output was saturated, when bad glitches during an out-of-lock time affect surrounding data that is in lock, and when calibration is missing for a section of data. Applying Category 1 flags removes these segments of time from the data to be analyzed. This subset of Science Mode, referred to as Category 1 Time, is analyzed by the high-mass search pipeline.

- Category 2 vetoes flag times when an auxiliary channel that has a well-known and understood coupling into the GW channel records data above a specified threshold. Category 2 flags have a low dead-time and well-crafted windows that pad the data after and/or before the auxiliary channel witnesses the disturbance [76]. Category 2 vetoes are applied atop Category 1 Time. In contrast to Category 1,

Table 4.1: The list of channels *a priori* deemed unsafe due to their physical coupling to the GW channel. Here LSC is the length-sensing and control subsystem, DARM is the differential arm motion, OMC is the output mode cleaner, and DAQ is a data acquisition system.

Channel name	Reason it is unsafe
LSC-DARM_ERR	This is the error signal for the differential arm motion, and is directly used in the calibration of the data into the GW strain (see Section 3.3).
LSC-DARM_CTRL	This is control signal used to push the mirrors so they remain in the null state. It is derived directly from DARM_ERR.
LSC-AS_{I,Q}	In S1-S5, the differential arm motion was derived from the quadrant photodiode at the anti-symmetric port, by looking at the beats between the main laser and the RF sidebands. These beats have both a cosine ("In-phase") component and a sine ("Quad-phase") component. The quad-phase (AS_Q) contains the GW information, but the in-phase (AS_I) signal could also contain GW information due to imperfections in the readout system. Though not used in the S6 scheme for the calculation of the GW signal, the hardware was left in its original locations (see ISCT4 box in Figure 3.10) and continued to record data.
LSC-REFL_{I,Q}	These channels record the same information as the LSC-AS_{I,Q} channels, but from RF photodiodes sensing the light reflected back to the symmetric port, rather than the anti-symmetric port. Though there is generally more noise at the symmetric port, the GW information is still contained in these channels.
OMC-{READOUT,NULLSTREAM}_OUT_DAQ	There are two photodiodes in the OMC (see Figure 3.9 and DCPD1 and DCPD2 in the HAM6 box of Figure 3.10) that are looking at half of a beam of light that has been split by a beamsplitter. These are the DCPDs used to measure the differential arm length in the S6 homodyne detection scheme. The READOUT is the sum of the signal in DCPD1 and DCPD2; The NULLSTREAM is their difference, which should be zero, but if the beamsplitter isn't perfect or if the gains of the photodiodes aren't identical, it will also contain the GW signal.

events produced by the high-mass pipeline that fall within Category 2 flags are simply removed after the analysis.

- In S6, Category 3 vetoes flag times when hardware injections (see Section 3.3.1) were performed (during previous science runs, the definitions were different). The events falling within Category 3 veto segments (which are applied atop Category 1 and 2 veto segments) must necessarily be removed before we start looking for astrophysical GW signals, but it is good to leave them in Category 2 Time so that data analysts can test their algorithms by trying to find them.

- Category 4 vetoes flag times when an auxiliary channel (or combination of channels) that is correlated with glitches in the GW channel goes above threshold, but the coupling between the auxiliary channels used in creating the Category 4 data-quality flags and the GW channel are not as well-understood and/or the dead-time is higher than for Category 2 vetoes [76]. Category 4 Time reflects the removal of data segments flagged by Category 1, 2, 3, and 4.

As distinct analyses looking for different astrophysical sources will be sensitive to different glitches in the GW channel, each analysis will define its own set of vetoes (except Category 1 and Category 3 (all CBC hardware injections), which are the same for all CBC). The following subsections describe the various methods of veto creation and give specific examples of those used in the S6 high-mass search. Note that the categorization scheme in S6 was different from that used in S5 and what we will return to in Advanced LIGO. In S5 and for Advanced LIGO, what is described above as Category 4 is known as Category 3, and hardware injections (used as Category 3 vetoes in S6) are not treated as a data-quality category.

4.2.1.1 Data-quality flags created from the data monitoring tools (DMT)

The most straightforward flags come from setting a threshold on a given auxiliary channel. These channels are monitored with a set of Data Monitoring Tools (DMT). Examples of vetoes created from the DMT are from overflows at photodiodes in the output mode cleaner or in the alignment or length-sensing and control subsystems; seismic activity above threshold at any of the various seismometers around the detector; the thermal compensation system at any of the various test masses measuring thermal deformations above a given threshold; the laser light dipping below an acceptable level of power in the arms; and when hardware injections are performed. These flags can be Category 1, 2, 3, or 4.

Thresholds are then chosen on the readout of a channel or a combination of channels, such that ratio of *dead-time* (the fraction of total data removed) over *efficiency* (the fraction of GW channel glitches removed) is kept below an acceptable value [88]. Once thresholds are picked, we look only at the readout of the safe auxiliary channels in order to remove times during which the detector is likely to be glitchy without looking at the GW channel itself. The length of the veto segment is defined by the length of time the channel is over threshold. However, sometimes it is statistically proven that there are glitches in the GW channel just before

or after the safe auxiliary channel goes above threshold. In this case, a *padding* (typically on the order of 1-8 s on both sides) is added to the veto segment.

4.2.1.2 Data-quality flags created by persons in the detector characterization group (DCH)

Sometimes, although signals in the GW channel and a particular auxiliary channel are correlated, the auxiliary channel can have glitches above a threshold that are not coincident with any glitches in the GW channel for the majority of cases. Thus, using this channel alone would cause an excessive dead-time. However, using this channel in conjunction with other pieces of information can result in useful data-quality flags.

A flag created to deal with seismic upconversion noise (see Section 4.1.3.3) is an example of such a DCH veto. The creation of this veto employed a version of the Omega algorithm (see Section 4.1.2) specifically tuned to find low-frequency excursions of noise in various auxiliary channels. The list of these low-frequency auxiliary channel events are compared to a list of events found in a search for low-mass CBC events in the GW channel. A statistical analysis tests the significance of coincidences between specific frequency bands in each auxiliary channel to the GW events. A set of vetoes with very low dead-time was then created from a union of the times where there are elevated frequency-specific glitches in the significant auxiliary channels [85].

It should be noted that the algorithm used in the previous paragraph is a variation on *hveto*, which uses a hierarchical approach to vetoing using channels whose triggers have a high statistical correlation with triggers in the GW channel. After the channel with the highest statistical correlation is chosen, it is removed, and the correlations are re-calculated. This method, though it achieves low dead-time and high efficiency with relatively few vetoes, was not used to create all the vetoes for the CBC searches despite the fact that in its generic application it could. See Reference [89] for a description of the *hveto* approach.

Another interesting veto specifically created by the DCH group was used to deal with the effects of loud glitches in the GW channel. This is a unique veto in that it directly uses the information contained in the GW channel. Therefore, this veto is only used at Category 4, which means it will not prevent us from detecting an anomalously loud GW signal — Category 3 data are still searched for detection candidates. The need for this veto arises directly from the matched-filter process, which is discussed in Section 7.3.3. Our implementation of the matched-filter used a smeared version of the inverse spectrum weighting in order to avoid artifacts due to spectral lines; see Section 7.3.3. An artifact of the inverse spectrum truncation procedure [90] is that a single loud short-duration glitch will manifest as a loud glitch with wings of triggers before and after it (see Figure 4.12). In order to remove the wing triggers from the data used to calculate the rate upper limit of the high-mass search, a window of 8 seconds on either side of an event in the GW channel with a matched-filter SNR > 250 is vetoed at Category 4. When following up potential GW candidates in Category 3 Time, the presence of this Category 4 flag can inform us as to the cause of the event.

Other DCH vetoes include those flagging times when a part of the calibration was wrong, when all of the magnetometers on site see the same event, and when the level of light in the output mode cleaner is varying above some threshold. DCH vetoes are also used to mark times when any sort of hardware injections are

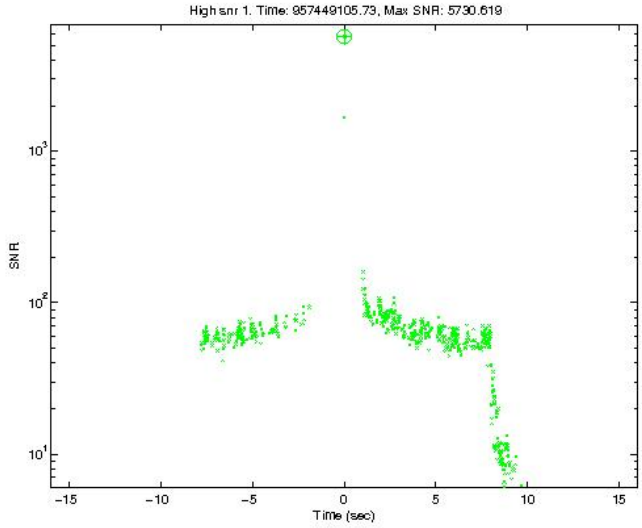

Figure 4.12: The penguin-wing effect of a very loud glitch in the GW channel.

performed; in S6, this is the definition of Category 3.

4.2.1.3 Used percentage vetoes (UPV)

The Used Percentage Veto (UPV) analysis uses KleineWelle (KW), as described in Section 4.1.1, (but can potentially use any other trigger-identifying algorithm) to identify glitches in the GW and auxiliary channels. It then looks for coincidences between an auxiliary glitch and a GW glitch (where the auxiliary channel glitch is within $\pm 1s$ away from the GW channel glitch). Note that there is a possibility that KW is picking up a true GW event and not an instrumental or environmental glitch, but the probability of such occurrences is low and thus will not interfere with the statistical analysis that follows [81].

At first pass, GW and auxiliary glitches are identified if they have a KW significance of 50 or higher. Subsequent passes raise the threshold on the KW significance of triggers in the auxiliary channels in steps of 50 up to 5000, so that the lowest threshold that gives a used percentage of 50% or higher on a given auxiliary channel may be chosen. The used percentage (UP) is defined for each auxiliary channel and each threshold as [88]:

$$\text{UP} \equiv 100 \times \frac{\text{\# of glitches above threshold in an auxiliary ch. coincident with a glitch in the GW ch.}}{\text{total \# of glitches above threshold in an auxiliary ch.}} \quad (4.9)$$

Potential flags are then defined in 1-s segments (with an additional padding of 1 s on either side) for the lowest KW significance threshold for the auxiliary channel that yields a UP $> 50\%$. We then compute their efficiency and dead-time specifically for the highmass search. In this context, efficiency is given by

$$\text{efficiency} \equiv 100 \times \frac{\text{\# of events in the GW ch. eliminated by the veto}}{\text{total \# of events in the GW ch.}}, \quad (4.10)$$

and dead-time by

$$\text{dead-time percentage} \equiv 100 \times \frac{\text{total time vetoed by the flag}}{\text{total time analyzed}}. \tag{4.11}$$

In applying the UPV flags to the highmass search, we considered using only those with an efficiency to dead-time ratio of 10 or greater, but we ended up using all the KW-defined UPV flags, since the cumulative dead-time was not significantly higher. Of course, no unsafe flags are used. See Section 4.2.1.5 for flag safety requirements. UPV flags are at Category 4.

4.2.1.4 Bilinear coupling vetoes (BCV)

Often, glitches will result from a combination of sources. For example, certain angular positions of a mirror can amplify the effect of fluctuations in the fast interferometer control servos. In the interferometer's ideal configuration, the mirrors are aligned with each other. If they drift away from their nominal places to a point where the laser beam is hitting a scattering center on the surface of a mirror, the scattered light will appear at several photodiodes where it usually would not, resulting in glitches seen in fast channels and the GW channel.

Bilinear coupling vetoes (BCVs) were created to capture this type of effect in an automated way. The BCV process entails creating a list of pseudo-channels, each of which is the product of a fast channel and a slow channel. The fast channels are typically captured at 16348 Hz; examples of fast channels include those monitoring and controlling the length of the Michelson and power-recycling cavities. In comparison, the slow channels are captured at below 4096 Hz; examples of slow channels include those monitoring the quadrant photodiodes and wavefront sensors in the angular-sensing and control subsystem [91]. See Table 3.1 for the speeds of various channels.

The first step of the BCV algorithm is to use the KW analysis (see Section 4.1.1) to create lists of triggers in the GW channel and 10 fast channels. Coincidences are formed between triggers less than a second apart in these two lists. Pseudo-channels are constructed for each fast-channel/slow-channel combination. 140 pseudo-channels were created for the S6 analysis. Consistency between glitches in the GW channel and a given pseudo-channel can be defined by their linear correlation coefficient [91],

$$r_{ij} = \frac{\langle h, p_{ij} \rangle}{\langle h, h \rangle \langle p_{ij}, p_{ij} \rangle}, \tag{4.12}$$

where $h(t)$ is the time-series of the glitch in the GW, $p(t) = x(t)y(t)$ is the pseudo-channel's time-series over the same amount of time, and $x(t)$ is a fast channel and $y(t)$ is a slow channel. The i and j label the channels. The inner product is defined as:

$$\langle a, b \rangle = \int_{f_{min}}^{f_{max}} \tilde{a}(f)\tilde{b}^*(f)df. \tag{4.13}$$

A threshold on r_{ij} is determined via a time-slide analysis, like in Section 7.4, such that only an acceptable

number of background triggers (as defined by the KW analysis) have an r_{ij} greater than the chosen threshold. The thresholds on r_{ij} are then used to create 1-second segments with no padding for the BCV data-quality flags [91].

Bilinear coupling vetoes have a remarkably low dead-time, resulting in an efficiency to dead-time ratio that is consistently above 100. Another plus for the BCV method is that it is able to veto low-SNR glitches in the GW channel. BCV flags are at Category 4.

4.2.1.5 Veto safety

Veto safety is extremely important because we do not want to accidentally veto any true GW signals. After the creation of all the data-quality flags for a given analysis time, we calculate each flag's safety probability using hardware injections (see Section 3.3.1) as follows:

$$\text{safety probability} \equiv 1 - F(\#\text{ of hardware injections vetoed} - 1; \#\text{ expected to be vetoed}), \tag{4.14}$$

where F is the Poisson cumulative density function. If the safety probability is less than 10^{-5}, the flag is not used.

Chapter 5

Review of Multivariate Statistical Classification/Machine Learning

Machine learning is a gigantic field whose tools overlap with multivariate statistical classifiers. Multivariate statistical classification is the process of using multi-dimensional information to assign events into two or more categories, or *classes*. Many algorithms for multivariate classification are supervised machine learning techniques, in which a set of events of known class (the *training set*) are used to train the classifier. Perhaps the most famous of these techniques is the artificial neural network (ANN), but there are a wide variety of techniques that offer better performance for particular problems. Other popular methods are support vector machines (SVMs) and decision trees. These algorithms are extremely useful when the dimensionality of the problem is too large for an analytical analysis or even a numerical regression analysis; they are also able to extract heretofore hidden correlations between the input dimensions. It is not obvious which machine learning algorithm will be the best for a given problem; thus, it is often necessary to try several and pick one based on the results [92] [93].

This chapter presents a review of the three algorithms that are used in the analysis described in Chapter 6 and the analyses in Section 8.3 and Section 9.1. Let us define several terms and ideas which are common to multivariate classification problems:

- *feature space*: the n-dimensional space used to characterize the events, where each event is described by an n-dimensional *feature vector*;
- *training set*: a set of events of known class that are used by the training algorithm to create a trained classifier that is then used to guess the class of unknown events in an entirely deterministic way based on their feature vectors;
- *validation set*: in some algorithms, a separate set of events, also of known class, is used during the training process to test against or actively suppress overtraining;
- *overtraining*: overtraining occurs when a classifier correctly classifies all or most of the events in the training set, but does poorly at classifying events not in the training set but drawn from the same

distribution;

- *generalization error*: the distance between the error on the training set and the error on the testing set. An overtrained classifier has a large generalization error.

- *testing/evaluation set*: a third set of events of known class, with no events that exist in the training and validation sets, which are ranked by a trained classifier in order to evaluate the performance of the classifier;

- *robustness*: robustness is an over-used descriptor that can mean: 1) classifiers are unlikely to get overtrained, even without using a validation set during training; 2) noise or missing data in the training set can still yield a strong classifier, or noise in the evaluation set does not prohibit good classification of the evaluation events; 3) classifiers can be used for a wide variety of problems.

The following sections review three machine learning algorithms used in this thesis. After training, each of these algorithms will, given an event, (deterministically) return a rank between 0 and 1 that describes how similar the event is to Class 0 versus Class 1 training events. This thesis describes three applications of machine learning:

- the separation of clean times (Class 0) from glitchy times (Class 1), see Chapter 6;

- the separation of accidental coincidences of instrumental/environmental noise triggers in the high-mass search (Class 0: high-mass background) from truly coincident signal-like triggers as found by the high-mass search (Class 1: high-mass signal), see Section 8.3;

- the separation of accidental coincidences of instrumental/environmental noise triggers in the ringdown search (Class 0: ringdown background) from truly coincident signal-like triggers as found by the ringdown-only search (Class 1: ringdown signal), see Section 9.1.

Setting a threshold on the rank between these classes allows us to classify unknown events into either Class 0 or Class 1. However, it is often useful to use the continuous rank rather than thresholding.

5.1 Artificial neural networks

The ANN is a machine learning technique based on the way in which data are processed in human brains [94, 95]. In the human brain, which is composed of a tremendous number of interconnected neurons, each cell performs only the simple task of responding to an input stimulus. However, when a large number of neurons form a complicated network structure, they can perform complex tasks such as speech recognition and decision-making.

A single neuron is composed of dendrites, a cell body, and an axon. When dendrites receive an external stimulus from other neurons, the cell body computes the signal. When the total strength of the stimulus is

greater than the synapse threshold, the neuron is fired and sends an electrochemical signal to other neurons through the axon. This process can be implemented with a simple mathematical model including nodes (analogous to the cell body), a network topology, and learning rules adopted to a specific data processing task. Nodes are characterized by their number of inputs and connecting weights (analogous to dendrites) and outputs (analogous to axons and synapses) [96]. The network topology (analogous to brain structure) is defined by the connections between the nodes. The learning rules prescribe how the connecting weights are initialized and evolve.

5.1.1 Multi-layer perceptron model

There are a large number of ANN models with different topologies. For the data-quality analysis described in this thesis in Chapter 6, we use one of the most widely-used models, the multi-layered perceptron (MLP) model,which has input and output layers of nodes as well as a few so-called hidden layers of nodes in between. The perceptron is analogous to the artificial neuron, but with the added advantage of a continuous output over a simple binary on/off [97].

The input vector for the input layer is a vector, x, whose length is equal to the dimensionality of the problem. The input for hidden layers and the output layer, called z to distinguish them from x, is a combination of the output from nodes in the previous layer; each layer has a tunable number of nodes. The nodes in adjacent layers are connected with individual connecting weights. The initial structure — the number of layers, neurons, and the initial value of connecting weights — is chosen by hand (via brute force experiment) and / or through an optimization scheme such as a Genetic Algorithm (GA).

For each layer, the output of a node (perceptron) $y_{l,i}$ can be expressed as a function of the input vector (the output of the nodes in the previous layer) times the weights connecting the layer to the previous one plus a bias. Mathematically, this translates to

$$y = f(w \cdot z + b), \tag{5.1}$$

which can be expressed in terms of vector components as:

$$y_{l,i}(z) = f_{l,i}\left(\sum_{j=0}^{N_{l-1}-1} w_{l,i,j}(z) y_{l-1,j}(z) + b_{l,i}(z)\right), \tag{5.2}$$

where l indexes the layer, i indexes the neurons in the l^{th} layer, j indexes the neurons in the previous layer, and b is a bias term that sets the threshold [98]. f is the activation function, which may be chosen to be the identity function, the ramp function, the step function, or a sigmoid function. The analysis described in

Chapter 6 and corresponding paper, Reference [99], uses the sigmoid function:

$$f\left(w \cdot z + b\right) = \left(1 + \mathrm{e}^{-2s(w \cdot z + b)}\right)^{-1}, \tag{5.3}$$

where s is a tunable parameter known as the steepness, and can be specified for each layer before the training process begins.

The training process involves an iterative updating of the weights (w) and biases (b); there are many different algorithms available to accomplish this; we use a specific back-propagation algorithm described in the following subsection.

The final layer has a single neuron and its output is a number between 0 and 1 that can be mapped to the ANN's estimate for the class of the event.

5.1.1.1 Resilient back-propagation

The analysis described in Chapter 6 uses an improved version of the resilient back-propagation algorithm [100] from the Fast Artificial Neural Network (FANN) library [101] called iRPROP. For each event, the algorithm calculates the error between the output of the final layer and the true class of the training event. The algorithm then propagates the errors for each event backwards through the network, updating the weights along the way [101]. In iRPROP, the direction in which the weight is updated is determined by the partial derivative of the error quantity with respect to the weight in question. In contrast to other techniques, the step-size for weight options is not determined by the absolute value of this partial derivative, but by the consistency or lack thereof of the sign of the derivative over the past two iterations of the algorithm and the pre-set minimum and maximum values allowed for a step [100]. This method allows for larger step sizes without sacrificing predictive power, and speeds up the algorithm by minimizing oscillations between weights.

5.2 Support vector machines

The SVM is a machine learning algorithm for binary classification on a vector space [102, 103]. It finds the optimal hyperplane that separates the two classes of training samples. This hyperplane is then used as the decision surface in feature space, and classifies events of unknown class depending on which side of the hyperplane they fall.

As before, x is the feature vector describing an event. A training set is composed of a set of $\{x_i, y_i\}$ where y_i is a scalar, here -1 or 1, indicating the true class of the event. i labels the different events in the training set. If the training set is separable by a hyperplane $w \cdot x - b = 0$, where w is the normal vector to the hyperplane and b is the bias, then the training samples with $y_i = 1$ satisfy the condition $w \cdot x_i - b \geq 1$, and the training samples with $y_i = -1$ satisfy the condition $w \cdot x_i - b \leq -1$. The SVM uses a quadratic

programming method to find the w and b that maximize the margin between the hyperplanes $w \cdot x - b = 1$ and $w \cdot x - b = -1$.

If the training samples are not separable in the original feature space, V_{d}, the SVM uses a nonlinear mapping, $\phi(x)$, into a higher dimensional vector space, V_ϕ, in which two classes of events can be separated. The decision hyperplane in V_ϕ corresponds to a non-linear surface in the original space, V_{d}. Thus, mapping the problem into a higher dimensional space allows the SVM to consider non-linear decision surfaces. The dimensionality of V_ϕ grows exponentially with the degree of the non-linearity of the decision surfaces in V_{d}. As a result, the SVM cannot consider arbitrary decision surfaces due to computational restraints; therefore, it is often true that the populations are not completely separable with this method. If the training samples are not separable after mapping, a penalty parameter, C, is introduced to weight the training error ξ. Finding the optimal hyperplane is reduced to the following quadratic programming problem [99]:

$$\min_{w,b,\xi} \left(\frac{1}{2} w \cdot w + C \sum_{i=1}^{N} \xi_i \right) , \tag{5.4a}$$

$$\text{subject to } y_i \cdot (w \cdot \phi(x_i) + b) \geq 1 - \xi_i \, , \tag{5.4b}$$

$$\xi_i \geq 0, \; i = 1, 2, ..., N \, , \tag{5.4c}$$

where the classification error for a single event is $\xi_i = 1 - y_i(x_i w_i - b)$ and N is the number of events in the training set [102]. When the solution is found, the SVM classifies a sample x_i by the decision function:

$$y(x_i) = \mathrm{sign} \left(w \cdot \phi(x_i) + b \right) \, . \tag{5.5}$$

5.2.1 LibSVM

In the analysis described in Chapter 6 and Reference [99], the open-source package LibSVM was used to perform the SVM analysis [104]. Like most SVM algorithms, it is not necessary to explicitly know $\phi(x)$; it is sufficient to specify $K = \phi(x_i)\phi(x_j)$, the *Kernel function*. There are many common choices for the Kernel function. In Reference [99], we used the Radial Basis Function:

$$K(x_i, x_j) = e^{-\gamma ||x_i - x_j||^2}, \tag{5.6}$$

where γ, along with C from Equation (5.4) are specified by the user; optimal values are chosen via brute force experiment.

Most importantly, rather than simply classifying an event, LibSVM can output a rank between 0 and 1.

5.3 Random forest of bagged decision trees

5.3.1 The binary tree

The basic unit of the forest is the binary decision tree. In our applications, the goal of the tree is to separate events of unknown class into two categories — e.g., signal or background (Section 8.3), or glitch or not (Chapter 6). In general, a tree has the following elements, also called *nodes*:

- *root*: the first node in a tree, at which all the training data starts;
- *branching point*: where a binary *split* is made such that a node splits into two daughter nodes — which events go to which daughter depends on the parameter and threshold chosen by the algorithm;
- *leaf*: a terminal node (no more splits are made).

The entire set of training data (for which the class is known) starts at the root node. For n-dimensional data, the i^{th} row of training data looks like:

$$(x_1, x_2, ...x_n, y, w)_i, \tag{5.7}$$

where x is the n-dimensional feature vector used in the previous two sections, $y = \{0, 1\}$ indicates the class to which it belongs, and w is the weight assigned to the event by the user (in the simplest case, all weights are set to 1).

In a generic self-creating tree, at each node, all thresholds on all feature-space dimensions are tested, and the one that best optimizes the chosen figure of merit is picked. If no dimension/threshold can improve the figure of merit, the node becomes a leaf. Otherwise, it is a branching point, and all events that have a numerical value of the chosen dimension lower than the chosen threshold take the "left" branch and the rest take the "right" branch. A simple choice for the figure of merit on a node, Q, is p, the correctly classified fraction of events [105]. Once the branching begins, each non-terminal node comes in pairs:

$$p_{\text{left}} = \frac{\sum_{\text{if } y_i=0} w_{i,\text{left node}}}{\sum w_{i,\text{left node}}} \text{ or} \tag{5.8}$$

$$p_{\text{right}} = \frac{\sum_{\text{if } y_i=1} w_{i,\text{right node}}}{\sum w_{i,\text{right node}}}, \tag{5.9}$$

where left and right are defined such that the right hand side of Equation (5.10) is maximized, if the figure of merit is symmetric with respect to the two classes, as p is. For asymmetric figures of merit, the split is chosen that maximizes either Q_{left} or Q_{right} [105]. Other figures of merit are discussed in Section 5.3.2.1.

The condition for becoming a terminal node for a symmetric figure of merit is

$$Q_{\text{parent node}} \sum_{i,\text{parent node}} w_i > Q_{\text{left node}} \sum_{i,\text{left node}} w_i + Q_{\text{right node}} \sum_{i,\text{right node}} w_i, \tag{5.10}$$

while for an asymmetric figure of merit it is

$$Q_{\text{parent node}} > \max(Q_{\text{left node}}, Q_{\text{right node}}). \tag{5.11}$$

There are other criteria that can be put in place beforehand to stop splitting. The package used in this thesis, which will be described in Section 5.3.2.1, only sets a minimum number of events allowed on a leaf [105].

After a tree is "grown" (i.e. trained), the structure of the tree is saved. The tree is a series of branching points, each defined by a dimension and a threshold. The leaves can be defined in a discrete or continuous manner. If discrete leaves are chosen, each leaf is labeled as either Class 0 or Class 1, depending on how many Class 0 and Class 1 training events landed on said leaf. If the leaves are labeled in a continuous manner, then they are each assigned a "rank":

$$r = \frac{\Sigma w_1}{\Sigma w_0 + \Sigma w_1}, \tag{5.12}$$

where w_1 and w_0 are the weights of each event on the leaf, and the sum is only over events on the leaf. If the weights are all set to 1, then this rank is simply the fraction of the total number of events on a leaf that are Class 1. When an event of unknown class is evaluated by the tree, it will deterministically end up on one leaf and is either assigned to a class (discrete leaves) or given a rank (continuous leaves).

The process of splitting is equivalent to recursively splitting the data up into rectangular regions, where the rectangles are analogous to the nodes, making them easy to interpret [105]. Other benefits of decision trees are:

- They are not only immune to complications caused by correlated dimensions, the correlations actually help the tree make better decisions [105];
- They can deal with mixed data types (float versus integer);
- They are more easily interpreted than other machine learning algorithms — i.e., not "black boxes";
- They are not computationally limited by a very large feature space [105].

Simple decision trees are often defined as a "weak" classifier. Some weaknesses are listed here:

- The decisions cannot be reversed — if the first split is bad, the tree will never recover; this can be thought of as an instability in the method [105];
- Simple decision trees generally offer poorer predictive power than neural networks [106];

- They can be victim to overtraining (the tree perfectly classifies the training set but fails at classifying a unique testing set from the same population). Therefore a validation set must be used.

Creating an ensemble (or "forest") of decision trees and averaging their output can mitigate the problems of a single decision tree [107]. A modern realization of this scheme is discussed in the following section.

5.3.2 Bagging and random forest technology

Random forests of bagged decision trees (RFBDTs) are a way to combine weak classifiers into a robust classifier. As in nature, a forest is comprised of many trees. By inserting randomness into the algorithm, we can ensure that each trained tree is different from the others. There are a variety of methods to insert randomness into the training procedure, as described in Reference [107]; this section will describe the method used in this thesis.

Bagging, short for *b*ootstrap *agg*regat*ing*, is a method that can be used to create multiple distinct training sets out of the original set of $(x_1, x_2, ...x_n, y, w)_i$. If the original set of training events has T events, each bootstrap replica will also have T events, but these events are chosen at random with replacement. This means that a particular $(x_1, x_2, ...x_n, y, w)_i$ can appear multiple times or not at all in a bagged training set [108]. Bagging can vastly improve the performance of unstable classifiers — in the case of decision trees, bad splits that happen by chance are averaged out when the trees are combined — but it should be noted that this procedure can be detrimental when applied to an already stable classifier. Reference [108] applies bagging to 7 different datasets (creating 100 trees for each original dataset) and finds an improvement of 6% - 77% in classification of test data.

One might be concerned about the training events that inevitably are not used to train a particular tree. By creating bootstrap replicas that are the same size as the original dataset, about 37% of the data are not included in each replica. If the replicas are twice the size of the original dataset, about 14% of the data are not included in each replica. Reference [108] notes that no improvement is made by choosing the larger size of the bootstrap replica; therefore, we use training set replicas that are the same size as the original training set. In general, as Breiman elegantly puts it: "Bagging goes a ways toward making a silk purse out of a sow's ear, especially if the sow's ear is twitchy."

Random technology is implemented in the analyses described in this thesis in the following manner: at each node, a subset of $(x_1, x_2, ...x_n)$ is randomly chosen. Only a threshold on one of the variables in this randomly chosen subset can be used to make the split. The number of variables in the subset can determine the strength of an individual tree (how well it can classify events that were not used in its training) and how correlated the trees are with each other. When correlation increases but strength remains the same, the error on a testing set increases. Choosing the optimal size of the subset is done via brute force experiment. Note that there are other ways to insert randomness into the trees; see [107] for a description of these.

RFBDTs have been shown to outperform neural networks, especially when the feature space is highly

dimensional (dozens or hundreds of dimensions) [105]. Training can be done with or without a validation set, since overtraining is often not an issue — increasing the number of trees cannot increase the generalization error in the same way that increasing the size of a Monte Carlo set cannot lead to a less accurate Monte Carlo integral [92]. Moreover, error estimates can be evaluated without a separate testing set — there are many trees in each each forest that were not trained on particular training events, as a result of the bagging procedure. The classification error on training events can be evaluated with every tree that did not use the event in its bootstrap aggregate training set. These *out-of-bag* estimates tend to over-estimate the error, since error tends to decrease as the number of trees used to classify increases. Another benefit of RFBDTs is that the trained forest is saved into a file that lists the splits of each tree, as well as the class (or continuous rank) of each node and leaf. Each testing event that is run through the saved forest deterministically lands on one of the leaves, and is thus categorized or ranked. Therefore, if the feature space is small enough, and the number of branches low enough, the decisions can be easily visualized.

5.3.2.1 StatPatternRecognition

The RFBDT analyses described in this thesis employ the StatPatternRecognition package created by Ilya Narsky, a former Caltech scientist working in high energy physics [109]. The package contains several different classifiers, including linear and quadratic discriminant analysis, bump hunting, boosted decision trees, bagged decision trees, random forest algorithms, and an interface to a neural network algorithm. The RFBDT classifier from this package has several tunable parameters:

- the number of trees in a forest, n ;
- the number or randomly sampled parameters chosen at each node, s;
- the figure of merit (also called a criterion for optimization), c, which can either be symmetric (equal focus on finding pure signal nodes and pure background nodes) or asymmetric (more focus on finding pure signal nodes, which is often useful in high energy physics);
- the minimum number of events allowed on a leaf, l;
- cross-validation.

Choosing these parameters generally involves performing many trials over possible choices. The increase in compute time must be considered along with overall performance. The training time of a RFBDT is of order $nsN \log N$, where N is the number of events in the training set [106]. The symmetric figures of merit from which we choose are:

- p: the correctly classified (weighted) fraction of events on node, as given by Section 5.3.1;
- $-2pq$: the negative *Gini index*, where $q = 1 - p$;

- $p \log_2 p + q \log_2 q$: the negative *cross-entropy*.

The options for asymmetric figures of merit are:

- $w_1/(w_1 + w_0)$: the *signal purity*, where w_1 is the sum of the weights of signal events on a node and w_0 is the sum of the weights of the background events on the node;
- $w_1/\sqrt{w_1 + w_0}$: the *signal significance*;
- $(w_1 + w_0)[1 - 2w_0/(w_1 + w_0)]_+^2$: the *tagging efficiency*, where the + indicates that the expression in the brackets is only used if it is positive; if it is negative, it is set to 0.

The package also comes with several tools to analyze the inputs and outputs of the algorithm, including:

- A summary table for each forest, listing the number of splits made on each variable in the feature vector and the total change in the figure of merit by each variable's splits;
- A tool to calculate the cross-correlations between all the variables in the feature space;
- A tool to combine the results of various classifiers.

Chapter 6

Multivariate statistical classifiers for data quality and detector characterization

Multivariate statistical classifiers (also referred to as machine learning algorithms (MLAs)) are a natural choice when looking for a tool to combine the information from the LIGO detectors' safe auxiliary channels (those not sensitive to GWs) in order to quantify the quality of the data and potentially characterize the detector, in a similar manner as the methods discussed in Section 4.1.3. The efficacy of several multivariate statistical classifiers was tested on two distinct sets of LIGO data, and is described in detail in Reference [99]:

- all of data taken by the 4 km-arm detector at Hanford, WA (H1) during LIGO's fourth science run (S4: 24 February – 24 March 2005). We will call this the *S4 data* in this chapter;
- some of the data taken by the 4 km-arm detector at Livingston, LA (L1) during one week (28 May – 4 June 2010) of LIGO's sixth science run (S6: 7 July 2009 – 20 October 2010). We will call this the *S6 data* in this chapter.

As H1 and L1 have different problems due to their geographical locations and differences in some of their subsystems, and as many commissioning and configuration changes took place between S4 and S6 — the most significant of which was the switch to DC readout, which totally changed the character of the GW data — there are considerable differences between the S4 data and the S6 data. That the multivariate statistical classifiers used in the analyses of these distinct datasets achieved similar success gives us confidence that these methods will be adaptable and robust when applied to future advanced detectors.

In the analyses described in this chapter, our two categories of times are *glitchy times* (Class 1) and *"clean" times* (Class 0). Glitches are defined in Section 4.1; here they are KleineWelle-identified transient events (see Section 4.1.1) in the GW channel. A glitchy time is defined by a window of ± 100 ms around one of these glitches. The "clean" times are defined by randomly chosen integer GPS seconds that contain only roughly Gaussian detector noise in the GW channel within a window of ± 100 ms (i.e., no KleineWelle

events within this window). A true GW signal, when it arrives at the detector, is superposed on the Gaussian (or in unideal cases, non-Gaussian) detector noise. If the signal's amplitude is high enough, it also would be identified by the specific search algorithm as a candidate transient event. The work described in this chapter and in Reference [99] is not directly concerned with finding true astrophysical signals, but rather with the efficient separation of clean times and glitchy times by only looking at information contained in the auxiliary channels. In the future, this can be folded into astrophysical searches in a manner that replaces traditional data-quality flags described in Chapter 4.

We characterize a time in either class by using information from the detector's auxiliary channels. Importantly, we record the same information for both classes of times. Each channel records a time-series measuring some non-GW degree of freedom, either in the detector or its environment. We first reduce the time-series of each auxiliary channel to a set of non-Gaussian transients using the KleineWelle analysis algorithm from Section 4.1.1, in a method described in the following subsection. Note that there are other methods to characterize a time-series besides using an event-finding algorithm like KleineWelle or Omega; analysis using these other methods is saved for a future publication.

6.1 Data preparation for use with the KleineWelle event-based method

The analysis described in this chapter runs the KleineWelle algorithm on each of the auxiliary channels in the safe channel list as well as the GW channel. The detected transients are ranked by their statistical significance, S, as defined in Section 4.1.1.

In order to create our training and evaluation datasets, we first run the KleineWelle algorithm on the GW channel. Whenever we find a trigger with $S > 35$, we store the time of the trigger. The Class 1 times contain the GW glitch trigger ± 100 ms. Note that it is possible for a trigger in the center of a Class 1 time window to be the result of a true GW, but the probability of this is so low in initial LIGO that the fraction of such events will not significantly contribute to the training of the classifiers — even for S6, the most sensitive of all science runs, the expected rate of detectable astrophysical sources is 10^{-9} Hz [20], while the rate of single detector noise transients (glitches) is 0.1 Hz. Even if a significant fraction of true GW signals make it into the glitch class, they should only manifest as a reduction in training quality, as these signals would have no correlations with (safe) auxiliary channels.

Meanwhile, the KleineWelle algorithm is run on each safe auxiliary channel, storing all triggers with $S > 15$ (below $S = 15$, we start picking up triggers due to fluctuations in random Gaussian noise). The information is combined such that we store the following parameters for each safe auxiliary channel for each glitch:

1. S: The significance of the single loudest transient in that auxiliary channel within ± 100 ms of t, the central time of the KW trigger in the GW channel;

2. Δt: The difference between the central time of the KleineWelle trigger found in the GW time-series (or in the case of Class 0, the randomly chosen GPS time at the center of the time window) and the central time corresponding to the auxiliary channel transient;

3. d: The duration of the auxiliary channel transient as reported by KleineWelle;

4. f: The central frequency of the auxiliary channel transient;

5. n: The number of wavelet coefficients clustered to form the auxiliary channel transient (a measure of time-frequency volume).

If no trigger in a particular auxiliary channel is found within 100 ms of a GW trigger, the 5 fields for said auxiliary channel are simply set to zero. 100 ms was chosen because most of the transient coupling timescales fall within this window [88]. However, future work should consider using a unique window tailored to each channel, as each potential noise source could have a unique coupling timescale to the GW channel.

For S6, we analyze 250 auxiliary channels, resulting in a 1250-dimensional feature vector. For S4, we analyze 162 channels (there were not as many channels and subsystems during S4), resulting in an 810-dimensional feature vector, x. In total, we have 2832 times in Class 1 for the S6 dataset and 16,204 times in Class 1 for the S4 dataset.

For both S4 and S6, the Class 0 times are defined by 10^5 randomly chosen times, excluding times where there is a GW trigger within ± 100 ms of the chosen time. After these times are chosen, we follow the same procedure as for Class 1 times, storing the same information into the feature vectors for both Class 0 and Class 1.

6.2 General formulation of the detection problem

The goal of this work is the robust identification of future glitches in the GW channel, by only looking at the auxiliary channels and not at the GW channel itself. This is directly related to the problem of robust detection and classification of GW signals in LIGO (and Virgo) data, as it will reduce the non-Gaussian background and improve the sensitivity of GW searches.

The given problem reduces to a binary prediction on whether a given auxiliary channel feature vector x describing a specific time belongs to Class 0 (clean times in the GW channel) or Class 1 (glitchy times in the GW channel). Though each of our classifiers can go beyond the binary and rank a time on the continuum between Class 0 and Class 1, we will begin the discussion in terms of the binary decision. In the feature space $x \in V_d$, this binary decision can be mapped into identifying domains for Class 1 times, V_1, and Class 0 times, V_0. The surface which separates these two domains can be called the decision surface. We would like to find the optimal decision surface separating the two classes in such a way that we maximize the probability of finding Class 1 times in V_1 at a fixed probability of miscategorizing Class 0 times in V_1. This essentially

minimizes the probability of incorrectly classifying times and is often referred to as the Neyman-Pearson criterion [94]. It can also be talked about in terms of the probability of glitch detection, equivalently the *glitch detection efficiency*, P_1, and the probability of classifying a clean sample as a glitch, equivalently the *false alarm probability*, P_0.

Finding the optimal decision surface analytically is an extremely difficult task if the feature vector contains more than a few dimensions. For high-dimensional problems like ours, MLAs are the state-of-the-art solution. The three MLAs considered (ANN, SVM, and RFBDT) are introduced in the previous chapter, Chapter 5. Because they differ significantly in their underlying algorithms and their approaches to classification, we can investigate the applicability of different types of MLAs to glitch identification in the GW data. All MLAs considered require training samples from both Class 1 and Class 0 and use these training sets to find the optimal classification scheme (equivalent to the optimal decision surface). In the limit of infinitely many samples and unlimited computational resources, different classifiers should recover the same theoretical result, the decision surface defined by the constant likelihood ratio; here, the likelihood ratio is defined by the ratio of the probability density function for a given feature vector to be in the glitch region to the probability density function for the given feature vector to be in the clean region of the feature space. To this end, it is critical that classifiers are trained and optimized using criteria consistent with this result. Apt optimization criteria are the fraction of correctly classified times and the Gini index criteria; these are used by ANN / SVM and RFBDT, respectively.

While all classifiers we investigate here should find the same optimal solution with sufficient data, in practice, the algorithms are limited by the finite number of samples in the training sets and by computational cost. The classifiers have to handle a large number of dimensions efficiently, many of which might be redundant or irrelevant. By no means is it clear that the MLA classifiers will perform well under such conditions. It is our goal to evaluate their performance for our application.

We evaluate their performance by computing reciever operating characteristic (ROC) curves. These curves, which map the classifiers' overall efficiencies at glitch detection as a function of false alarm probability ($P_1(P_0)$), are objective and can be directly compared. For a MLA, we define glitch detection efficiency,

$$P_1(r_*) = \frac{\text{\# of Class 1 times with } r_{\text{MLA}} > r_*}{\text{total \# of Class 1 times}}, \tag{6.1}$$

and the false alarm probability,

$$P_0(r_*) = \frac{\text{\# of Class 0 times with } r_{\text{MLA}} > r_*}{\text{total \# of Class 0 times}}, \tag{6.2}$$

as functions of a threshold r_* on the MLA rank r_{MLA}. We use ROC curves to evaluate performance instead of the traditional dead-time and efficiency (See Section 4.2.1.3) because it allows us to look at the effect of varying the threshold r_* on the continuous rank r_{MLA} between Class 0 and Class 1. The y-axis of the ROC curve (P_1) is simply the efficiency/100 (extend Equation (4.10) to all traditional data-quality vetoes being

considered) of the Category set of data-quality flags being used by a search (see, for example, Section 4.2.1). The x-axis of the ROC curve (P_0) is analogous to dead-time; however, they are not exactly equal. This is because the dead-time for the set of data-quality flags being used by a search (extend Equation (4.11) to all traditional data-quality vetoes being considered) is the fraction of *total* time removed. In comparison, P_0 is the fraction of *clean* time removed. Be that as it may, for a typical rate of glitches of $\sim$0.1 Hz, the P_0 and dead-time measures are almost identical in the most relevant region of $P_0 \leq 10^{-2}$.

In addition to comparing the MLA classifiers to each other, we benchmark them using ROC curves from the OVL algorithm [110]; see Section 6.2.2. This method constructs segments of data to be vetoed using a hard time window and a threshold on the significance of transients in the auxiliary channels. The veto segments are constructed separately for different auxiliary channels and are applied in the order of decreasing correlation with the GW triggers. By construction, only pairwise correlations between a single auxiliary channel and the GW channel are considered by the OVL algorithm (in contrast to BCV, Section 4.2.1.4). These results have a straightforward interpretation and provide a good sanity check.

In order to make the classifier comparison as fair as possible, we train and evaluate their performances using exactly the same data. Furthermore, we use a round-robin procedure for the training-evaluation cycle, which allows us to use all available glitch and clean samples. Samples are randomized and separated into ten equal subsets. To classify times in the k^{th} subset, we use classifiers trained on all but the k^{th} subset. In this way, we ensure that training and evaluation are done with disjoint sets so that any over-training that might occur does not bias our results.

An MLA classifier's output is called a rank, $r_{\mathrm{MLA}} \in [0, 1]$; a separate rank is assigned to each glitch and clean sample. Higher ranks generally denote a higher confidence that the time is glitchy. A threshold on this rank maps to the probability of false alarm, P_0, by computing the fraction of clean samples with greater or equal rank. Similarly, the probability of detection or efficiency, P_1, is estimated by computing the fraction of glitches with greater or equal rank. Essentially, we parametrically define the ROC curve, $P_1^{\mathrm{OPT}}(P_0)$, with a threshold on the classifier's rank. Synchronous training and evaluation of the classifiers allow us to perform a fair comparison and to investigate various ways of combining the outputs of different classifiers. We discuss our findings in detail in Section 6.2.3.1 and Section 6.2.3.2.

6.2.1 Tuning the machine learning algorithms (ANN, SVM, RFBDT)

As introduced in Chapter 5, each of the machine learning algorithms under consideration has several tunable options. For ANN, these are the number of hidden layers, the number of neurons per layer, and the activation function. Two hidden layers were chosen, each with 15 neurons (for the runs with the full datasets). For the reduced-data runs, the number of neurons was decreased to avoid over-training. A sigmoid activation function, shown in Equation (5.3), with steepness $s = 0.5$ in the hidden layers and $s = 0.9$ in the output layer. Unlike for SVM and RFBDT, each dimension in the feature space was re-scaled to fit in the range [0,1]. For

each auxiliary channel, the Δt dimension was transformed by

$$\Delta t' = -\text{sign}(\Delta t) \log |\Delta t| \tag{6.3}$$

prior to the re-scaling. This was done to better resolve very small values of Δt.

For SVM, the main tuning choice is the kernel function, for which we choose the Radial Basis Function (Equation (5.6)). The choice for γ=0.0078125 in this function, as well as C=8 in Equation (5.4a), was chosen by testing various value pairs of γ and C on a logarithmically spaced grid. The optimal choice was made by choosing the pair with the largest value of

$$\int_{P_0=0.001}^{P_0=0.05} P_1(P_0) d(\ln P_0). \tag{6.4}$$

For RFBDTs, the tunable parameters are the number of trees in a forest (n), the number of randomly sampled dimensions at each split (s), the minimum number of training samples (from either class) on a leaf (l), and the criterion for optimization (c); see Section 5.3.2.1 for a list of the optimization criteria. The choices tried for these parameters were $n = 100, 200, 500$; $s = 32, 64, 128, 256, 512$; $l = 2, 4, 8, 16, 32, 64$; and $c = 1, 2, 3, 4, 5, 6, 7, 8, 9$. Larger values of n and s significantly increase the compute time for the training of a forest. Nominal choices of $n = 100$, $s = 64$, $l = 4$, and $c = 5$ (the Gini index) were used, while one of the parameters was varied. Based on maximizing P_1 at $P_0 = 0.01$, final choices of 100 trees, 64 randomly picked variables at each split, a minimum number of 8 training samples on a leaf, and the Gini index were made. Increasing n and s led to slight improvements that were not considered worth the extra compute time.

For each of the classifiers, since P_1 did not vary significantly, the values were not retuned for the S6 data.

6.2.2 Ordered veto list as a benchmark

The OVL algorithm assumes transients in certain auxiliary channels are more correlated with the glitches in the GW channel and looks for a hierarchy of correlations between auxiliary and GW glitches, much like the *hveto* algorithm mentioned in Section 4.2.1.2. It begins by generating a list of triggers in the safe auxiliary channels and the GW channel using KW (but any trigger-identifying algorithm could be used). For the auxiliary channels' triggers, different lists of segments are created for various time windows, [$\pm$ 25 ms, $\pm$ 50 ms, $\pm$ 100 ms], and KW significance thresholds, [15, 25, 30, 50, 100, 200, 400, 800, 1600]. These segments can be thought of as data-quality flags like those described in Section 4.2.1. If triggers from the GW channel fall within these segments, they can be vetoed. A figure of merit for these segments is the *efficiency over dead-time*:

$$\epsilon/f = \frac{n_c/N}{\Delta t/T} \cong \frac{n_c}{\langle n_c \rangle}, \tag{6.5}$$

where n_c is the number of GW triggers falling within one of the segments considered (i.e., the number of GW channel triggers in coincidence with the auxiliary channel triggers), N is the total number of GW channel

triggers, Δt is the total amount of time contained in the segments, and T is the total amount of time in the stretch of data. If the triggers in the auxiliary channel and the GW channel are from uncorrelated Poisson processes, the efficiency over dead-time can be re-written as the ratio of coincident triggers divided by the expected number of coincident triggers based solely on chance, $\langle n_c \rangle$.

The list of segments for the auxiliary channel/time window/significance threshold combination with the highest efficiency over dead-time is considered first. The segments that overlap with a GW channel trigger and the GW channel trigger are then removed (i.e., both N and T are reduced), and ϵ/f is calculated for the next set of segments. This procedure is repeated for each set of segments (i.e., each auxiliary channel/time window/significance threshold combination). The ϵ/fs calculated during this procedure introduce a new ordering for the sets of segments. A segment list is removed from consideration of future iterations if $\epsilon/f \leqslant 3$. The procedure is repeated following the new order for the sets of segments. In practice, less than 10 iterations of this procedure are needed to converge on the optimal ordering of the sets of segments.

The OVL algorithm defines the veto-configuration rank for each segment list, r_{OVL}, as the efficiency over dead-time calculated at the final iteration of the algorithm. Unlike the ranks for the MLAs, r_{OVL} is not restricted to [0,1]; in fact, its range is $[3, \infty)$.

We find that only 47 out of 162 auxiliary channels in S4 data and 35 out of 250 auxiliary channels in S6 data appear on the final list. Below, we refer to this subset of channels as the "OVL auxiliary channels." For a more detailed description of the OVL algorithm, see Reference [110].

The procedure for optimizing the ordered list of veto configurations can be considered a training phase. An ordered list of veto configurations optimized for a given segment of data can be applied to another segment of data. Veto segments are generated based on the transients in the auxiliary channels and the list of configurations. Performance of the algorithm is evaluated by counting fractions of removed glitches and clean samples, and computing the ROC curve. As with our classifiers, we use the round-robin procedure for OVL's training-evaluation cycle.

6.2.3 Testing the algorithms' robustness at finding glitches while keeping low dead-time

One of the main goals of this study is to establish if machine learning methods can successfully identify transient instrumental and environmental artifacts in LIGO GW data. The potential difficulty arises from high dimensionality and the fact that information from a large number of dimensions might be either redundant or irrelevant. Furthermore, the origin of a large fraction of glitches is unknown in the sense that their cause has not been pinpointed to a single instrumental or environmental source. In the absence of such deterministic knowledge, one has to monitor a large number of auxiliary channels and look for statistically significant correlations between transients in these channels and transients in the GW channel. These correlations, in principle, may involve more than one auxiliary channel and may depend on the transients' parameters in an

extremely complicated way. Additionally, new kinds of artifacts may arise if one of the detector subsystems begins to malfunction (see Section 3.1.1). Likewise, some auxiliary channels' coupling strengths to the GW channel may be functions of the detector's state (e.g,. optical cavity configuration and mirror alignment and couplings explained in Section 4.2.1.4). Depending on the detector's state, the same disturbance witnessed by an auxiliary channel may or may not cause a glitch in the GW channel. This information cannot be captured by the KleineWelle-derived parameters of the transients in the auxiliary channels alone and requires extending the current method. We leave these problems to future work.

Because of the uncertainty in the types and locations of correlations, we include as many auxiliary channels and their transients' parameters as possible. However, this forces us to handle a large number of features, many of which might be either redundant or irrelevant. Our classifiers may be confused by the presence of these superfluous features and their performance may suffer. One can improve performance by reducing the number of features and keeping only those that are statistically significant. However, this requires preprocessing the input data and tuning, which may be extremely labor intensive. On the other hand, if the classifier can ignore irrelevant dimensions automatically without a significant decrease in performance, it can be used as a robust analysis tool for real-time glitch identification and detector characterization. By efficiently processing information from all auxiliary channels, a classifier will be able to identify new artifacts and help to diagnose problems with the detector.

In order to determine our classifiers' robustness, we perform a series of runs in which we vary the dimensionality of the input data and evaluate the classifiers' performance. First, we investigate how their efficiency depends on which elements of the feature vector are used. We expect that not all of the five parameters (S, Δt, f, d, n) are equally informative. Naively, S and Δt, reflecting the disturbance's amplitude in the auxiliary channel and its degree of coincidence with the transient in GW channel, respectively, should be the most informative. Potentially, the frequency, f, duration, d, and the number of wavelet coefficients, n, may carry useful information if only certain transients observed in auxiliary channels produce glitches. However, it is possible that these parameters are only correlated with the corresponding parameters of GW transient, which we do not incorporate in this analysis. Such correlations, even if not broadened by frequency-dependent transfer functions, would require analysis specialized to specific GW signals and goes beyond the scope of this work. We perform a generic analysis, not relying on the specific characteristics of the GW transients.

Anticipating that some of the parameters could be irrelevant, we prepare several data sets by removing features from the list: (S, Δt, f, d, n). We prepare these data sets for both S4 and S6 data and run each of the classifiers through the training-evaluation round-robin cycles described in Section 6.2. We evaluate their performance by computing the ROC curves, shown in Figure 6.1.

We note the following relative trends in the ROC curves for all classifiers. The omission of the transient's duration, d, and the number of wavelets, n, has virtually no effect on efficiency (P_1). The ROC curves are the same to within our error, which is less than $\pm$ 1 % for our efficiency measurement, based on the total number of glitch samples and the normal approximation for binomial confidence interval, $\sqrt{P_1(1-P_1)/N}$.

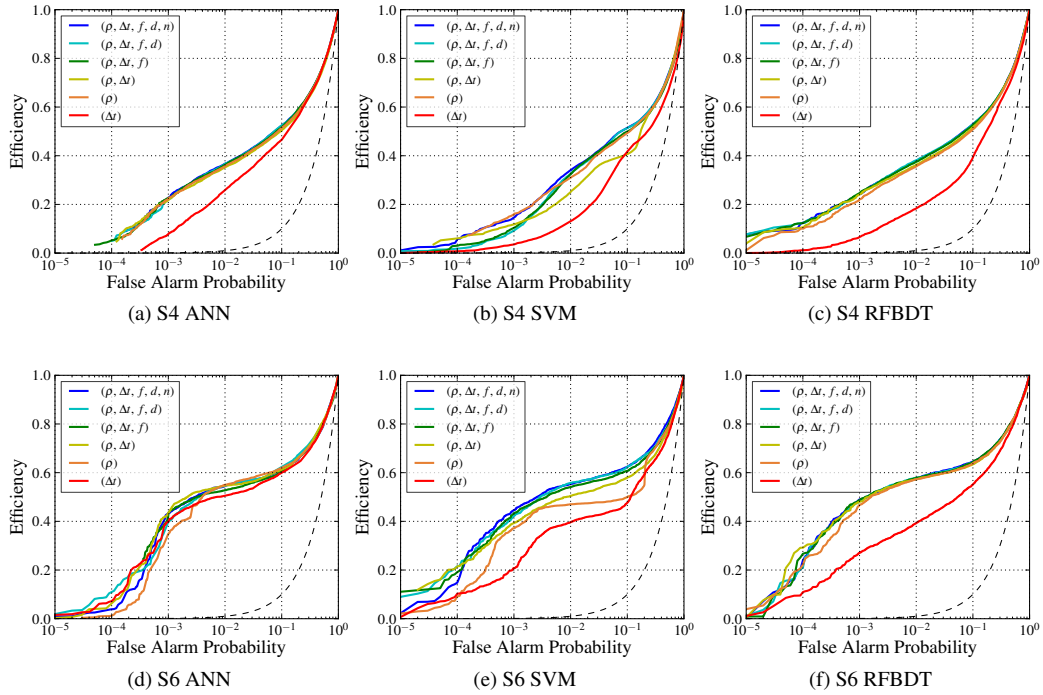

(a) S4 ANN (b) S4 SVM (c) S4 RFBDT

(d) S6 ANN (e) S6 SVM (f) S6 RFBDT

Figure 6.1: Varying sample features. We expect some of the five features recorded for each auxiliary channel to be more useful than others. To quantitatively demonstrate this, we train and evaluate our classifiers using subsets of our sample data, with each subset restricting the number of auxiliary channel features. We observe the general trend that the significance, S, and time difference, Δt, are the two most important features. Between those two, S appears to be marginally more important than Δt. On the other hand, the central frequency, f, the duration, d, and the number of wavelet coefficients in the KW trigger, n, all appear to have very little effect on the classifiers' performance. Importantly, our classifiers are not impaired by the presence of these superfluous features and appear to robustly reject irrelevant data without significant efficiency loss. The black dashed line represents a classifier based on random choice.

Omission of the frequency, f, slightly reduces the efficiency of SVM (Figure 6.1b and Figure 6.1e), but has no effect on either ANN or RFBDT. A comparison between the ROC curves for (S, Δt), (S) and (Δt) data sets shows that while a transient's significance (S, but called ρ in the figure legends) is the most informative parameter, including the time difference generally results in better overall performance. Of the three MLA classifiers, SVM seems to be the most sensitive to whether the time difference is used in addition to significance. RFBDT, as it appears, relies primarily on significance, which is reflected in poor performance of the (Δt)-only ROC curves in Figure 6.1c and Figure 6.1f. The trend for ANN is not as clear. In S4 data, including timing does not change the ROC curve (Figure 6.1a), while in S6 data it improves it (Figure 6.1d). Overall, we conclude that based on these tests, most, if not all, the information about detected glitches is contained in the (S, Δt) pair. At the same time, keeping irrelevant features does not seem to have a negative effect on our classifiers' performance.

The OVL algorithm, which we use as a benchmark, ranks and orders the auxiliary channels based on the strength of correlations between transient disturbances in the auxiliary channels and glitches in the GW

channel. The final list of OVL channels includes only a small subset of the available auxiliary channels, 47 (of 162) in S4 data and 35 (of 250) in S6 data. The rest of the channels do not show statistically significant correlations. It is possible that these channels contain no useful information for glitch identification, or that one has to include correlations involving multiple channels and/or other features to exract the useful information. In the former case, throwing out irrelevant channels will significantly decrease our problem's dimensionality and may improve the classifiers' efficiency. In the latter case, classifiers might be capable of using higher-order correlations to identify classes of glitches missed by OVL.

We prepare two sets of data to investigate these possibilities. In the first data set, we use only the OVL auxiliary channels and exclude information from all other channels. In the second data set, we further reduce the number of dimensions by using only S and Δt. We apply classifiers to both data sets, evaluate their performance, and compare it to the run over the full data set (all channels and all features). Figure 6.2 shows the ROC curves computed for these test runs.

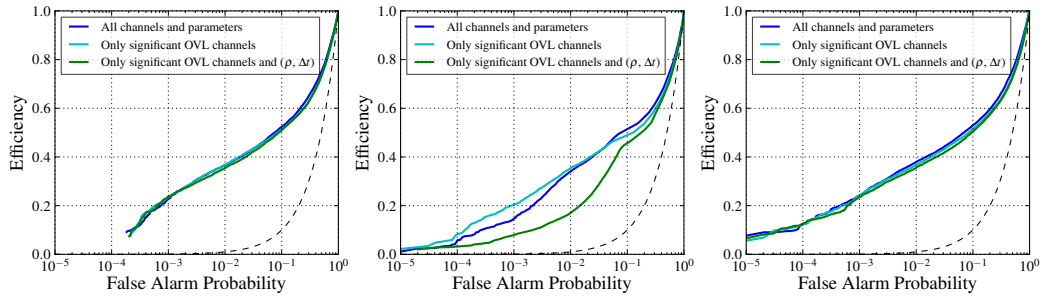

(a) S4 ANN (b) S4 SVM (c) S4 RFBDT

(d) S6 ANN (e) S6 SVM (f) S6 RFBDT

Figure 6.2: Reducing the number of channels. One way to reduce the dimensionality of our feature space is to reduce the number of auxiliary channels used to create the feature vector. We use a subset of auxiliary channels identified by OVL as strongly correlated with glitches in the gravitational-wave channel (light blue). We notice that for the most part, there is not much efficiency loss when restricting the feature space in this way. This also means that very little information is extracted from the other auxiliary channels. The classifiers can reject extraneous channels and features without significant loss or gain of efficiency. We also restrict the feature vector to only include the significance, S (but called ρ in the legends), and the time difference, Δt, for the OVL auxiliary channels (green). Again, there is not much efficiency loss, suggesting that these are the important features and that the classifiers can robustly reject unimportant features automatically. The black dashed line represents a classifier based on random choice.

In both S4 and S6 data, the three curves for RFBDT (Figure 6.2c and Figure 6.2f) lay on the top of each other, demonstrating that this classifier's performance is not affected by the data reduction. ANN shows slight improvement in its performance for the maximally reduced data set in the S6 data (Figure 6.2d), and no discernible change in the S4 data (Figure 6.2a). SVM exhibits the most variation of the three classifiers. While dropping the auxiliary channels not included in the OVL list has a very small effect on SVM's ROC curve, further data reduction leads to an efficiency loss (Figure 6.2b and Figure 6.2e). Viewed together, the plots in Figure 6.2 imply that, on one hand, non-OVL channels can be safely dropped from the analysis, but on the other hand, the presence of these uninformative channels does not reduce our classifiers' efficiency. This is reassuring. As previously mentioned, one would like to use these methods for automated real-time classification and detector diagnosis, in which case monitoring as many channels as possible allows us to identify new kinds of glitches and potential detector malfunctions. For example, an auxiliary channel that previously showed no sign of a problem may begin to witness glitches. If excluded from the analysis based on its previous irrelevance, the classifiers would not be able to identify glitches witnessed by this channel or warn of a problem.

Another way in which input data may influence a classifier's performance is by limiting the number of samples in the training set. Theoretically, the larger the training sets, the more accurate a classifier's prediction. However, larger training sets come with a much higher computational cost and longer training times. In our case, the size of the glitch training set is limited by the glitch rate in the gravitational-wave channel and the duration of the detector's run. We remind the reader that we use four weeks from the S4 run from the H1 detector and one week from the S6 run from the L1 detector to collect glitch samples. One would like to use shorter segments to better capture non-stationarity of the detector's behavior. However, having too few glitch samples would not provide a classifier with enough information. Ultimately, the size of the glitch training set will have to be tuned based on the detector's behavior. We have much more control over the size of the clean training set, which is based on completely random times when the detector was operating in the science mode. In our simulations, we start with 10^5 clean samples, but it might be possible to reduce this number without loss of efficiency, thereby speeding up classifier training.

We test how the classifiers' performance is affected by the size of the clean training set in a series of runs in which we gradually reduce the number of clean samples available. Runs with 100%, 75%, 50%, and 25% of the total number of clean samples available for training are supplemented by a run in which the number of clean training samples is equal to the number of glitch training samples (16% in S4 data and 2.5% in S6 data). In addition, we perform one run in which we reduce the number of glitch training samples by half, but keep 100% of the clean training samples. While not completely exhaustive, we believe these runs provide us with enough information to describe the classifiers' behavior. In all of these runs, we use all available samples for evaluation, employing the round-robin procedure. Figure 6.3 demonstrates changes in the ROC curves due to the variation of training sets.

RFBDT performance (Figure 6.3c and Figure 6.3f) is not affected by reduction of the clean training set

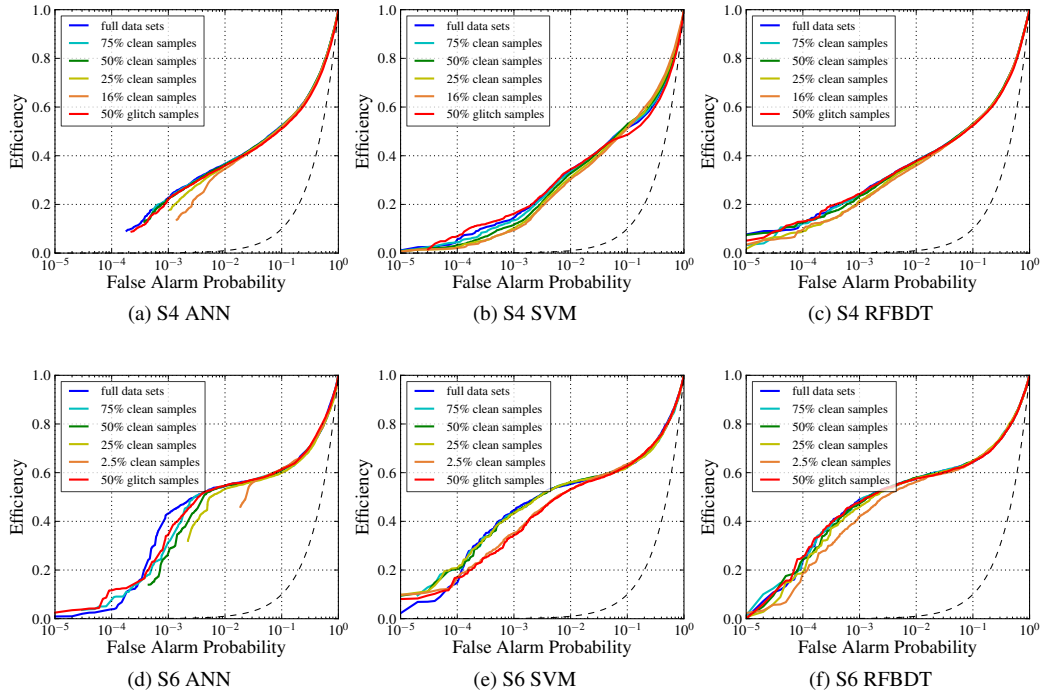

(a) S4 ANN (b) S4 SVM (c) S4 RFBDT

(d) S6 ANN (e) S6 SVM (f) S6 RFBDT

Figure 6.3: Varying the size of training data sets. In our sample data, the number of glitches is limited by the actual glitch rate in the LIGO detectors and the length of the analysis time we use. However, we can construct as many clean samples as necessary because we sample the auxiliary channels at random times. In general, classifiers' performance will increase with larger training data sets, but at additional computational cost. We investigate the effect of varying the size of training sets on the classifiers' performance, and observe only small changes even when we significantly reduce the number of clean samples. We also reduce the number of glitch samples, observing that the classifiers are more sensitive to the number of glitches provided for training. This is likely due to the smaller number of total glitch samples, and reducing the number of glitches may induce a severe undersampling of feature space. The black dashed line represents a classifier based on random choice.

in the explored range, with the only exception being the run over S6 data, where size of the clean training set is to 2.5% of the original. In this case, the ROC curve shows an efficiency loss on the order of 5% at a false alarm probability of $P_0 = 10^{-3}$. Also, cutting the glitch training set by half does not affect RFBDT efficiency in either S4 or S6 data.

SVM's performance follows very similar trends, shown in Figure 6.3b and Figure 6.3e, demonstrating robust performance against the reduction of the clean training set and suffering appreciable loss of efficiency only in the case of the smallest set of clean training samples. Unlike RFBDT, SVM seems to be more sensitive to variations in the size of glitch training set. The ROC curve for the 50% glitch set in S6 data drops 5%-10% in the false alarm probability region of $P_0 = 10^{-3}$ (Figure 6.3e). However, this does not happen in the S4 run (Figure 6.3e). This can be explained by the fact that S4 glitch data set has five times more samples than the S6 set. Even after cutting it in half, the S4 set provides better sampling than the full S6 set.

ANN is affected most severely by training set reduction (Figure 6.3a and Figure 6.3d). First, its overall performance visibly degrades with the size of the clean training set, especially in the S6 runs (Figure 6.3d).

However, we note that the ROC curve primarily drops near a false alarm probability of $P_0 = 10^{-3}$, while it remains the same near $P_0 = 10^{-2}$ (for all but the 2.5% set). The higher P_0 value is more important in practice because a probability of false alarm of 10^{-2} is still tolerable and, at the same time, the efficiency is significantly higher than at $P_0 = 10^{-3}$. This means that we are likely to operate a real-time monitor near $P_0 = 10^{-2}$ rather than near 10^{-3}. Reducing the training sample introduces an artifact on ANN's ROC curves, not seen on either RFBDT or SVM. Here, the false alarm probability's range decreases with the size of the clean training set. This is due to the fact that with the ANN configuration parameters used in this analysis, ANN's rank becomes more degenerate when fewer clean samples are available for training, meaning that multiple clean samples in the evaluation set are assigned exactly the same rank. This is in general undesirable, because a continuous, non-degenerate rank carries more information and can be more efficiently incorporated into gravitational-wave searches. The degeneracy issue of ANN and its possible solutions are treated in detail in Reference [111].

We would like to highlight the fact that in our test runs, we use data from two different detectors and during different science runs, and that we test three very different classifiers. The common trends we observe are not the result of peculiarities in a specific data set or an algorithm. It is reasonable to expect that they reflect generic properties of the detectors' auxiliary data as well as the MLA classifiers. Extrapolating this to future applications in advanced detectors, we find it reassuring that the classifiers, when suitably configured, are able to monitor large numbers of auxiliary channels while ignoring irrelevant channels and features. Furthermore, their performance is robust against variations in the training set size. In the next sections we compare different classifiers in their bulk performance as well as in sample-by-sample predictions using the full data sets.

6.2.3.1 Evaluating and comparing classifiers' performance

The most relevant measure of any glitch detection algorithm's performance is its detection efficiency, the fraction of identified glitches, P_1, at some probability of false alarm, P_0. The ROC curve is the key figure of merit and can be used to assess an algorithm's efficiency throughout the entire range of false alarm probabilities, and objectively compare it to other methods. The upper limit for acceptable values of probability of false alarm depends on application. In the problem of glitch detection in GW data, we set this value to $P_0 = 10^{-2}$, which corresponds to 1% of true GW transients falsely labeled as glitches. Another way to interpret this is that 1% of the clean science data are removed from searches for gravitational waves.

Our test runs, described in the previous section, demonstrate the robustness of the MLA classifiers against the presence of irrelevant features in the input data. We are interested in measuring a classifier's efficiency in the regime maximally resembling the real-life application in which no prior information about relevance of the auxiliary channels is given. For this purpose, we use the full S4 and S6 data sets, all channels and all parameters. Using exactly the same training/evaluation sets for all our classifiers allows us to assign four ranks (r_{ANN}, r_{SVM}, r_{RF}, r_{OVL}) to every sample and compute the probability of false alarm, $P_0(r_i)$ and

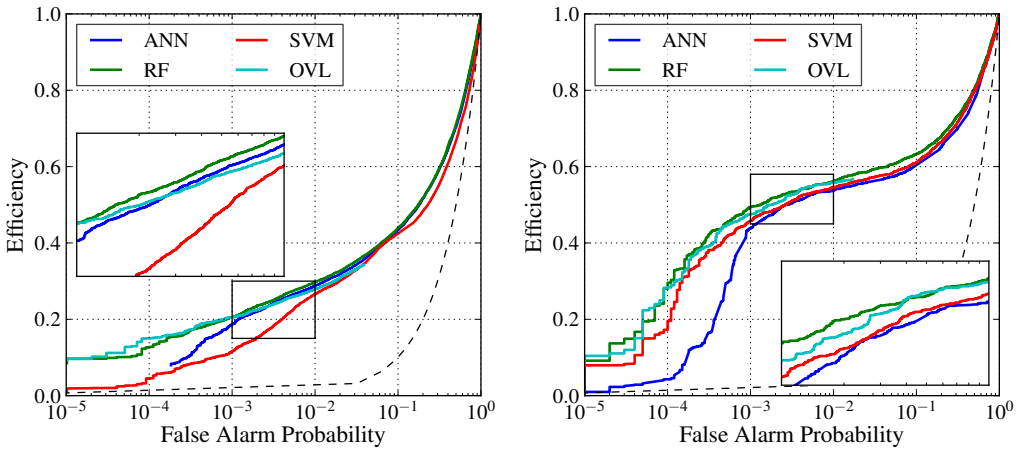

(a) S4 ROC curves

(b) S6 ROC curves

Figure 6.4: Comparing algorithmic performance. We directly compare the best performance for RFBDT (green), ANN (blue), SVM (red), and OVL (light blue) using the full data sets. We see that all the classifiers perform similarly, particularly in S6. There is a general trend of higher performance in S6 than in S4, which we attribute to differences in the types of glitches present in the two data sets. We should also note that all the MLA classifiers achieve performance similar to our benchmark, OVL, but RFBDT appears to perform marginally better for a large range of the False Alarm Probability. The dashed line corresponds to a classifier based on random choices.

efficiency, $P_1(r_i)$. While the ranks cannot be compared directly, these probabilities can. Any differences in classifiers' predictions, in this case, are from the details and limitations of the methods themselves, and are not from the training data.

Glitch samples separated in time by less than a second are likely to be caused by the same auxiliary disturbance. Even if they are not, GW transient candidates detected in a search are typically "clustered" with a time window ranging from a few hundred milliseconds to a few seconds, depending on the length of the targeted GW signal. Clustering implies that among all candidates within the time window, only the one with the highest statistical significance will be retained. In order to avoid double counting of possibly correlated glitches and to replicate conditions similar to a real-life GW search, we apply a clustering procedure to the glitch samples with a one-second time window. In this time window, we keep the sample with the highest significance, S, of the transient in GW channel. The ROC curves computed after clustering are shown in Figure 6.4 for ANN, SVM, RFBDT and OVL for both S4 and S6 data.

All our classifiers show comparable efficiencies in the most relevant range of the probability of false alarm for practical applications (10^{-3} – 10^{-2}). Of the three MLA classifiers, RFBDT achieves the best efficiency in this range, with ANN and SVM getting very close near $P_0 = 10^{-2}$. Relative to other classifiers, SVM performs worse in the case of S4 data, and ANN's efficiency drops fast at $P \leq 10^{-3}$. The most striking feature on these plots is how closely the RFBDT and the OVL curves follow each other in both S4 and S6 data (Figure 6.4a and Figure 6.4b, respectively). In absolute terms, the classifiers achieve significantly higher efficiency for S6 than for S4 data, 56% versus 30% at $P_0 = 10^{-2}$. We also note that the clustering procedure

has more effect on the ROC curves in S4 than in S6 data. In the former case, the efficiency drops by 5 - 10% (compare to the curves in Figures 6.3a to 6.3c), whereas in the latter it stays practically unchanged (compare to Figures 6.3d to 6.3f). The reason for this is not clear. In the context of detector evolution, the S6 data are much more relevant for advanced detectors. At the same time, we should caution that we use just one week of data from the S6 science run, and larger scale testing is required for evaluating the effect of the detector's non-stationarity.

The ROC curves characterize the bulk performance of the classifiers, but they do not provide information about what kind of glitches are identified. To gain further insight into the distribution of glitches before and after classification, we plot cumulative histograms of the significance, S, in the GW channel for glitches before any glitch removal, and those that remain after removing the glitches detected by each of the classifiers at $P_0 \leq 10^{-2}$. We also plot a cumulative histogram of all glitches before any glitch removal. These cumulative histograms are shown in Figure 6.5. They show the effect of each classifier on the distribution of glitches in the GW channel. In both the S4 and S6 data sets, the tail of the glitch distribution, containing samples with the highest significance, is reduced. At the same time, as is clear from the plots, many glitches in the mid range of significances are also removed, contributing to overall lowering of the background for transient GW searches. The fact that our classifiers remove low-significance glitches while some of the very high-significance glitches are left behind indicates that there is no strong correlation between amplitude of glitches in GW channel and their detectability. This in turn implies that we either do not provide all necessary information for identification of these high-significance glitches in the input feature vector or the classifiers somehow do not take advantage of this information. Given the close agreement between various classifiers that we observe in the ROC curves (Figure 6.4) and the histograms of glitch distributions (Figure 6.5), the former alternative seems to be more plausible. Alternatively, our choices of the thresholds and the coincidence windows that went into the construction of the feature vectors might not be optimal. Also, heretofore unincluded features characterizing the state of the detector, which may amplify transient disturbances in the auxiliary channels and induce glitches in the GW channel, might be crucial for identifying glitches missed in the current analysis. Investigation of these possibilities is left to future work.

Although the ROC curves (Figure 6.4) and the histograms (Figure 6.5) provide strong evidence that all classifiers detect the same glitches, they do not give a clear quantitive picture of the overlap between these methods. To see this more clearly, we define subsets of glitches based on which combination of classifiers detected them with a probability of false alarm less than 10^{-2}. We determine overlaps between the MLA classifiers by constructing a bit-word diagram (Figure 6.6). It clearly demonstrates a high degree of redundancy between the classifiers. The fraction of glitches detected by all three MLA classifiers is 91.1% for S6 data and 78.5% for S4 data. For comparison, we also construct a bit-word diagram for the clean samples, shown in the same figure, which are falsely identified as glitches with probability of false alarm less than 10^{-2}. The classifiers' predictions for clean samples are distributed almost uniformly. This suggests that our classifiers select clean samples nearly independently, or at least with a much lower level of correlation than

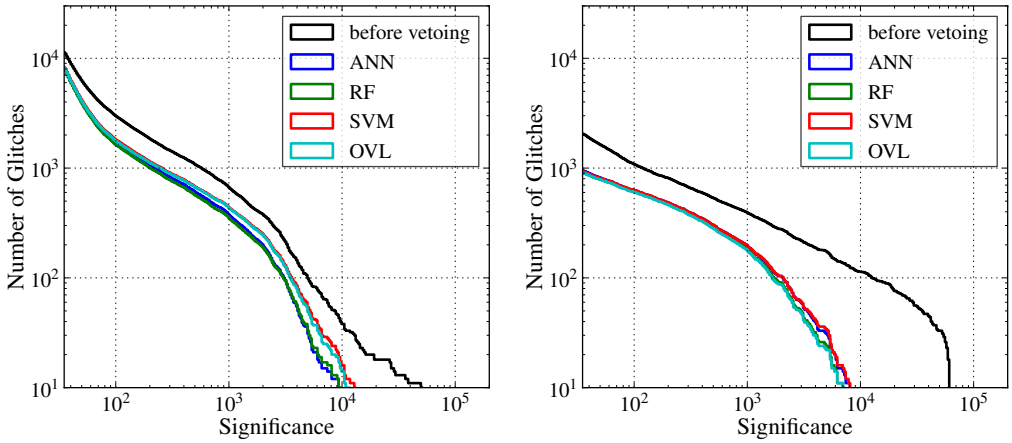

(a) S4 glitches

(b) S6 glitches

Figure 6.5: Comparing cumulative distributions of glitches before and after applying classifiers at 1 % FAP. Note that a couple of curves on the S6 data plot lie atop one another. This cumulative histogram shows the number of glitches that remain with a KleineWelle significance in the GW channel greater than or equal to the threshold given by the value on the x-axis. We see that all of our classifiers remove similar fractions of glitches at 1% FAP. This corresponds to their similar performances in Figure 6.4, with efficiencies near 30% and 55% for S4 and S6 data, respectively. We also see that the classifiers tend to truncate the high-significance tails of the non-Gaussian transient distributions, particularly in S6. What is more, we are also reducing the rate of the medium-significance triggers, which means there will be fewer instances of accidental coincidence of noise triggers between detectors.

for glitches.

Next, we compare the MLA classifiers to OVL. In order to reduce the number of possible pairings, we combine the MLA classifiers following the maximum-likelihood-ratio algorithm described in more detail in the Section 6.2.3.2. In short, this algorithm picks the most statistically significant prediction out of the three MLA classifiers for each time. We denote the combined classifier as $\mathrm{MLA}_{\mathrm{max}}$. As in the previous case, we construct the bit-word diagram for both glitch and clean samples detected with the probability of false alarm less than 10^{-2} (Figure 6.7). The redundancy is even stronger. The fraction of glitches detected by $\mathrm{MLA}_{\mathrm{max}}$and OVL is 94.9% for S6 data and 85.4% for S4 data. The full bit-word histograms show the same behavior and we omit them here.

6.2.3.2 Methods for combining classifiers

On a fundamental level, the MLA classifiers search for a one-parameter family of decision surfaces in the feature space, $x \in V_{\mathrm{d}}$, by optimizing a detection criterion. The parameter labeling the decision surfaces can be mapped into a continuous rank, $r_{\mathrm{MLA}}(x) \in [0, 1]$. This rank reflects the odds for a sample, x, to correspond to a glitch in the GW channel. As we discuss in the appendix to Reference [99], if the classifiers use consistent optimization criteria, they theoretically should arrive at the same optimal decision surfaces and make completely redundant predictions. In other words, their ranks would be functionally dependent. In

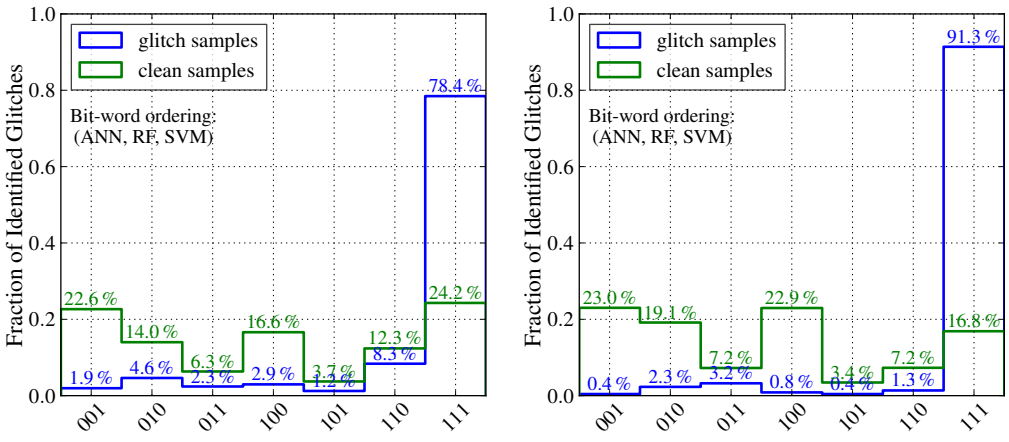

(a) S4 bit-word histogram for MVCs

(b) S6 bit-word histogram for MVCs

Figure 6.6: Redundancy between MLA classifiers. These histograms show the fractions of glitches identified by a given set of classifiers at 1% probability of false alarm (blue). The abscissa is labeled with bit-words, which are indicators of which classifier found that subset of glitches (e.g., 011 corresponds to glitches that were not found by ANN, but were found by RFBDT and SVM). The quoted percentages represent the fractions of glitches identified by any classifier at 1%, rather than the fractions of the total number of glitches in the data set. Note that all our classifiers show a remarkable amount of redundancy in that the vast majority of glitches are identified by all three MLA classifiers (bit-word $= 111$). Comparatively, the clean samples (green) have a much flatter distribution and seem to be spread somewhat evenly across most combinations of classifiers. This suggests that the classifiers are much more correlated on their selection of glitches than they are on their selection of clean samples.

practice, however, different classifiers often lead to different results, primarily due to the limitations in the number of samples in the training sets and/or computing resources. For instance, different classifiers may be more or less sensitive to different types of glitches. In this case, one should be able to detect a larger set of glitches by combining their output. Furthermore, the classifiers may be strongly correlated in the ranks they assign to glitch samples, but only weakly correlated when classifying clean samples. Again, by combining the output of different classifiers, we may be able to extract information about these correlations and improve the total efficiency of our analysis.

This last case appears to be applicable to our data set. From Section 6.2.3.1, we see that at a probability of false alarm of 1%, all classifiers remove nearly identical sets of glitches (to within 10% for the S6 data). However, the classifiers agree to a significantly lesser extent on the clean samples they remove (Figure 6.6). This suggests that the correlations between the classifiers' predictions are different for glitches and clean samples, and that fcombining the classifiers' output could possibly lead to an improved analysis.

The general problem of combining the results from multiple, partially redundant analysis methods has been addressed in the context of GW searches in [112]. Treating the output of the classifiers, namely their

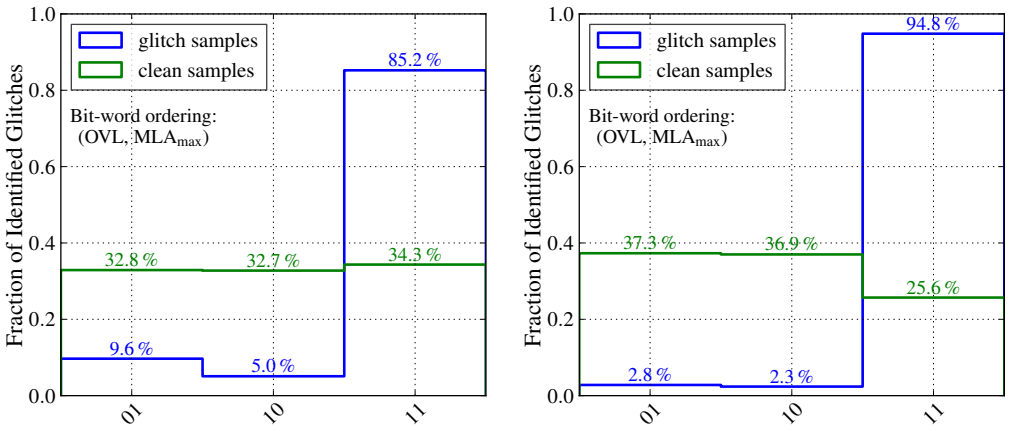

(a) S4 bit-word histogram for $\mathrm{MLA}_{\mathrm{max}}$and OVL

(b) S6 bit-word histogram for $\mathrm{MLA}_{\mathrm{max}}$and OVL

Figure 6.7: Redundancy between $\mathrm{MLA}_{\mathrm{max}}$and OVL. This figure is similar to Figure 6.6, except these histograms only compare the results of combining the MLA classifiers into a single unified classifier ($\mathrm{MLA}_{\mathrm{max}}$) and OVL. Even though OVL only considers pairwise correlations between auxiliary channels and the GW channel, we see that it predominantly identifies the same glitches as $\mathrm{MLA}_{\mathrm{max}}$. This suggests that the glitches identified by the MLA classifiers only display pairwise correlations between a single auxiliary channel and the gravtiational-wave channel, and adding more channels does not add much. We also see that these classifiers are highly correlated on their selection of glitches (blue), but much less correlated on their selection of clean samples (green).

ranks, as new data samples, one arrives at the optimal combined ranking given by the joint likelihood ratio:

$$\Lambda_{\mathrm{joint}}(\vec{r}) = \frac{p(\vec{r}\,|\,1)}{p(\vec{r}\,|\,0)}\,, \tag{6.6}$$

where $\vec{r} \equiv (r_{\mathrm{ANN}}, r_{\mathrm{SVM}}, r_{\mathrm{RF}})$ is the vector of the MLA ranks assigned to a sample, x, and $p(\vec{r}\,|\,1)$ and $p(\vec{r}\,|\,0)$ are the probability density functions for the rank vector in the case of glitch and clean samples, respectively. We should point out that we can modify this ranking by multiplying by the ratio of prior probabilities ($p(1)/p(0)$) to match the rankings for individual classifiers without affecting the ordering assigned to samples. Typically, these conditional probability distributions are not known, and computing the joint likelihood ratio from first principles is not possible. One has to develop a suitable approximation. We try several different approximations when combining algorithms.

Our first approximation, and perhaps the simplest, estimates the likelihood ratio for each classifier separately and assigns the maximum to the sample. This method should be valid in the two limits: extremely strong correlations and extremely weak correlations between the classifiers. It was first suggested and applied in the context of combining results of multiple GW searches in [112]. We estimate the individual likelihood ratios in two ways: 1) as the ratio of cumulative density functions (cdf) and 2) as the ratio of kernel density estimates for the probability density function (pdf). Though a proper estimate should involve the pdfs, the advantage of using cdfs is that we already calculate them when evaluating the efficiency and probability of false

alarm for each classifier to create the ROC curves. They should approximate the ratio of pdfs reasonably well in the tail of the distributions, when the probability of false alarm is low. This assumes that pdfs are either slowly varying or simple (e.g., power law or exponential) decaying functions of the rank. However, at large values of the probability of false alarm or in the case when the probability distributions exhibit complicated functional dependence on the rank, our approximation may break down and we will have to resort to the more fundamental ratio of the pdfs. Explicitly, we estimate the joint likelihood ratio using

$$L_1(\vec{r}) \equiv \max_{r_j} \left\{ \frac{\int_{r_j}^1 p(r'_j \mid 1)\, \mathrm{d}r'_j}{\int_{r_j}^1 p(r'_j \mid 0)\, \mathrm{d}r'_j} \right\} = \max_{r_j} \frac{P_1(r_j)}{P_0(r_j)}\,, \tag{6.7}$$

where j runs over our various classifiers. We refer to this method as $\mathrm{MLA}_{\max}$when introducing it in the context of Figure 6.7.

We also construct smooth one-dimensional pdfs for clean and glitch samples from their ranks using Gaussian kernel density estimation [113]. These estimates were built using a constant bandwidth equal to 0.05 in the rank space, which ranges from 0 to 1. Based on this, we define the approximate combined rankings:

$$L_2(\vec{r}) \equiv \max_{r_j} \left\{ \frac{p(r_j \mid 1)}{p(r_j \mid 0)} \right\}. \tag{6.8}$$

It is by no means true that we can always approximate the multi-dimensional likelihood ratio (Equation (6.6)) with the maximum over a set of one-dimensional likelihood ratios. If we can better model the multi-dimensional probability distributions, we should be able to extract more information. To this end, we also implement a slightly more complicated combining algorithm. We observe that the algorithms are highly correlated on which glitches they remove, and less correlated on the clean samples (see Figure 6.6). We therefore approximate $p(\vec{r} \mid 1) \approx \max_{r_j}\{p(r_j \mid 1)\}$ and $p(\vec{r} \mid 0) \approx \prod_j p(r_j \mid 0)$, which assumes that the algorithms are completely uncorrelated for the clean samples. Λ_{joint} is then approximated by

$$L_3(\vec{r}) \equiv \frac{\max_{r_j}\{p(r_j \mid 1)\}}{\prod_i p(r_i \mid 0)}\,. \tag{6.9}$$

Again, we compute the individual pdfs using Gaussian kernel density estimation.

More subtle, but still useful, correlations between the ranks assigned by different classifiers cannot be accounted for by these simple analytical approximations. Estimating the multi-dimensional probability distributions is a difficult task, and under-sampling quickly becomes the dominant source of error when expanding to higher than two dimensions. Rather than developing a complicated analytic model, we can use one of the MLA classifiers to compute the combined rank. We use RFBDT to attempt to combine the ranks from each classifier and construct an estimate of the full (three-dimensional) joint likelihood ratio.

We compare the methods for combining the classifiers by computing ROC curves, which are shown in Figure 6.8. We reproduce only the S6 curves because the S4 data shows the same trends.

All combined methods result in very similar ROC curves and, when compared to the OVL curve, they do

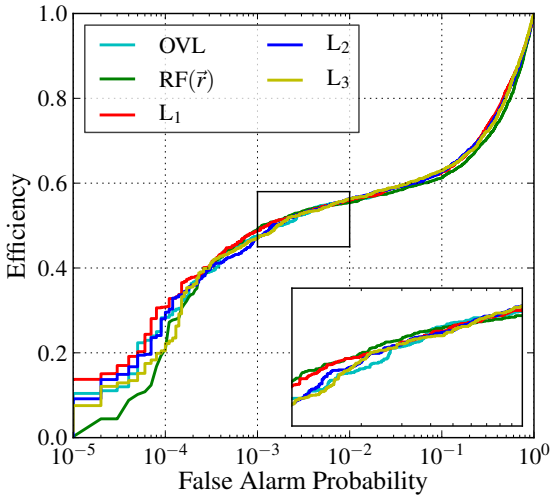

Figure 6.8: Comparison of different combining algorithms using S6 data. This figure compares the performance of our various schemes for combining the output of the three MLA classifiers. We note that all four algorithms, L_1 (Equation (6.7)), L_2 (Equation (6.8)), L_3 (Equation (6.9)), and using RFBDT to classify times based on the MLA output vector $\vec{r}$, agree to a remarkable degree. The fact that our simple analytic algorithms perform just as well as the RFBDT suggests that there are not many subtle correlations between the classifiers' output. The MLA combining algorithms do not perform much better than OVL. Comparing these curves with Figure 6.4 shows that the combined performance does not exceed the individual classifier's performances. This suggests that the individual MLA classifiers each extract almost all of the useful information from our feature vectors, and that they identify the same types of glitches. These conclusions are further supported by Figure 6.6.

not seem to improve the overall performance by more than a few percent. These combined results lead us to conclude that the individual classifiers have already reached nearly optimal performance for the given input data, and that their combination, while increasing their robustness, cannot improve the overall efficiency. Basically, all the useful information has been extracted already.

Although it is not immediately apparent, these combining schemes do add robustness to our identification of glitches. The combining algorithms are able to ignore underperforming classifiers and reject noisy input fairly well, and we see that they tend to select the best performance from the individual classifiers. By comparing Figure 6.8 with Figure 6.4, we see that the combining algorithms follow the best ROC curve from Figure 6.4, even when individual classifiers are not performing equitably. This is most evident at extremely low probabilities of false alarm. This robustness is important because it can protect a combined glitch identification algorithm from bugs in a single classifier. In this way, the combining algorithm essentially acts as an automatic cross-reference between individual MLA classifiers.

6.3 Conclusions and additional benefits of this approach

We have applied various machine learning algorithms (the artificial neural network, the support vector machine, and the random forest of bagged decision trees) to the problem of identifying transient noise ar-

tifacts (glitches) in GW data from LIGO detectors by only using information extracted from the auxiliary channels. Our main goal of establishing the feasibility of using MLAs for robust detection of instrumental and environmental glitches based on information from auxiliary detector channels, in a manner that is easily automated, objective, and un-biased, has been achieved. This is notable because the dimensionality of our feature space can be as high as 1250 (and will be even higher in Advanced LIGO), which makes classification of times in this feature space a challenging task.

Our tests show that the classifiers can efficiently handle extraneous features, such as redundant or missing data, without affecting their performance. Likewise, we find that the classifiers are generally robust against changes in the size of the training set. The most important result of our investigation is the confirmation that the MLA classifiers can be used to make use of information from a large number of auxiliary channels, many of which might be irrelevant or redundant, without a loss of efficiency. These classifiers can be used to develop a real-time monitoring and detector characterization tool to identify non-Gaussian and non-stationary features of the GW strain data. Moreover, replacing the traditional "Category" method of data quality (described in Section 4.2) with a data quality rank assigned by a machine learning algorithm provides the additional benefit of switching from a binary flag that essentially removes events from search results to a continuous ranking that describes the glitchiness of the GPS time of the event. This continuous ranking can be folded into a detection statistic for a search for a specific astrophysical signal, much in the way that the χ^2 statistic is folded into the signal-to-noise ratio in the high-mass search (see Section 7.3.6).

Quantitatively, we have established the robustness of the classifiers against changes in the input data and the presence of irrelevant, missing, or redundant parameters by evaluating the algorithms' performance in terms of ROC curves. We have also quantified the classifiers' impact on the overall distribution of glitches in the gravitational-wave channel and the redundancy of their predictions. We find that at a false alarm probability of 1%, all classifiers demonstrate comparable performance and achieve 30% and 56% efficiency at identifying single-detector glitches above our nominal threshold when tested on the S4 and S6 data, respectively.

In all tests we benchmark the MLA classifiers against the OVL classifier, which was optimized to detect pairwise correlations between transients in single auxiliary channels and transients in the gravitational-wave channel. Somewhat unexpectedly, the MLA classifiers demonstrate a very high level of redundancy with the OVL classifier, achieving similar efficiency as measured by the ROC curves. The thorough time-by-time comparison shows 85% and 95% redundancy in glitch detection between the MLA and the OVL classifiers for S4 and S6 data, respectively. Moreover, only a small subset of all channels, 47 (of 162) in S4 data and 35 (of 250) in S6 data, contributes to the total efficiency. This indicates that the input data are dominated by simple pairwise correlations, and that the higher-order correlations are either subdominant or altogether not present in feature vectors we provided. This interesting insight into the structure of the data could not have been gained without application of MLAs.

As a final test of our study, we explore several ways of combining the output of several classifiers (includ-

ing OVL) in order to increase the robustness of their predictions and possibly improve combined efficiency. Following general principles for combining multiple analysis methods, we suggest several approximations for the optimal combined ranking given by the joint likelihood ratio. We test our approximations and find that they perform similarly to and do not improve upon the efficiencies of individual classifiers.

Based on these results, we conclude that the three MLA classifiers used in this study are all able to achieve robust and competitive classification performance for our set of data. The RFBDT classifier was the most robust against the form (range, shape, scaling, number) of input data, while ANN and SVM benefit from reshaping certain input parameters along physical arguments. Since all classifiers achieve similar limiting performance and identify most of the same glitchy times, we conclude that they are all roughly equally effective as classifiers, given the information they were given.

Lastly, each of these classifiers outperforms the traditional data-quality flag veto structure as described in Section 4.2.1. Figure 6.9 illustrates this by plotting the efficiency versus dead-time for three categories of vetoes for the burst search (the most generic search for CBCs, as it is simply looking for sine-Gaussians). The dead-time is not exactly equal to P_0, since P_0 is the fraction of clean times vetoed, and dead-time is the fraction of all data vetoed by a given set of flags. However, they are closely related, and this plot illustrates an important point. Here, the efficiency for the Category vetoes is defined by the fraction of GW channel triggers found by the Omega pipeline with an SNR of 8 or greater. The glitches in the MLA analysis were found with a KW significance of 35, corresponding to an SNR of $\sim \sqrt{2 * 35} \sim 8.4$ Not only can automated procedures like those described in this chapter outperform traditional data-quality vetoing procedures, their operating dead-time is much more flexible.

6.3.1 Future work

Our tests have indicated that we have reached the limit of extracting information via a KleineWelle analysis of the auxiliary channels with our available tools (MLAs). Future improvement in classification efficiency is therefore likely to come from including additional sources of useful information, rather than refinements to the algorithms themselves. There are many other ways to extract information from the auxiliary channels. A simple change would be to use the Omega algorithm described in Section 4.1.2 instead of the KleineWelle algorithm to identify transients in the auxiliary channels. However, we do not have to stop there. Each auxiliary channel's data are a time series, and for certain channels it makes sense to use the value, derivative, and acceleration of the channel at a specific time; channels we expect to be useful in this way are the "slow" channels described in Section 4.2.1.4, such as those monitoring the angular positions of the mirrors.

An advantage of MLA classifiers is that they can incorporate various potentially diverse types of information and establish correlations between multiple parameters. Thus, we can conceivably use information from a transient-identifying algorithm like KleineWelle or Omega for the fast channels and more slowly-varying baseline information about the detector subsystems into the same classifier. The rate of glitches in the fast channels coupling to the GW channel can depend on the value and rate of change/acceleration of the slow

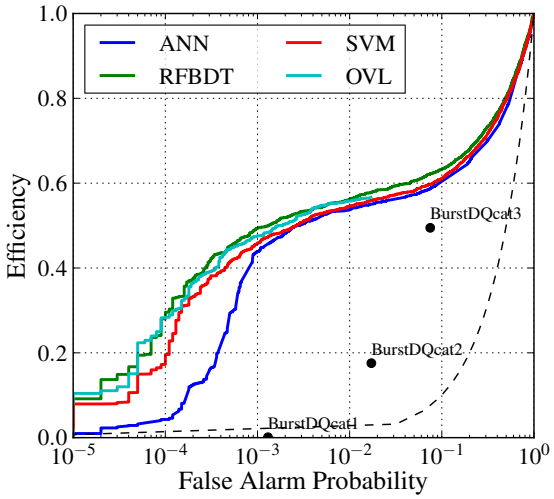

Figure 6.9: Comparing the best performance for RFBDT (green), ANN (blue), SVM (red), and OVL (light blue) using the full S6 data sets to the application of the traditional data-quality flag vetoes for the burst search. BurstDQcat1 shows the efficiency at vetoing glitches in the GW channel with an SNR above 8 with Category 1 Burst data-quality flags applied. BurstDQcat2 shows the efficiency at vetoing glitches in the GW channel with an SNR above 8 with Category 1 and 2 Burst data-quality flags applied. BurstDQcat3 shows the efficiency at vetoing glitches in the GW channel with an SNR above 8 with Category 1, 2, and 3 Burst data-quality flags applied. The Burst data-quality flags were defined for the gamma ray burst search, which looks for excess power using the Omega algorithm (see Section 4.1.2). An SNR of 8 was chosen, because the threshold for KW significance for the GW channel was 35, which roughly translates to an SNR of 8. The data-quality flags for the burst search are quite similar to the high-mass data-quality flags described in Section 4.2.1, except Burst Category 3 is like high-mass Category 4.

channels' time-series in a complicated way. Machine learning should be able to automatically identify such non-linear correlations, even if they are not known previously.

Future work will also focus on tuning and applying the MLA and OVL classifiers to searches for GWs from specific astrophysical sources. As previously mentioned, using a MLA to quantify the glitchiness of the data allows us to provide a continuous rank, $r_{\mathrm{MLA}} \in [0, 1]$, rather than a binary flag. The OVL classifier's output can be also converted into a rank which, although by construction is discrete, is not a binary flag. Future work will focus on an optimal way to fold this rank directly into searches for gravitational waves as a parameter characterizing a candidate event along with the rest of the data from the gravitational-wave channel, as opposed to a standard approach of vetoing entire segments of flagged data based on a hard threshold on data quality.

Chapter 7

Data analysis methods in the search for black hole binary systems

The search described in this thesis is an all-sky, all-time search for high-mass coalescing binaries in multi-detector data. Here, all-time means that we do not assume *a priori* when a GW signal might be arriving at the detectors; we are only restricted by the calendar time of the data we are searching in. All-sky means that we do not presume from what area of the local universe a GW might be originating. The data looked at in this search, as described in Reference [17], are from LIGO's sixth science run and Virgo's second and third science run (S6-VSR2/3), which were during the calendar years of 2009-2010.

There have been many all-sky, all-time searches for both high-mass and low-mass coalescing binary systems. These searches have all relied on variation of the two-stage (sometimes called *hierarchical* in the literature) coincidence-based pipeline described in Section 7.3, the heart of which is a matched-filter for waveform templates. Starting with LIGO's second science run (S2), a single-stage version of the pipeline was used to search for binary black hole systems with component masses between 3 and 20 $M_{\odot}$ [114], and also for neutron star binary systems with component masses between 1 and 3 $M_{\odot}$ [115]. In S2, there was much less data to analyze and the χ^2 signal-consistency test was not used, so the second stage was not necessary. In S3, a search was conducted to specifically look for spinning binary black hole systems, using the Buonanno-Chen-Vallisneri method for waveform construction; more asymmetric sources ($1 < m_1/M_{\odot} < 3$ and $12 < m_2/M_{\odot} < 20$) were considered, as the precession effects of spinning systems are more apparent here [116]. The non-spinning inspiral-only searches in S3 and S4 data were presented in the same paper (Reference [117]), with component masses as small as .35 $M_{\odot}$ (primordial black holes) and a maximum total mass of 40 $M_{\odot}$ in S3 and 80 $M_{\odot}$ in S4. Notably, the results in Reference [117] were the first published with the effective SNR as the ranking statistic and the use of a two-stage pipeline like the one described in this chapter, the heart of which is described in Reference [90].

By S5, the analyses and publications started being split into low-mass and high-mass searches, because we finally had full inspiral-merger-ringdown waveforms for the high-mass systems. Prior to the inclusion of Virgo, two (for historical reasons) low-mass searches were published, each for systems with total mass

between 2 and 35 $M_{\odot}$. Reference [118] covered the first year of operation during S5, which included 186 days of science data. Reference [56] covered the analysis of months 13-18 of operation, but the results included the first year as a prior, so the presented upper limits on the rate of CBCs were cumulative. A third paper presented the first combined analysis of joint LIGO-Virgo data in an all-sky search for CBCs. The analyzed data were the last 6 months of LIGO's S5 and the 4 months of Virgo's science run 1 (VSR1) [54], and the results from the first two S5 papers were used as a prior. It should be noted that there were four detectors to consider (H1, H2, L1, V1), creating 11 possible detector combinations with two or more detectors and presenting a new challenge for the collaboration. As a result, the inverse false alarm rate ranking system (see Section 7.6) was developed [55]. A similar analysis was carried out for S6 and VSR2 and VSR3, except H2 was not analyzed and H1, L1, and V1 had improved sensitivity [4]. The mass space for the S6-VSR2/3 low-mass search was restricted to less than 25 $M_{\odot}$ so that there would be no overlap with the high-mass search, as the overlap could necessitate a trials factor [58].

There was only a single high-mass search published for S5, and it included only LIGO data [23] — Virgo's noise profile during S5 was not very sensitive to the low frequencies that contain the most information about the coalescence of high-mass systems [119]. This search analyzed H1, H2, and L1 data for systems with total mass between 25 and 100 $M_{\odot}$, and was the first to use full inspiral-merger-ringdown waveforms. A joint LIGO-Virgo search was performed for the S6-VSR2/3 (H1, L1, V1) data, again targeting systems with total mass between 25 and 100 $M_{\odot}$ [17]. The S6-VSR2/3 data were the last collected before the detectors were turned off to prepare for Advanced LIGO and Virgo. The specifics for the S6-VSR2/3 high-mass search are described in detail in the following sections.

It should be noted that all the searches just referenced are coincidence-based — the data from each detector are analyzed separately and candidate GW events are identified when triggers from two or more different detectors are coincident in time and matched to similar waveform templates. Theoretically, there is a superior method we can use to perform an all-sky, all-time search for coalescing binaries in multi-detector data: the coherent search. Coherent searches line up the data in the various detectors with appropriate time delay for different source locations on the sky, and find coherent triggers when the amplitude and phases line up [120]. At the time of analysis, we believed that coherent searches were overly computationally expensive and also unnecessary, since we could perform the coherent analysis on only the top events produced by the two-stage low-threshold coincident search described below. However, research in this area is ongoing.

7.1 The inputs to the search

The inputs to the search are the calibrated data from each detector from the times when it is in Science Mode; these are known as *science segments* [63]. For the search outlined in this thesis, the total operating time for S6/VSR2-VSR3 data were split into 9 *analysis periods*, each between $\sim$ 4.4 and $\sim$ 11.2 weeks long. The divisions into these periods were sometimes based on an extended downtime due to an upgrade/repair of

the detector hardware or software, but were sometimes arbitrarily made to create manageably-sized analysis periods and to crudely capture the slowly time-varying detector performance between commissioning breaks. Each analysis period is composed of the science segments for each detector. The beginning of each science segment is determined by the operator and Science Monitor, declaring, after lock acquisition and a moment for the violin suspension modes to damp down, that the detector's data are adequate. The end of the science segment is determined by the detector going out-of-lock. The quality of the data in each analysis period is variable — this is where the veto segments come into play. We define Category 1 vetoes for data which are egregiously bad even in Science Mode, and only analyze data that pass the Category 1 vetoes. The Category 2, 3, and 4 vetoes are applied at the end of the analysis pipeline, effectively removing triggers from the already-analyzed Category 1 data. See Section 4.2.1 for a more in-depth discussion of the data-quality flags and vetoes. The amount of data in each analysis period at each category level is in Table 7.1; and total coincident (observation) time is given in Table 7.2.

7.2 The signals we are looking for

This chapter focuses on describing the search for the gravitational waveforms from the coalescence of a black hole and a neutron star or two black holes, whose total mass is between 25 and 100 $M_{\odot}$. The theoretical shape of these waveforms can be calculated using various methods. The two methods used in this search are described in Section 2.2.1.1 (EOBNR) and Section 2.2.1.2 (IMRPhenom). Ignoring spin, a waveform is described by 7 extrinsic parameters and 2 intrinsic parameters. The extrinsic parameters are distance (D), sky location (described by two angles α, δ), polarization angle (ι), and inclination angle (ψ), and time and phase at coalescence. The time and phase at coalescence are maximized over during the analysis, while the other parameters are buried in the SNR.

In non-spinning systems, there are only two intrinsic parameters; these describe the component masses of the objects in the binary. Different combinations of the component masses m_1 and m_2 could be used, but we tend to use the chirp mass,

$$\mathcal{M} \equiv (m_1 + m_2)\eta^{3/5}, \tag{7.1}$$

and the symmetric mass ratio,

$$\eta \equiv \frac{m_1 m_2}{(m_1 + m_2)^2}. \tag{7.2}$$

η and $\mathcal{M}$ are the quantities that are naturally found in the analytical formulae for the waveforms in the post-Newtonian expansion. We are much better at determining the chirp mass than the symmetric mass ratio [121].

Our spinning IMRPhenom waveforms currently incorporate only aligned spin systems. The total spin of the system is generally condensed into a single number, as in Equation (2.22), but it represents the 6 total spin parameters of a binary system ($\overrightarrow{S_1}$ and $\overrightarrow{S_2}$: the spin vectors of each of the compact objects).

We target signals using waveform templates that do not incorporate the effects of spin because we were

Table 7.1: The *analysis periods* for S6-VSR2/3, the data from which were taken by the LIGO and Virgo detectors from 7 July 2009 to 20 October 2010. The first three entries are from Virgo's second science run (VSR2) and the last two entries are from Virgo's third science run (VSR3).

GPS time	Detectors	Science Data	Category 1	Category 2	Category 3	Category 4
931035296-935798487	H1, L1, V1					
	H1	27.51 d	26.48 d	25.07 d	24.95 d	21.65 d
	L1	25.60 d	25.36 d	23.76 d	23.68 d	21.53 d
	V1	49.71 d	48.75 d	47.09 d	46.92 d	45.27 d
937800015-944587815	H1, L1, V1					
	H1	39.52 d	39.18 d	38.61 d	38.48 d	37.36 d
	L1	21.33 d	20.63 d	19.81 d	19.74 d	18.47 d
	V1	58.93 d	58.87d	54.90 d	54.87 d	51.45 d
944587815-947260815	H1, L1, V1					
	H1	20.10 d	20.05 d	19.75 d	19.68d	16.55 d
	L1	20.54 d	2048 d	20.15 d	20.08 d	19.27 d
	V1	22.82 d	22.77 d	18.26 d	18.25 d	16.44 d
949449543-953078487	H1, L1					
	H1	24.98 d	24.93 d	24.88 d	24.78 d	23.99 d
	L1	25.69 d	25.64 d	25.57 d	25.47 d	24.01 d
953078343-957312087	H1, L1					
	H1	27.47 d	27.13 d	26.71 d	26.63 d	23.10 d
	L1	31.31 d	31.28 d	31.13 d	31.01 d	28.52 d
957311943-961545687	H1,L1					
	H1	27.96 d	27.92 d	27.73 d	27.61 d	25.97 d
	L1	22.26 d	22.19 d	21.95 d	21.86 d	20.15 d
961545543-965174487	H1,L1					
	H1	27.48 d	27.21 d	26.77 d	26.67 d	22.61 d
	L1	23.80 d	23.55 d	23.20 d	23.12 d	20.49 d
956174343-968544087	H1,L1,V1					
	H1	23.78 d	23.76 d	23.59 d	23.41 d	20.59 d
	L1	29.40 d	29.37 d	29.16 d	28.95 d	26.13 d
	V1	21.48 d	20.36 d	18.67d	18.64 d	17.13 d
968543943-971622087	H1,L1,V1					
	H1	23.47 d	22.32 d	21.03 d	20.85 d	18.53 d
	L1	22.01 d	21.67 d	21.21 d	21.03 d	16.38 d
	V1	28.92 d	28.84 d	28.44 d	28.40 d	26.91 d

Table 7.2: The total amount of coincident time (when two or more detectors were taking data) for S6-VSR2/3, the data from which were taken by the LIGO and Virgo detectors from 7 July 2009 to 20 October 2010. The first three entries are from Virgo's second science run (VSR2) and the last two entries are from Virgo's third science run (VSR3). Each detector combination is known as an *observation time*, and a single observation time from an analysis period is known as an *analysis time*. Note a couple cases of the analysis time going up from Category 3 to Category 4; this is due to H1L1V1 time being turned into double time after the application of vetoes removed a significant amount of Category 4 time for one of the detectors.

GPS time	Coincident detectors	Category 2	Category 3	Category 4
931035296-935798487	H1, L1	1.29 d	1.29 d	1.25 d
	H1, V1	11.96 d	11.91 d	10.77 d
	L1, V1	10.42 d	10.37 d	10.01 d
	H1, L1, V1	9.05 d	9.02 d	7.07 d
937800015-944587815	H1, L1	2.37 d	2.36 d	2.61 d
	H1, V1	19.52 d	19.46 d	17.86 d
	L1, V1	5.49 d	5.48 d	5.04 d
	H1, L1, V1	5.61 d	5.59 d	4.80 d
944587815-947260815	H1, L1	4.56 d	4.54 d	4.51 d
	H1, V1	3.43 d	3.42 d	2.69 d
	L1, V1	3.81 d	3.80 d	4.38 d
	H1, L1, V1	7.96 d	7.94	5.79 d
949449543-953078487	H1, L1	15.34 d	15.27 d	13.94 d
953078343-957312087	H1, L1	17.46 d	17.39 d	13.93 d
957311943-961545687	H1, L1	13.09 d	13.03 d	11.50 d
961545543-965174487	H1,L1	15.58 d	15.52 d	12.21 d
965174343-968544087	H1,L1	6.26 d	6.21 d	5.65 d
	H1, V1	2.28 d	2.27 d	2.53 d
	L1, V1	4.21 d	4.18 d	4.55 d
	H1, L1, V1	11.49 d	11.40 d	8.57 d
968543943-971622087	H1,L1	3.29 d	3.26 d	2.79 d
	H1, V1	5.31 d	5.25 d	6.39 d
	L1, V1	4.26 d	4.22 d	3.84 d
	H1, L1, V1	11.82 d	11.74 d	8.00 d
	Total	327.44 d	194.92 d	170.68 d

not prepared to build a template bank that covers spin space. A template bank that includes spin will have to span a new dimension — increasing the number of templates needed and the computational time for each run of the matched-filter. We still believe that at some level, these templates capture astrophysical signals from spinning sources, and we will quantify our sensitivity for spinning signals later in Section 7.8.1. Moreover, including non-aligned (precessing) spins adds another layer of complexity — the distinction between extrinsic and intrinsic parameters becomes blurred. As the spinning system evolves in time, the orbital plane precesses due to spin-orbit coupling, so the polarization and inclination angles are also changing with time and are dependent on the spins of the system.

The following section describes how we search for the astrophysical signals that we expect to look like these waveforms.

7.3 The two-stage search pipeline for an all-sky all-time search for compact binary coalescences — *ihope*

The pipeline is given calibrated data and the configuration details for a given run, and returns a list of *candidate gravitational wave events*. Figure 7.1 outlines the main steps in the pipeline. Although Figure 7.1 illustrates a pipeline for a three-detector network comprised of H1, H2, and L1, *ihope* is designed to work for an arbitrary set of two or more detectors. For the S6-VSR2/3 high-mass search, there were three detectors considered — H1, L1, and V1. The *ihope* pipeline considers each detector's data separately to begin with. For each *analysis period* for each detector, the data comes to us in a series of *science segments*, and the times flagged by Category 1 are removed. As each detector has a different duty cycle, there are different combinations of detectors operating at different times. For S6-VSR2/3, there are unique H1L1, H1V1, L1V1, and H1L1V1 operating times. These are referred to as *observation times*. We will refer to the observation time from a particular analysis period as an *analysis time*.

The science segments for each analysis time are then prepared for the matched-filter analysis. See Figure 7.2 — each science segment is split into 2048-s *analysis chunks*, with the final chunk overlapping the prior by the amount necessary, but we do not consider triggers from the overlap region in the last analysis chunk. A consequence of this method is that science segments shorter than 2048 s are not analyzed. Each 2048 s is assumed to have a relatively stationary noise profile. The power spectral density of each detector, re-calculated every 2048 s, is used to whiten the data so that the matched-filter is closer to optimal and also to recreate a new template bank for each analysis chunk.

As seen in Figure 7.2, the 2048 s are split up into overlapping 256-s *analysis segments* in order to better estimate the power spectral density. The noise in various frequency bins is calculated for each analysis segment, and the median value for each bin is used. This prevents loud glitches from corrupting the power spectral density, as will be explained in the following section.

The matched-filtering is then performed, during which each template is slid against all the data, which has been split into the 256-s analysis segments (analysis segments are not to be confused with science segments defined above). Each time the SNR of the matched-filter goes above threshold, the GPS time is stored. These single-detector triggers are then clustered. The lists of clustered single-detector triggers from different detectors are then compared, in order to find triggers that are coincident in time and mass between detectors. New, reduced template banks are then created. These only contain the templates that were matched in the triggers that were found in coincidence. The matched-filter is then run again using these new template banks. For this second stage of the matched-filter, a χ^2 time-series is calculated in addition to the SNR time-series. Only triggers that are above the SNR threshold and below the χ^2 threshold are stored, clustered over, and looked for in coincidence between detectors. Each step is described in further detail below.

Figure 7.1: An outline of the two-stage matched-filter pipeline *ihope* for an all-sky all-time search for compact binary coalescences. Although the diagram lists the analysis path for an H1-H2-L1 network, the pipeline works for an arbitrary set of two or more detectors.

7.3.1 Data preparation

The first step in the pipeline is to prepare the calibrated Science Data from each interferometer; we typically prepare about 5 weeks of data at a time. The science segments are modified by the application of Category 1 vetoes, since we do not trust any data that have been flagged as Category 1. The science segments from each detector are then cross-referenced with each other — if a detector's science segment does not overlap with that of any other detectors, we do not analyze it, since we require all final candidate gravitational wave events to be found in coincidence.

The heart of the pipeline is a matched-filter, which is the optimal method for searching for a known signal form in Gaussian noise. Therefore, we try to make our data as Gaussian as possible at the start. This begins with the application of the Category 1 vetoes (see Section 4.2.1), which remove data when the detector was not in the design configuration required for Science Data. The surviving data are then downsampled from 16384 Hz to 2024 Hz (we can do this because, in contrast to low-mass search, none of the high-mass waveform templates extend beyond the Nyquist frequency of 1024 Hz). These data are then split into many smaller segments, each of which overlaps with its adjacent segments by half (see Figure 7.2). For the high-mass search, the length of these segments is 256 s, which translates to 52488 samples per segment. The entire 256-s segment is Fourier-transformed, but only the central 128 s in each analysis segment are searched for GWs.

The 256-s segments are Fourier-transformed because the matched-filter is applied in the frequency domain. Because the data are real to begin with, only a real-to-half complex forward fast Fourier transform is needed, which saves computation time. Also for each segment, the average-power spectral density is calculated. The one-sided power spectral density for a single segment is defined by

$$S(f) =< \tilde{n}(f)\tilde{n}^*(f) >= \frac{1}{2}S_n(|f|)\delta(f - f'). \tag{7.3}$$

For the high-mass search, we use a median average instead of the mean, as the mean can be overly sensitive to a large glitch or GW in the segment. The data times the template ($\tilde{s}(f)\tilde{h}^*(f)$) is then divided by this average-power spectral density during the matched-filter calculation, effectively whitening the data and the template. The median estimator of the average-power spectrum can be expressed as

$$\kappa^2 S[k] = \alpha^{-1}\text{median}\{\kappa^2 P_0[k], \kappa^2 P_1[k], ..., \kappa^2 P_{N_s-1}[k]\}, \tag{7.4}$$

where k is an index describing different frequency bins and the P subscript indicates each 256-s segment within the 2048-s chunk. κ is a scaling factor used to avoid floating-point errors. α is a scaling factor used to move the median to the mean in the case of Gaussian noise. The $P_n[k]$ are normalized periodograms which are the modulus-squared of the discrete Fourier transform of windowed data [90].

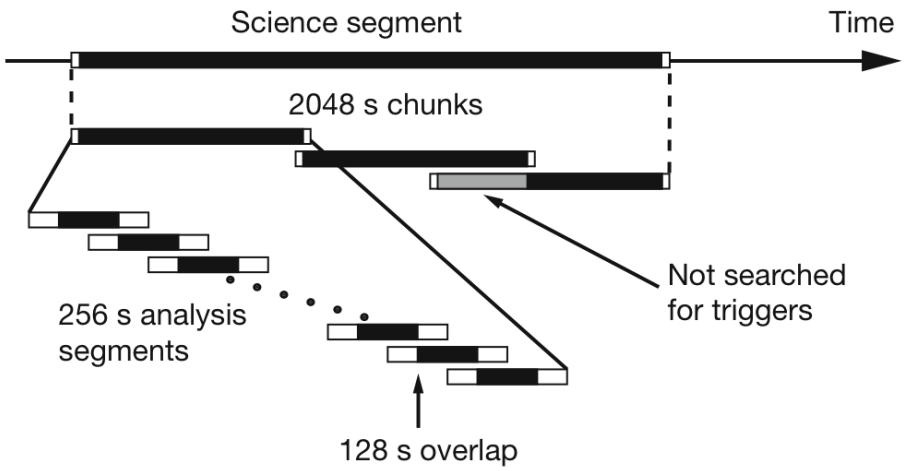

Figure 7.2: A graphic explaining the division of a science segment into 2048-s chunks used for template bank creation, and the 256-s segments analyzed.

7.3.2 Template bank generation

Because the LIGO and Virgo detectors are broadband, their sensitivity varies over both frequency and time. To capture the time-variability of a single detector, we calculate the power spectral density for each 2048-s chunk and create a new template bank for this chunk. The overlap between different templates depends on the power spectral density in the same way that an inner product in curved space-time depends on the metric.

The waveform model used for each template is the EOBNR model, described in Section 2.2.1.1. It should be noted that at the time of the analysis, a second version of the EOBNR waveforms existed, but the first was used for the waveforms in the template bank for historical reasons. This does not lead to a significant inefficiency in our search, since the mismatch between version 1 and version 2 is less than the mismatch between adjacent templates in the template bank [17].

Each template bank is created to cover the high-mass space in such a way that the inspiral portion of adjacent templates overlap each other by at least 97%. The templates are laid out in τ_0-τ_3 space, where $\tau_0(\mathcal{M})$ and $\tau_3(\mathcal{M},\eta)$ are chirp times for the 0^{th} and 3^{rd} order post-Newtonian expansions of the analytical inspiral waveform. They can be written as

$$\tau_0 \equiv \frac{5}{256(\pi f_0)^{8/3}}\mathcal{M}^{-5/3}, \tag{7.5}$$

$$\tau_3 \equiv \frac{5}{192\eta^{2/5}(\pi f_0)^2}\left(\frac{743}{336}+\frac{11}{4}\eta\right)\mathcal{M}^{-1}. \tag{7.6}$$

The $\tau_0 - \tau_3$ space is chosen because the distance between templates in this space is relatively uniform, making it easier to use a hexagonal placement algorithm [122]. Compare the template bank for a 2048-s

chunk of data in $\tau_0 - \tau_3$ space in Figure 7.3 to the one in $\mathcal{M}_{chirp} - \eta$ space in Figure 7.4 and the one in component-mass space in Figure 7.5. However, uniform template placement in this space is appropriate only for post-Newtonian inspiral templates; it is, at best, a crude approximation for our inspiral-merger-ringdown templates. Future work aims to improve upon this template placement algorithm [123].

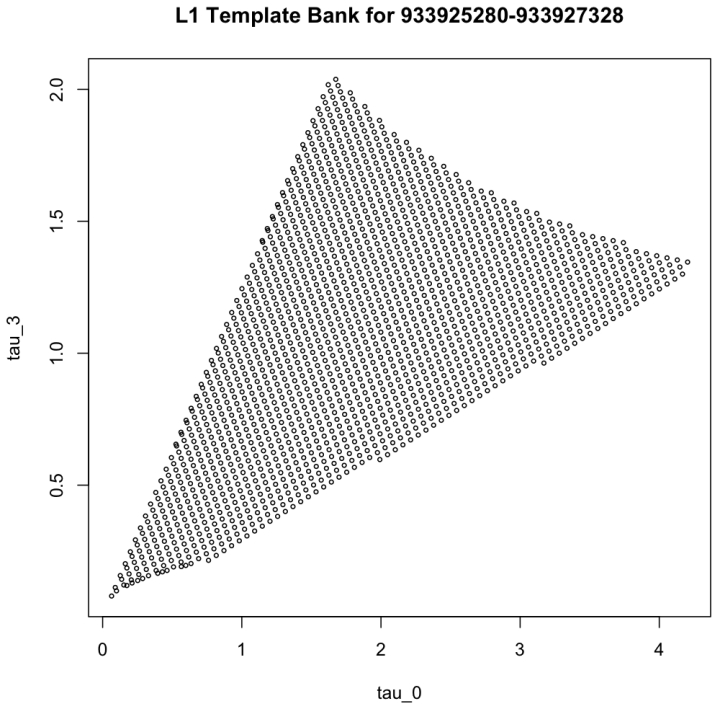

Figure 7.3: The template bank for a 2048-s chunk of L1 data, as represented in $\tau_0 - \tau_3$ space.

In order to keep the required overlap between adjacent templates in a detector with non-stationary noise, a new template bank is created for each 2048 seconds of each detector's data. However, it is important to note that as the total mass of the system increases, the merger and ringdown become more significant, so the overall match between adjacent templates can be lower than 97%, as only the inspiral portion was used to calculate the match. This translates to an inefficiency at finding injected signals.

Each waveform template is normalized to represent a system with an effective distance D_{eff} = 1 Mpc. The effective distance

$$D_{\text{eff}} = D \left[F_+^2 \left(\frac{1 + \cos^2 \iota}{2} \right)^2 + F_\times^2 \cos^2 \iota \right]^{-1/2} \tag{7.7}$$

folds in the inclination angle ι and sky location and polarization (contained in the antenna pattern factors F_+ and $F_\times$ — see Equation (3.3) and Equation (3.4)) into the distance, making the effective distance equal to the distance to the binary if it were face-on and directly above the given detector. Still, not every binary system

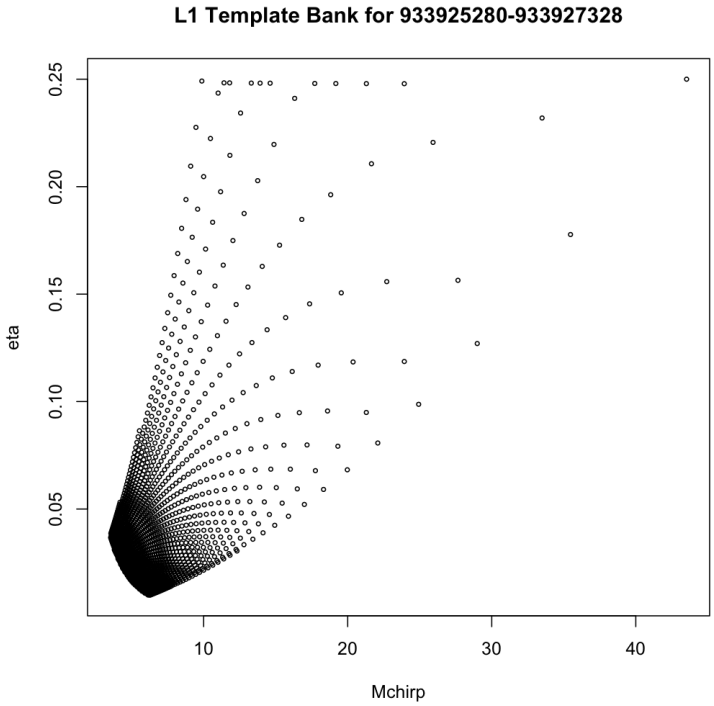

Figure 7.4: The template bank for a 2048-s chunk of L1 data, as represented in $\mathcal{M}_{chirp} - \eta$ space.

at 1 Mpc will produce equally loud GWs. Therefore we compute a normalization constant for each template:

$$\sigma_m^2 = 4 \int_0^\infty \frac{|\tilde{h}_m(f)|^2}{S(f)} df, \tag{7.8}$$

where m is the index over templates and $S(f)$ is the power spectral density for the 2048 s of data, as defined in Equation (7.3).

7.3.3 The matched-filter

The matched-filter part of the algorithm compares the data $s(t)$ with each template $h_m(t)$ and is done in the frequency domain. Though the calculation is actually implemented in a discretized manner [90], I write the integral formula here for ease of understanding. The matched-filter produces a complex time-series given by

$$z_m(t) = 4 \int_0^\infty \frac{\tilde{s}(f)[\tilde{h}_m^*(f)]}{S(f)} e^{2\pi i f t} df. \tag{7.9}$$

We can turn this into a signal-to-noise ratio (SNR) by dividing by the normalization constant in Equation (7.8),

$$\rho_m(t) = \frac{|z_m(t)|}{\sigma_m}. \tag{7.10}$$

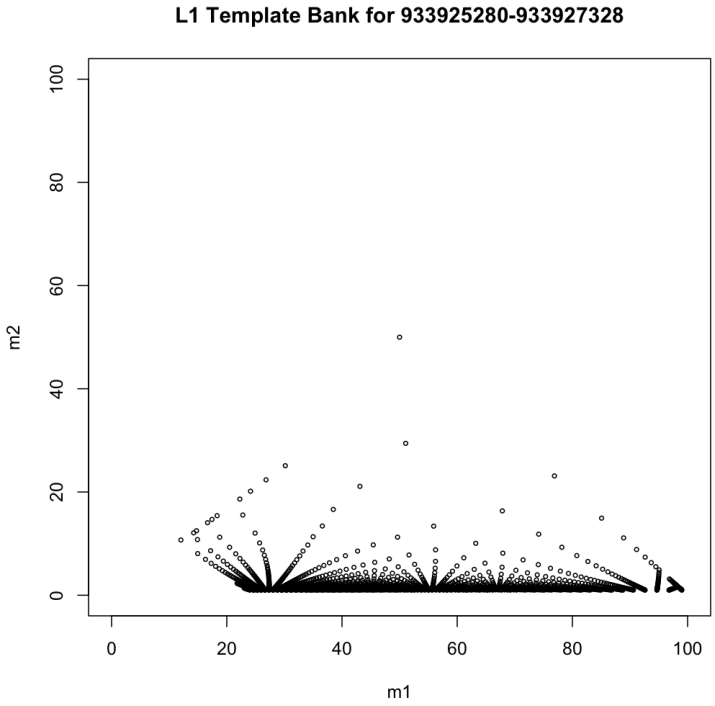

Figure 7.5: The template bank for a 2048-s chunk of L1 data, as represented in component-mass space. Notice the higher density of templates in regions of larger-mass ratios and the extremely sparse template density near the $m_1 = m_2 = 50\ M_\odot$ corner. The lower left corner has some templates that fall below the $m_1 + m_2 = 25\ M_\odot$ line. These templates can catch systems within the high-mass search space, but with component (anti-)aligned spins such that the combined spin parameter is positive (see Equation (2.22)). As explained in Section 2.2.1.2 and shown in Figure 2.13 and Figure 2.15, a system with a positive combined spin parameter will have a longer waveform than the equivalent system with $\chi = 0$ — these waveforms will tend to match templates with lower masses since lowering the total mass of the system (keeping the mass ratio constant) also produces longer waveforms.

By taking the absolute value of z, we effectively maximize over the coalescence phase. The expectation value of ρ^2 is $\left\langle \rho_m^2 \right\rangle = 2$ because the sine and cosine parts of the complex time-series each has an expectation value of 1.

The discretized version of Equation (7.9) is

$$z_{n,m}[j] = 4\Delta f \Sigma_{k=1}^{\frac{N-1}{2}} \frac{\kappa \tilde{s}_n[k] \kappa \tilde{h}_m^*[k]}{\kappa^2 S[k]} e^{2\pi i j k/N}, \tag{7.11}$$

where n labels the 256-s segment and m labels the template. $\Delta f = (N\Delta t)^{-1}$, where $N = 2048/256$ is the number of analysis segments in a 2048-s chunk of data and Δt is the sample rate, which is 1/2048 s/sample. j is the index that labels time steps, and k is the index that labels frequency bins. Here again, κ is a number on the order of 10^{23}, used to minimize the effect of round-off error.

There is a subtlety here that is worth mentioning because it causes the data-quality features that were discussed in Section 4.2.1.2. Equation (7.9) can be looked at as a convolution of the data $\tilde{s}(f)$ with the inverse

power spectrum $1/S(f)$, which has many narrow line features. The periodograms used in the calculation of the power spectrum use exactly the 256-s segments that are being analyzed, which means that the entire 256-s segment is corrupted by these features. In order to remove these narrow line features, we coarse-grain the power spectrum with something called *inverse spectrum truncation*. This process involves constructing a quantity $Q[k]$, by which we will multiply the data before we perform the matched-filter.

$$\kappa^{-2}Q[k] = \left|\Delta t \Sigma_{t=0}^{N-1} \kappa^{-1} q_T[j] e^{-2\pi i j k/N}\right|^2, \tag{7.12}$$

where $q_T[j]$ is 0 in the middle of the segment, for $\frac{T_{spec}}{2\Delta t} \leqslant j < N - \frac{T_{spec}}{2\Delta t}$, and is

$$q[j] = \kappa \Delta f \Sigma_{j=0}^{N-1} \sqrt{\frac{1}{\kappa^2 S[k]}} e^{2\pi i j k/N} \tag{7.13}$$

at the beginning and end of the segment. This means that the first and last T_{spec} seconds of the 256-s segment are doubly corrupted, in addition to the T_{chirp} seconds of the data that are corrupted at the beginning of the segment due to filter wraparound for the finite segment duration. The benefit of this procedure is that the center of the data segment has all the sharp spectral features smoothed out. Since the adjacent segments overlap by more than $T_{spec}+T_{chirp}$, this causes no loss of data. It does, however, cause a loud glitch that once had a duration of less than a second to produce smaller glitches up to ± 8 s on either side, as in Figure 4.12.

For each template m, we record every time the SNR time-series $\rho_m(t)$ goes above 5.5. We then *cluster* these over the length of the template plus 1 second (as some of the templates are too short to provide efficient clustering); we save the instance of the highest SNR as a *trigger*. The triggers found in different templates but within 10 milliseconds of each other are also clustered over, choosing to keep the trigger from the template that produced the highest SNR. The peak of the SNR occurs at time t_0, which is then stored as the time of the trigger. This entire matched-filter process is done for every segment for each detector, producing a list of triggers for each detector analyzed. The SNR time-series is not stored — only the peak SNR is stored, along with the time of the trigger and the information gleaned from the matching template. After this first stage of matched-filter, clustering over templates, and clustering between templates, an example of the SNR distribution can be seen in the pink curve in Figure 7.6.

7.3.4 Coincidence between detectors

We are looking for triggers that are coincident in both time (within the light-travel time between detectors, plus errors) and mass (component masses as represented in the $\tau_0 - \tau_3$ space). We take up to 3600 s of coincident data at a time (we are limited by which detectors have Science Data at any given time, and how long the Science Data lasts) and identify triggers coincident between two or more detectors.

The first step is checking that any two triggers in the coincidence are coincident in time. The window for coincidence is 2 times the worst timing accuracy between the detectors (on the order of 1 ms) plus the light

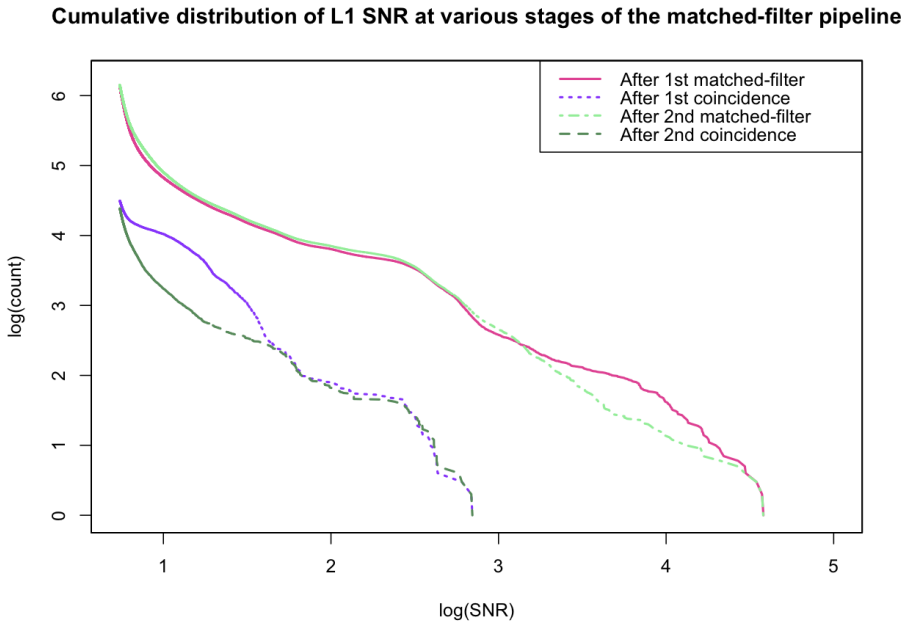

Figure 7.6: Cumulative histograms of the SNR of triggers found in L1 during 931035296-935798487, starting at the SNR threshold of 5.5. Solid pink curve: the distribution of SNR after the first matched-filter stage, 1,323,560 total triggers. Dotted purple curve: the distribution of SNR after the first coincidence stage, 93,417 triggers. Dot-dashed seafoam curve: the distribution of SNR after the second matched-filter stage: 1,404,409 triggers. Dashed green curve: the distribution of SNR after the second coincidence stage: 24,319 triggers. The log is base 10.

travel time of the Earth's diameter, since the interferometers cannot be farther apart than this. If this simple coincidence is passed, error ellipsoids are constructed in $t_0 - \tau_0 - \tau_3$ space. The comparison between these ellipsoids is known as the *E-thinca* test.

After coincidence and clustering, the distribution of single detector triggers can be seen in the purple curve in Figure 7.6. Note that the number of L1 triggers has been reduced by about 40% from the number of triggers after the first matched-filter stage.

7.3.5 The second stage of template bank creation, matched-filter, and coincidence

These coincident triggers are then used to form template banks known as trigbanks, which greatly reduces the number of templates for the second pass of the algorithm (see the difference between the $\times$s and circles in Figure 7.7). We do this because we want to perform a computationally-expensive χ^2 signal-consistency test (described in detail in the following subsection) on each found trigger, but we thought that those found prior to first stage coincidence would be too numerous. The second stage of the matched-filter is essentially the same as the first, but with only the templates that matched triggers found in coincidence at the first stage. For single-detector triggers with an SNR above threshold, the signal-consistency tests described in the following section are performed. This is followed by another coincidence test.

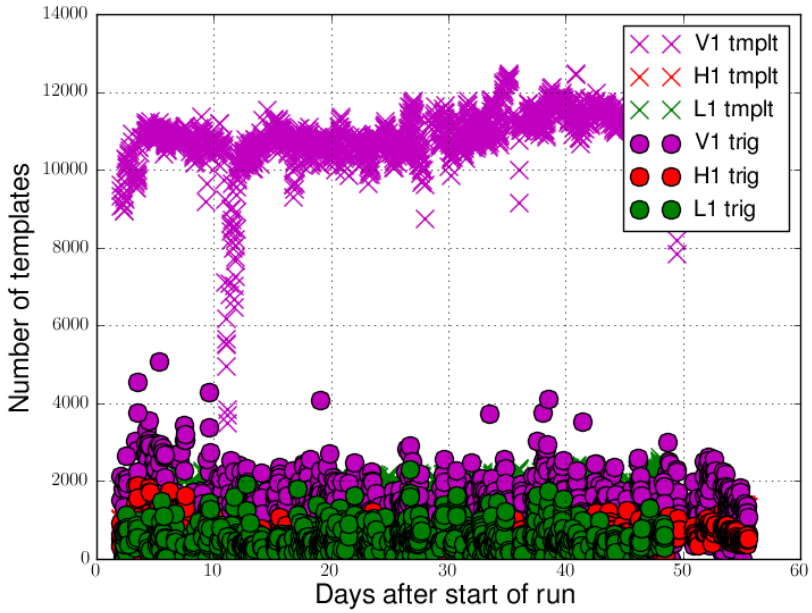

Figure 7.7: The variation in template-bank size and the trigbank size for each 2048-s chunk over the course of the S6-VSR2/3 run.

The distribution of single-detector trigger SNRs after this second stage of matched-filter and clustering, as described in Section 7.3.3, is shown in the seafoam curve in Figure 7.6. In comparison to the pink curve, we don't actually have fewer single inspiral triggers after the second matched-filtering stage. This is acceptable because our computational power has increased since the inception of the algorithm; however, it is glaringly obvious that a new algorithm must be designed for future searches. After the second stage of coincidence, the distribution of single-detector SNRs is shown as the green curve in Figure 7.6.

7.3.6 A χ^2 test for the consistency of the frequency content of the data with the waveform template

If the noisy detector data were Gaussian, applying a threshold on the combined SNR of a coincident trigger would optimally separate signals from detector background. However, the data are far from Gaussian (see Section 4.1), so additional quantities are computed for each coincident trigger in order to better separate signals from background. The most powerful such quantity is the χ^2 signal-consistency test [90]. This quantity checks that the frequency content that contributed to the SNR is consistent with that of Gaussian noise with or without a true astrophysical signal superimposed [124]. A glitch will have an excess of high or low frequencies contributing to the SNR.

For a true astrophysical signal, if we break the SNR time-series into p bins, we expect that each bin will have an SNR of ρ/p, where ρ is the peak SNR of the time-series $\rho(t)$. Based on this knowledge, we compute

the following quantity

$$\chi^2(t) = \sum_{i=1}^{p} (\rho_i(t) - \rho/p)^2, \tag{7.14}$$

where ρ_i is the SNR contribution from the i_{th} bin, and we choose p=10 bins for this search. The bins are constructed so that the matched template contributes an equal amount of SNR to each bin. Therefore, this quantity will be χ^2-distributed with $2p - 2$ degrees of freedom in the presence of Gaussian noise with or without the superposition of a true astrophysical signal that matches the template.

However, it is likely that due to our 3% (or more, for regions where the merger and ringdown are significant) mismatch between neighboring templates, our signal will not exactly match the template. This introduces a non-centrality parameter to the χ^2 distribution. Therefore, rather than thresholding on χ^2, we threshold on

$$\Xi(t) = \frac{\chi^2(t)}{p + \rho(t)^2}. \tag{7.15}$$

Looking at the distribution of Ξ values for representative signal and background events (which are described in the following subsections), we determined a threshold of 10 on Ξ at the time of the peak SNR to be reasonable and effective. Triggers with Ξ greater than 10 are removed from the list of single detector triggers.

7.3.7 A final clustering stage

The coincident triggers are then clustered again, such that for every coincidence, the surrounding 10 seconds are searched for a louder coincidence (where loudness is defined by the ranking statistic, as discussed in Section 7.6) and only the loudest coincidence is kept. The reasoning behind this is that if there was a loud glitch within 10 seconds of a candidate GW event, we would not have faith that the candidate event was a true astrophysical signal. The distribution of SNRs after this final clustering stage is shown in Figure 7.8.

7.3.8 The candidate gravitational wave events

The final candidate gravitational wave events are the clustered ellipsoidally coincident triggers, each having an SNR of greater than 5.5 and a Ξ value of less than 10 in each detector, and a final 10-s clustering applied. Several pieces of information are saved for each trigger in the coincidence, including:

- the detector whose data contained the trigger,
- the coalescence time of the trigger (nanosecond precision),
- the duration of the template matched to the trigger,
- the amplitude of the template,
- the effective distance of the found trigger,

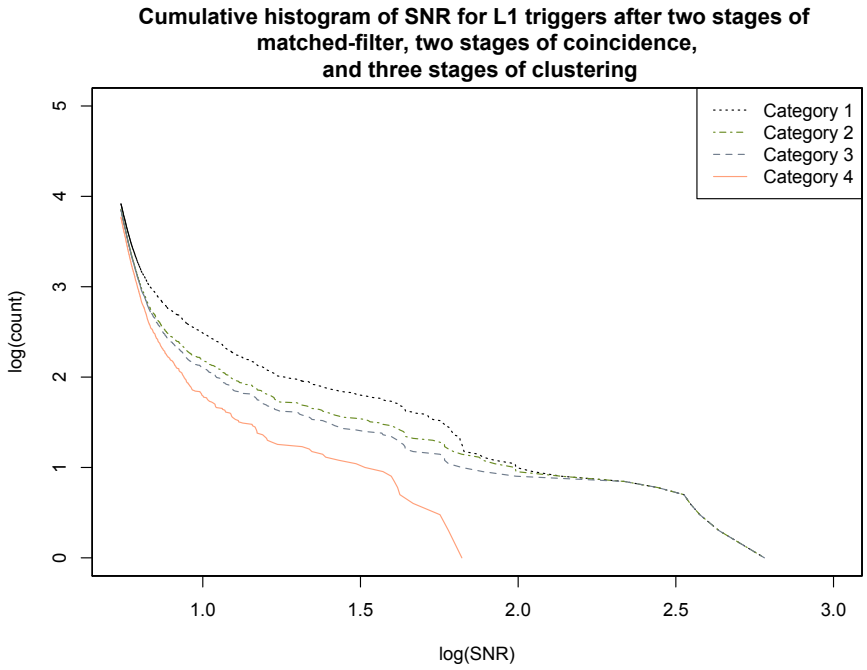

Figure 7.8: The cumulative histogram of the SNR for L1 triggers in the GW data after the second stage of matched-filtering, with clustering over and between templates applied each time, cuts on χ^2 applied, two stages of mass-time coincidence, and a final clustering over 10 s. Triggers with vetoes from Categories 1-4 applied are labeled. There are 8290 triggers in Category 1 (dotted salmon curve), 7181 in Category 2 (dot-dashed green curve), 7105 in Category 3 (dashed grey curve), and 5884 in Category 4 (solid salmon curve). The triggers could have been part of an H1L1, L1V1, or H1L1V1 coincidence. The log is base 10.

- the duration of the matched template,
- the coalescence phase of the found trigger,
- the component masses, chirp mass, and η of the found trigger,
- the SNR of the found trigger,
- the χ^2 of the found trigger,
- the number of degrees of freedom for the χ^2
- the chirp times τ_0, τ_1, τ_2, τ_3, τ_4, τ_5, of the post-Newtonian expansions of the matched template,
- the values and degrees of freedom for two alternate χ^2 calculations,
- the r^2 duration for the trigger (the amount of time the χ^2 time-series is above a threshold in a window around the peak SNR) [125],
- an event id used to identify the trigger.

In order to rank these events, we must determine their false alarm rate (FAR), which quantifies how likely it is that the event is due to the random coincidence of background triggers. The FAR calculation will be described in detail in Section 7.7. In order to perform the FAR calculation, we must first get an estimation of the rate of such accidental coincidences of background triggers.

7.4 The estimation of the background — accidental coincidences between detectors (timeslides)

The background for these searches is the accidental coincidence of noise triggers in two or more detectors. In order to estimate the rate of such accidental coincidences, we perform multiple (typically of order 100) time shifts of the data. Each time shift moves the data from the different detectors with respect to each other in multiples of 5 seconds. Since the light-travel time between detectors is on the order of tens of milliseconds, any coincidences found between detectors whose data have been time-shifted are certainly due to random chance. The shifts are done on a ring, whose circumference is the length of the stretch of the coincident data used in the coincidence step in Section 7.3.4. The ellipsoidal coincidence test is performed, and a list of coincidences found in the time-shifted data are stored. This approach ensures that the analyzed coincidence segments are the same for the in-time and time-shifted triggers. It also ensures that the noise profile of the detector is relatively the same in the new time-shifted coincidences as it was in the in-time coincidences, thus providing an accurate description of the in-time background.

This method has two main benefits. The first is that we are certain that there are no true gravitational waves described in our set of background events. The second is that we have 100 times the number of background events that we have in non-time-shifted data. A disadvantage is that with of order 100 time slides, one can only estimate false alarm probabilities (FAPs) of order 1% or greater (while we require much smaller FAPs for the first detection of GWs). Another disadvantage is that GW signals might still contaminate these background estimations (i.e., one of the two or three triggers in the coincidence could still be due to a true astrophysical event).

The triggers found in coincidence in time-shifted data are often referred to as *timeslides*. Because the actual foreground has not been time-shifted, it is often referred to as *zerolag*.

7.5 The injection of simulated signals to test our efficiency and make astrophysical statements

To measure our efficiency, we must inject simulated signals into the gravitational-wave data and quantify our ability to recover these. These are often referred to as *software injections*. We find the candidate gravitational wave events caused by these injected signals with the exact same search pipeline described earlier in

this chapter, with one added step — the candidate gravitational wave event must also be coincident with the injected signal. In the published results, we enforce only time coincidence within a window of 1 s [17]. We do not require that a template similar to the injected one was found, as we would not have this luxury with a true astrophysical signal.

We use software injections to calculate our sensitivity — the distance to which we can see CBCs as a function of their intrinsic parameters (i.e., masses). We also use them, in conjunction with the foreground and background events found by the high-mass pipeline, to calculate rate upper limits on the number of CBCs per unit volume per unit time.

We inject non-spinning waveforms from the EOBNRv2 family; see Section 2.2.1.1 for an introduction to these waveforms. We also inject spinning (aligned and anti-aligned spins only) and non-spinning waveforms from the IMRPhenomB family; see Section 2.2.1.2.

For this search, we choose that the injections cover our total mass range of 25 - 100 $M_{\odot}$ in such a way that the injected component masses are distributed uniformly for the EOBNRv2 injections. Each set of injections might cover a mass range smaller than or beyond 25 - 100 $M_{\odot}$, such that the aggregate of all the injection runs covers the 25 - 100 $M_{\odot}$ region, while ensuring there are enough injections covering the edges of the region. The specific limits for the mass distributions are enumerated below, but each distribution is still uniform in component mass.

For the IMRPhenomB injections, the waveforms are only trusted up to mass ratios of 10:1, so the waveforms are injected such that their distribution is uniform in both total mass and mass ratio. The minimum and maximum mass ratios are 1 and 10, respectively. Additionally, for the spinning IMRPhenomB injections, the spin parameter (see Equation (2.22)) is uniformly distributed between -.85 and .85.

For each GW injected, we must also specify the extrinsic parameters. We randomly choose the sky locations. The inclination angles produce a uniform distribution in $\cos\iota$, with ι in the range [0,π]. The polarization angles are distributed uniformly between 0 and 2π. These values are reasonable because the Cosmological Principle says that we are not in a special location or orientation with respect to (extragalactic) astrophysical sources. Picking the distance between the detector and the source is a more delicate matter. Beyond our neighboring galaxies, we can assume that any type of source will be distributed uniformly in volume. Unfortunately, placing injected signals uniformly in volume produces far too many injections beyond our sensitive distance (which is a strong function of mass, so we can't simply pick one maximum sensitive distance), resulting in too few injections for a proper efficiency calculation and wasted computer time. Therefore, we choose a mix of uniform in distance and uniform in the log base 10 of the distance. We then evaluate the detection efficiency as a function of distance, and compute the sensitive volume as a function of source mass (see Section 7.8).

For each *injection run*, we insert the injections into the data at the beginning of the search pipeline, taking care that each is separated in time so they don't overlap. Therefore, they are injected every $724.077 + \epsilon$ s, where ϵ is a random number between 0 and 300. As this necessarily limits the total number of injections

produced, we perform several injection runs, itemized here:

- 3 sets of non-spinning IMRPhenomB waveforms with distances distributed uniformly in distance between 10 and 600 Mpc, $1 \leqslant m_1/m_2 \leqslant 10$, $25\ M_\odot \leqslant M_{total} \leqslant 100\ M_\odot$,
- 2 sets of non-spinning IMRPhenomB waveforms with distances distributed uniformly in log(distance) between 75 and 1 Mpc, $1 \leqslant m_1/m_2 \leqslant 10$, $25\ M_\odot \leqslant M_{total} \leqslant 100\ M_\odot$,
- 3 sets of spinning IMRPhenomB waveforms with distances distributed uniformly in distance between 10 and 600 Mpc, $1 \leqslant m_1/m_2 \leqslant 10$, $25\ M_\odot \leqslant M_{total} \leqslant 100\ M_\odot$
- 2 sets of spinning IMRPhenomB waveforms with distances distributed uniformly in log(distance) between 75 and 1,000 Mpc, $1 \leqslant m_1/m_2 \leqslant 10$, $25\ M_\odot \leqslant M_{total} \leqslant 100\ M_\odot$
- 3 sets of non-spinning EOBNRv2 waveforms with distances distributed uniformly in distance between 1 and 500 Mpc, $10\ M_\odot \leqslant m_1 \leqslant 99\ M_\odot$, $1\ M_\odot \leqslant m_2 \leqslant 19\ M_\odot$, $20\ M_\odot \leqslant M_{total} \leqslant 109\ M_\odot$,
- 3 sets of non-spinning EOBNRv2 waveforms with distances distributed uniformly in distance between 5 and 750 Mpc, $19\ M_\odot \leqslant m_1 \leqslant 81\ M_\odot$, $19\ M_\odot \leqslant m_2 \leqslant 54\ M_\odot$, $38\ M_\odot \leqslant M_{total} \leqslant 109\ M_\odot$,
- 2 sets of non-spinning EOBNRv2 waveforms with distances distributed uniformly in log(distance) between 15 and 600 Mpc, $10\ M_\odot \leqslant m_1 \leqslant 99\ M_\odot$, $1\ M_\odot \leqslant m_2 \leqslant 19\ M_\odot$, $20\ M_\odot \leqslant M_{total} \leqslant 109\ M_\odot$,
- 2 sets of non-spinning EOBNRv2 waveforms with distances distributed uniformly in log(distance) between 60 and 1,000 Mpc, $19\ M_\odot \leqslant m_1 \leqslant 81\ M_\odot$, $19\ M_\odot \leqslant m_2 \leqslant 54\ M_\odot$, $20\ M_\odot \leqslant M_{total} \leqslant 109\ M_\odot$.

Figure 7.9 is a scatterplot of the component masses for all the non-spinning IMRPhenomB injections made during the first analysis period of S6-VSR2/3 (see Table 7.1). The pink outline indicates the edge of the template bank we are searching for. The blue line is the line of symmetry, above which the $m_2 > m_1$ system is equivalent to the $m_1 > m_2$ system. In our statements of sensitive range and rate upper limit of astrophysical high-mass CBC sources, we only use found injections with injected component masses bounded by the blue-pink-red-pink quadrilateral. This is because the red line indicates a mass ratio (m_2/m_1) of 4; IMRPhenomB waveforms with mass ratios greater than this have not been tested against numerical relativity (see Section 2.2.1.2). The distribution of injected component masses for the spinning IMRPhenomB waveforms is similar to Figure 7.9. The same injections in Figure 7.9 are visualized in chirp mass - symmetric mass ratio space in Figure 7.10. The density of points is different because a distribution that is uniformly distributed in total mass and mass ratio is not uniformly distributed in the $\mathcal{M}$ - η plane.

Figure 7.11 is a scatterplot of the component masses for all the EOBNRv2 injections made during the first analysis period of S6 (see Table 7.1). As the EOB approach is modeled on a test particle orbiting an effective

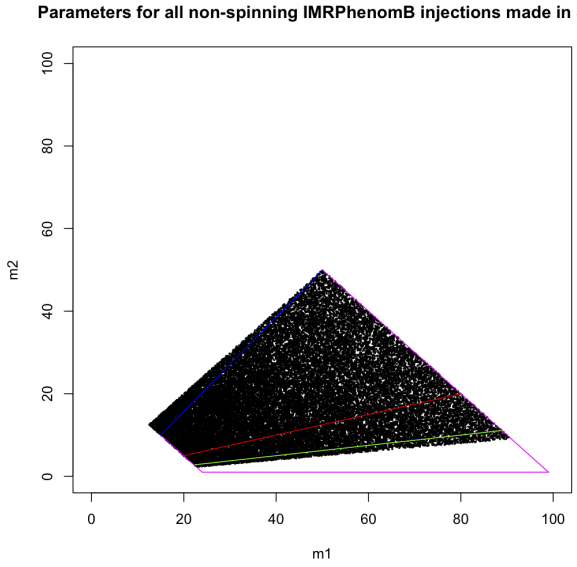

Figure 7.9: The distribution of injected component masses for IMRPhenomB injections made during S6a, the first analysis period of S6 (GPS time: 931035296-935798487), for all of the non-spinning sets of injections described in the above list. The distribution for spinning IMRPhenomB injections is similar. The pink lines indicate the edges of the template bank. The blue line indicates the line of symmetry, above which the $m_2 > m_1$ system is equivalent to the $m_1 > m_2$ system. The red line indicates a mass ratio (m_2/m_1) of 4. Found injections with an injected mass greater than 4 (below the red line) are not used in the calculation of the search's sensitive range statement nor in the search's astrophysical upper limit statement. The green line indicates a mass ratio of 8. We considered using found injections with injected mass ratios between 4 and 8 in our sensitive range statement, but decided against it for our publication (Reference [17]).

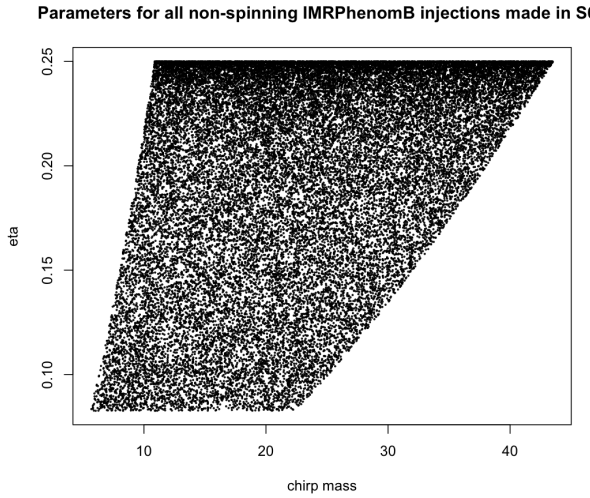

Figure 7.10: The distribution of injected masses in $\mathcal{M}_{chirp} - \eta$ space for all the non-spinning IMRPhenomB injections made during S6a, the first analysis period of S6 (GPS time: 931035296-935798487), as described in the above list. The axes on this plot are simple transformations of the axes on Figure 7.9, see Equation (7.1) and Equation (7.2). The distribution for spinning IMRPhenomB injections is similar.

potential, the EOBNRv2 waveforms should be trusted in the limit of large mass ratios (unlike the IMRPhenomB waveforms). However, as the EOBNRv2 waveforms were only tested against numerical relativity a maximum mass ratio of 6 (see Section 2.2.1.1), and for consistency with the use of the IMRPhenomB-injected waveforms, we again only use the found EOBNRv2 injections with injected component masses bounded by the blue-pink-red-pink quadrilateral in our calculation of the rate upper limit of high-mass CBCs. Nonetheless, we use all the found EOBNRv2 injections within the blue-pink-pink-pink quadrilateral in our statement of sensitive range for high-mass CBC sources. The points outside of this quadrilateral are simply an artifact of performing extra injection runs with the goal of increasing the number of statistics at the edges of the quadrilateral. The same injections in Figure 7.11 are visualized in chirp mass - symmetric mass ratio space in Figure 7.12. The density of points is different because a distribution that is uniformly distributed in component mass (i.e., the m_1 - m_2 plane) is not uniformly distributed in the $\mathcal{M}$ - η plane.

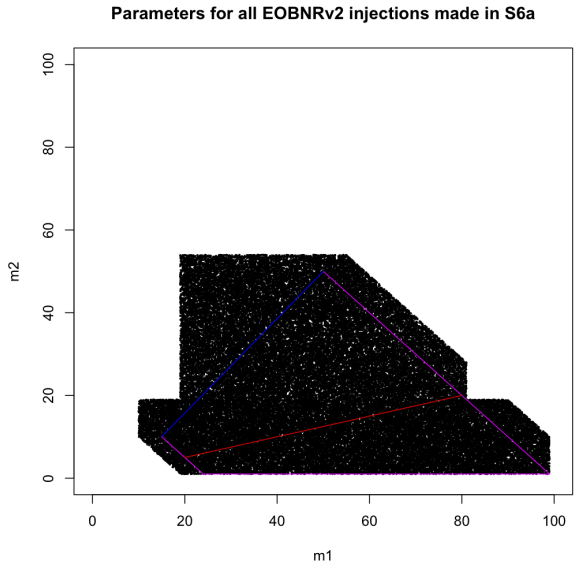

Figure 7.11: The distribution of injected component masses for EOBNRv2 injections made during S6a, the first analysis period of S6 (GPS time: 931035296-935798487), for all of the EOBNRv2 sets of injections described in the above list. The pink lines indicate the edges of the template bank. The blue line indicates the line of symmetry, above which the $m_2 > m_1$ system is equivalent to the $m_1 > m_2$ system. The red line indicates a mass ratio (m_2/m_1) of 4. Found injections with an injected mass greater than 4 (below the red line) are not used in the calculation of the search's astrophysical upper limit statement, but can be used to estimate the sensitive range for such systems. The jaggedness of the edges outside the colored line boundaries is an artifact of the way the injections were made, as described in the text.

The variations in the distance ranges for each set of injections enumerated in the above list can be visualized in Figure 7.13 for IMRPhenomB injections and Figure 7.14 for EOBNRv2 injections.

Other distributions of interest are: the distribution of coalescence phase, which is random and uniform (see Figure 7.15); the distribution of sky locations, which is uniform in longitude and cos(latitude) (see Figure 7.16); the distribution of inclination angles, which is uniform in the cosine of the angle (see Figure 7.17);

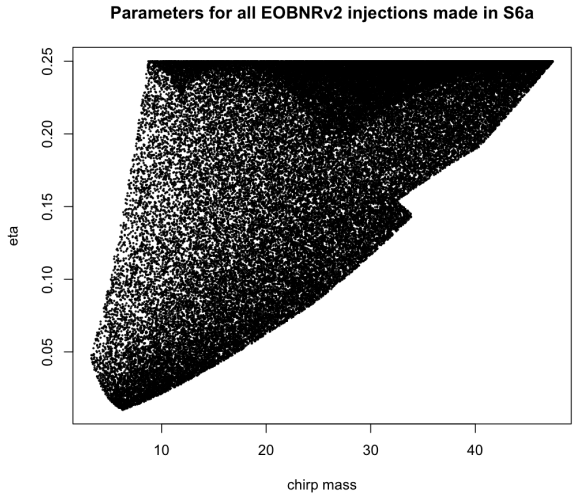

Figure 7.12: The distribution of injected masses in $\mathcal{M}_{chirp} - \eta$ space for EOBNRv2 injections made during S6a, the first analysis period of S6 (GPS time: 931035296-935798487), for all of the EOBNRv2 sets of injections described in the list of injection sets in the text. The axes on this plot are simple transformations of the axes on Figure 7.11; see Equation (7.1) and Equation (7.2).

the distribution of polarization angles, which is uniform from 0 to 2π (see Figure 7.17); and the distribution of component spins, which is uniform and random (see Figure 7.18).

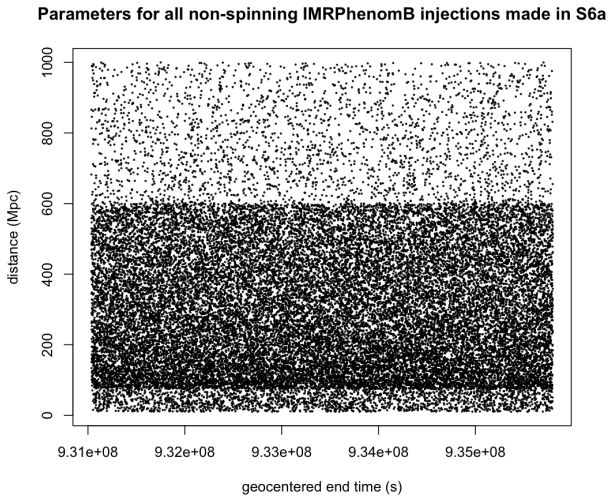

Figure 7.13: The distribution of injected distance versus geocentered end time for IMRPhenomB injections made during S6a, the first analysis period of S6 (GPS time: 931035296-935798487), for all of the non-spinning sets of injections described in the above list. The distribution for spinning IMRPhenomB is similar.

The efficiency versus distance of finding all the EOBNRv2 injections performed during H1L1V1 time during the first analysis period of S6-VSR2/3 is shown in Figure 7.19 after the first stage of matched-filter and coincidence; for the same injections, the efficiency versus effective distance (see Equation (7.7)) is shown

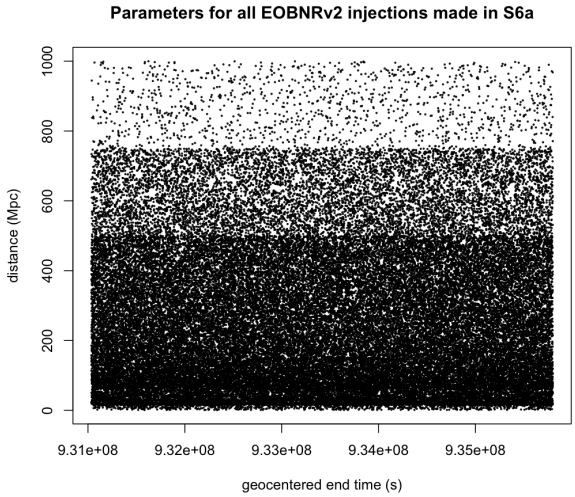

Figure 7.14: The distributions of injected distance versus geocentered end time for EOBNRv2 injections made during S6a, the first analysis period of S6 (GPS time: 931035296-935798487), for all of the EOBNRv2 sets of injections described in the above list.

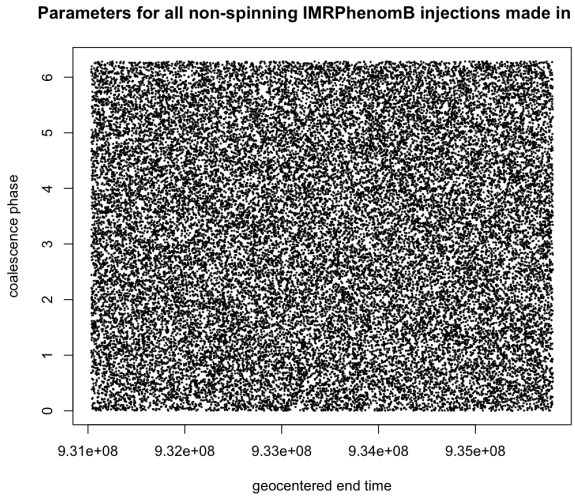

Figure 7.15: The distribution of injected coalescence phase versus geocentered end time for IMRPhenomB injections made during S6a, the first analysis period of S6 (GPS time: 931035296-935798487), for all of the non-spinning sets of injections described in the above list. The distribution for spinning IMRPhenomB is similar, as is the distribution for EOBNRV2 injections.

in Figure 7.20. The efficiency versus effective distance decreases after the application of the Category 1-4 vetoes because there are fewer coincident segments of time between the detectors — see Figure 7.21. The injections are made into coincident science segments at Category 1.

Similarly, for the IMRPhenomB injections found in coincidence after the first stage of matched-filter and coincidence, the efficiency versus distance is shown in Figure 7.22, and the efficiency versus effective distance is shown in Figure 7.23. After the application of vetoes in Categories 1-4, the efficiency is shown in

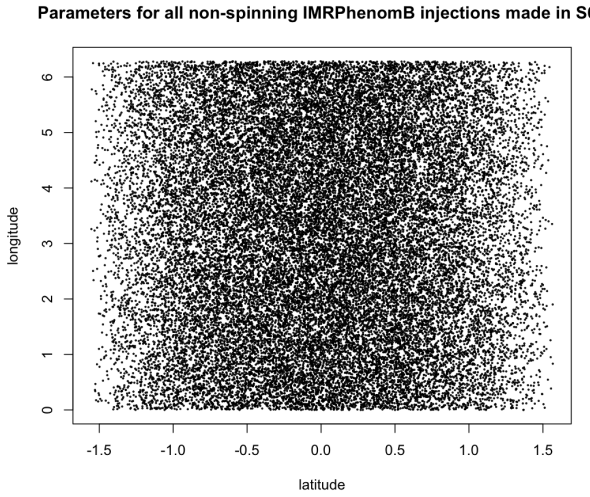

Figure 7.16: The distribution of injected sky locations for IMRPhenomB injections made during S6a, the first analysis period of S6 (GPS time: 931035296-935798487), for all of the non-spinning sets of injections described in the above list. The distribution for spinning IMRPhenomB is similar, as is the distribution for EOBNRV2 injections.

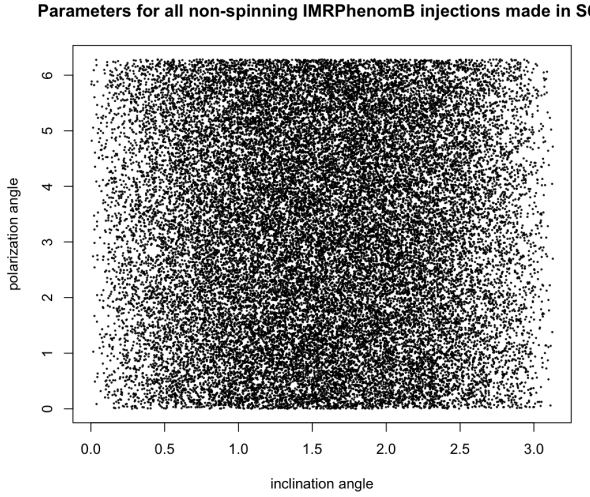

Figure 7.17: The distribution of injected inclination and polarization angles for IMRPhenomB injections made during S6a, the first analysis period of S6 (GPS time: 931035296-935798487), for all of the non-spinning sets of injections described in the above list. The distribution for spinning IMRPhenomB is similar, as is the distribution for EOBNRV2 injections.

Figure 7.24 versus effective distance.

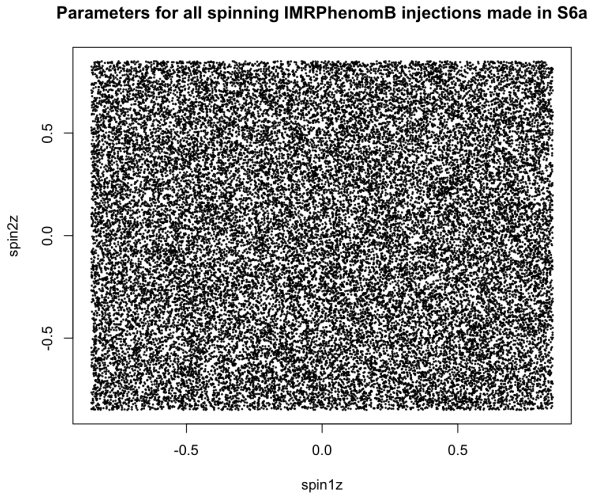

Figure 7.18: The distribution of injected spins, which are all aligned and pointing in the z-direction, for IMRPhenomB injections, for all of the spinning sets of injections described in the above list.

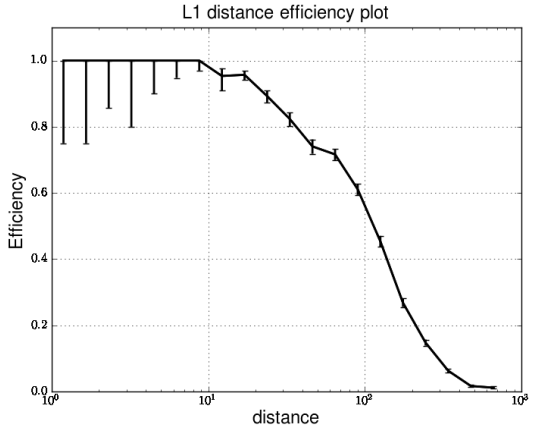

Figure 7.19: The efficiency at finding injections performed during S6a, the first analysis period of S6 (GPS time: 931035296-935798487), from all sets of EOBNRv2 waveforms enumerated above. These injections have been found in coincidence between L1 and at least one other detector during H1L1V1 time, as of the first stage of matched-filter and coincidence. The efficiency is plotted versus the binned injected distance (in Mpc) of each waveform.

7.6 A ranking statistic for candidate GW events

The first step in determining if our list of candidate gravitational wave events contains any true astrophysical signals is to decide on the ranking statistic. One of the earliest ranking statistics was the combined effective SNR, which was developed by looking at scatterplots of found injections and timeslides in the SNR-χ^2 plane. An analytical formula for effective SNR is given by

$$\rho_{\rm eff} = \frac{\rho}{[\chi^2_r(1+\rho^2/\beta)]^{1/4}}, \tag{7.16}$$

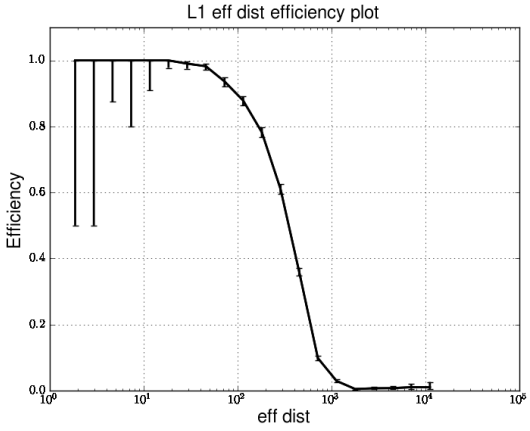

Figure 7.20: The efficiency at finding injections performed during S6a, the first analysis period of S6 (GPS time: 931035296-935798487), from all sets of EOBNRv2 waveforms enumerated above. These injections have been found in coincidence between L1 and at least one other detector during H1L1V1 time, as of the first stage of matched-filter and coincidence. The efficiency is plotted versus the binned injected effective distance (see Equation (7.7)) (in Mpc) of each waveform.

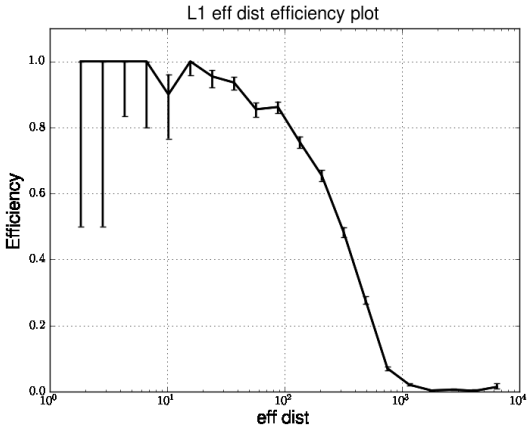

Figure 7.21: The efficiency at finding injections performed during S6a, the first analysis period of S6 (GPS time: 931035296-935798487), from all sets of EOBNRv2 waveforms enumerated above. These injections have been found in coincidence between L1 and at least one other detector during H1L1V1 time, at the end of the high-mass pipeline with Categories 1-4 of vetoes applied. The efficiency is plotted versus the binned injected effective distance (see Equation (7.7)) (in Mpc) of each waveform.

where ρ is the SNR and χ^2_r is the reduced χ^2 value, equal to $\chi^2/(2p-2)$, where p is the number of bins used in the χ^2 calculation. p is 18 for the low-mass search and 10 for the high-mass search. β is a tunable number that is set to 250 in the low-mass search and 50 in the high-mass search. The combined effective SNR is the effective SNR for each detector's trigger in the coincidence, added in quadrature.

This statistic was used in several searches, both as a ranking statistic and as a detection statistic. In Reference [56], effective SNR was still used as the ranking statistic, but was converted to an inverse false alarm rate (IFAR) for the detection statistic used in calculating upper limits and detection statements. The

Figure 7.22: The efficiency at finding injections performed during S6a, the first analysis period of S6 (GPS time: 931035296-935798487), from all sets of IMRPhenomB waveforms enumerated above. These injections have been found in coincidence between L1 and at least one other detector during H1L1V1 time, as of the first stage of matched-filter and coincidence. The efficiency is plotted versus the binned injected distance (in Mpc) of each waveform.

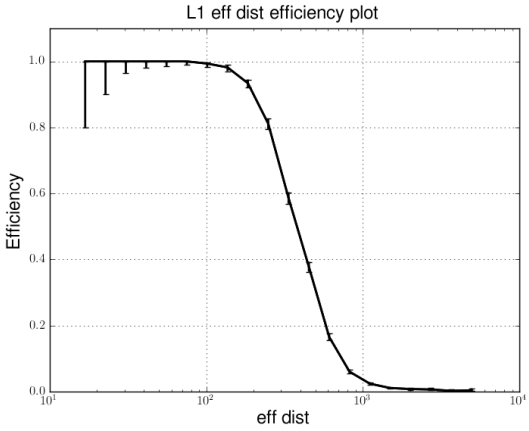

Figure 7.23: The efficiency at finding injections performed during S6a, the first analysis period of S6 (GPS time: 931035296-935798487), from all sets of IMRPhenomB waveforms enumerated above. These injections have been found in coincidence between L1 and at least one other detector during H1L1V1 time, as of the first stage of matched-filter and coincidence. The efficiency is plotted versus the binned injected effective distance (see Equation (7.7)) (in Mpc) of each waveform.

false alarm rate (FAR) calculation will be discussed in the following section. Prior to Reference [56], the ranking statistic was used as the detection statistic.

The ranking statistic has also gone through an evolution. In Reference [58], a statistic called new SNR was created, and the detection statistic was the IFAR calculated from the values of the combined new SNR.

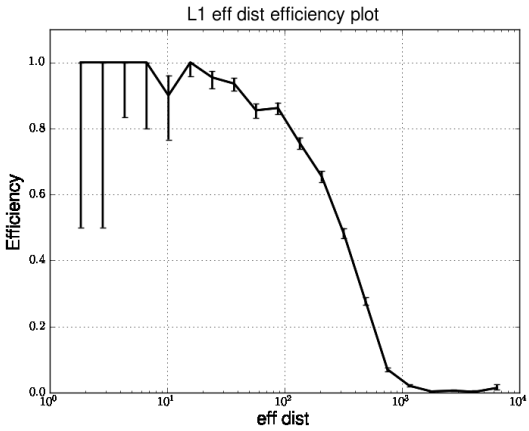

Figure 7.24: The efficiency at finding injections performed during S6a, the first analysis period of S6 (GPS time: 931035296-935798487), from all sets of IMRPhenomB waveforms enumerated above. These injections have been found in coincidence between L1 and at least one other detector during H1L1V1 time, at the end of the high-mass pipeline with Categories 1-4 of vetoes applied. The efficiency is plotted versus the binned injected effective distance (see Equation (7.7)) (in Mpc) of each waveform.

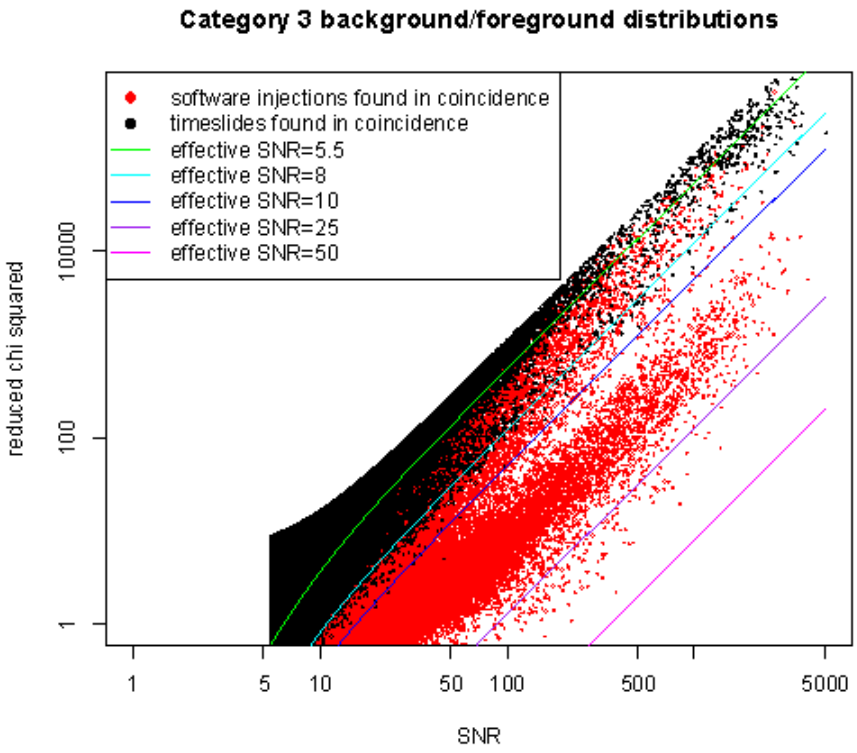

Figure 7.25: A scatterplot of the χ^2 versus SNR for single detector triggers from H1 that are part of a coincidence. The estimated background using timeslides (black) are plotted atop the found software injections (red), which do extend all the way to the left below the timeslide points. The sharp line on the left is due to the Ξ cut described in Equation (7.14). The colored lines trace curves of constant $\rho_{\rm eff}$.

For a single detector, the new SNR is given by

$$\rho_{\text{new}} = \begin{cases} \frac{\rho}{[1+(\chi_r^2)^3/2]^{1/6}} & \text{for } \chi_r^2 > 1 \\ \rho & \text{for } \chi_r^2 \leqslant 1. \end{cases} \tag{7.17}$$

The new SNR improves upon the effective SNR, especially where the χ_r^2 is less than 1 — the effective SNR was prone to overweighting triggers (giving a $\rho_{\text{eff}} > \rho$) whose χ_r^2 have gone below 1 due to statistical fluctuations.

A further improvement was made to the ranking statistic for the high-mass search described in this thesis and in Reference [17]. The high-mass SNR takes into account the fact that the χ^2 test is not as accurate nor effective for triggers that have been matched to shorter templates because there are fewer cycles of the waveform in the detector's band. To take this into account, we split the triggers into two broad categories — those that have been matched to a template whose duration is less than 0.2 s and those that have been matched to a template whose duration is greater than 0.2 s.

$$\rho_{\text{high}} = \begin{cases} \rho_{\text{eff}} & \text{for short-duration triggers and all triggers from V1 during VSR3,} \\ \rho_{\text{new}} & \text{for long-duration triggers and all triggers from V1 during VSR2.} \end{cases} \tag{7.18}$$

These decisions were made empirically, by looking at scatterplots like those in Figure 7.25.

Keep in mind that since all candidate gravitational wave events must be found in coincidence, we use a combined ranking statistic. For the highmass search, this is the high-mass SNR added in quadrature for each detector in the coincidence. For a double-coincidence, this is

$$\rho_{\text{coincidence}} = \sqrt{\rho_{\text{high}_1}^2 + \rho_{\text{high}_2}^2}, \tag{7.19}$$

while for a triple-coincidence, this is

$$\rho_{\text{coincidence}} = \sqrt{\rho_{\text{high}_1}^2 + \rho_{\text{high}_2}^2 + \rho_{\text{high}_3}^2}, \tag{7.20}$$

where the subscript references different detectors. This combined high-mass SNR is used as the ranking statistic in the IFAR calculations; this IFAR is the detection statistic of the high-mass search.

7.7 False alarm rate calculations

By using an IFAR as the detection statistic, we can prevent candidate gravitational wave events in a particular region of parameter space that have a high ranking statistic from obscuring candidate gravitational wave events in other regions of parameter space; see, for example, how a search using both high-mass and low-mass templates will produce background that obscures low-mass signals in Figure 1.1. This is accom-

plished by dividing the parameter space into regions with similar characteristics and calculating the FAR for each candidate gravitational wave event in that region, based on the candidate's ranking statistic value and the distribution of ranking statistic for the timeslides in that region. The FAR for a candidate gravitational wave event is equal to the number of timeslides with a ranking statistic greater than that of the candidate, divided by the total amount of time searched for the timeslides. For the low-mass search for which the IFAR method was introduced, the ranking statistic was the combined effective SNR. For the high-mass search outlined in this thesis, the combined high-mass SNR was used as the ranking statistic. The regions for which the FARs are calculated separately are the 4 different types of observation time — when only H1 and L1 were operating, when only H1 and V1 were operating, when only L1 and V1 were operating, and when all three detectors were operating — and the 2 different regions used for the detection statistic: short-duration events and long-duration events. By dividing up triggers into short- and long-duration, we can avoid having high-SNR short-duration triggers from glitches contaminate the detection statistic for the long-duration triggers.

After the FARs are calculated for each candidate gravitational wave event in each region, the FARs are combined, normalizing for the observation time and accounting for the number of regions. In the end, a combined FAR of $1/T$ means that during the observation time T, there is expected to be a single background trigger as loud as the event under consideration [56]. IFAR of an event is simply related to its FAR:

$$\text{IFAR} = \frac{1}{\text{FAR}}. \tag{7.21}$$

7.8 The loudest event statistic and sensitivity

The probability of detecting n GW events, given a rate of $R = \mu$ CBCs in the mass space considered by the high-mass search, per volume per time, is:

$$p(n|\mu) = \frac{\mu^n e^{-\mu}}{n!}, \tag{7.22}$$

as the GW signals are expected to be Poisson distributed with a mean number of μ. We can use Bayes' theorem to construct the posterior probability for the rate, given the observation of n events:

$$p(\mu|n) = \frac{p(n|\mu)p(\mu)}{\int p(n|\mu)p(\mu)d\mu}, \tag{7.23}$$

where $p(\mu)$ is the prior probability distribution of the expected number of events for our search.

Using the *loudest event statistic* means that we set the threshold for detection at the FAR of our loudest foreground event, $\widehat{\text{FAR}}$ [126]. The value of this $\widehat{\text{FAR}}$ for each of our analysis times is listed in Table 8.1. We use this threshold when calculating our *sensitivity*. In general, this sensitivity will be a function of the component masses of the CBC system considered. In order to capture this dependence, we calculate the

sensitivity separately for different bins in component mass. The first step in evaluating the sensitivity is calculating the efficiency of recovering our software injections in each set of mass bins, as a function of distance to the source:

$$\overline{E}_{i,j}(r) = \frac{N_{i,j\text{ found}}(r)}{N_{i,j\text{ performed}}(r)}, \tag{7.24}$$

where i and j label the bins for the masses of each of the objects in the binary, and the bar indicates that we have averaged over sky position and orientation. To be considered found, the injection must have a lower FAR than the loudest foreground event. This efficiency is calculated separately for each of the analysis times in our experiment; each row in Table 7.2 is one analysis time. The efficiency can be used to calculate the sensitive volume of each of the analysis times:

$$V_{i,j} = \int 4\pi r^2 \overline{E}_{i,j}(r) dr. \tag{7.25}$$

The total sensitivity of the search is then simply

$$[VT]_{i,j} = \sum_{t=1}^{t=24} V_{i,j}^t * T^t, \tag{7.26}$$

where t indexes the analysis time, T is the length of the analysis time, and the sensitivity VT is still specified separately for each pair of mass bins i, j.

7.8.1 Upper limit calculation for the rate of high-mass binary mergers

We also use the loudest event statistic to calculate our upper limits on the volume-time density of mergers of black hole binary systems in the mass ranges considered. The subtlety of this approach is whether to consider the loudest foreground event signal or background. If it is considered background, then we have the probability of detecting 0 events:

$$p(0|\mu) = e^{-\mu} = e^{-RVT}, \tag{7.27}$$

where VT is the total sensitivity of the search as defined in Equation (7.26); R is the rate (per volume, per time) of CBC coalescences in the mass space defined by the high-mass search. $\mu = RVT$ is the expected number of signal events, depending on the value of R, whose posterior probability density function we wish to determine. Again, the calculations are performed for each pair of mass bins i, j, but I will drop the subscripts in this section. On the other hand, if the loudest foreground event is considered signal, we have the probability of detecting 1 event:

$$p(1|\mu) = \mu e^{-\mu}. \tag{7.28}$$

We can express both of these possibilities with the single equation:

$$p([0,1]|\mu) = \frac{(1+\mu\Lambda)e^{-\mu}}{\int(1+\mu\Lambda)e^{-\mu}d\mu}, \tag{7.29}$$

where Λ is generally described as

$$\Lambda = \frac{d\ln p_{\text{signal}}(x)}{dx}\left(\frac{d\ln p_{\text{background}}(x)}{dx}\right)^{-1}, \tag{7.30}$$

where the distributions for these probabilities are taken from our injections (signal) and timeslides (background) in terms of $x = -\widehat{\text{FAR}}_t T_t$ for the loudest event statistic (where the analysis time index t is written out to make it explicit that the statistic is different for each analysis time). Assuming the background is a Poisson process,

$$p_{\text{background}}(x) = e^x, \tag{7.31}$$

so Λ can simplify to

$$\Lambda_t = \frac{d\ln V_t(\widehat{\text{FAR}})}{d\widehat{\text{FAR}}}\frac{1}{T_t}, \tag{7.32}$$

where t indexes the analysis time and V is defined as in Equation (7.25). $\Lambda = 0$ corresponds to the loudest foreground event being background and $\Lambda = \infty$ corresponds to the loudest event being signal [23].

We compute the Bayesian likelihoods (which are proportional to the numerator in Equation (7.29)) for this posterior probability distribution for each analysis time, marginalizing over the statistical uncertainties in the volume due to the finite number of software injections; see Reference [127] for details. The likelihoods for each analysis period are then multiplied. The prior probabilities are taken from the results of the search for high-mass CBCs in LIGO's S5 data. The calibration uncertainty is marginalized over at this final stage because the nature of the errors implies they are significantly correlated between analysis times. In order to turn this posterior into a rate statement, we normalize the posterior and integrate it to 90%. This gives us a 90% confidence upper limit on the rate of high-mass CBCs.

It should be mentioned that there are uncertainties in the waveforms, but these are not taken into account. The calibration errors that gave us a systematic uncertainty of 42% in volume are so overestimated that we feel it is okay to not add in the additional uncertainty in the waveforms, which is hard to quantify in the first place (since we don't have any astrophysical waveforms to compare our theoretical ones to anyway!).

The upper limit calculation is the main scientific result of a search for GWs, in the absence of detection. Because astrophysical observations of systems of interest are rare (see Section 2.1), placing an upper limit of the volume-time density of such merging systems is extremely scientifically valuable.

7.9 Blind Analysis

Performing a blind analysis allows us to make modifications to our search pipeline without consciously or sub-consciously biasing our results. For LIGO-Virgo CBC searches, a blind analysis means we run the whole analysis, as described above, and only look at the results from timeslides, injections, and 10% of the zerolag (known as the *playground*). Looking at the timeslides and injections allows us to fine-tune our data-quality vetoes, matched-filter, trigger clustering, coincidence windows, signal-based vetoes, and detection statistic; as well as perform several sanity-checks. All tuning is done to maximize the separation of these estimated background and simulated foreground events, and thus avoiding knowingly (or unknowingly) elevating or killing specific candidate GW events. We allow ourselves to look at 10% of the true foreground, simply to catch any mistakes that might have propagated in the zerolag portion of the analysis. This 10% (600 s out of every 6370 s) is not used in our calculation of the search sensitivity (above the loudest non-playground zerolag event) or upper limit on merger rates of CBCs. Performing such a blind analysis and only "opening the box" to look at the zerolag candidate gravitational wave events after all tuning has been performed prevents over-tuning, which has the potential to produce false or biased results. Loud events occurring in the playground are still considered as candidate GW events.

There are arguments to be made against strictly adhering to the policy of only opening the box once. The main argument is that a new or improved detection statistic can result in a significantly better search producing tighter upper limits on merger rates and even a direct detection of GWs. Of course, I am inclined to promote this argument — the box was opened for the S6-VSR2/3 high-mass search and the results were published in Reference [17]; and looking for GWs with the multivariate analysis described in Section 8.3 amounts to opening the box twice. However, if a fixed IFAR threshold is used instead of the loudest event statistic, the sensitivity of the two searches can be compared without opening the box twice.

7.10 Criteria for detection

All Category 3 events with an IFAR larger than the tenth loudest Category 3 background coincident event are considered as candidate GW events. Each (or at least the top 10, ordered by IFAR) of these events then goes through a *follow-up* procedure, which includes both automated and human analyses. The follow-up procedure contains the following steps, which are not necessarily done in an exact order:

- Look at the data-quality information at and around the time of the event. Flags that were defined but not used as vetoes could be on and hint at an environmental/instrumental cause of the signal seen in the GW channel. A flag that is on before or after the candidate event can also hint at an environmental/instrumental cause.

- Check that the interferometers were operating normally with a reasonable level of sensitivity around the time of the event. This includes looking in the detector logs for any information that might have

been missed earlier.

- Look at the time-frequency spectrogram of the trigger in the GW channel. A sufficiently loud GW would have a familiar chirp signal (increase in amplitude and frequency as time goes forward); see, for example, Figure 3.14.

- Take a closer look at all the seismic information available for each detector. The Omega pipeline (see Section 4.1.2) is used to identify seismometer channels that are active around the time of the event. Spectrograms of each channel's activity are looked at in order to identify any qualitative differences from the nominal noise. The Kleine-Welle glitch-identification algorithm (see Section 4.1.1) is also run on the seismometer channels. Scatter plots of the Kleine-Welle significance versus time of triggers found in the seismometers are studied, in order to see if the candidate event is coincident with elevated seismic noise at any location along the interferometers. There may be noise in these seismometer channels that was not high enough to produce a data-quality veto, but significant enough to cause a disturbance that propagates through the detector's components.

- For the same reason, check the other environmental channels and look at their spectrograms and scatterplots around the time of the candidate event as we did for the seismometer channels. These include data taken by magnetometers, microphones, accelerometers, radio receivers, temperature sensors, and weather stations around the detector; see Figure 3.7.

- Similarly, look at the instrumental channels' spectrograms and Kleine-Welle significance scatterplots. These include data taken by the IO, COC, COS, SUS, LSC, ASC, SEI, OMC, TCS, CDS, and DAQ subsystems. See Section 3.1.1 for descriptions of these subsystems.

- Check the weekly glitch reports to see if there was any information about the glitchiness of the interferometers that we may have missed.

- Produce a plot of the SNR and χ^2 time-series of the GW candidate event in each detector. A true, loud GW signal would have a large peak at the time of coalescence that is distinct from the level of noise around it. The χ^2 should be symmetric and have a dip at the time of coalescence.

- Look at the signal-based parameters of the candidate event in each detector. This mainly entails seeing how similar in time and mass the triggers were in each detector.

- Look at the bank χ^2 values. However, the calculation of the bank χ^2 was not turned on at the onset of our analysis. The bank χ^2 is described in Reference [128].

- Run a coherent analysis. This was not implemented for our analysis.

- Determine if the candidate is stable against changes in segmentation. If the signal disappears if we change the divisions of the science segments (see Section 7.3), it is likely not due to an astrophysical signal.

- Determine if the candidate is stable against changes in calibration that are consistent with systematic uncertainties.

If the answer to any of the previous steps indicates a clear environmental or instrumental disturbance that caused the signal seen in the GW channel in any of the detectors that were part of the coincidence, the checklist can be abandoned and the candidate event is no longer considered. On the other hand, if there is still a chance that the signal seen is due to a true astrophysical source, a Bayesian parameter estimation procedure is performed to get more accurate mass and spin information about the event; see, for example, Reference [121], Reference [129], Reference [130], and Reference [131]. Additionally, the ringdown and burst search pipelines can be run to see if they also find an event at the same time. We also check to see if there are any electromagnetic triggers around the same time as our candidate event.

7.11 Changes that will be made to this pipeline for Advanced LIGO searches

Several features described in this chapter will be eliminated in future searches for compact binary coalescences in Advanced LIGO data. The first of these is hierarchical part — the second stage was only created because of the fear that we would have too many triggers from the first stage to be able to compute the time-intensive χ^2 veto. With alternative methods of computing a χ^2 statistic, this will no longer be an issue, and eliminating the second stage will make it easier to track the effect of single-detector glitches on the astrophysical results. The second is that a fixed template bank in each detector will be used in the future, which will enable us to require that the exact same template is found in each detector, eliminating the need for the ellipsoidal coincidence test. Both of these changes have been found to have negligible effect on the sensitivity of the search pipeline [132].

Chapter 8

Results of searches for high mass binary signals

We performed a blind search for black hole binary systems with total mass between 25 and 100 $M_{\odot}$ with a loudest event statistic as described in the previous chapter. The data searched over was taken from July 7, 2009 to October 20, 2010 (see Table 7.1 for a detailed list of data taken and Table 7.2 for the total amount of coincident data) — 154.38 days at Category 4 after the removal of playground data). These data are known as S6-VSR2/3 because they were taken during LIGO's science run 6 and Virgo's 2nd and 3rd science runs. The main results of this search are published in Reference [17]. The maximum sensitive distance was 300 Mpc (for an equal-mass system of 40 $M_{\odot}$ total) — almost a billion light years! We did not detect gravitational waves, but we did set a 90% confidence-level upper limit on the rate of black hole binary coalescences as a function of mass; for example, for component masses between 19 and 28 $M_{\odot}$), the upper limit is 3.3×10^{-7} Mpc^{-3}yr^{-1}. Given the total amount of coincident data at Category 4, this translates to 4.17 mergers if the observable volume is taken to be $(300\text{ Mpc})^3$. We also evaluated our efficiency at finding both spinning and non-spinning signals using the FAR of the loudest foreground event as the detection threshold.

8.1 Efficiency at finding simulated gravitational wave signals

Here, efficiency is a measure of the number and distance of found software injections with an IFAR greater than (for Reference [17]) the IFAR of the loudest foreground (zerolag) event. This is in not the same as the efficiency discussed in Section 7.5, where the efficiency was defined simply by the software injections found (above a fixed SNR threshold of 5.5 and passing the χ^2 test) in at least two detectors, using the high-mass analysis pipeline, and the total number and distribution of software injections performed.

When using the loudest event statistic, there is a different IFAR (and thus FAR) threshold for each analysis period and observation time. For S6-VSR2/3, there are 24 of these analysis times (the number of rows, besides the total in Table 7.2. The FAR thresholds for each analysis time are in Table 8.1.

The efficiency of our search is defined by the number of software injections we find with a FAR less

Table 8.1: The false alarm rate of the loudest foreground (zerolag) event ($\widehat{\mathrm{FAR}}$, in events per year) and the expected false alarm rate of the loudest foreground (zerolag) event ($\breve{\mathrm{FAR}}$, in events per year), for each analysis time in S6-VSR2/3. The expected loudest foreground FAR, $\breve{\mathrm{FAR}}$, is simply the inverse of the length of the analysis period, expressed in years.

Analysis period	Observation time	$\widehat{\mathrm{FAR}}$	$\breve{\mathrm{FAR}}$
931035296-935798487	H1, L1	162.90	134.97
	H1, V1	19.97	19.97
	L1, V1	33.08	33.18
	H1, L1, V1	35.23	82.02
937800015-944587815	H1, L1	217.85	227.79
	H1, V1	26.15	15.38
	L1, V1	259.47	121.24
	H1, L1, V1	126.06	69.13
944587815-947260815	H1, L1	67.10	87.47
	H1, V1	225.64	476.42
	L1, V1	251.59	173.14
	H1, L1, V1	52.72	274.71
949449543-953078487	H1, L1	40.05	182.09
953078343-957312087	H1, L1	24.89	31.08
957311943-961545687	H1, L1	119.12	52.11
961545543-965174487	H1, L1	0.947	33.11
956174343-968544087	H1, L1	14.15	60.33
	H1, V1	7.73	1.407
	L1, V1	26.45	131.36
	H1, L1, V1	1.95	54.93
968543943-971622087	H1, L1	620.74	593.46
	H1, V1	70.01	25.53
	L1, V1	110.95	58.90
	H1, L1, V1	22.98	7.40

than the FAR threshold (here, that of the loudest foreground trigger). The efficiency during the course of S6-VSR2/3 can be seen for all the EOBNRv2 injections in Figure 8.1, for all the non-spinning IMRPhenomB injections in Figure 8.2, and for all the spinning IMRPhenomB injections in Figure 8.3. The errors on these efficiencies are binomial counting errors:

$$\sigma_E^2 = \frac{E(1-E)}{N}, \tag{8.1}$$

where E is defined as in Equation (7.24), except in this section I have used total mass bins instead of pairs of component mass bins.

8.2 Null result and search sensitivity/upper limit on astrophysical events

The null result (i.e., the absence of the detection of GWs) was concluded from a search for GWs specifically from systems with total mass between 25 and 100 $M_\odot$, using the search pipeline as described in

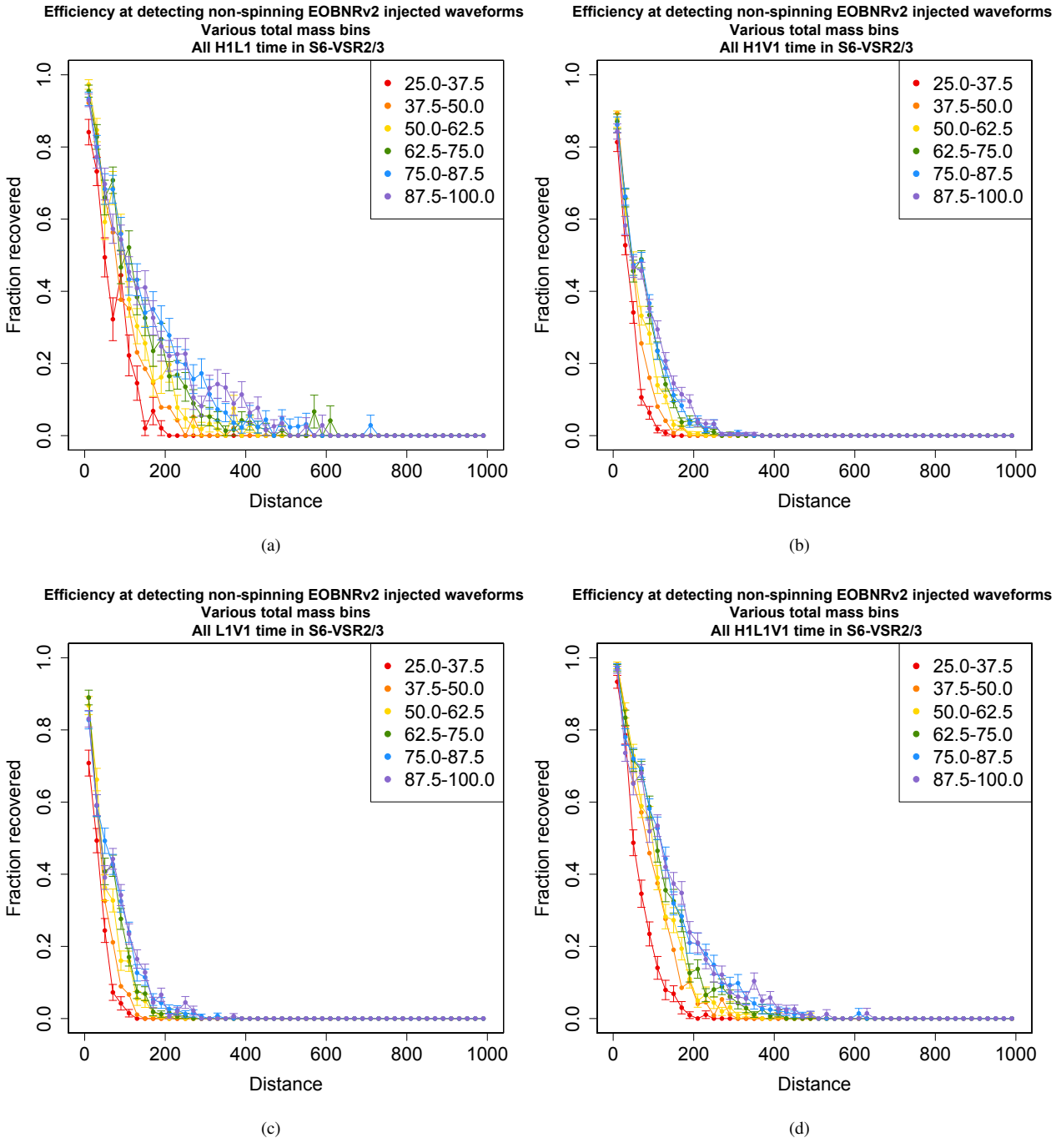

(a) (b) (c) (d)

Figure 8.1: The efficiency at recovering EOBNRv2 injections with a FAR less than that of the loudest foreground event. The colors indicate bins of total mass. 40 distance bins were used. The error bars reflect binomial counting errors. Any bumps at distances greater than 500 Mpc are due to noise triggers in two or more detectors that happen to be coincident with each other and with the injected signal. S6-VSR2/3 data at Category 4.

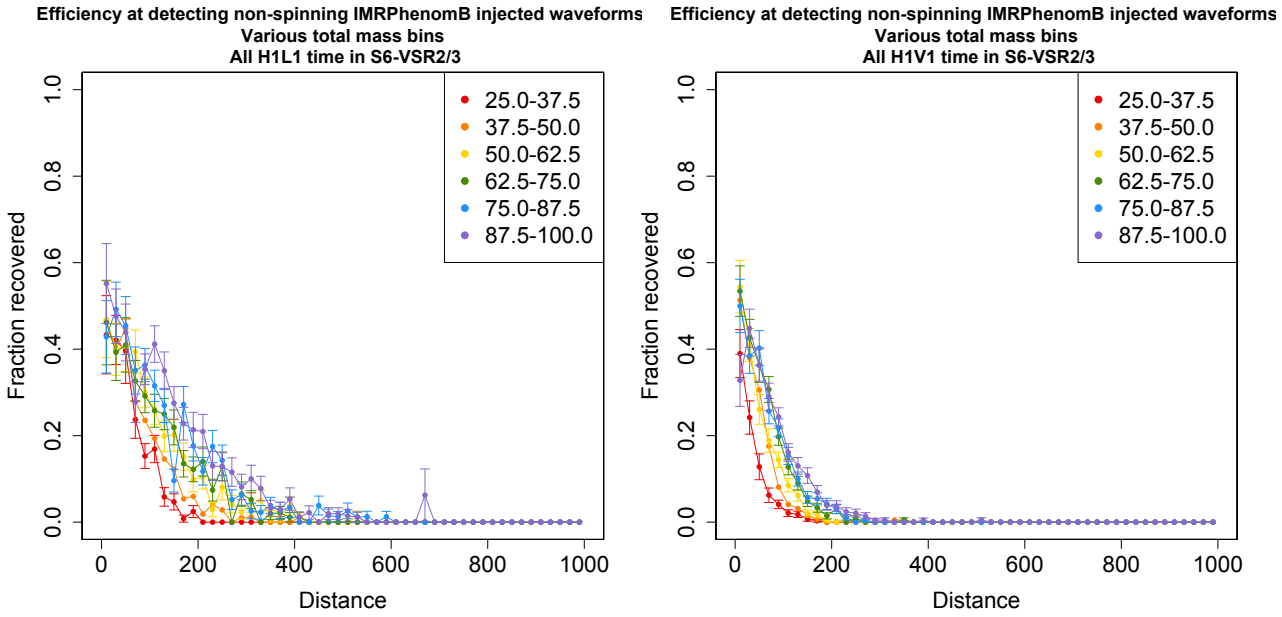

(a)

(b)

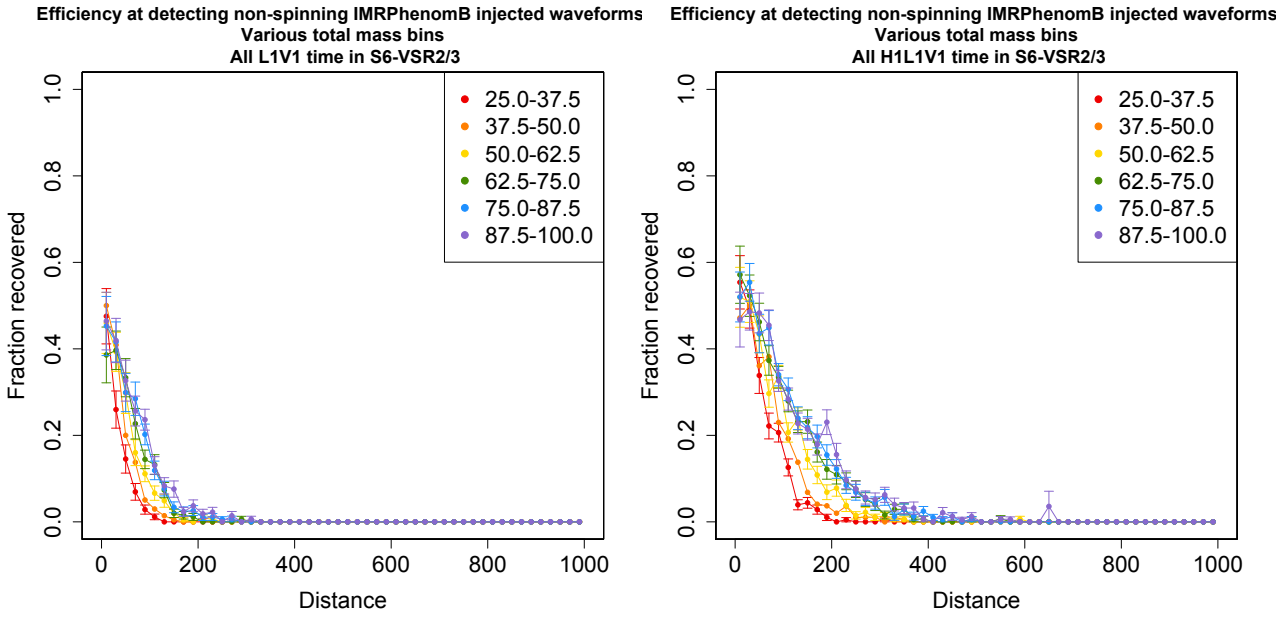

(c)

(d)

Figure 8.2: The efficiency at recovering non-spinning IMRPhenomB injections with a FAR less than that of the loudest foreground event. The colors indicate bins of total mass. 40 distance bins were used. The error bars reflect binomial counting errors. Any bumps at distances greater than 500 Mpc are due to noise triggers in two or more detectors that happen to be coincident with each other and with the injected signal. S6-VSR2/3 data at Category 4.

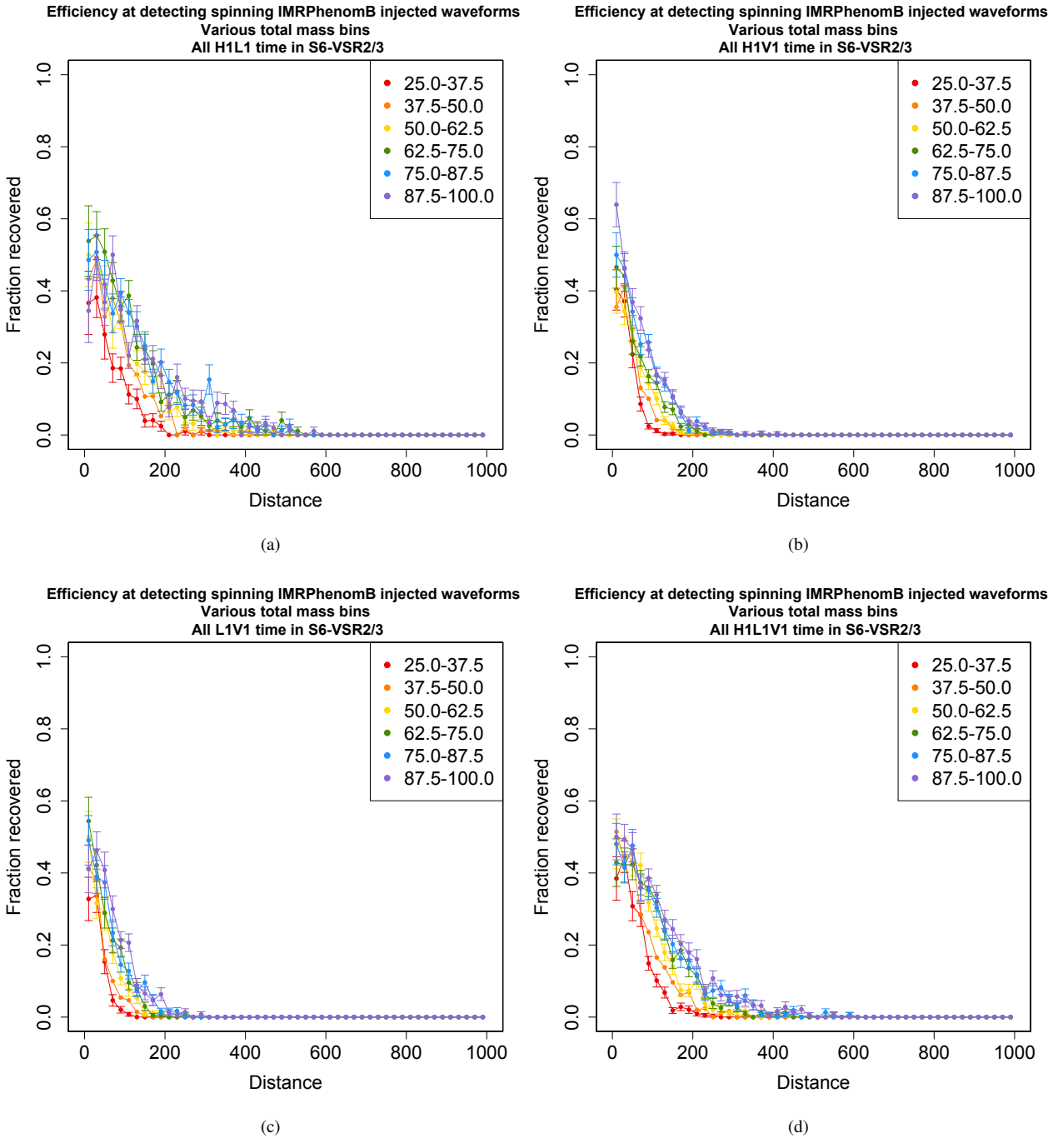

(a) (b) (c) (d)

Figure 8.3: The efficiency at recovering spinning IMRPhenomB injections with a FAR less than that of the loudest foreground event. The colors indicate bins of total mass. 40 distance bins were used. The error bars reflect binomial counting errors. Any bumps at distances greater than 500 Mpc are due to noise triggers in two or more detectors that happen to be coincident with each other and with the injected signal. S6-VSR2/3 data at Category 4.

Chapter 7. The ranking statistic for coincident events produced by the pipeline was the combined ρ_{high}, given by Equation (7.18). In order to compare events from different analysis periods and observation times, this ranking statistic was turned into an inverse false alarm rate (IFAR). The IFAR, our detection statistic, was calculated in the following manner. First, for each analysis period, each observation time is considered separately (remember, the number of analysis periods multiplied by the number of observation times is the number of analysis times: 24). For each analysis time, the candidate GW events from the zerolag, timeslides, and injection runs are split into two groups: those with a minimum template duration (among the templates matched in each detector) less than 0.2 s, and those with a minimum template duration greater than 0.2 s. In the case of H1L1V1 observation time, these groups are further split by the combination of detectors that produced the event — i.e., H1L1, H1V1, L1V1, and H1L1V1. The FAR for each event is equal to the number of timeslide events (in the same analysis time/template duration/detector combination group) with a ranking statistic greater than the event being considered. See Figure 8.4 for a cumulative histogram of the IFARs at this stage. Then, the FARs are combined across the template duration groups and coincident detectors for a single analysis period. This combining process necessitates re-normalizing the FARs. Because some of the groups have lower minimum IFAR values (the vertical lines in Figure 8.4) than others, we normalize by the number of groups with IFARs lower than the old IFAR. See Figure 8.5 for a cumulative histogram of the combined IFARs for a single analysis period.

Cumulative histograms of the IFAR are used as a visual means to identify potential gravitational wave events. Any zerolag event that lies to the right of the grey lines that trace each of the 100 timeslide experiments has a lower FAR than we expect for a background event, given our analysis (i.e., a false alarm probability (FAP) $< 1\%$). Sometimes, however, there is a dearth of timeslide events for a particular detector combination. This will falsely elevate a given zerolag event in the same category. Prior to opening the box, we decided that we will combine the background from an adjacent analysis period if this is the case.

We can see from Figure 8.5 that no foreground (zerolag) events lie to the right of the timeslide distributions; all foreground events are consistent with expected background. The same can be said for the other analysis periods. Thus, no candidate GW events were found with FAP $< 1\%$ in this search.

The calculated combined FARs are then used to calculate the sensitivity of the search and the astrophysical upper limits on the rate of high-mass CBCs, as described in Section 7.8 and Section 7.8.1. The search sensitivities are calculated separately for the EOBNRv2 injections, the spinning IMRPhenomB injections, and the non-spinning IMRPhenomB injections. This is done because each set of waveforms is trusted over a different set of mass ranges. As the EOBNRv2 injections have been checked against numerical relativity for the largest spread of total masses and mass ratios, these are the only injections used for evaluating the upper limit. The upper limit calculation used the S5 results as a prior. Table 8.2 summarizes the sensitivity (in terms of distance) and upper limit results from Reference [17]. Figure 8.6 visualizes the upper limits (left panel) and sensitive distances (right panel) in component-mass space. The sensitive distances in Table 8.2 and the right panel of Figure 8.6 are in good semi-quantitative agreement with the expectations (see Section 2.2.2), which

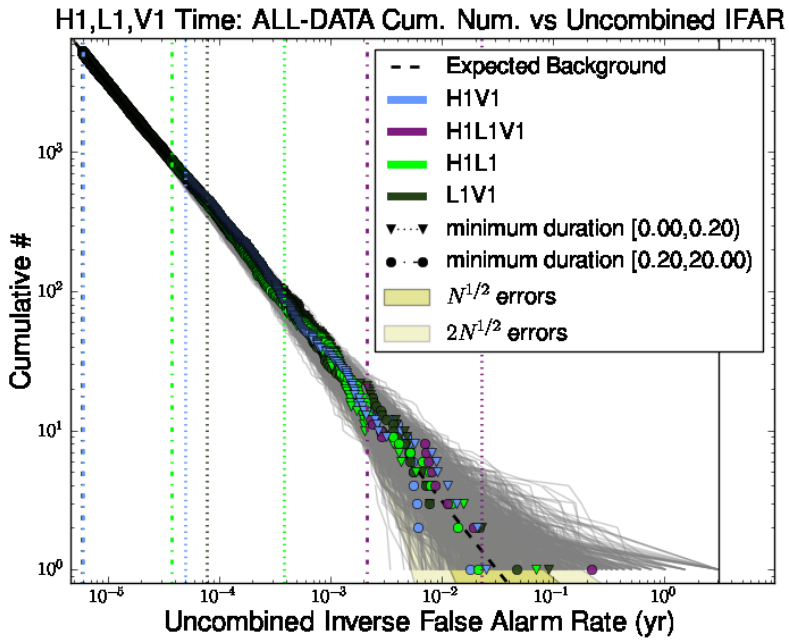

Figure 8.4: A cumulative histogram of the uncombined IFARs for the H1L1V1 observation time of a single analysis period (965174343-3369744). The 100 grey lines trace the cumulative IFARs for each timeslide experiment. The colored dots indicate coincident events for each detector combination involved in the zerolag candidate GW event. The expected background dashed line traces the length of the observation divided by the value on the x-axis (the expected number of events with IFAR greater than or equal to a given IFAR is equal to the length of the observation time divided by the IFAR).

assume Gaussian noise and an SNR threshold of 8. Note that the horizon distances shown in Figure 2.19 are a factor of 2.26 larger than the sensitive distances, since the horizon distance calculation assumes optimally oriented CBCs. IMRPhenomB waveforms can be used to calculate our sensitive distance for CBCs whose component objects are spinning (remember, we restrict ourselves to the cases where the spin vectors of each component object are parallel to each other). The sensitive distance calculated with the IMRPhenomB waveforms is visualized in Figure 8.7 for different total mass and combined spin ranges.

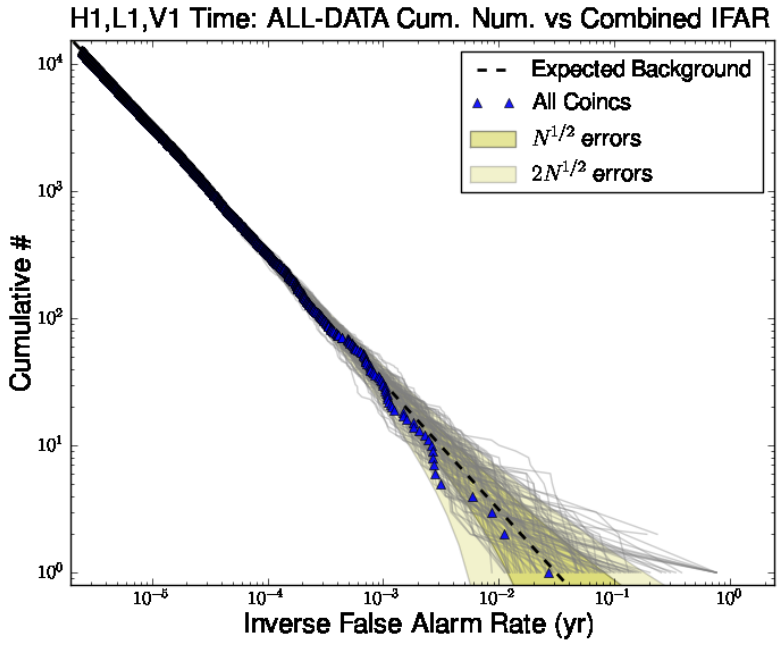

Figure 8.5: A cumulative histogram of the combined (across each group in Figure 8.4) IFARs for the H1L1V1 observation time of a single analysis period (965174343-3369744). The 100 grey lines trace the cumulative IFARs for each timeslide experiment. The colored dots indicate coincident events for all detector combinations involved in the zerolag candidate GW event. The expected background dashed line traces the length of the observation divided by the value on the x-axis (the expected number of events with IFAR greater than or equal to a given IFAR is equal to the length of the observation time divided by the IFAR).

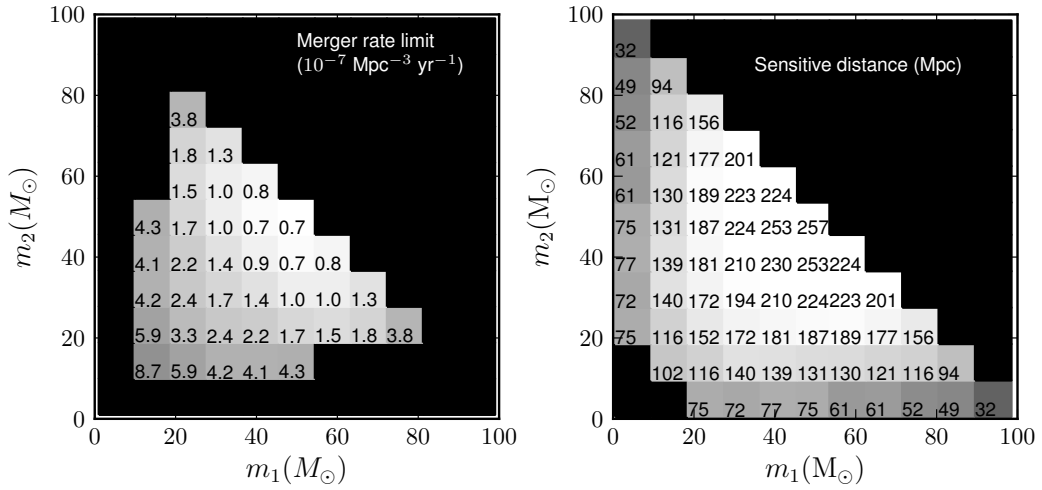

(a) (b)

Figure 8.6: *Left*—Upper limits (90% confidence) on BBH coalescence rates in units of $10^{-7}\mathrm{Mpc}^{-3}\mathrm{yr}^{-1}$ as a function of binary component masses, evaluated using EOBNRv2 waveforms. *Right*—Average sensitive distance for this search to binary systems described by EOBNRv2 signal waveforms, in Mpc [17].

Table 8.2: The search's sensitive distances and coalescence rate upper limits, quoted over $9\,M_\odot$-wide component-mass bins labelled by their central values. We also quote the chirp mass $\mathcal{M}$ at the center of each bin. The sensitive distance in Mpc (averaged over the observation time and over source sky location and orientation) is given for EOBNR waveforms in S5 data rescaled for consistency with NR results [23], and for EOBNRv2, IMRPhenomB non-spinning ("PhenomB nonspin") and IMRPhenomB spinning ("PhenomB spin") waveforms in the S6-VSR2/3 data. The last two columns report 90%-confidence rate upper limits in units of $10^{-7}\,\mathrm{Mpc}^{-3}\mathrm{yr}^{-1}$, for bins with component mass ratios $1 \leq m_1/m_2 \leq 4$, for S5 data (revised relative to [23]) and the cumulative upper limits over S5 and S6-VSR2/3 data, as presented in this work.

Waveforms			EOBNR	EOBNR	PhenomB nonspin	PhenomB spin	EOBNR	EOBNR
Search data			S5	S6-VSR2/3	S6-VSR2/3	S6-VSR2/3	S5	S5 + S6-VSR2/3
m_1	m_2	$\mathcal{M}$	Distance	Distance	Distance	Distance	UL	UL
$(M_\odot)$	$(M_\odot)$	$(M_\odot)$	(Mpc)	(Mpc)	(Mpc)	(Mpc)	$\left(\frac{10^{-7}}{\mathrm{Mpc}^3\,yr}\right)$	$\left(\frac{10^{-7}}{\mathrm{Mpc}^3\,yr}\right)$
14	14	13	81	102	105	106	18	8.7
23	14	16	95	116	126	126	12	5.9
32	14	18	102	140	132	135	8.8	4.2
41	14	21	107	139	141	145	7.8	4.1
50	14	22	107	131	137	149	8.2	4.3
23	23	20	116	152	148	149	7.4	3.3
32	23	24	133	172	172	179	4.9	2.4
41	23	27	143	181	178	183	4.3	2.2
50	23	29	145	187	188	198	3.4	1.7
59	23	32	143	189	188	192	3.2	1.5
68	23	34	140	177	180	191	3.7	1.8
77	23	36	119	156	176	170	5.6	3.8
32	32	28	148	194	190	197	3.4	1.7
41	32	32	164	210	219	220	2.5	1.4
50	32	35	177	224	221	214	1.9	1.0
59	32	38	174	223	221	214	2.0	1.0
68	32	40	162	201	199	210	2.4	1.3
41	41	36	183	230	222	224	1.6	0.9
50	41	39	191	253	253	258	1.4	0.7
59	41	43	194	224	239	236	1.4	0.8
50	50	44	192	257	218	217	1.4	0.7

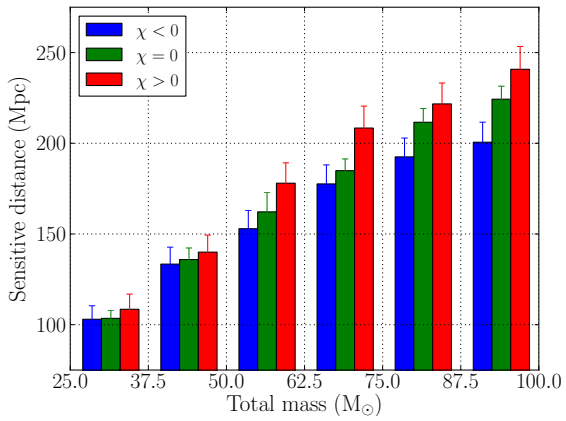

Figure 8.7: Dependence on aligned spin and total mass of the averaged sensitive distance of our search to phenomenological inspiral-merger-ringdown waveforms. For each of 6 bins in total mass M, we show the sensitivity for IMRPhenomB signals with negative aligned spin parameter χ (left), non-spinning signals (centre) and signals with positive aligned spin parameter (right). The simulated signal parameters were restricted to mass ratios between 1 and 4 and aligned spins between -0.85 and 0.85 [17].

8.3 Improvements to the analysis using multivariate statistical classifiers

The detection statistic used in Reference [17] took into account the SNR and χ^2 of each detector in the coincidence (as a direct input to the ranking statistic, ρ_{high}); it also took into account the detectors involved in the coincidence and the minimum duration of the templates found by each detector. However, there are many more pieces of information that could be included in a detection statistic: the mass parameters of the templates found in each detector, other χ^2-like signal-based vetoes, timing accuracy information, and even data-quality information. Each of these dimensions has a distribution of values that greatly overlap between signal and background (see the figures in Section 8.3.1.4). It is difficult and dangerous to try and combine these into a single formula via regression or quantitative analyses. On the other hand, multivariate statistical classifiers are able to take many parameters and return a single number that either classifies or ranks events. Here, the classification problem is to separate signal ("Class 1": either astrophysical or software injection) from background ("Class 0": either accidental coincidences in the foreground or in the timeslides). Remember that each signal or background event is the result of triggers found in coincidence in two or more detectors.

8.3.1 Random forest of bagged decision trees as a classifier trained on signal-based information

I used the random forest of bagged decision trees (RFBDT), as introduced in Section 5.3 and used as one of the classifiers in Chapter 6, to combine the signal-based information from the matched-filter pipeline into a single ranking statistic for high-mass black hole binary coalescences. The data-quality information was not included in this analysis (but may be in future work). The classifier is trained on our estimated background (timeslides) and simulated signals (injections). Once trained, the forest is frozen (it does not change) and can be used to evaluate timeslide, injection, and zerolag events. Here, by evaluate we mean take in the feature vector describing the event and return a single number between 0 and 1, where 0 is more background-like and 1 is more signal-like.

There are many challenges in training a classifier. In the following subsections, I describe several of the challenges specific to my search for high-mass CBCs.

8.3.1.1 Handling the different qualities of the different detector combinations

The first challenge to consider is how to treat the variety of coincidence types — in general, we have H1L1, H1V1, L1V1, and H1L1V1 coincidences (but some analysis periods only have the H1L1 type because V1 was not operating). A deeper subtlety is that some H1L1 coincidences, for example, are from H1L1 observation time, while others are from H1L1V1 observation time. The distinction is important — if V1 is operating, but does not see a trigger at the same time as H1 and L1, there is less trust that the H1L1

coincidence came from an astrophysical event. Of course, we look at all such double coincidences in triple time; different detectors will be oriented differently with respect to the same incoming GW, and thus experience a different amount of strain (see Equation (3.2)). Also, the sensitivity as a function of frequency is different in each of the three detectors. After careful consideration, I decided to train different classifiers on different double combinations — for a single analysis period I train three classifiers, one each for H1L1, H1V1, and L1V1 coincidences. H1L1V1 coincidences are split into their constituent doubles, and the ranks are recombined at a later time (see Section 8.3.1.5). This solves two problems. First, the coincidences from different types of doubles have a different character due to the different sensitivities and orientations of the instruments; training each type of double with a different classifier allows us to use this to our advantage. Second, we have many fewer triply-coincident timeslide events than triply-coincident found injections (as we should, since timeslide coincidences are purely due to random chance); this imbalance would make training a classifier to separate triply-coincident signals from triply-coincident background difficult, since we have so few triply-coincident background events. However, we would still like to place a premium importance on the triply-coincident events, since our ideal detection would be a triple coincidence. Therefore, I include a dimension that reflects this; see Section 8.3.1.4.

8.3.1.2 Choosing good examples of signal and background for our training sets

The second challenge is that (as we have not yet detected any gravitational waves) we can only create our Class 1 samples by injecting simulated signals into the gravitational-wave data. We find these coincident triggers with the exact same search pipelines and algorithms we use to search for gravitational waves (see Section 7.3). A found injection is defined by a time coincidence between such a coincident trigger and the injected signal (see Section 7.5). The coincidence window used in the published search (Reference [17]) was 1 s. However, this is a large window, considering that the window for coincidence between detectors is (2x timing accuracy of a single detector ($\sim$ 1 ms) + light travel time of the Earth's diameter (42.5 ms)), which is less than 0.2 s. There is a chance that an accidental coincidence of noise between two detectors happens within 1 s of an injected signal; this results in injections misidentified as found. We do not want to use any misidentified injections in our training sets, as they will taint the purity of our training set. For the purposes of training our classifier, we want to create a set of *well-found* injections. To do this, I shrink the window between the coincidence found in the detectors and the injected signal to 10 ms.

In addition, we cross-check the list of triggers found in the gravitational-wave data for a single detector with the list of injected signals. If the trigger identified via coincidence as the trigger associated with the injection existed prior to the injection of the simulated signal, we remove it from our list of well-found injections. Since it existed prior to the injection, we can be sure that it was only found in time coincidence with the injection due to unlucky timing. Leaving "found" injections like this in our training set leads to the association of noise triggers in the gravitational-wave data with Class 1 events, despite them almost certainly being part of Class 0.

8.3.1.3 Round-robin procedure for training and evaluating the performance of the classifier

Each forest is trained on timeslides and injections as representative samples of our background and signal. The trained forest can then be used to evaluate our zerolag (foreground) triggers. However, it is important to evaluate the efficiency of the forest at classifying signal and background on our known samples of signal and background (our injections and timeslides). In order to have the smallest errors on the classification efficiency, we would like to evaluate each of our injections with a forest. In addition to evaluating our efficiency at classifying, we would like to evaluate our efficiency in terms of the volume of sky we are sensitive to, as well as use the timeslides and injections for upper limit statements (see Section 7.8.1). In fact, the upper limit procedure depends on the value of the detection statistic for all timeslides.

This brings us to our third challenge — how to use all of our timeslides and injections for training the forest (the more training samples, the better the predictive power of a classifier), but also rank all of our timeslides and injections without evaluating an event with a forest that was trained on itself. Evaluating an event with a forest that was trained with it leads to inflated estimates of efficiency and fewer instances of falsely identifying a background trigger as a signal than reality would suggest. In order to both train and evaluate with all events, yet not have any event evaluated with a forest that was trained on itself, we employ a round-robin procedure. Samples are separated into K subsets of roughly equal size. To classify events in the k^{th} subset, we use a forest trained on all but the k^{th} subset. In this way, we ensure that training and evaluation are done with disjoint sets so that any over-training that might occur does not bias our results. We choose $k = 10$, which means that 90% of the events of known class are used to train a forest. The 10% of events not included in that subset are then evaluated by that forest. This process is repeated 10 times until all events of known class have been evaluated with a forest that was not trained using themselves. Increasing k brings marginal benefit in that more events are used to train each forest, but also increases computational cost.

There is an added complexity due to the fact that we train only with the well-found injections, but must evaluate all of the injections found by the original search pipeline in order to do a true comparison of the methods. To do this, we order all of our well-found injections by GPS time and divide this list into 10 parts. The times marking the boundaries between the 10 parts are stored and then used to divide the original found injections into the 10 sets. This ensures that a found injection that is simply a poorly-found copy of the well-found injection will not be evaluated by a forest that was trained with the well-found injection.

8.3.1.4 Inputs to the classifier

Each RFBDT contains $n = 100$ trees. Each branch on each tree is set to randomly choose $s = 6$ elements of the input vector for splitting (see Section 5.3.2). At each branching point, various thresholds are tested on each of these 6 elements, and the best threshold/element combination is chosen to split on. The branches turn into leaves when the branching point has only $l = 5$ events on it, or when the criterion for optimization can no

longer be improved. The trees are set to stop creating new branches when the node (which becomes a leaf) has only 5 training events on it. The figure of merit for splitting is the cross-entropy (see Section 5.3.2.1). These RFBDT parameters were all chosen by trial and comparisons of the receiver operating characteristic (ROC) curve, which plots the efficiency (software injections identified as signal) versus the false alarm fraction (timeslides identified as signal). Sometimes choices resulting in moderate improvements in the ROC curve were not used because they did not merit the increase in compute time, which is on the order of $nsN \log N$, where N is the number of events in the training set [106]. Each training and evaluation event is described by a feature vector, whose dimensions include:

- ethinca (see Section 7.3.4 and Figure 8.8),
- dt, the absolute value of the difference in arrival time (see Figure 8.9),
- relative difference in chirp mass between the two detectors in the coincidence (see Equation (7.1) and Figure 8.10),
- relative difference in eta (see Equation (7.2) and Figure 8.11),
- SNR in first detector (see Equation (2.23) and Figure 8.12),
- SNR in second detector (see Equation (2.23) and Figure 8.13),
- χ^2 in the first detector (see Equation (7.14) and Figure 8.14),
- χ^2 in the second detector (see Equation (7.14) and Figure 8.15),
- effective SNR in first detector (see Equation (7.16) and Figure 8.16),
- effective SNR in second detector (see Equation (7.16) and Figure 8.17),
- the r^2 duration in the first detector (see following paragraph and Figure 8.18),
- the r^2 duration in the second detector (see following paragraph and Figure 8.19),
- continuous χ^2 in the first detector (see the following paragraph and Figure 8.20),
- continuous χ^2 in the second detector (see the following paragraph and Figure 8.21),
- the combined ρ_{high} SNR of the coincidence (this is the combined effective SNR of the triple coincidence if the double being considered by the forest was originally part of a triple coincidence) (see Equation (7.19) and Equation (7.20) and Figure 8.22).

The r^2 veto duration and continuous χ^2 values are calculated for each trigger during the high-mass pipeline, but are not used in the standard analyses described in Section 7.3. The r^2 veto duration measures the amount of time that Ξ (see Equation (7.15)) is above 0.0002, within 6 s of the trigger [125]. The

continuous χ^2 performs a sum of squares of the residual of the SNR time series and the autocorrelation time series of a single detector trigger.

It is important not to include dimensions that can improve our efficiency at classifying our injected simulated signals, but would not help in identifying true astrophysical GW signals. This is why the raw values of the matched mass parameters are not included — we choose injections that span the mass space of the high-mass search, but these are not informed by astrophysical priors. Similarly, this is why the number of detectors involved in the coincidence is not used — the fraction of injections found in triple coincidence so exeeds the fraction of timeslides found in triple coincidence, it could almost be considered an artificial improvement in efficiency.

Yet I include the SNRs, for which the distribution for injections is artificially louder than that of the background (see Figure 8.12, Figure 8.13, Figure 8.16, Figure 8.17, Figure 8.22. These distributions are the result of choices made in Section 7.5, where the main goal was to make sure the injections covered the mass space over which we would be setting rate upper limits.

Similarly, the distribution of χ^2 for the injections has an excess of large values. This is because the SNR time-series of a loud trigger is likely to get a large χ^2 value, as described in Section 7.3.6; see Figure 8.23.

Dimensions such as the r^2 duration do not look that useful; see Figure 8.18 and Figure 8.19. The r^2 duration was constructed as a signal-based veto for a low-mass search. Its thresholds were not tuned for the high-mass search. Though not used as a veto, it was calculated by the analysis pipeline. Though it is not helpful, it does not hurt to include it — as was shown in Figure 6.1, the inclusion of superfluous dimensions does not tend to harm the RFBDT.

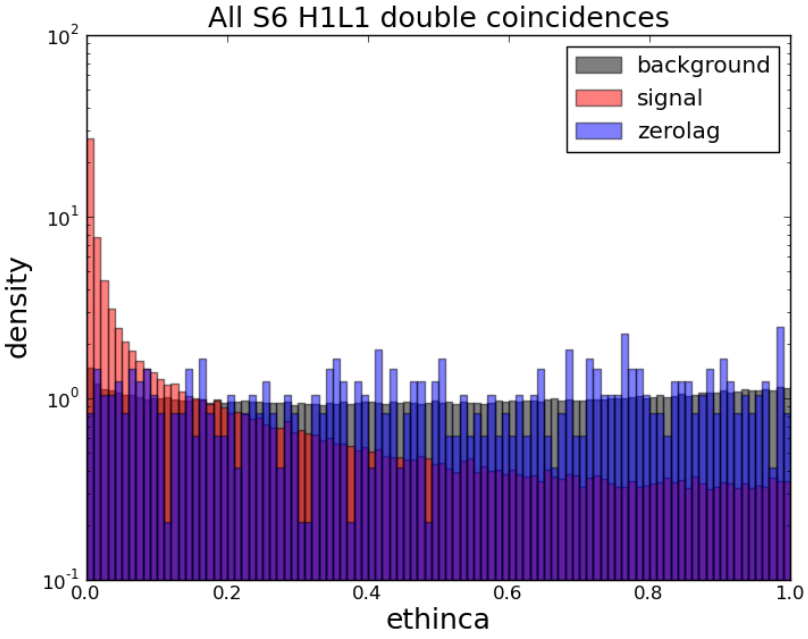

Figure 8.8: Normalized histograms of the distribution of the ethinca values for all coincidences involving H1 and L1 in S6 for timeslides (black), signal (red), and zerolag (blue). The color bars are transparent, so the overlap of the distributions can be seen. The data were all S6 Category 4 coincidences involving H1 and L1.

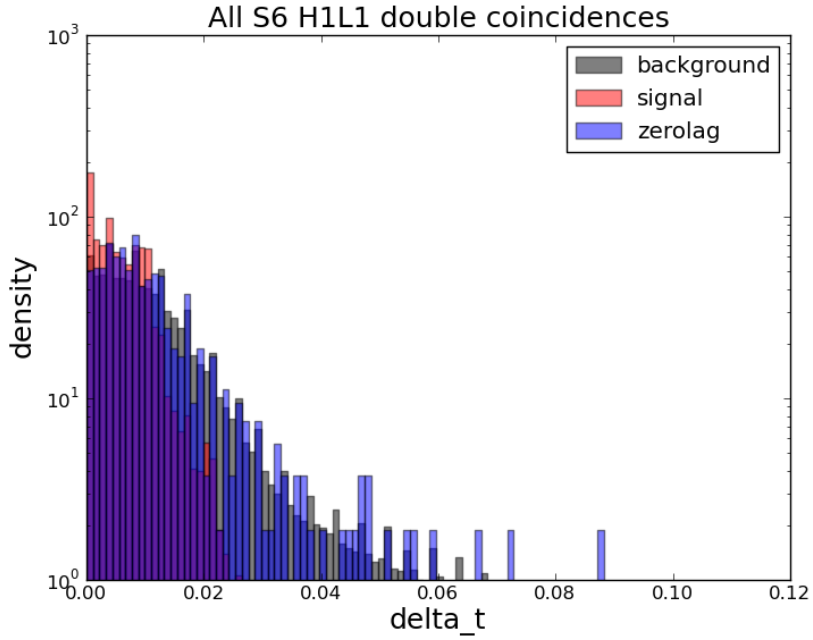

Figure 8.9: Normalized histograms of the distribution of the absolute difference in coalescence times between H1 and L1 for all coincidences involving H1 and L1 for timeslides (black), signal (red), and zerolag (blue). The color bars are transparent, so the overlap of the distributions can be seen. The data were all S6 Category 4 coincidences involving H1 and L1.

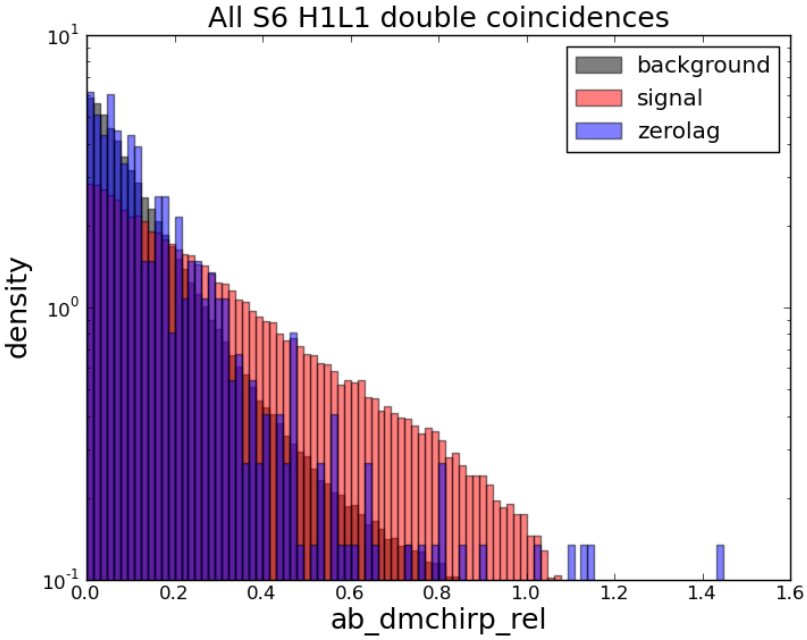

Figure 8.10: Normalized histograms of the distribution of the relative difference in chirp mass between H1 and L1 for all coincidences involving H1 and L1 for timeslides (black), signal (red), and zerolag (blue). The color bars are transparent, so the overlap of the distributions can be seen. The data were all S6 Category 4 coincidences involving H1 and L1.

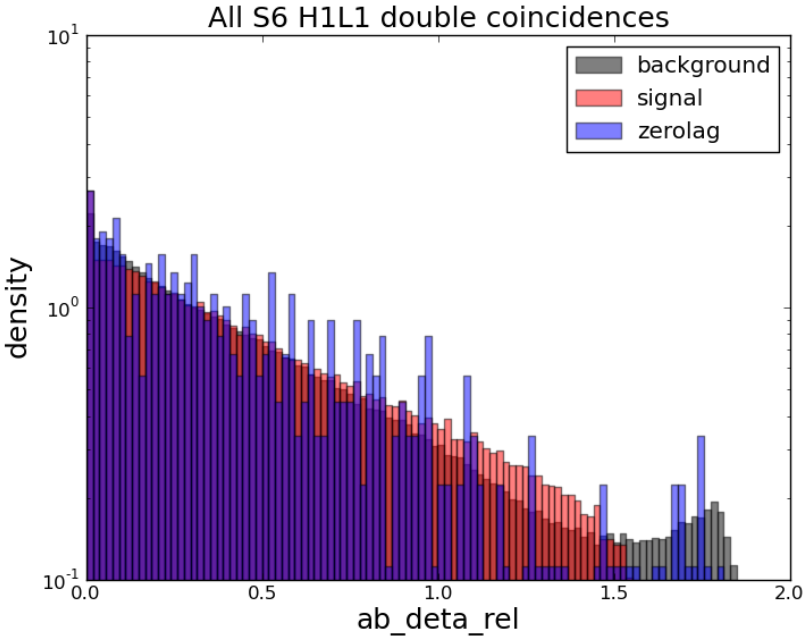

Figure 8.11: Normalized histograms of the distribution of the relative difference in the symmetric mass ratio between H1 and L1 for all coincidences involving H1 and L1 for timeslides (black), signal (red), and zerolag (blue). The color bars are transparent, so the overlap of the distributions can be seen. The data were all S6 Category 4 coincidences involving H1 and L1.

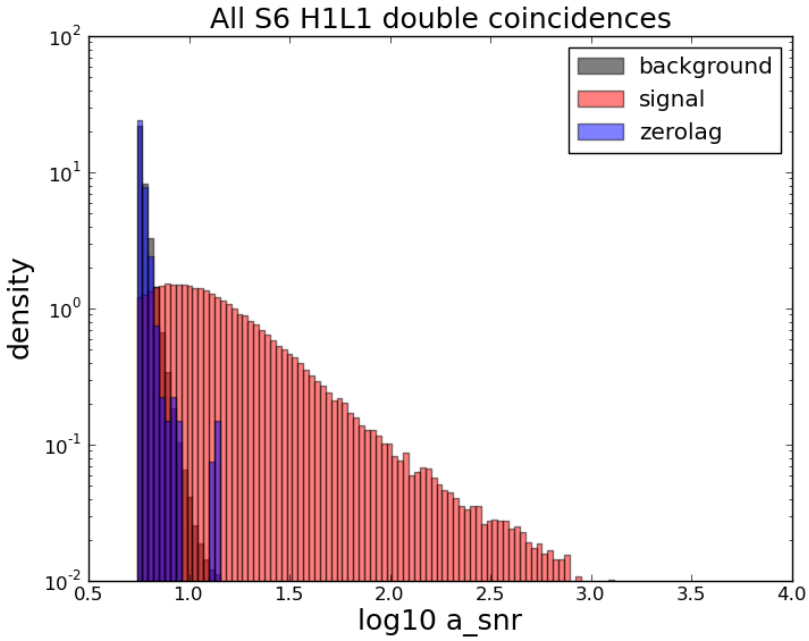

Figure 8.12: Normalized histograms of the distribution of the SNR in H1 for all coincidences involving H1 and L1 for timeslides (black), signal (red), and zerolag (blue). The color bars are transparent, so the overlap of the distributions can be seen. The data were all S6 Category 4 coincidences involving H1 and L1.

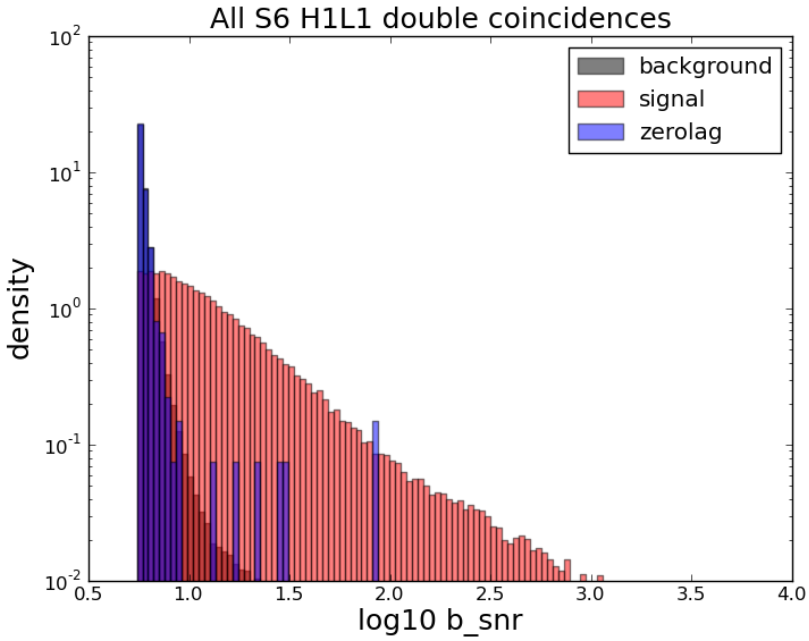

Figure 8.13: Normalized histograms of the distribution of the SNR in L1 for all coincidences involving H1 and L1 for timeslides (black), signal (red), and zerolag (blue). The color bars are transparent, so the overlap of the distributions can be seen. The data were all S6 Category 4 coincidences involving H1 and L1.

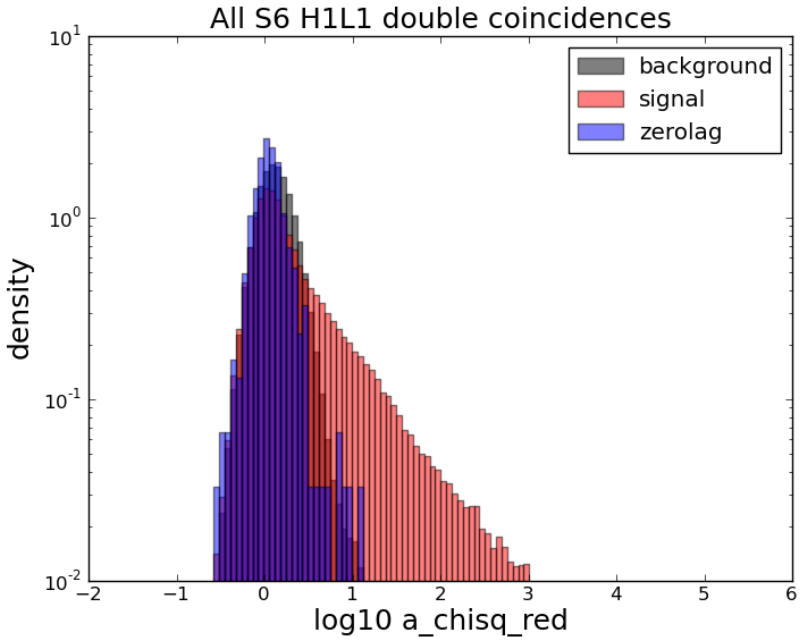

Figure 8.14: Normalized histograms of the distribution of the reduced χ^2 in H1 for all coincidences involving H1 and L1 for timeslides (black), signal (red), and zerolag (blue). The color bars are transparent, so the overlap of the distributions can be seen. The data were all S6 Category 4 coincidences involving H1 and L1.

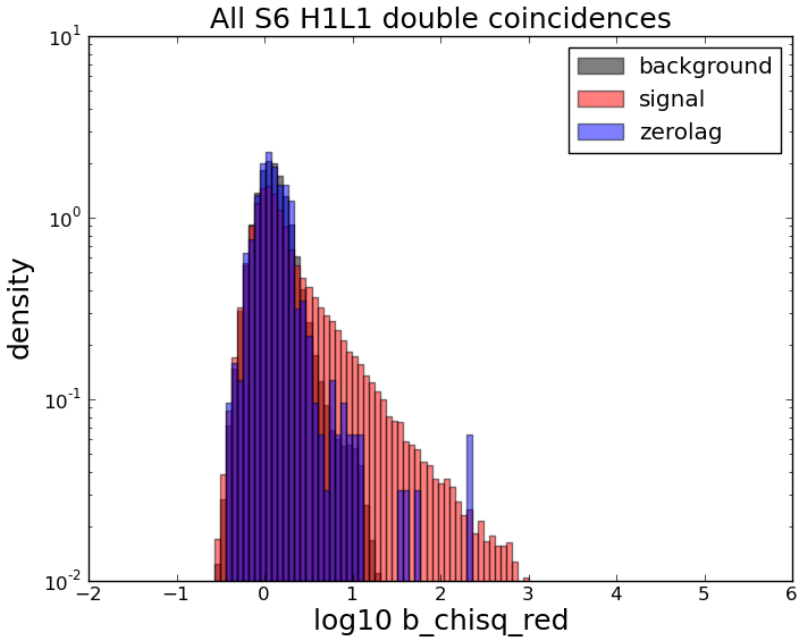

Figure 8.15: Normalized histograms of the distribution of the reduced χ^2 in L1 for all coincidences involving H1 and L1 for timeslides (black), signal (red), and zerolag (blue). The color bars are transparent, so the overlap of the distributions can be seen. The data were all S6 Category 4 coincidences involving H1 and L1.

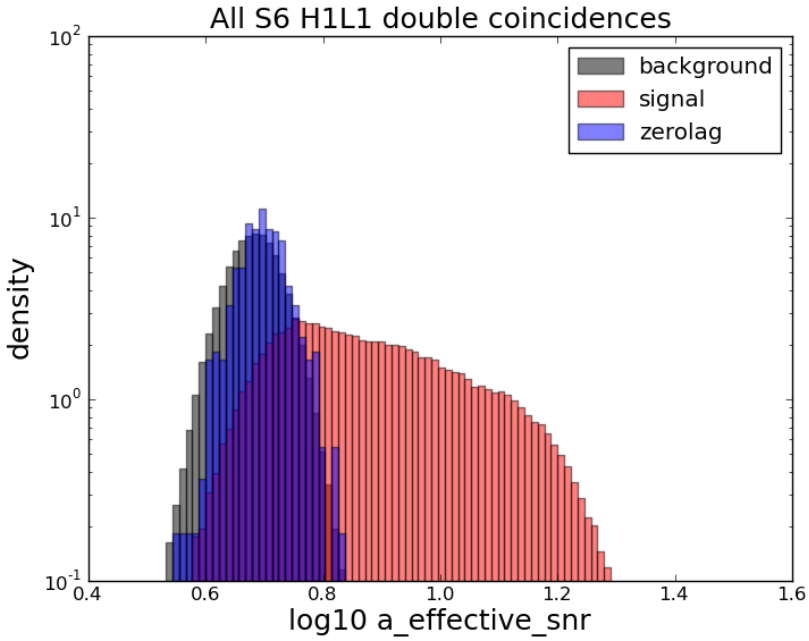

Figure 8.16: Normalized histograms of the distribution of the effective SNR in H1 for all coincidences involving H1 and L1 for timeslides (black), signal (red), and zerolag (blue). The color bars are transparent, so the overlap of the distributions can be seen. The data were all S6 Category 4 coincidences involving H1 and L1.

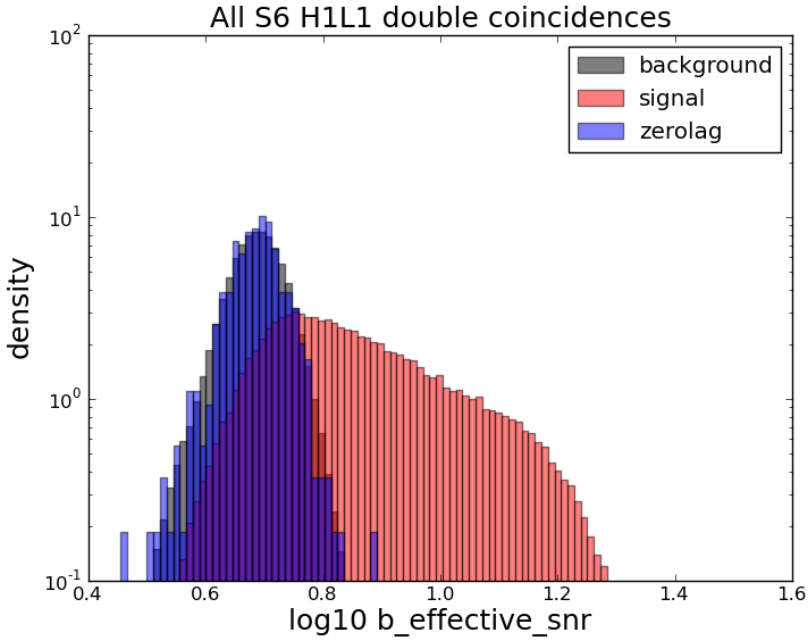

Figure 8.17: Normalized histograms of the distribution of the effective SNR in L1 for all coincidences involving H1 and L1 for timeslides (black), signal (red), and zerolag (blue). The color bars are transparent, so the overlap of the distributions can be seen. The data were all S6 Category 4 coincidences involving H1 and L1.

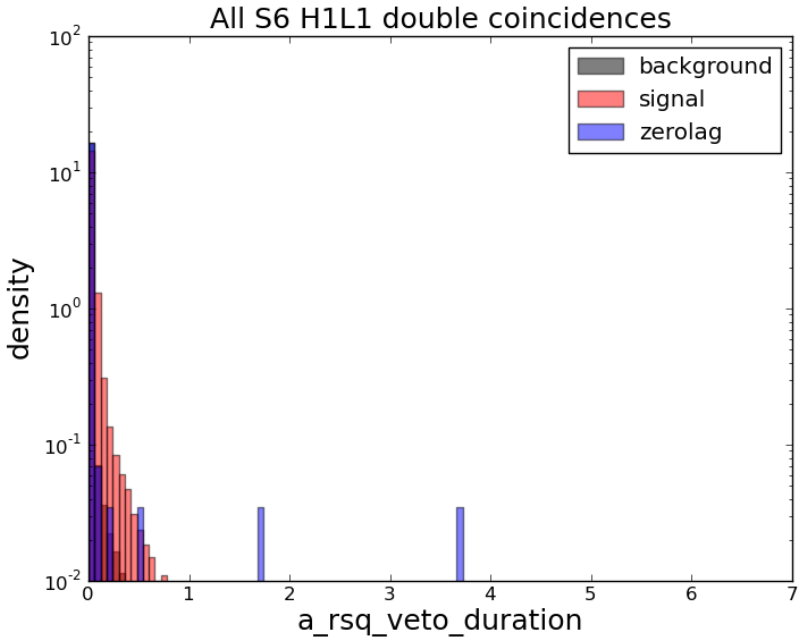

Figure 8.18: Normalized histograms of the distribution of the r^2 veto duration in H1 for all coincidences involving H1 and L1 for timeslides (black), signal (red), and zerolag (blue). The color bars are transparent, so the overlap of the distributions can be seen. The data were all S6 Category 4 coincidences involving H1 and L1.

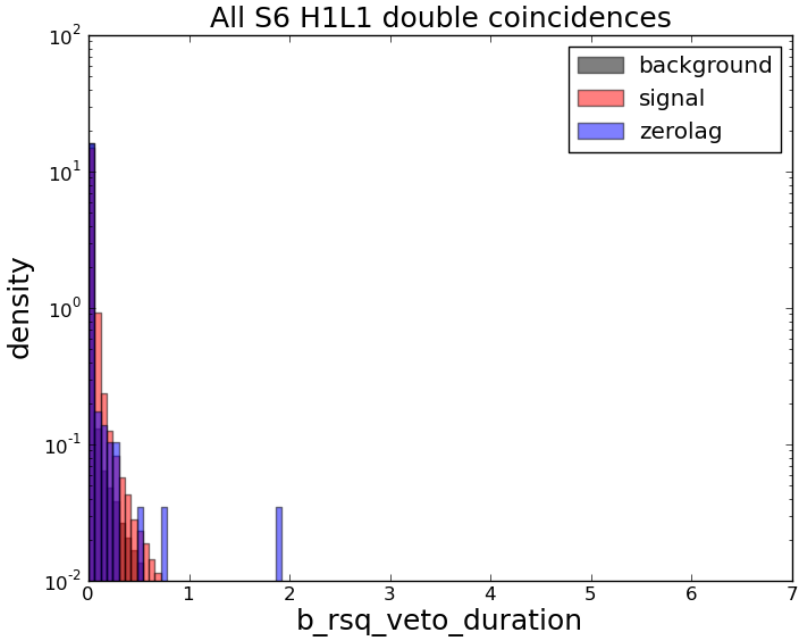

Figure 8.19: Normalized histograms of the distribution of the r^2 veto duration in L1 for all coincidences involving H1 and L1 for timeslides (black), signal (red), and zerolag (blue). The color bars are transparent, so the overlap of the distributions can be seen. The data were all S6 Category 4 coincidences involving H1 and L1.

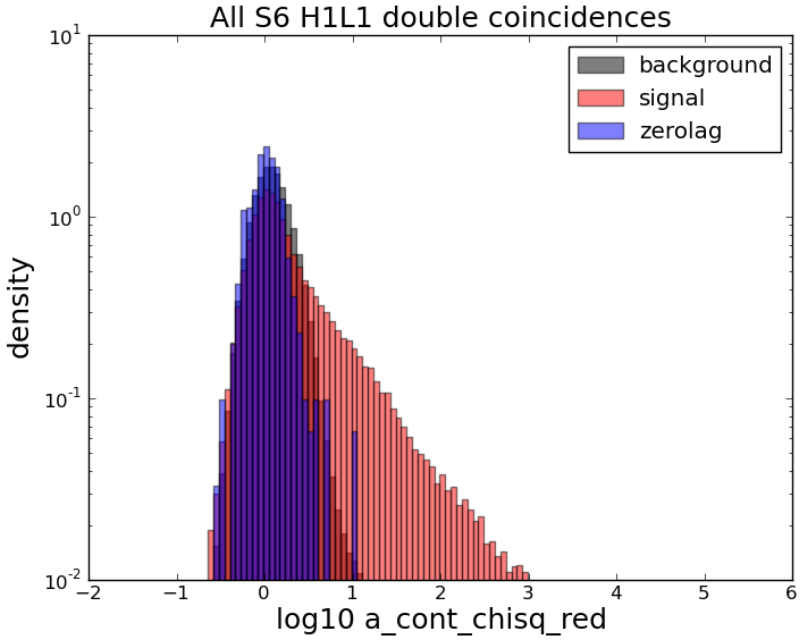

Figure 8.20: Normalized histograms of the distribution of the reduced continuous χ^2 in H1 for all coincidences involving H1 and L1 for timeslides (black), signal (red), and zerolag (blue). The color bars are transparent, so the overlap of the distributions can be seen. The data were all S6 Category 4 coincidences involving H1 and L1.

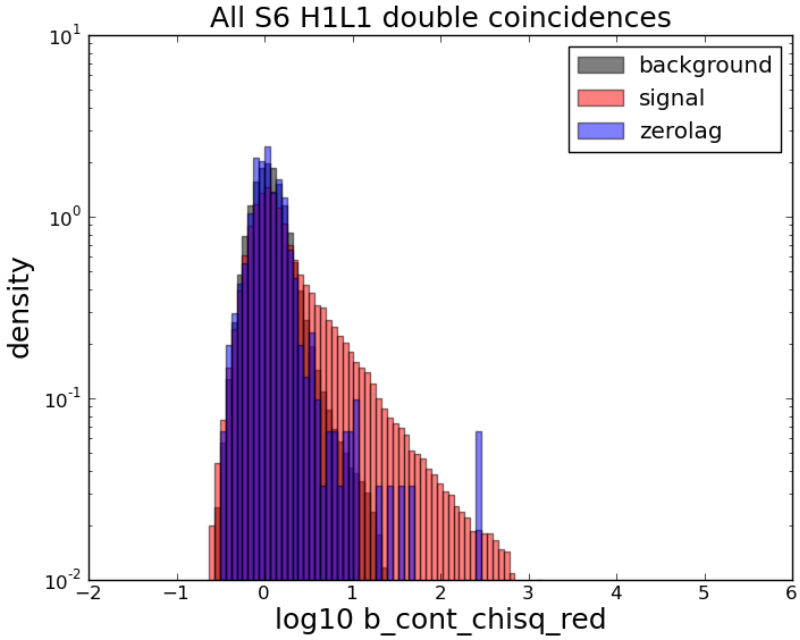

Figure 8.21: Normalized histograms of the distribution of the reduced continuous χ^2 in L1 for all coincidences involving H1 and L1 for timeslides (black), signal (red), and zerolag (blue). The color bars are transparent, so the overlap of the distributions can be seen. The data were all S6 Category 4 coincidences involving H1 and L1.

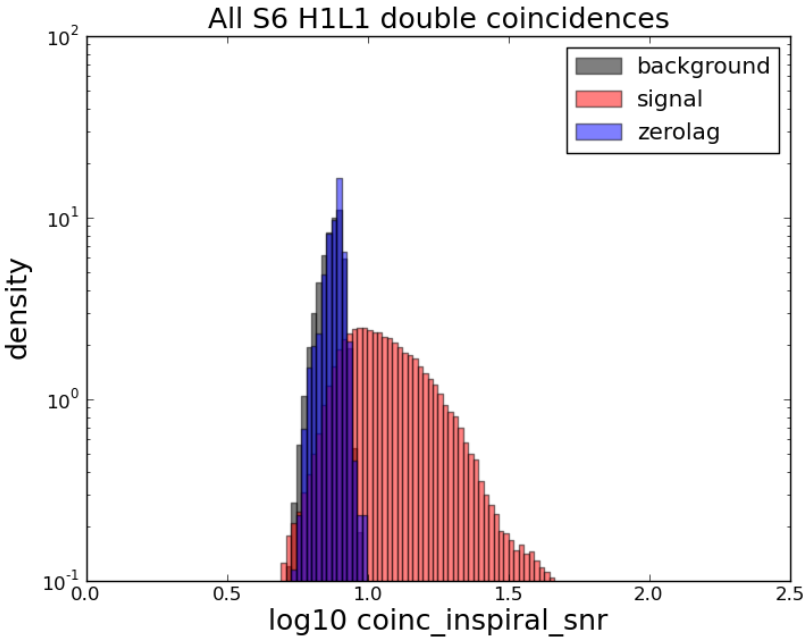

Figure 8.22: Normalized histograms of the distribution of ρ_{high} for timeslides (black), signal (red), and zerolag (blue). ρ_{high} has been added in quadrature for all the detectors in the coincidence, which is sometimes just H1 and L1, but sometimes also includes V1. The color bars are transparent, so the overlap of the distributions can be seen. The data were all S6 Category 4 coincidences involving H1 and L1.

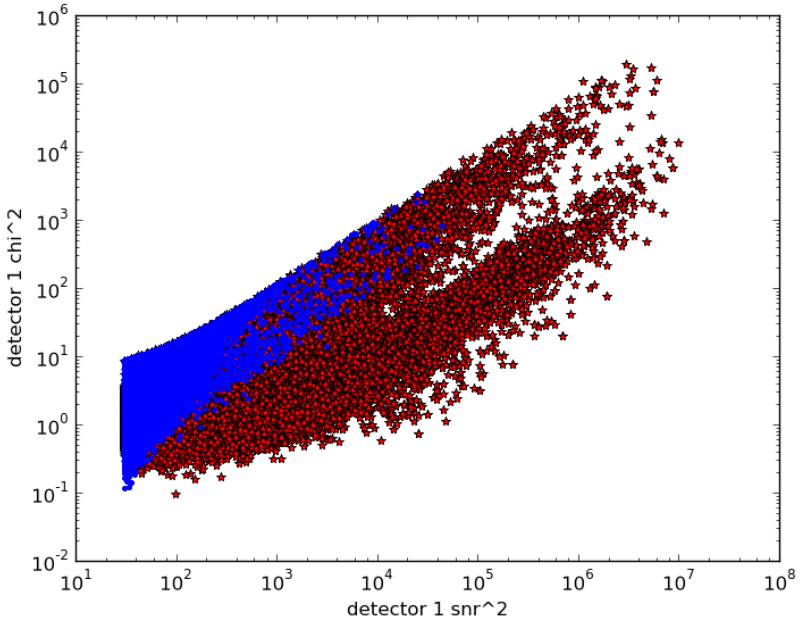

Figure 8.23: H1 χ^2 versus H1 ρ^2. Red stars: all found injections (signal). Blue points: all timeslides (background). The data were all S6 Category 4 coincidences involving H1 and L1.

8.3.1.5 Turning the classifier output into a detection statistic

Each of the 9 analysis times (see Table 7.1) is considered separately, as in the high-mass pipeline. For each analysis time, for each combination of two detectors in S6-VSR2/3 — H1L1, H1V1, L1V1 — I train 10 trained forests (one for each iteration of the round-robin) on the timeslides and injections. Each of these trained RFBDTs is saved, and the timeslides and injections from the corresponding round-robin events are evaluated with the saved forest. The foreground (zerolag) events are evaluated with one of the forests.

Each event ranked by a forest is returned a rank in a completely deterministic manner. As the ranks range from 0 to 1, they could loosely be considered probabilities of being signal. This allows us to turn the rank into a likelihood ratio:

$$\mathcal{L}_{\mathrm{MVSC}}^{\mathrm{double}} = \frac{r}{1-r}, \tag{8.2}$$

where r is the rank given to an event by the trained RFBDT. For triples, which are split into three sets of doubles for training and evaluation, we multiply the likelihood ratios:

$$\mathcal{L}_{\mathrm{MVSC}}^{\mathrm{triple}} = \mathcal{L}_{\mathrm{MVSC}}^{\mathrm{H1L1}} \times \mathcal{L}_{\mathrm{MVSC}}^{\mathrm{H1V1}} \times \mathcal{L}_{\mathrm{MVSC}}^{\mathrm{L1V1}}. \tag{8.3}$$

This $\mathcal{L}_{\mathrm{MVSC}}$ is the new ranking statistic for the search, analogous to the combined ρ_{high} in Section 7.6. As we did in Section 7.7, we can calculate FARs of each event based on the distributions of $\mathcal{L}_{\mathrm{MVSC}}$ for timeslides. Here, at first pass, the FAR is calculated separately for each analysis time, and only if the observation time is H1L1V1 do we further split the events into two categories — those from double coincidences and those from triple coincidences. Thus, only the FARs from triple time need to be combined and re-normalized.

8.3.1.6 Efficiency and sensitivity comparisons between the RFBDT analysis and the standard analysis

The multivariate analysis described in this chapter can be compared to the published result in Reference [17] without opening the box — by choosing a different FAR threshold for calculating the sensitivity, rather than the loudest event statistic described in Section 7.8. For example, we can choose the expected loudest FAR:

$$\breve{\mathrm{FAR}} = \frac{1}{T}, \tag{8.4}$$

where T is the total livetime of the analysis chunk being considered with Category 4 vetoes applied and playground time removed. The rightmost column of Table 8.1 lists these new FAR thresholds. Since these thresholds differ from the thresholds used in Section 8.1 and Section 8.2 (listed in the penultimate column in Table 8.1), I recalculate the efficiency and sensitivity for the original search with the combined ρ_{high} statistic using these expected far thresholds in order to make a fair comparison between the methods.

In Figure 8.24 the efficiency at finding EOBNRv2 signals in various groups of total mass is compared for FARs calculated with MVSC-based ranking statistic and FARs calculated with the combined ρ_{high} statistic,

both using a FAR threshold at the expected loudest event. Though the curves are similar, in the MVSC case, each curve is a bit higher. In Figure 8.25, the efficiency is compared for the IMRPhenomB injections; only those with mass ratios between 1 and 4 are considered. The improvement for the IMRPhenomB-calculated efficiency using MVSC is not as strong as the EOBNRv2-improvement.

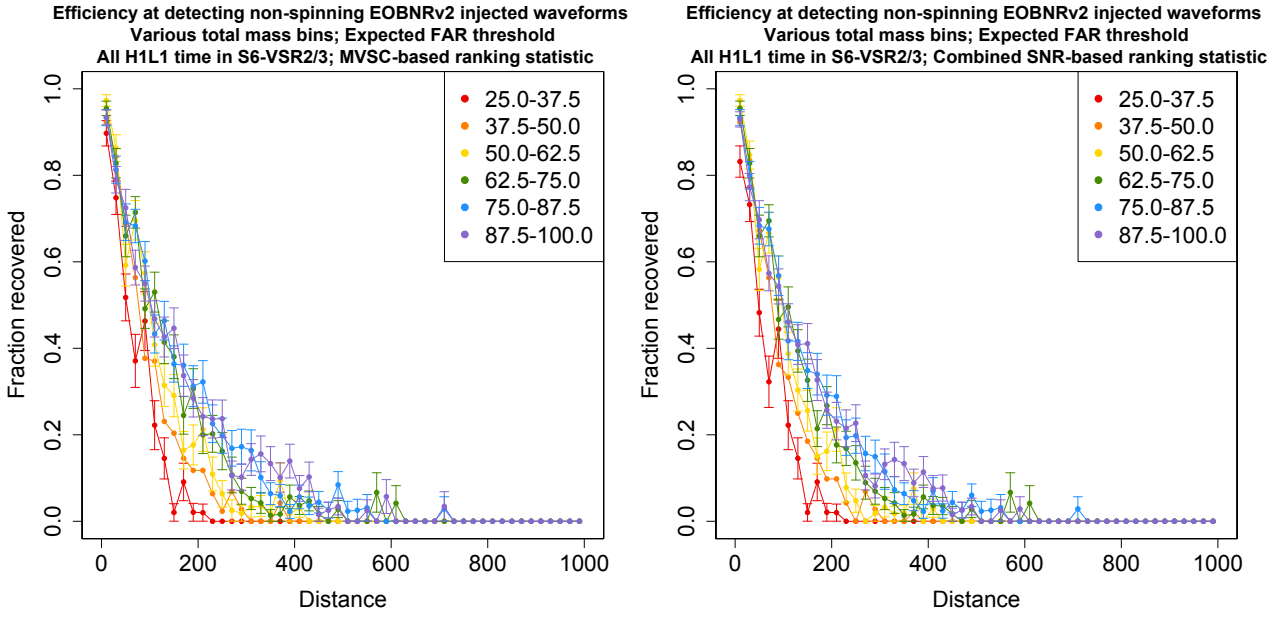

(a) (b)

Figure 8.24: The efficiency at recovering EOBNRv2 injections with a FAR less than that of the expected loudest foreground event. The top panel uses FARs calculated from the MVSC result, as described in Section 8.3.1.5. The bottom panel uses FARs calculated from ρ_{high}, given by Equation (7.18); compare to Figure 8.1, which used the loudest foreground event instead of the expected loudest. The colors indicate bins of total mass, as expressed in $M_{\odot}$. 40 distance bins were used. The error bars reflect binomial counting errors. Any bumps at distances greater than 500 Mpc are due to noise triggers in two or more detectors that happen to be coincident with each other and with the injected signal. S6-VSR2/3 data at Category 4.

The EOBNRv2 injections were used to re-calculate the search's VT sensitivity (as these were the injections used to calculate the upper limits in Section 8.2), using the expected loudest foreground event's FAR as the threshold. Figure 8.26 visualizes the relative improvement of the multivariate statistical classification method. The raw values of the sensitivities for each method are shown in Figure 8.27, Figure 8.28, Figure 8.29, Figure 8.30.

The sensitive distances of the searches can also be compared. As sensitive distance is a strong function of mass, the sensitive distances for various component mass pairs are listed in Table 8.3. When using the multivariate statistical classifier to calculate the ranking statistic, the sensitive distance is consistently higher than when using the combined high-mass SNR statistic. The sensitive distances are again compared to each other, along with the sensitive distances from Table 8.2, and the expected sensitivity based on the discussion in Section 2.2.2, in Figure 8.31 (component mass ratio of 1), Figure 8.32 (component mass ratio of 0.6 to 0.8),

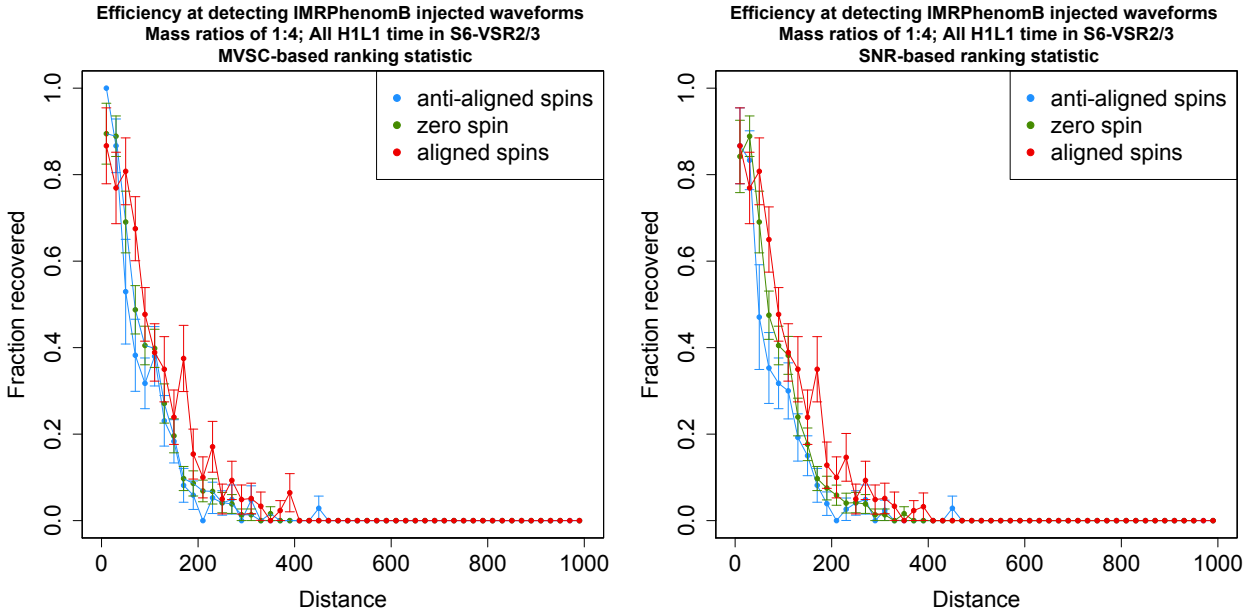

(a) (b)

Figure 8.25: The efficiency at recovering IMRPhenomB injections with a FAR less than that of the expected loudest foreground event. The top panel uses FARs calculated from the MVSC result as described in Section 8.3.1.5. The bottom panel uses FARs calculated from ρ_{high}, given by Equation (7.18). The colors indicate the spins of the injected waveforms. 40 distance bins were used. The error bars reflect binomial counting errors. Any bumps at distances greater than 500 Mpc are due to noise triggers in two or more detectors that happen to be coincident with each other and with the injected signal. S6-VSR2/3 data at Category 4.

Figure 8.33 (component mass ratio of 0.4 to 0.6), and Figure 8.34 (component mass ratio of 0.2 to 0.4). The expected sensitivity is calculated for both a single-detector SNR threshold of 8 (what we generally use when quoting sensitive distance), and a single-detector SNR threshold of 7. For the most part, the multivariate statistical analysis with an expected loudest FAR threshold has a larger reach than what is expected based on Gaussian noise with a single-detector SNR threshold of 7. The fact that almost all of the ranges are above the expected sensitivity based on a single-detector SNR threshold of 8 means that we did a very thorough job with the data-quality flags described in Section 4.2 and that our data is close to Gaussian already. However, using a multivariate statistical classifier can help detect signals that seem to be buried in the noise if we are looking at SNR and χ^2 values alone to rank our candidate events.

8.3.1.7 [redacted]

[redacted]

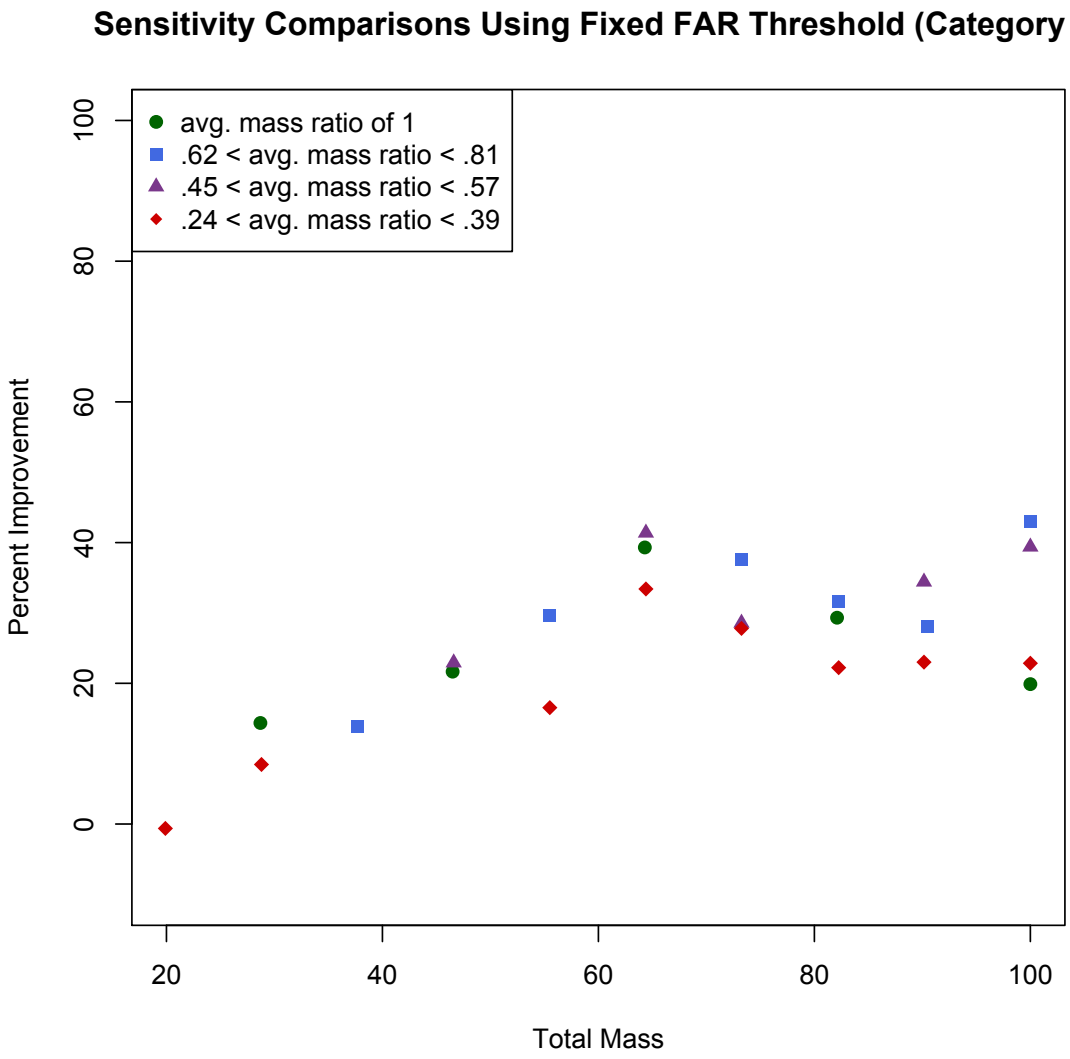

Figure 8.26: A comparison of the search sensitivity (volume $\times$ time), calculated using EOBNRv2 injections, using a multivariate statistical classifier (MVSC) as the ranking statistic versus the combined ρ_{high} as the ranking statistic. FARs were calculated for each background and simulated signal event as described in Section 8.3.1.5 and Section 8.2 for MVSC and ρ_{high}, respectively. The classifier used for the MVSC result is the random forest of bagged decision trees (RFBDT). For both ranking statistics, the expected FAR thresholds (FĂR in Table 8.1) were used in the sensitivity calculation. As the sensitivity is dependent on both total mass and the ratio of the component masses, the sensitivity is shown as a function of total mass with different symbols for various mass ratios. Green circle: the component objects have approximately equal-mass. Blue square: the ratio, at the center of the bins, of the component masses is around 0.715. Purple triangle: the ratio, at the center of the bins, of the component masses is around 0.51. Red diamond: the ratio, at the center of the bins, of the component masses is around 0.315. The width of the bins are 8.9 $M_{\odot}$, and the total mass is also expressed in $M_{\odot}$. The percent improvement is the MVSC result and the ρ_{high} result divided by the ρ_{high} result.

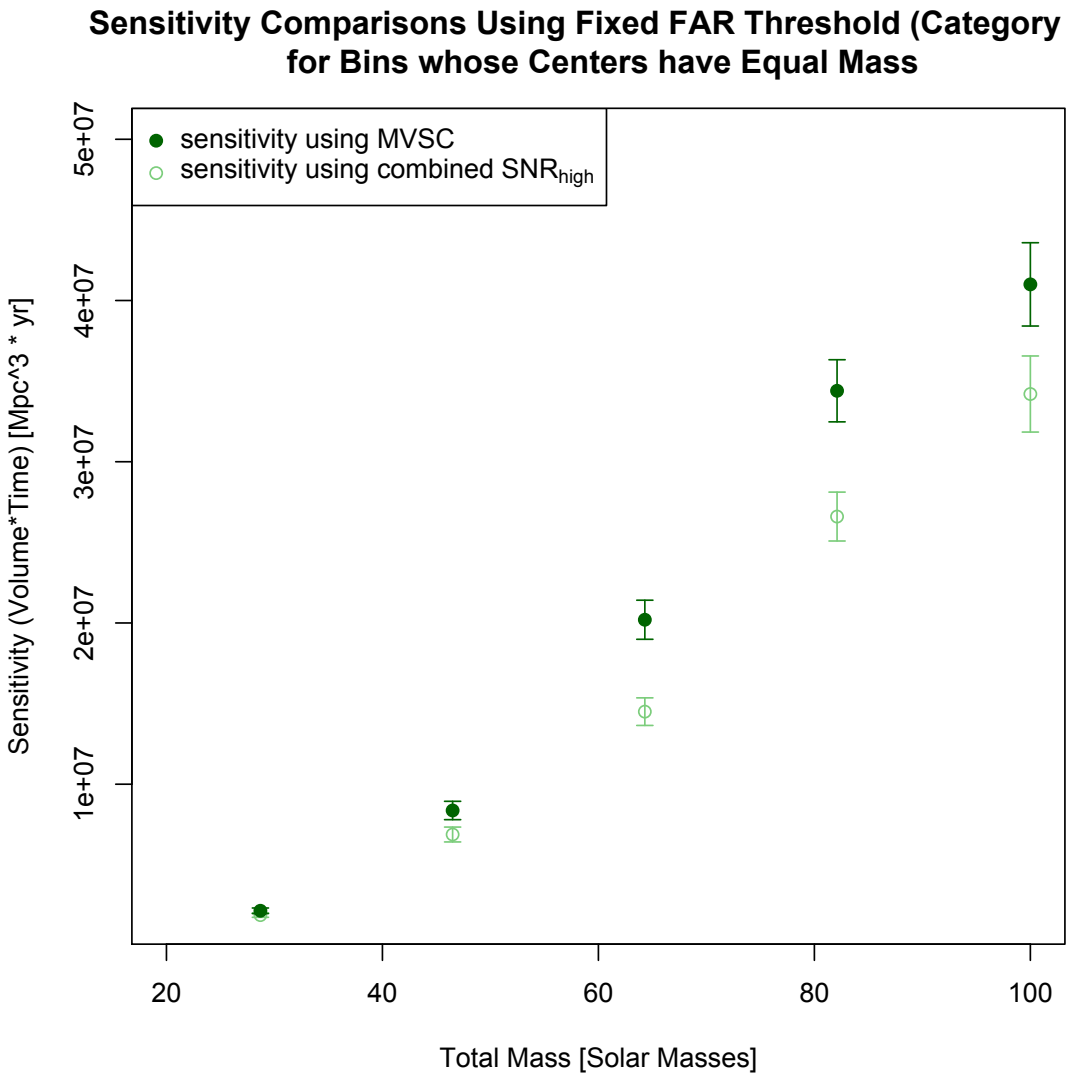

Figure 8.27: A comparison of the search sensitivity (volume $\times$ time), calculated using EOBNRv2 injections, using a multivariate statistical classifier (MVSC) as the ranking statistic versus the combined ρ_{high} as the ranking statistic. FARs were calculated for each background and simulated signal event, as described in Section 8.3.1.5 and Section 8.2 for MVSC and ρ_{high}, respectively. The classifier used for the MVSC result is the random forest of bagged decision trees (RFBDT). For both ranking statistics, the expected FAR thresholds (F$\breve{\text{A}}$R in Table 8.1) were used in the sensitivity calculation. Solid circle: the results using RFBDTs to calculate the ranking statistic. Open circle: the results using the ρ_{high} as the ranking statistic. The sensitivity bins considered are those whose centers have equal-mass; the width of the bins are 8.9 $M_{\odot}$, and the total mass is also expressed in $M_{\odot}$.

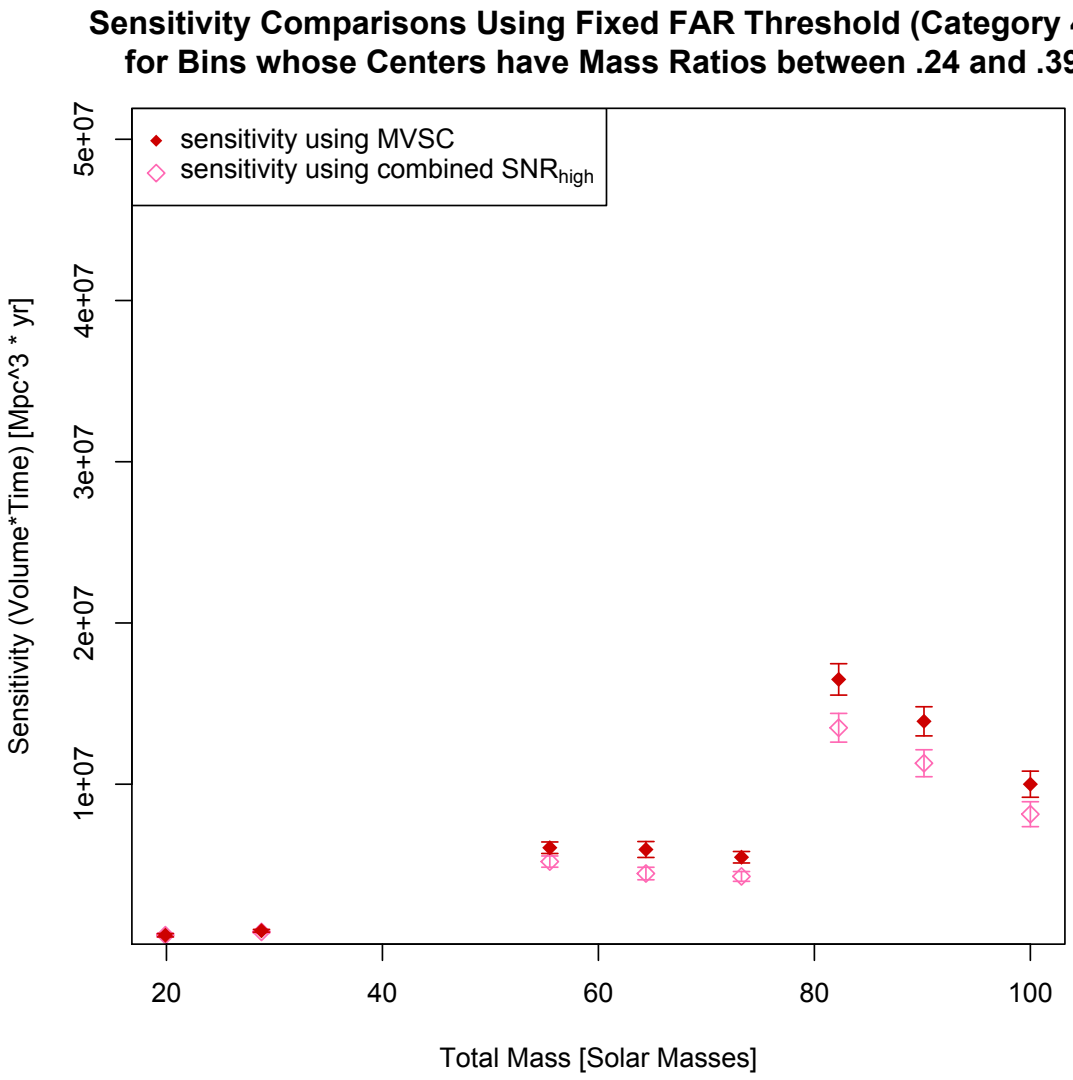

Figure 8.28: A comparison of the search sensitivity (volume $\times$ time), calculated using EOBNRv2 injections, using a multivariate statistical classifier (MVSC) as the ranking statistic versus the combined ρ_{high} as the ranking statistic. FARs were calculated for each background and simulated signal event, as described in Section 8.3.1.5 and Section 8.2 for MVSC and ρ_{high}, respectively. The classifier used for the MVSC result is the random forest of bagged decision trees (RFBDT). For both ranking statistics, the expected FAR thresholds (F$\breve{\text{A}}$R in Table 8.1) were used in the sensitivity calculation. Solid diamond: the results using RFBDTs to calculate the ranking statistic. Open diamond: the results using the ρ_{high} as the ranking statistic. The sensitivity bins considered are those whose centers have a ratio around 0.315; the width of the bins are 8.9 $M_{\odot}$, and the total mass is also expressed in $M_{\odot}$.

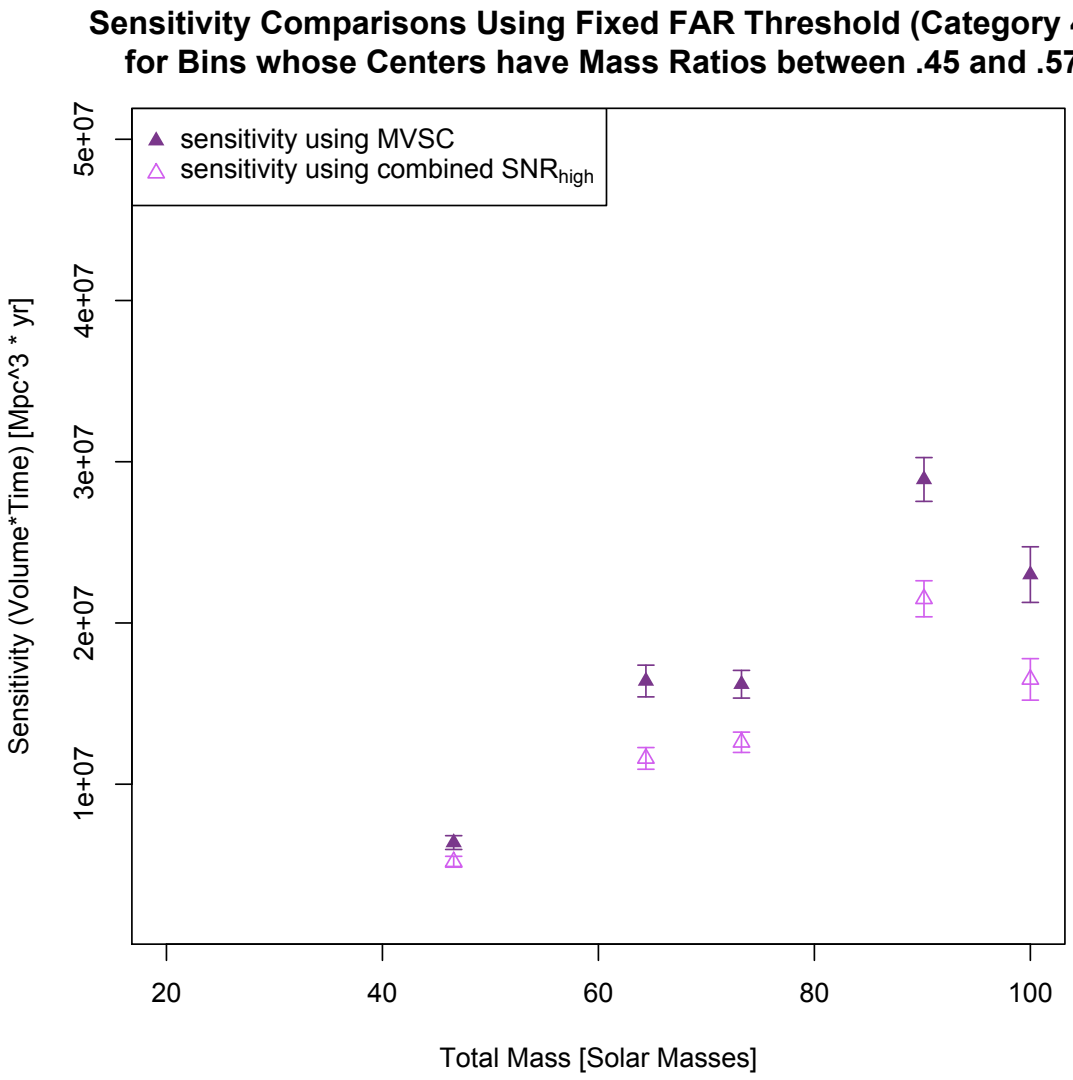

Figure 8.29: A comparison of the search sensitivity (volume $\times$ time), calculated using EOBNRv2 injections, using a multivariate statistical classifier (MVSC) as the ranking statistic versus the combined ρ_{high} as the ranking statistic. FARs were calculated for each background and simulated signal event, as described in Section 8.3.1.5 and Section 8.2 for MVSC and ρ_{high}, respectively. The classifier used for the MVSC result is the random forest of bagged decision trees (RFBDT). For both ranking statistics, the expected FAR thresholds ($\breve{\text{FAR}}$ in Table 8.1) were used in the sensitivity calculation. Solid triangle: the results using RFBDTs to calculate the ranking statistic. Empty triangle: the results using the ρ_{high} as the ranking statistic. The sensitivity bins considered are those whose centers have a ratio around 0.51 (not including the cases where the bin centers are exactly equal); the width of the bins are 8.9 $M_{\odot}$, and the total mass is also expressed in $M_{\odot}$.

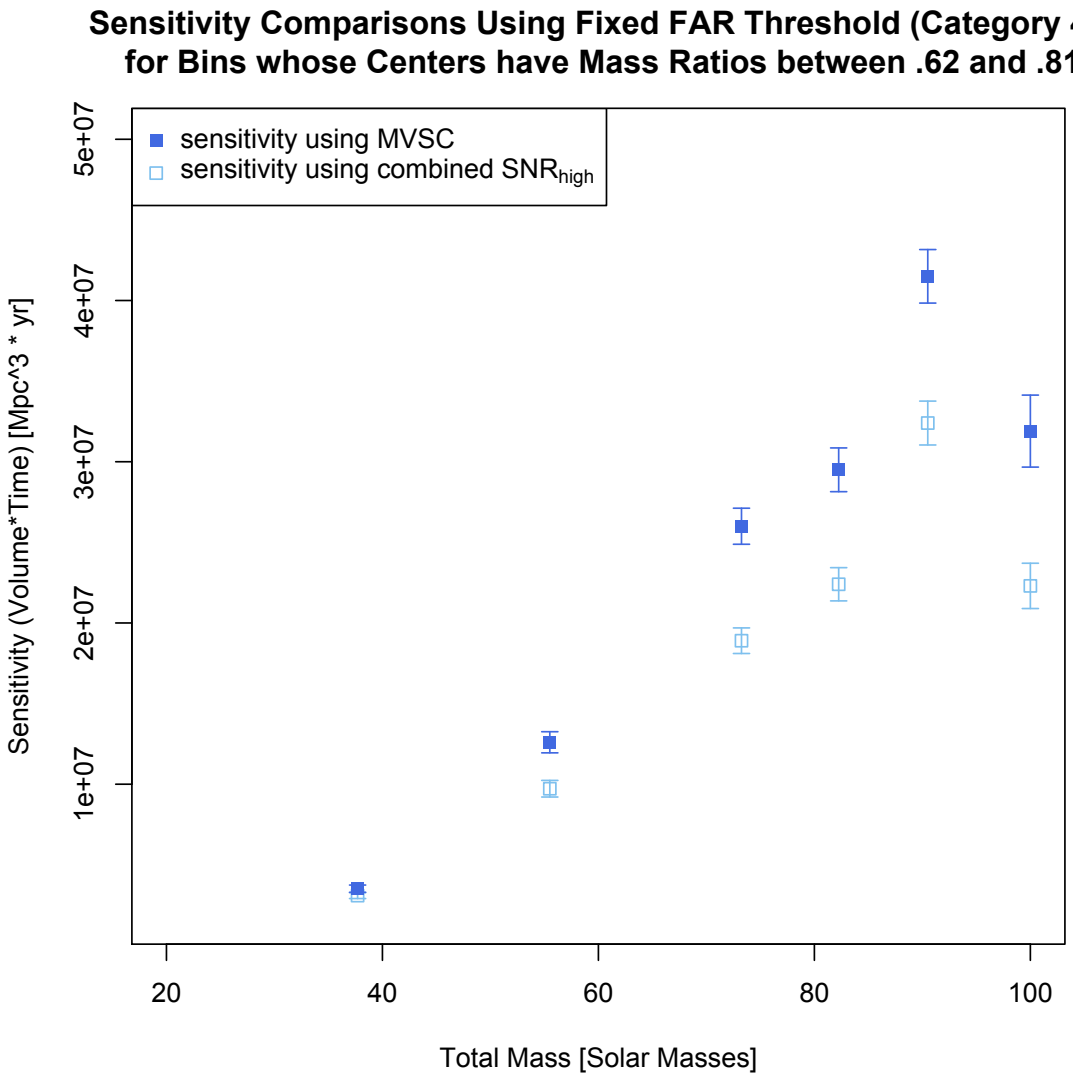

Figure 8.30: A comparison of the search sensitivity (volume $\times$ time), calculated using EOBNRv2 injections, using a multivariate statistical classifier (MVSC) as the ranking statistic versus the combined ρ_{high} as the ranking statistic. FARs were calculated for each background and simulated signal event, as described in Section 8.3.1.5 and Section 8.2 for MVSC and ρ_{high}, respectively. The classifier used for the MVSC result is the random forest of bagged decision trees (RFBDT). For both ranking statistics, the expected FAR thresholds ($\breve{\text{FAR}}$ in Table 8.1) were used in the sensitivity calculation. Solid square: the results using RFBDTs to calculate the ranking statistic. Open square: the results using the ρ_{high} as the ranking statistic. The sensitivity bins considered are those whose centers have a ratio around 0.715; the width of the bins are 8.9 $M_{\odot}$, and the total mass is also expressed in $M_{\odot}$.

Table 8.3: Search sensitive distances, quoted over 9 $M_\odot$-wide component mass bins labelled by their central values. The sensitive distance in Mpc (averaged over the observation time and over source sky location and orientation) is given for EOBNR waveforms, non-spinning IMRPhenomB waveforms, and spinning IMRPhenomB waveforms separately. Both $\mathcal{L}_{\rm MVSC}$ and $\rho_{\rm high}$ were used as the ranking statistics for a FAR; the FAR of the expected loudest event (F$\breve{\rm A}$R) was used to calculate the sensitivity. Compare to the sensitive distances listed in Table 8.2, which were calculated using the loudest event statistic. In this table, all the sensitive distances were calculated using a threshold at the expected loudest event, rather than at the loudest foreground event. The rightmost column calculates the expected sensitive distance based on the steps in Section 2.2.2, using a single-detector SNR threshold of 8 for detection and the mode average of the L1 spectrum during S6. As L1 was usually the second most sensitive detector, this makes it a good estimate for the sensitivity of the search. The expected sensitive distance uses a purely Gaussian noise profile and does not take into account any complexities of our pipeline (template bank, loudest event statistic, various vetoes and thresholds).

		EOBNR	EOBNR	PhenomB nonspin	PhenomB nonspin	PhenomB spin	PhenomB spin	Expected
m_1	m_2	$\mathcal{L}_{\rm MVSC}$	$\rho_{\rm high}$	$\mathcal{L}_{\rm MVSC}$	$\rho_{\rm high}$	$\mathcal{L}_{\rm MVSC}$	$\rho_{\rm high}$	Distance
($M_\odot$)	($M_\odot$)	(Mpc)	(Mpc)	(Mpc)	(Mpc)	(Mpc)	(Mpc)	(Mpc)
14	14	107	102	109	105	113	106	90
23	14	126	120	129	125	133	128	107
32	14	153	143	150	140	149	140	116
41	14	151	143	151	142	159	149	123
50	14	150	136	161	146	178	163	125
23	23	168	157	167	156	172	159	136
32	23	192	176	196	179	196	183	157
41	23	210	187	210	189	211	189	166
50	23	209	192	215	197	224	207	168
59	23	210	197	212	197	209	197	166
68	23	199	185	203	185	206	193	162
77	23	178	166	187	178	186	164	152
32	32	225	202	227	203	225	201	186
41	32	245	220	250	225	247	228	201
50	32	255	233	259	234	238	222	206
59	32	254	230	253	232	249	223	205
68	32	235	210	234	213	254	229	197
41	41	269	247	267	247	251	232	224
50	41	286	263	289	266	284	268	234
59	41	262	233	273	247	265	246	235
50	50	285	268	283	273	241	218	251

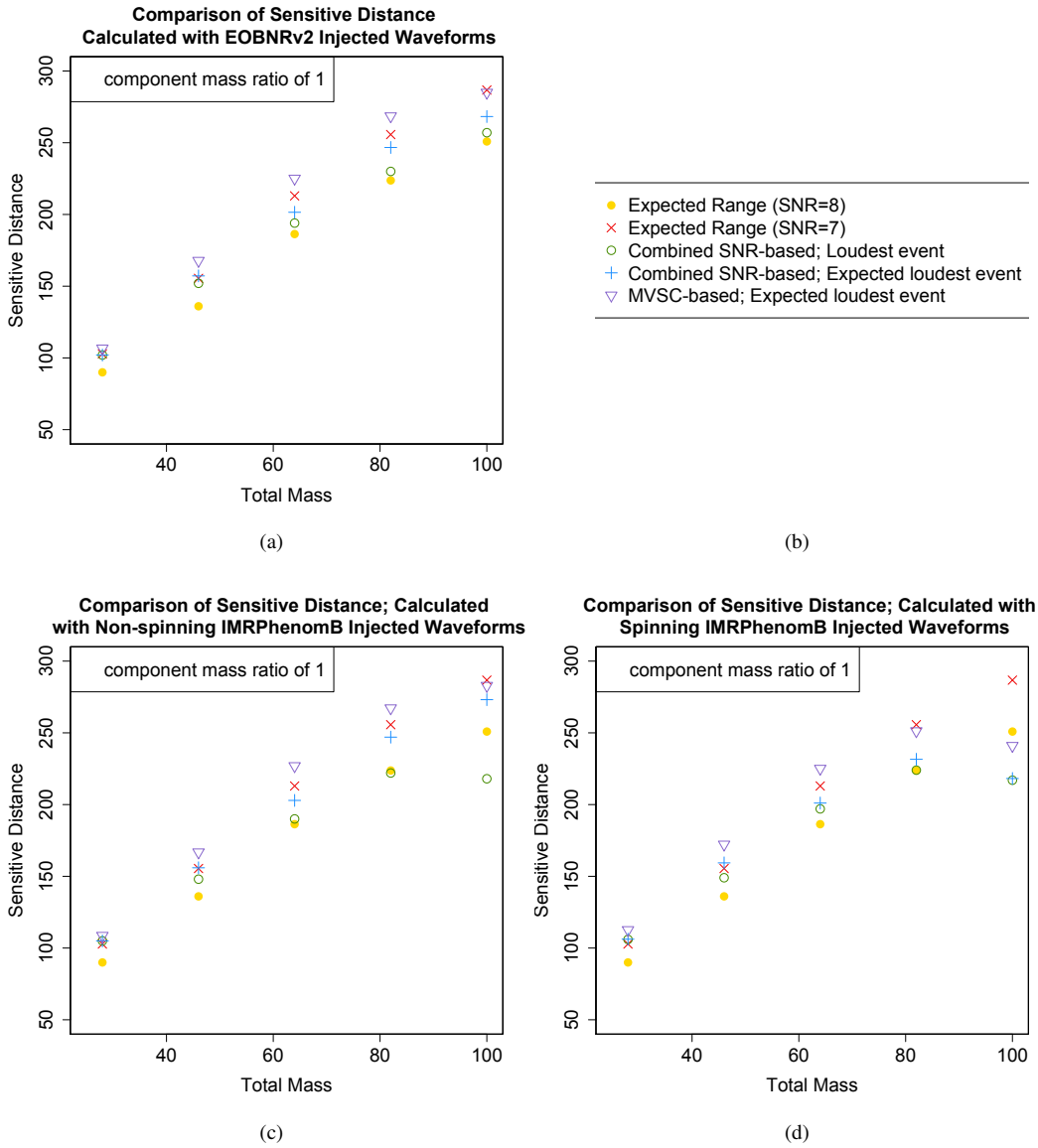

Figure 8.31: Solid yellow circles: the expected sensitive distance, calculated with IMRPhenomB waveforms and using only the Gaussian noise profile of L1 (L1 is often our second weakest detector), during S6 (see Section 2.2.2), using a single-detector SNR threshold of 8. Red Xs: the expected sensitive distance, calculated with IMRPhenomB waveforms and using only the Gaussian noise profile of L1, during S6, using a single-detector SNR threshold of 7. Open green circles: the calculated sensitive distance, using ρ_{high} as the ranking statistic and the FAR of the loudest foreground event as the detection threshold ($\widehat{FAR}$). Blue crosses: the calculated sensitive distance, using ρ_{high} as the ranking statistic and the FAR of the expected loudest foreground event as the detection threshold ($\breve{\text{FAR}}$). Purple triangles: the calculated sensitive distance, using $\mathcal{L}_{\text{MVSC}}$ as the ranking statistic and the FAR of the expected loudest foreground event as the detection threshold ($\breve{\text{FAR}}$). The bin widths for each point are 18 $M_{\odot}$. Only bins with centers with mass ratios of 1 are used. The top panel's sensitivities (purple, blue, green) are calculated using EOBNRv2 injections. The left panel's sensitivities (purple, blue, green) are calculated using non-spinning IMRPhenomB injections. The right panel's sensitivities (purple, blue, green) are calculated using spinning IMRPhenomB injections.

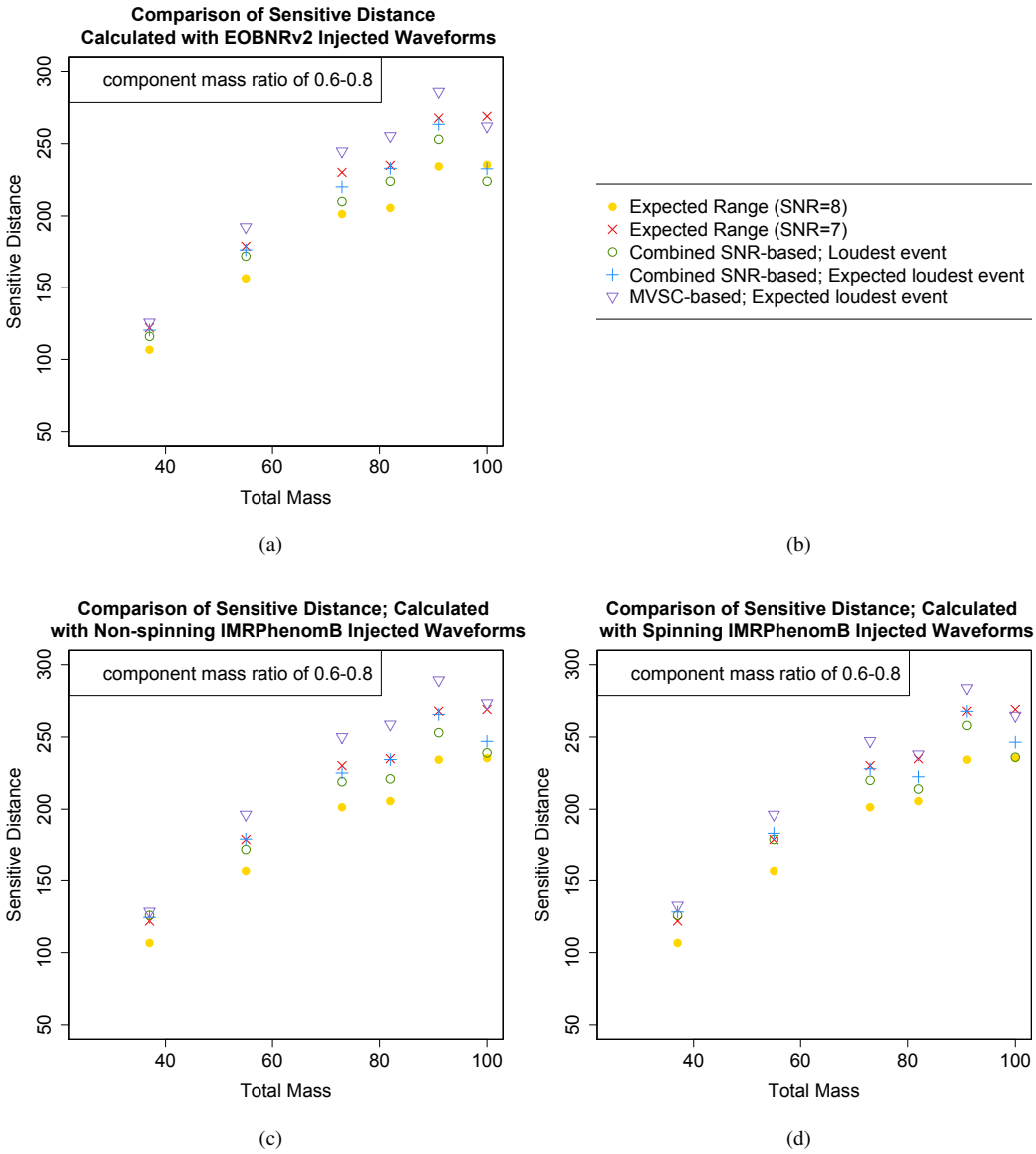

Figure 8.32: Solid yellow circles: the expected sensitive distance, calculated with IMRPhenomB waveforms and using only the Gaussian noise profile of L1 (L1 is often our second weakest detector), during S6 (see Section 2.2.2), using a single-detector SNR threshold of 8. Red Xs: the expected sensitive distance, calculated with IMRPhenomB waveforms and using only the Gaussian noise profile of L1, during S6, using a single-detector SNR threshold of 7. Open green circles: the calculated sensitive distance, using ρ_{high} as the ranking statistic and the FAR of the loudest foreground event as the detection threshold ($\widehat{FAR}$). Blue crosses: the calculated sensitive distance, using ρ_{high} as the ranking statistic and the FAR of the expected loudest foreground event as the detection threshold ($\breve{\mathrm{FAR}}$). Purple triangles: the calculated sensitive distance, using $\mathcal{L}_{\mathrm{MVSC}}$ as the ranking statistic and the FAR of the expected loudest foreground event as the detection threshold ($\breve{\mathrm{FAR}}$). The bin widths for each point are 18 $M_{\odot}$. Only bins with centers with mass ratios between 0.6 and 0.8 are used. The top panel's sensitivities (purple, blue, green) are calculated using EOBNRv2 injections. The left panel's sensitivities (purple, blue, green) are calculated using non-spinning IMRPhenomB injections. The right panel's sensitivities (purple, blue, green) are calculated using spinning IMRPhenomB injections.

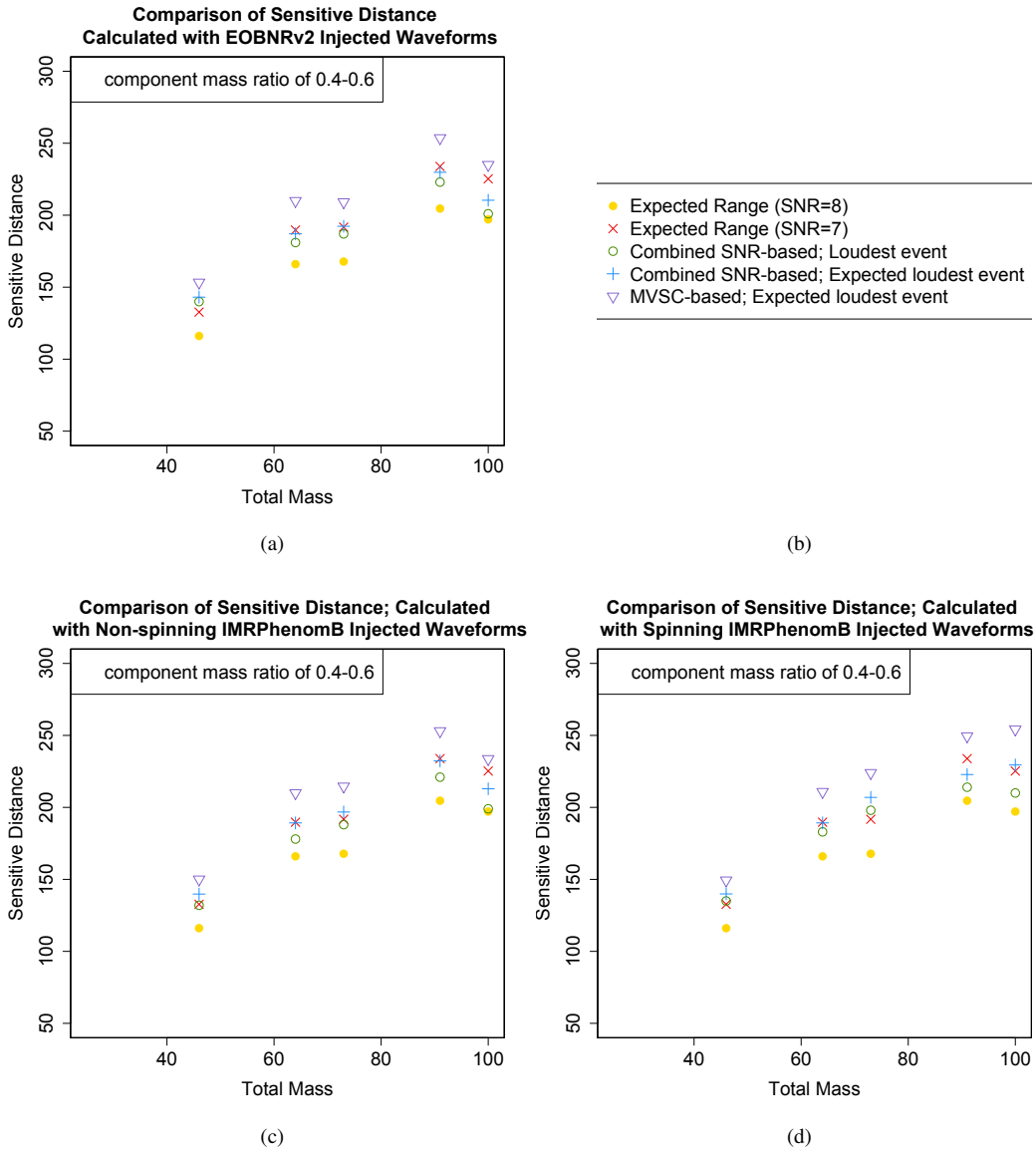

Figure 8.33: Solid yellow circles: the expected sensitive distance, calculated with IMRPhenomB waveforms and using only the Gaussian noise profile of L1 (L1 is often our second weakest detector), during S6 (see Section 2.2.2), using a single-detector SNR threshold of 8. Red Xs: the expected sensitive distance, calculated with IMRPhenomB waveforms and using only the Gaussian noise profile of L1, during S6, using a single-detector SNR threshold of 7. Open green circles: the calculated sensitive distance, using ρ_{high} as the ranking statistic and the FAR of the loudest foreground event as the detection threshold ($\widehat{FAR}$). Blue crosses: the calculated sensitive distance, using ρ_{high} as the ranking statistic and the FAR of the expected loudest foreground event as the detection threshold ($\breve{\text{FAR}}$). Purple triangles: the calculated sensitive distance, using $\mathcal{L}_{\text{MVSC}}$ as the ranking statistic and the FAR of the expected loudest foreground event as the detection threshold ($\breve{\text{FAR}}$). The bin widths for each point are 18 $M_{\odot}$. Only bins with centers with mass ratios between 0.4 and 0.6 are used. The top panel's sensitivities (purple, blue, green) are calculated using EOBNRv2 injections. The left panel's sensitivities (purple, blue, green) are calculated using non-spinning IMRPhenomB injections. The right panel's sensitivities (purple, blue, green) are calculated using -spinning IMRPhenomB injections.

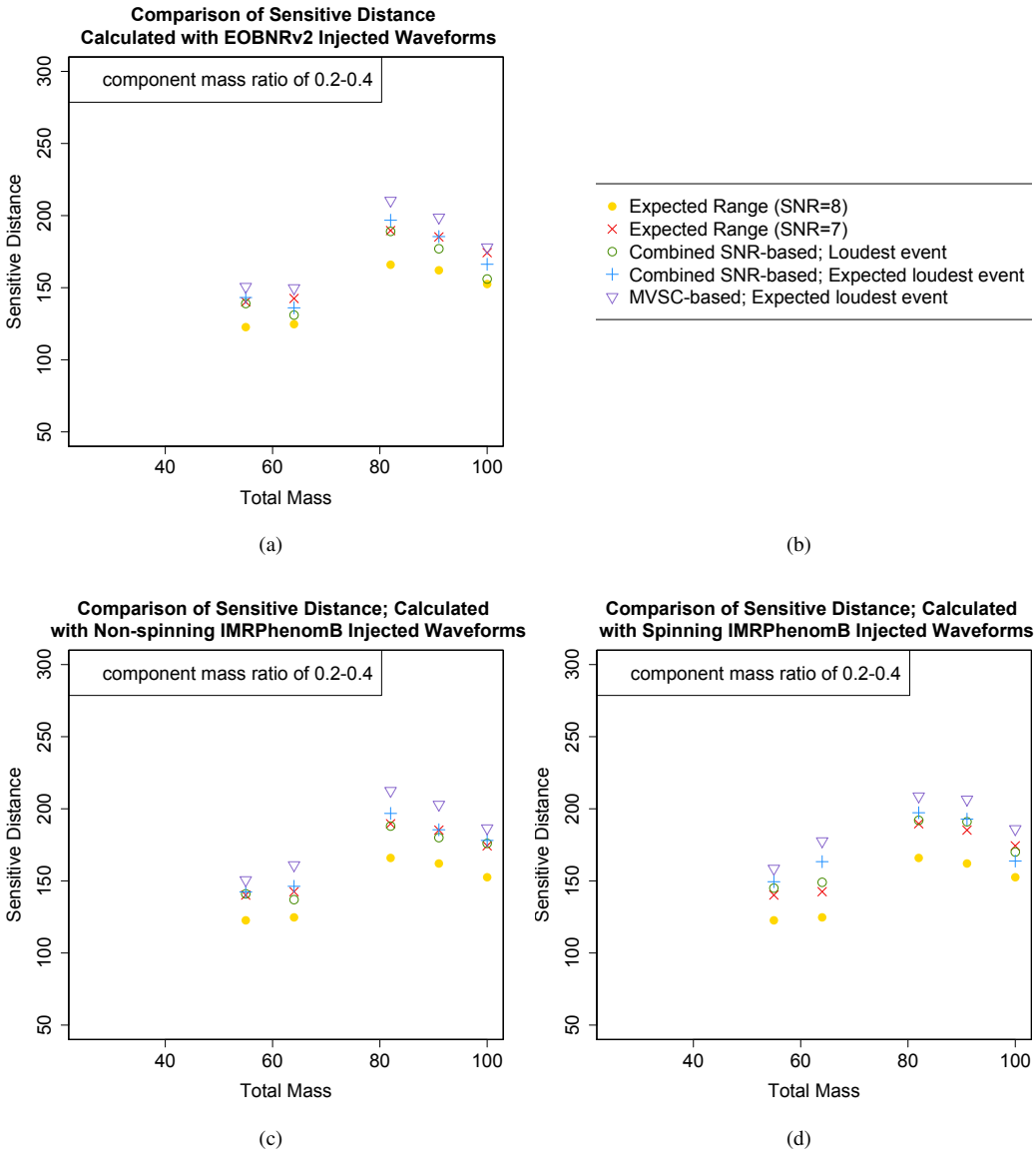

Figure 8.34: Solid yellow circles: the expected sensitive distance, calculated with IMRPhenomB waveforms and using only the Gaussian noise profile of L1 (L1 is often our second weakest detector), during S6 (see Section 2.2.2), using a single-detector SNR threshold of 8. Red Xs: the expected sensitive distance, calculated with IMRPhenomB waveforms and using only the Gaussian noise profile of L1, during S6, using a single-detector SNR threshold of 7. Open green circles: the calculated sensitive distance, using ρ_{high} as the ranking statistic and the FAR of the loudest foreground event as the detection threshold ($\widehat{FAR}$). Blue crosses: the calculated sensitive distance, using ρ_{high} as the ranking statistic and the FAR of the expected loudest foreground event as the detection threshold ($\breve{\mathrm{FAR}}$). Purple triangles: the calculated sensitive distance, using $\mathcal{L}_{\mathrm{MVSC}}$ as the ranking statistic and the FAR of the expected loudest foreground event as the detection threshold ($\breve{\mathrm{FAR}}$). The bin widths for each point are 18 $M_{\odot}$. Only bins with centers with mass ratios between 0.2 and 0.4 are used. The top panel's sensitivities (purple, blue, green) are calculated using EOBNRv2 injections. The left panel's sensitivities (purple, blue, green) are calculated using non-spinning IMRPhenomB injections. The right panel's sensitivities (purple, blue, green) are calculated using non-spinning IMRPhenomB injections.

8.3.1.8 Additional information from the multivariate statistical classifier

As mentioned in Section 5.3.2.1, the RFBDT algorithm lists how useful each of the feature space's dimensions were in training the forests. For the first analysis period in S6-VSR2/3, the variable importance can be seen in Figure 8.35 and Figure 8.36. The more often a dimension is chosen to split on, the better it is at separating the classes. Splits are only made if they will increase the optimization criterion, here the Gini index $-2p(1-p)$, where p is the fraction of correctly classified events. According to Figure 8.35 and Figure 8.36, ethinca, which measures the distance between events seen in coincidence in two detectors in time and template space, is the most useful dimension. This is interesting because, as can be seen in Figure 8.8, the distributions for our simulated signal and background overlap over the entire range of ethinca values. No cut on this dimension can isolate a region of pure signal or pure background. However, there are an order of magnitude more Class 1 (signal) training events with ethinca values below 0.1 than Class 0 (background) training samples. Because the training events at a particular branching point on a tree depend on the previous splits, this information becomes valuable after splits on variables like the absolute difference in arrival time (Figure 8.9) and the SNR in each coincident detector (Figure 8.12 and Figure 8.13) have been made.

8.3.2 Conclusions from using a multivariate statistical classifier to calculate the rank of events in the high-mass search

Figure 8.26, Figure 8.31, Figure 8.32, Figure 8.33, and Figure 8.34 demonstrate that a multivariate statistical classifier trained on signal-based information about each candidate GW event can significantly improve our ability to distinguish signal from background, thereby increasing the sensitivity of a search for BHBs. The improvement makes sense, considering that the original detection statistic only incorporated the SNR and χ^2 values for each detector in the coincidence (and to a lesser extent the duration of the templates identified with the matched-filter). In contrast, the random forest of bagged decision trees was working with a 15-dimensional feature space.

The classifier used, the random forest of bagged decision trees, outputs the dimensions that were the most useful in training the forest. The most important dimension in the S6-VSR2/3 analysis was ethinca, a parameter that describes how close the triggers found in two detectors are in time and mass parameters. For a coincidence-based search, it makes sense that the most valuable dimension at identifying signal versus background is one that describes coincidence.

8.3.2.1 Future work

Several avenues are available to improve upon this multivariate statistical classifier. The first is to more carefully curate signal-based information in the feature vector describing an event. For example, loosening the parameters on the r^2 duration calculation might result in the dimension containing more information. Other χ^2 tests can be used. We can also start incorporating information from the SNR and χ^2 time-series,

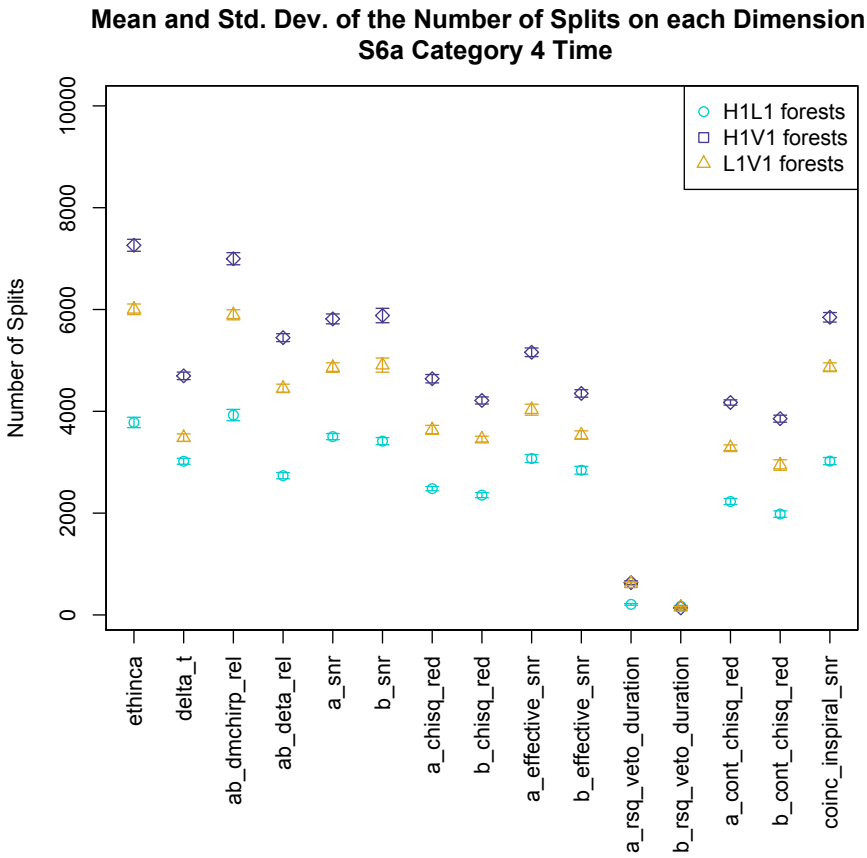

Figure 8.35: The number of splits on each of the dimensions in the training feature vectors. The mean of the results from each round-robin training set is plotted; the error bars indicate the standard deviation from the mean. It is important to note that the round-robin forests are not independent. Since we have 10 round-robin sets, each round robin is $8/9 \times 100\%$ similar. Thus, it is reassuring that the error bars are so small.

such as the amount of power in various frequency bins, the skew, and kurtosis.

Second, rather than working with the data after Category 3 and/or Category 4 vetoes have been applied, we could work with data that has had only had the egregiously bad segments removed. Rather than removing them outright, we can include them in our training samples, along with a dimension that describes the data quality (i.e., one created by a multivariate statistical classifier that trains on information in the auxiliary channels, as in Chapter 6).

Third, weighting the injections such that they more accurately represent the uniform-in-volume aspect of the astrophysical signals we expect should be tried.

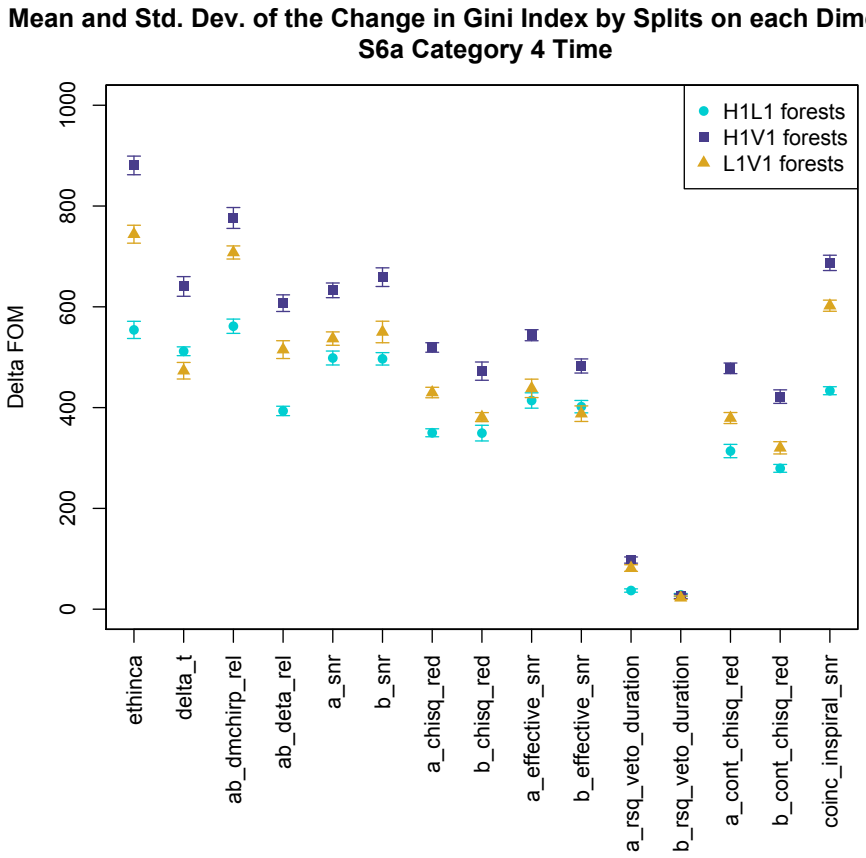

Figure 8.36: The total change in the optimization criterion (FOM), the Gini Index, by splits on each of the dimensions in the training feature vectors (see Section 5.3). The mean of the results from each round-robin training set is plotted; the error bars indicate the standard deviation from the mean. It is important to note that the round-robin forests are not independent. Since we have 10 round-robin sets, each round robin is $8/9 \times 100\%$ similar. Thus, it is reassuring that the error bars are so small.

Chapter 9

Application of RFBDTs to the search for black hole ringdown signals

As introduced in Chapter 1, the signal from the coalescence of two black holes can be described in three parts: the inspiral, the merger, and the ringdown. As the total mass of the binary system increases, the frequency of the inspiral phase decreases and thus falls out of the sensitive band of the given detector; see Figure 2.17 for the LIGO detectors' sensitivity curves and Figure 2.18 for Virgo's sensitivity curve. In fact, for enhanced LIGO (S6), we do not analyze data below 40 Hz, because the seismic noise rises too steeply at low frequencies (see Figure 3.16). Similarly, for Virgo during VSR2/3, we do not analyze data below 30 Hz.

Even systems at the higher end of the high-mass search space do not have a full cycle in LIGO's band during the inspiral stage of the coalescence (see Table 2.2). However, the merger and ringdown can fall nicely within the sensitive band of the enhanced LIGO or Virgo detectors. See, for example, the 50 + 50 $M_{\odot}$ system in Figure 2.12. As the total mass of the system increases, the ringdown can produce a significant strain, measurable by our detectors.

A search for the ringdown signature of the merger of black hole binaries (BHBs) with total mass between 50 and 450 $M_{\odot}$ was performed for both S5 and S6-VSR2/3 data; the results were published in Reference [18]. In S5, coincident detectors considered are H1L1, H1H2L1, and H2L1; H1H2 coincidences are not considered because the noise is correlated. In S6, the coincident detectors considered are H1L1, H1V1, L1V1, and H1L1V1. The base search is a matched-filter similar to the one described in Chapter 7, except:

- The templates for the matched-filter are single-mode ringdown templates described by their frequency (f_0: [50,2000] Hz) and quality factor (Q: [2,20]);
- The same template bank, whose adjacent templates overlap by 97% in white detector noise, is used in each detector;
- The pipeline has only one stage, and no χ^2 check is performed;
- During S5, an amplitude consistency check is applied when H1 and H2 are operating (since they are co-located, their SNRs should be strongly correlated);

- Coincidence between triggers in different detectors is determined by their metric distance in (f_0, Q, t)-space;
- The efficiency of the search is calculated for both inspiral-merger-ringdown waveforms (EOBNRv2), as well as ringdown-only waveforms.

9.1 Multivariate statistical classifiers in ringdown search

As in the high-mass search (see Section 8.3), we can use the output of the search pipeline as input to a multivariate statistical classifier. Again, we use the random forest of bagged decision trees (RFBDT, see Section 5.3.2). As before, we train separate forests for each pair of detectors in the search time (see Section 8.3.1.5). We train the classifier on timeslides (to represent Class 0: background) and waveforms injected into the data (to simulate Class 1: signal). For the application to the ringdown search, the feature vector describing events has the following elements:

1. dt, the absolute value of the difference in the peak time of the trigger in each detector;
2. df, the absolute value of the difference in the frequency of the template found in each detector;
3. dQ, the absolute value of the difference in the frequency of the template found in each detector;
4. ds^2, the metric distance between the templates matched in each detector;
5. SNR in the first detector;
6. SNR in the second detector;
7. the ratio of SNRs;
8. the sum of SNRs for each detector in the original coincidence (for triple coincidences, this is a sum of three terms);
9. the SNRs for each detector in the original coincidence, added in quadrature (for triple coincidences, this is a sum of three terms);
10. chopped-L statistic combining the SNRs in each detector, which was used as the detection statistic for double coincident events in the S4 ringdown search [11];
11. effective distance as measured by the first detector;
12. effective distance as measured by the second detector;
13. the ratio of effective distances;
14. the absolute difference of the effective distances;

15. g_{tt}, the average time-time metric coefficient for the two matched templates;
16. g_{ff}, the average frequency-frequency metric coefficient for the two matched templates;
17. g_{QQ}, the average quality factor-quality factor metric coefficient for the two matched templates;
18. g_{tf}, the average frequency-time metric coefficient for the two matched templates;
19. g_{tq}, the average time-quality factor metric coefficient for the two matched templates;
20. g_{fQ}, the average frequency-quality factor metric coefficient for the two matched templates;
21. a binary 0 or 1 indicating if the *hveto* algorithm flagged the time in the first detector as being of poor data quality (only used in the S6-VSR2/3 dataset);
22. a binary 0 or 1 indicating if the *hveto* algorithm flagged the time in the second detector as being of poor data quality [89] (only used in the S6-VSR2/3 dataset).

Unlike in the high-mass search, the RFBDT did not show immediate improvement over the quadrature-combined SNR statistic in separating signal and background in the operating region of low false alarm fraction. A RFBDT with 100 trees was first tried for the S5 data, with the feature space spanned by the first 8 dimensions in the list above, with various combinations of the number of events per leaf and the number of dimensions randomly selected for splitting also tried. Additional dimensions from the list above were added to the feature space and kept after it was observed they increased or maintained the efficiency at classifying signals at low fractions of misclassifying background. We used receiver operating characteristic (ROC) curves to visualize this performance.

In the end, RFBDTs were used with 200 trees, a minimal number of 5 events per leaf, and a random subset of 12 of the 20 (18 for S5) dimensions generated at each branching point. The criterion for optimization was the negative cross-entropy $p\log_2 p+(1-p)\log_2(1-p)$, where p is the correctly classified fraction of training events on a node.

9.1.1 Efficiency and upper limits on the rates of astrophysical sources

The ranking statistic $\mathcal{L}_{\mathrm{MVSC}}$, given by Equation (8.3) and Equation (8.2), is used. As in Section 7.7, this ranking statistic is turned into false alarm rates (FARs), which are then used to calculate the upper limits. The loudest event statistic was used (see Section 7.8). Efficiency at finding EOBNRv2-injected waveforms was used to calculate the sensitive range of the search (see Figure 9.1) and a 90% confidence upper limit on the coalescence rates of two black holes with total mass between 50 and 450 $M_{\odot}$, with component mass ratios of 1 and 4, in mass bins of width 50 $M_{\odot}$(see Figure 9.2). The rate upper limit calculation is described in Section 7.8.1. Here, the rate upper limit is calculated using the S5 data and a uniform prior. The S5 result is then used as a prior for the rate upper limit calculation for S6-VSR2/3. For BHBs with total masses between 100 and 150 $M_{\odot}$, a rate upper limit $6.9\times10^{-8}\mathrm{Mpc}^{-3}yr^{-1}$ was set.

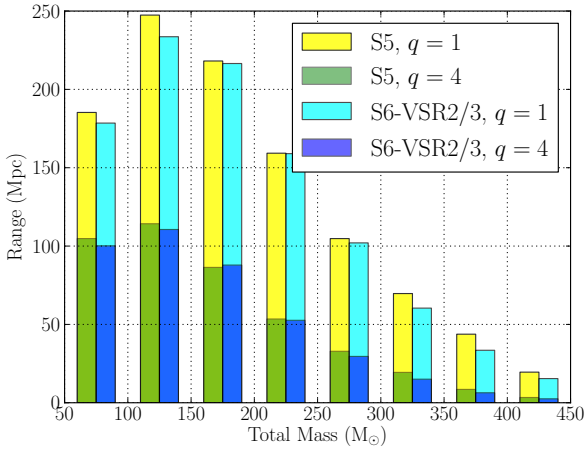

Figure 9.1: The average sensitive distances to EOBNRv2-injected waveforms, using the ringdown search as described in the text. Yellow: the sensitivity during S5 for equal-mass BHBs. Green: the sensitivity during S5 for BHBs with a ratio of component masses equal to 4. Cyan: the sensitivity during S6-VSR2/3 for equal-mass BHBs. Blue: the sensitivity during S6-VSR2/3 for BHBs with a ratio of component masses equal to 4. The bin width is 50 $M_\odot$ [18].

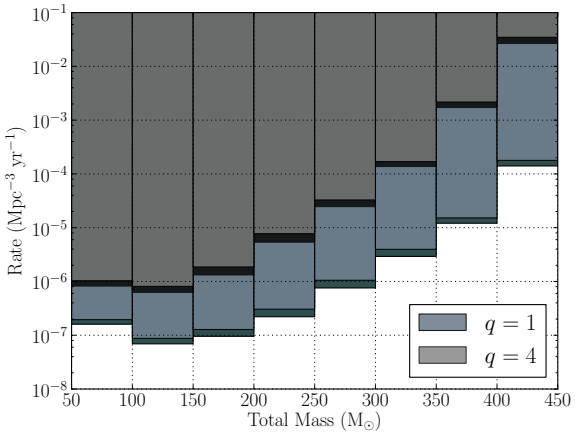

Figure 9.2: The upper limits on the rate of BHBs, computed using the loudest event statistic on a ranking statistic calculated by a multivariate statistical classifier. EOBNRv2 waveforms are used to calculate the efficiency. Blue-grey: component mass ratios of 1 (S5 + uniform prior). Grey: component mass ratios of 1:4 (S5 + uniform prior). Dark teal: component mass ratios of 1:4 (S6-VSR2/3 + S5 prior). Black: component mass ratios of 1 (S6-VSR2/3 + S5 prior). The bin width is 50 $M_\odot$ [18].

An upper limit of $4 \times 10^{-8}\text{Mpc}^{-3}yr^{-1}$ was placed on the rate of perturbed intermediate mass black holes, using injected ringdown signals with masses between 86 and 146 $M_\odot$. These injections assumed a fixed ringdown efficiency of 1% (see Reference [18]) and a uniform distribution of spins between 0 and .99. Here, spin is cL/GM^2, where c is the speed of light, L is the angular momentum of the black hole, and M is its mass. This upper limit is 3 orders of magnitude stricter than the limit set in Reference [133], which used data from LIGO science run 4. However, the increase in total analysis time, due to the longer length of S5+S6-VSR2/3 coupled with the fact that all observation times contribute (in S4 only H1H2L1 was

considered), was on the order of ~ 32. Moreover, the results in S4 were limited by the least sensitive detector, H2; in S5+S6-VSR2/3, L1 was often the least sensitive detector. The difference in sensitivity between L1 and H2 yields an expected improvement of ~ 27 in the upper limits.

9.1.2 Conclusions from this search for ringdown signals

Unlike for the high-mass search described in Chapter 8, we did not perform the search using a combined SNR-based ranking statistic. Therefore, we do not have a direct measure of the efficacy of the multivariate statistical classifier. We can however, compare the 90% rate upper limit from Figure 9.2 to other searches for BHBs in the same mass range. One such search, described in Reference [134], looks for unmodeled bursts rather than using a template bank [135]. The upper limit was calculated using EOBNRv2 injections — systems with a total mass of 100 $M_{\odot}$ were calculated to have a rate upper limit of $1.3 \times 10^{-7}\mathrm{Mpc}^{-3}yr^{-1}$. For the same total mass, a 90% confidence rate upper limit of $7 \times 10^{-8}\mathrm{Mpc}^{-3}yr^{-1}$, was calculated by the high-mass search; see Table 8.2. We consider these upper limits to be consistent, considering the range of methods. The astrophysical upper limit, which assumes that all globular clusters are sufficiently massive and have a high enough binary fraction to form one of these systems in their lifetime, is $4 \times 10^{-10}\mathrm{Mpc}^{-3}yr^{-1}$ [18].

A methods paper for the use of the random forest of bagged decision trees in the ringdown search is in preparation.

Chapter 10

Summary of this work

The gravitational-wave observatories in Hanford, WA (LIGO H1), Livingston, LA (LIGO L1), and Cascina, Italy (Virgo) are pushing boundaries of both instrumental science and astrophysics. The possibilities for research are vast. In this thesis, I have reviewed my contribution to three areas of this research.

The first is the search for compact binary coalescences from systems with total mass between 25 and 100 $M_{\odot}$ (the high-mass search) during the joint LIGO-Virgo data period S6-VSR2/3. I made significant contributions to the search that was published in Reference [17], including: 1) creating the veto definer files that describe the data quality during S6-VSR2/3 in a way that is pertinent to high-mass CBC signals (see Section 4.2.1); 2) running the analysis pipeline (see Chapter 7); and 3) deciding on the number and distance ranges of the various sets of injection runs (see Section 7.5). The results of this search are summarized in Table 8.2. These results were based on a ranking statistic that combines the signal-to-noise of the signal in each detector and a χ^2 statistic that measures how well the signal in each detector matches our waveform templates in a way that takes the length of the template into consideration (see Equation (7.18)). However, the analysis pipeline produces useful information beyond these values. I used a multivariate statistical classifier known as a random forest of bagged decision trees to combine this 15-dimensional information into a new ranking statistic. Using this multivariate statistical classifier increases the sensitive volume of the search by up to about 40%, depending on the mass of the CBC system (see Figure 8.26).

My second contribution is to general methods for measuring the data quality of the LIGO detectors. The goal of this work was to see if it is possible to replace the traditional system of data-quality flags and vetoes with a multivariate approach using information from the auxiliary channels recording information about the state of the instrument and its environment. I applied the random forest of bagged decision trees method to the classification of "glitchy" versus "clean" data for two datasets: H1 during S4 (810-dimensional feature space); and L1 during S6 (1250-dimensional feature space). My results were compared to two other multivariate statistical classifiers: the artificial neural network and the support vector machine; the analysis was published in Reference [99]. Each classifier produced comparable efficiency at classifying glitchy data. They outperformed the data-quality vetoes defined for a search for generic gravitational-wave burst signals, but did not outperform an ordered list of pairwise correlations between the auxiliary channels and the

gravitational-wave channel. See Figure 6.9 for a summary of the results.

My third contribution is to the search for the ringdown signals from the coalescence of black hole binary systems with total mass between 50 and 450 $M_{\odot}$and ringdowns from perturbed intermediate mass black holes with masses between 100 and 150 $M_{\odot}$. I collaborated with the group leading this search to help incorporate the random forest of bagged decision trees method into the search pipeline so that its result could be used as the ranking statistic for the search; see Section 9.1. The results for this search were published in Reference [18].

10.1 Future work

In terms of multivariate statistical classification for the high-mass search, several improvements could be made. The first is that we did not utilize the ability to weight our training samples. By weighting more distant injections more, we may be able to improve our sensitivity — not only will we be able to detect CBCs at a farther distance, but the number of sources increases uniformly in volume. Moreover, perhaps having the entire training set of injections look as though it was from thousands of sources distributed uniformly in volume is the right thing to do, if we are truly trying to represent a set of astrophysical signals.

The second is that rather than running the multivariate analysis after the application of Category 3 or 4 vetoes (see Section 4.2.1), we could run it after the application of only Category 1 vetoes (which remove only egregiously bad data) and have the feature vector include a dimension (or several) that describes the data quality at the time of the candidate gravitational-wave event, along with the signal-based information. Alternatively, we could train two classifiers — a signal-based classifier and a data-quality classifier, each of whose training samples describe the same GPS times. The results of these two classifiers could be combined into a single ranking statistic by a simple analytical formula or yet another multivariate classifier.

For the multivariate statistical classification as applied to data quality, a pipeline is currently being developed to train the classifiers and use them to rank data in a low-latency real-time manner.

Further improvements to this application of multivariate statistical classification to data quality could be made by including information that characterizes the auxiliary channels' time-series around the time being considered, rather than simply identifying triggers in the time-series.

10.2 Long term outlook for the field

After the Advanced LIGO and Virgo detectors (and hopefully, LIGO-India) have been taking data for a year or so, we can look forward to actual detections of gravitational waves — realistic estimates predict 20 black hole binary coalescences within the sensitive volume of the advanced detectors, within one year of coincident observation time [21]. The low-frequency sensitivity of the LIGO detectors is also expected to improve (see Figure 10.1 — allowing us to detect higher mass systems (total masses up to 1050 $M_{\odot}$ [136]).

With multiple detections, we will learn about the mass and spin distributions of the component objects in coalescing black hole binary systems; these distributions will be windows into the formation scenarios of black hole binary systems. We will also be able to probe the strong-field regime of General Relativity. Even if there are no detections, the results will still be extremely valuable to astrophysics. More stringent upper limits on the rates of black hole binary coalescences will allow us to place tighter constraints on the parameters of various formation scenarios. As reviewed in Section 2.1, the computer simulations of these formation scenarios rely on many parameters for which there are no observational constraints. Detections (or the lack thereof) of black hole binary systems will allow us to constrain (for example) natal kick velocity distributions, the metallicity content of galaxies, and the parameters of mass-transfer in stellar binaries.

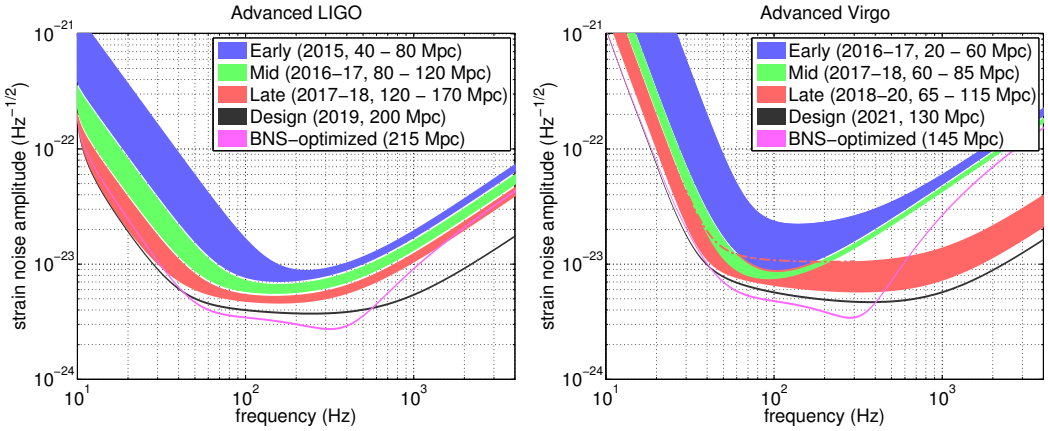

Figure 10.1: The best estimates of Advanced LIGO (left) and advanced Virgo (right) strain sensitivities as a function of frequency. The dates indicate the expected improvement in sensitivity over several commissioning phases. The black curve is the design sensitivity, which we hope to reach in 2019 for Advanced LIGO and 2021 for advanced Virgo. The distances in the legend are the sensitive range for detection of a binary neutron star system [19].

Of course the science is not limited to black hole binaries; we may also detect coalescing neutron star systems, spinning single neutron stars, the gravitational-wave background from the early universe, gravitational-wave evidence for pre-Big Bang models [137], gravitational-wave bursts from supernovae explosions and cosmic string kinks and cusps, or sources not yet anticipated.

Despite their improved sensitivity, the advanced detectors may result in new challenges in terms of data quality. There will be orders of magnitude more auxiliary channels measuring the state of the detector and its environment, and thus defining data quality will become trickier. Using multivariate statistical classifiers on these auxiliary channels to measure data quality may prove to be very useful. We won't know if this is necessary until we start taking data with the advanced detectors — depending on commissioning, the data could be wonderfully Gaussian, horribly glitchy, or somewhere in between.

Bibliography

[1] K. Belczynski, V. Kalogera, and T. Bulik. A comprehensive study of binary compact objects as gravitational wave sources: Evolutionary channels, rates, and physical properties. *The Astrophysical Journal*, 572:407, 2002.

[2] K. Belczynski, M. Dominik, T. Bulik, R. O'Shaughnessy, C. Fryer, and D. E. Holz. The effect of metallicity on the detection prospects for gravitational waves. *The Astrophysical Journal*, 715:L138–L141, June 2010.

[3] R. M. O'Leary, F. A. Rasio, J. M. Fregeau, N. Ivanova, and R. O'Shaughnessy. Binary mergers and growth of black holes in dense star clusters. *The Astrophysical Journal*, 637:937–951, February 2006.

[4] J. Abadie et al. Sensitivity achieved by the LIGO and Virgo gravitational wave detectors during LIGO's Sixth and Virgo's Second and Third Science Runs. arXiv:1203.2674v2 [gr-qc], 2012.

[5] J. Aasi et al. The characterization of Virgo data and its impact on gravitational-wave searches. *Class.Quant.Grav.*, 29:155002, 2012.

[6] The LIGO Scientific Collaboration. Characterization of the LIGO detectors during their Sixth Science Run. 2013. In preparation.

[7] K. L. Dooley, M. A. Arain, D. Feldbaum, V. V. Frolov, M. Heintze, D. Hoak, E. A. Khazanov, A. Lucianetti, R. M. Martin, G. Mueller, et al. Characterization of thermal effects in the enhanced LIGO input optics. arXiv:1112.1737v1 [physics.ins-det], 2011.

[8] K. L. Dooley. *Design and performance of high laser power interferometers for gravitational-wave detection*. PhD thesis, Florida University, 2011.

[9] R. DeRosa, J. C. Driggers, D. Atkinson, H. Miao, V. Frolov, M. Landry, J. A. Giaime, and R. X. Adhikari. Global feed-forward vibration isolation in a km scale interferometer. *Classical and Quantum Gravity*, 29(21):215008, 2012.

[10] T. T. Fricke, N. D. Smith-Lefebvre, R. Abbott, R. Adhikari, K. L. Dooley, M. Evans, P. Fritschel, V. V. Frolov, K. Kawabe, J. S. Kissel, et al. DC readout experiment in enhanced LIGO. *Classical and Quantum Gravity*, 29(6):065005, 2012.

[11] L. M. Goggin. *A search for gravitational waves from perturbed black hole ringdowns in LIGO data*. PhD thesis, California Institute of Technology, 2008.

[12] D. A. Brown. *Search for gravitational radiation from black hole MACHOs in the Galactic halo*. PhD thesis, University of Wisconsin–Milwaukee, 2004.

[13] D. C. Coyne. The laser interferometer gravitational-wave observatory (LIGO) project. In *Aerospace Applications Conference*, volume 4, pages 31–61. IEEE, 1996.

[14] A. Lazzarini and R. Weiss. LIGO science requirements document (SRD). *Internal LIGO document E950018-02-E*, 1995.

[15] A. Di Credico. Glitch investigations with Kleine Welle. *Internal LIGO document G050158*, 2013.

[16] S. K. Chatterji. *The search for gravitational wave bursts in data from the Second LIGO Science Run*. PhD thesis, Massachusetts Institute of Technology, 2005.

[17] J. Aasi et al. Search for gravitational waves from binary black hole inspiral, merger, and ringdown in LIGO-Virgo data from 2009-2010. *Physical Review D*, 87:022002, Jan 2013.

[18] J. Aasi et al. Search for gravitational wave ringdowns from perturbed intermediate mass black holes in LIGO-Virgo data from 2005-2010. arXiv:1403.5306v1 [gr-qc], 2014.

[19] J. Aasi et al. Prospects for localization of gravitational wave transients by the advanced LIGO and advanced Virgo observatories. arXiv:1304.0670v1 [gr-qc], 2013.

[20] J. Abadie et al. Predictions for the rates of compact binary coalescences observable by ground-based gravitational-wave detectors. *Classical and Quantum Gravity*, 27:173001, March 2010.

[21] I. Mandel, D. A. Brown, J. R. Gair, and M. C. Miller. Rates and characteristics of intermediate mass ratio inspirals detectable by advanced LIGO. *The Astrophysical Journal*, 681:1431–1447, July 2008.

[22] J. M. Fregeau, S. L. Larson, M. C. Miller, R. O'Shaughnessy, and F. A. Rasio. Observing IMBH-IMBH binary coalescences via gravitational radiation. *The Astrophysical Journal*, 646:L135–L138, August 2006.

[23] J. Abadie et al. Search for gravitational waves from binary black hole inspiral, merger and ringdown. *Physical Review D*, 83:122005, 2011. Erratum: ibid. **86**, 069903(E) (2012).

[24] S. Chandrasekhar. On the equations governing the perturbations of the schwarzschild black hole. *Proceedings of the Royal Society of London. A. Mathematical and Physical Sciences*, 343(1634):289–298, 1975.

[25] V. Kalogera, K. Belczynski, C. Kim, R. O'Shaughnessy, and B. Willems. Formation of double compact objects. *Physics Reports*, 442:75–108, April 2007.

[26] S. Rosswog and M. Brüggen. *Introduction to high-energy astrophysics*. Cambridge University Press, Cambridge, 2007.

[27] K. Belczynski, A. Buonanno, M. Cantiello, D. E Holz, C. L. Fryer, I. Mandel, M. C. Miller, and M. Walczak. The formation and gravitational-wave detection of massive stellar black-hole binaries. arxiv:1211.0546 [astro-ph.HE], 2014.

[28] K. Belczynski, R. E. Taam, V. Kalogera, F. A. Rasio, and T. Bulik. On the rarity of double black hole binaries: Consequences for gravitational wave detection. *The Astrophysical Journal*, 662:504–511, June 2007.

[29] B. W. Carroll and D. A. Ostlie. *An introduction to modern astrophysics*. Addison-Wesley, Reading, 1996.

[30] R. O'Shaughnessy, V. Kalogera, and K. Belczynski. Binary compact object coalescence rates: The role of elliptical galaxies. *The Astrophysical Journal*, 716:615–633, June 2010.

[31] K. Belczynski, V. Kalogera, F. A. Rasio, R. E. Taam, A. Zezas, T. Bulik, T. J. Maccarone, and N. Ivanova. Compact object modeling with the StarTrack population synthesis code. *The Astrophysical Journal Supplement Series*, 174:223–260, January 2008.

[32] A. K. Pradhan and S. N. Nahar. *Atomic astrophysics and spectroscopy*. Cambridge University Press, Cambridge, 2011.

[33] R. Freedman, R. Geller, and W. J. Kaufmann. *Universe: The solar system*. W. H. Freeman and Company, New York, 2010.

[34] Paul A Crowther. Stellar winds from massive stars. In D. Vanbeveren, editor, *The Influence of Binaries on Stellar Population Studies*, pages 215–230. Kluwer Academic Publishers, Dordrecht, 2001.

[35] C. A. Tremonti, T. M. Heckman, G. Kauffmann, J. Brinchmann, S. Charlot, S. D. M. White, M. Seibert, E. W. Peng, D. J. Schlegel, A. Uomoto, et al. The origin of the mass-metallicity relation: Insights from 53,000 star-forming galaxies in the sloan digital sky survey. *The Astrophysical Journal*, 613(2):898, 2004.

[36] S. F. Portegies Zwart and S. L. W. McMillan. Black hole mergers in the universe. *The Astrophysical Journal*, 528:L17, 2000.

[37] R. M. O'Leary, R. O'Shaughnessy, and F. A. Rasio. Dynamical interactions and the black-hole merger rate of the Universe. *Physical Review D*, 76:061504, Sep 2007.

[38] R. M. O'Leary, B. Kocsis, and A. Loeb. Gravitational waves from scattering of stellar-mass black holes in galactic nuclei. *Monthly Notices of the Royal Astronomical Society*, 395:2127–2146, June 2009.

[39] M. C. Miller and V. M. Lauburg. Mergers of stellar-mass black holes in nuclear star clusters. *The Astrophysical Journal*, 692:917–923, February 2009.

[40] T. Bulik, K. Belczynski, and A. Prestwich. IC10 X-1/NGC300 X-1: The very immediate progenitors of BH-BH binaries. *The Astrophysical Journal*, 730:140, 2011.

[41] J. D. E. Creighton and W. G. Anderson. *Gravitational-wave physics and astronomy: An introduction to theory, experiment and data analysis*. John Wiley & Sons, Weinheim, 2011.

[42] B.S. Sathyaprakash and B. F. Schutz. Physics, astrophysics and cosmology with gravitational waves. *Living Reviews in Relativity*, 12(2), 2009.

[43] M. Shibata and K. Taniguchi. Coalescence of black hole–neutron star binaries. *Living Reviews in Relativity*, 14(6), 2011.

[44] E. Berti et al. Inspiral, merger and ringdown of unequal mass black hole binaries: A multipolar analysis. *Physical Review D*, 76:064034, 2007.

[45] A. Buonanno, B. R. Iyer, E. Ochsner, Y. Pan, and B. S. Sathyaprakash. Comparison of post-Newtonian templates for compact binary inspiral signals in gravitational-wave detectors. *Physical Review D*, 80 (8):084043, October 2009.

[46] S. Chandrasekhar and S. Detweiler. The quasi-normal modes of the Schwarzschild black hole. *Proceedings of the Royal Society of London. Series A, Mathematical and Physical Sciences*, 344:441–452, 1975.

[47] A. Buonanno, Y. Chen, Y. Pan, H. Tagoshi, and M. Vallisneri. Detecting gravitational waves from precessing binaries of spinning compact objects. II. Search implementation for low-mass binaries. *Physical Review D*, 72:084027, 2005.

[48] A. Buonanno and T. Damour. Effective one-body approach to general relativistic two-body dynamics. *Physical Review D*, 59:084006, 1999.

[49] Y. Pan, A. Buonanno, M. Boyle, L. T. Buchman, L. E. Kidder, H. P. Pfeiffer, and M. A. Scheel. Inspiral-merger-ringdown multipolar waveforms of nonspinning black-hole binaries using the effective-one-body formalism. *Physical Review D*, 84(12):124052, December 2011.

[50] P. Ajith, M. Hannam, S. Husa, Y. Chen, B. Bruegmann, N. Dorband, D. Mueller, F. Ohme, D. Pollney, C. Reisswig, L. Santamaria, and J. Seiler. "Complete" gravitational waveforms for black-hole binaries with non-precessing spins. arXiv:0909.2867v1 [gr-qc], 2009.

[51] J. Smith (for the LIGO Scientific Collaboration). The path to the enhanced and advanced LIGO gravitational-wave detectors. *Classical and Quantum Gravity*, 26(11):114013, June 2009.

[52] S. Ballmer, V. Frolov, R. Lawrence, W. Kells, G. Moreno, K. Mason, D. Ottaway, M. Smith, C. Vorvick, P. Willems, et al. Thermal compensation system description. *Optics Letters*, 29(22):2635–2637, 2004.

[53] A. Brooks et al. Mitigating thermally-induced optical distortions in the enhanced LIGO gravitational wave detector. 2014. In preparation.

[54] J. Abadie et al. Sensitivity to gravitational waves from compact binary coalescences achieved during LIGO's Fifth and Virgo's First Science Run. arXiv:1003.2481v3 [gr-qc], 2010.

[55] J. Abadie et al. Search for compact binary coalescences in LIGO and Virgo data from S5 and VSR1. *Physical Review D*, 82:102001, 2010.

[56] B. Abbott et al. Search for gravitational waves from low mass binary coalescences in the first year of LIGO's S5 data. *Physical Review D*, 79:122001, 2009.

[57] J. Abadie et al. Search for gravitational waves from intermediate mass binary black holes. *Physical Review D*, 85:102004, 2012.

[58] J. Abadie et al. Search for gravitational waves from low mass compact binary coalescence in LIGO's Sixth Science Run and Virgo's Science Runs 2 and 3. *Phys. Rev. D*, 85:082002, 2012.

[59] G. M. Harry for the LIGO Scientific Collaboration. Advanced LIGO: the next generation of gravitational wave detectors. *Classical and Quantum Gravity*, 27(8):084006, 2010.

[60] K. Somiya. Detector configuration of KAGRA–the Japanese cryogenic gravitational-wave detector. *Classical and Quantum Gravity*, 29(12):124007, 2012.

[61] T. Corbitt and N. Mavalvala. Review: Quantum noise in gravitational-wave interferometers. *Journal of Optics B: Quantum and Semiclassical Optics*, 6(8):S675, 2004.

[62] B. Abbott et al. LIGO: The laser interferometer gravitational-wave observatory. *Reports on Progress in Physics*, 72:076901, 2009.

[63] T. Accadia et al. Calibration and sensitivity of the Virgo detector during its Second Science Run. *Classical and Quantum Gravity*, 28:025005, 2011.

[64] M. E. Zucker. Protecting installed core optics from particulates. *Internal LIGO document, LIGO-T080067-v1*, 2009.

[65] J. Giaime, P. Saha, D. Shoemaker, and L. Sievers. A passive vibration isolation stack for LIGO: design, modeling, and testing. *Review of Scientific Instruments*, 67:208, 1996.

[66] R. Abbott, R. Adhikari, G. Allen, D. Baglino, C. Campbell, D. Coyne, E. Daw, D. DeBra, J. Faludi, P. Fritschel, et al. Seismic isolation enhancements for initial and advanced LIGO. *Classical and Quantum Gravity*, 21(5):S915, 2004.

[67] R. Adhikari. *Sensitivity and Noise Analysis of 4 km Laser Interferometric Gravitational Wave Antennae*. PhD thesis, MIT, 2004.

[68] A. Gerhardt. A search for sources of anthropogenic seismic noise hindering interferometer lock. Advanced undergraduate project, MIT, Cambridge, MA, 2004.

[69] R. Bork, R. Abbott, D. Barker, and J. Heefner. An overview of the LIGO control and data acquisition system. arXiv:physics/0111077v1 [physics.ins-det], 2001.

[70] W. Kells. Core optics components requirements (1064 nm). *Internal LIGO document E950099-04*, 1996.

[71] M. Smith. Core optics support - design requirements document. *Internal LIGO document T970071*, 1997.

[72] LIGO Scientific Collaboration. Instrument science white paper. *Internal LIGO Document T1100309-V5*, 2011.

[73] K. Mason and M. Zucker. ASC initial alignment subsystem final design. *Internal LIGO document T980019*, 1998.

[74] LIGO Scientific Collaboration. Environmental influences on the LIGO gravitational wave detectors during the 6th Science Run, 2013. In preparation.

[75] N. Christensen (for the LIGO Scientific Collaboration and the Virgo Collaboration). LIGO S6 detector characterization studies. *Classical and Quantum Gravity*, 27(19):194010, 2010.

[76] J. Slutsky, L. Blackburn, D. A. Brown, L. Cadonati, J. Cain, M. Cavaglia, S. Chatterji, N. Christensen, M. Coughlin, S. Desai, G. Gonzalez, T. Isogai, E. Katsavounidis, B. Rankins, T. Reed, K. Riles, P. Shawhan, J. R. Smith, N. Zotov, and J. Zweizig. Methods for reducing false alarms in searches for compact binary coalescences in LIGO data. *Classical and Quantum Gravity*, 27(16):165023, 2010.

[77] J. Abadie et al. Calibration of the LIGO gravitational wave detectors in the Fifth Science Run. *Nuclear Instruments and Methods in Physics Research Section A*, 624:223–240, 2010.

[78] D. A. Brown (for the LIGO Scientific Collaboration). Testing the LIGO inspiral analysis with hardware injections. *Classical and Quantum Gravity*, 21:S797–S800, 2004.

[79] H. B. Callen and T. A. Welton. Irreversibility and generalized noise. *Physical Review*, 83(1):34–40, 1951.

[80] C. M. Caves. Quantum-mechanical noise in an interferometer. *Physical Review D*, 23(8):1693, 1981.

[81] S. Chatterji, L. Blackburn, G. Martin, and E. Katsavounidis. Multiresolution techniques for the detection of gravitational-wave bursts. *Classical and Quantum Gravity*, 21(20):S1809, 2004.

[82] L. Blackburn. Kleinewelle technical document. *Internal LIGO document T060221-00-Z*, 2007.

[83] S. G. Mallat. A theory for multiresolution signal decomposition: The wavelet representation. *IEEE Transactions on Pattern Analysis and Machine Intelligence*, 11(7):674–693, 1989.

[84] D. Macleod. Using Omega search on auxiliary channels for detector improvement. *Internal LIGO document G1100331*, 2011.

[85] D.M. Macleod, S. Fairhurst, B. Hughey, A. P. Lundgren, L. Pekowsky, J. Rollins, and J. R. Smith. Reducing the effect of seismic noise in LIGO searches by targeted veto generation. *Classical and Quantum Gravity*, 29:055006, 2012.

[86] J. Li. Enhancing clustering performance in Omega pipeline. *Internal LIGO document G1000479*, 2010.

[87] D. Jiles. *Introduction to magnetism and magnetic materials*. Chapman & Hall / CRC, Boca Raton, 1998.

[88] T. Isogai for the LIGO Scientific Collaboration. Used percentage veto for LIGO and Virgo binary inspiral searches. In *Journal of Physics: Conference Series*, volume 243, page 012005. IOP Publishing, 2010.

[89] J. R. Smith, T. Abbott, E. Hirose, N. Leroy, D. MacLeod, J. McIver, P. Saulson, and P. Shawhan. A hierarchical method for vetoing noise transients in gravitational-wave detectors. *Classical and Quantum Gravity*, 28(23):235005, 2011.

[90] B. Allen, W. G. Anderson, P. R. Brady, D. A. Brown, and J. D. E. Creighton. FINDCHIRP: An algorithm for detection of gravitational waves from inspiraling compact binaries. *Physical Review D*, 85(12):122006, June 2012.

[91] P. Ajith, T. Isogai, N. Christensen, R. Adhikari, A. B. Pearlman, A. Wein, A. J. Weinstein, and B. Yuan. Instrumental vetoes for transient gravitational-wave triggers using noise-coupling models: The bilinear-coupling veto. arXiv:1403.1431v1 [gr-qc], 2014.

[92] I. Narsky and F. C. Porter. *Statistical analysis techniques in particle physics: Fits, density estimation and supervised learning*. Wiley-VCH, Weinheim, 2013.

[93] Y. S. Abu-Mostafa, M. Magdon-Ismail, and H. Lin. *Learning from data: A short course*. AMLBook, 2012.

[94] T. Hastie, R. Tibshirani, and J. Friedman. *The elements of statistical learning: Data mining, inference, and prediction*. Springer Science + Business Media, New York, 2nd edition, 2009.

[95] R. Hecht-Nielsen. Theory of the backpropagation neural network. In *Proceedings of International Joint Conference on Neural Networks*, volume 1, pages 593–605. IEEE, Washington, 1989.

[96] S. N. Sivanandam, S. N. Deepa, and S. Sumathi. *Introduction to neural networks using Matlab 6.0*. Tata McGraw-Hill Education, New Delhi, 2006.

[97] F. Rosenblatt. The perceptron: a probabilistic model for information storage and organization in the brain. *Psychological Review*, 65(6):386, 1958.

[98] P. S. R. Diniz. *Adaptive filtering: algorithms and practical implementation*. Springer Science + Business Media, New York, 2013.

[99] R. Biswas, L. Blackburn, J. Cao, R. Essick, K. A. Hodge, E. Katsavounidis, K. Kim, Y.-M. Kim, E. O. L. Bigot, C.-H. Lee, J. J. Oh, S. H. Oh, E. Son, R. Vaulin, X. Wang, and T. Ye. Application of machine learning algorithms to the study of noise artifacts in gravitational-wave data. *Physical Review D*, 88:062003, Sep 2013.

[100] C. Igel and M. Hüsken. Improving the Rprop learning algorithm. In H. Bothe and R. Rojas, editors, *Proceedings of the Second International ICSC Symposium on Neural Computation (NC 2000)*, pages 115–121. ICSC Academic Press, 2000.

[101] S. Nissen et al. Fast Artificial Neural Network Library. Software available at `http://leenissen.dk/fann/wp/`, 2000.

[102] C. Cortes and V. Vapnik. Support-vector networks. *Machine Learning*, 20(3):273–297, 1995.

[103] N. Cristianini and J. Shawe-Taylor. *An introduction to support vector machines and other kernel-based learning methods*. Cambridge University Press, Cambridge, 1st edition, 2000.

[104] C.-C. Chang and C.-J. Lin. LIBSVM: A library for support vector machines. *ACM Transactions on Intelligent Systems and Technology*, 2:27:1–27:27, 2011. Software available at `http://www.csie.ntu.edu.tw/~cjlin/libsvm`.

[105] I. Narsky. StatPatternRecognition: A C++ package for statistical analysis of high energy physics data. arXiv:physics/0507143v1 [physics.data-an], 2005.

[106] I. Narsky. New developments in pattern classification of high energy physics data. Content available at `http://www.hep.caltech.edu/~narsky/SPR_Caltech_Oct2005.pdf`, 2005.

[107] L. Breiman. Random forests. *Machine Learning*, 45(1):5–32, 2001.

[108] L. Breiman. Bagging predictors. *Machine Learning*, 24(2):123–140, 1996.

[109] I. Narsky. StatPatternRecognition. Software available at `http://statpatrec.sourceforge.net/`.

[110] R. Essick, L. Blackburn, and E. Katsavounidis. Optimizing vetoes for gravitational wave transient searches. arXiv:1303.7159v2 [astro-ph.IM], 2013.

[111] Y.-M. Kim, S. H. Oh, E. J. Son, K. Kim, C.-H. Lee, and J. J. Oh. GA-ANN applications to LIGO auxiliary channels for noise artifact identification. 2013. In preparation.

[112] R. Biswas, P. R. Brady, J. Burguet-Castell, K. Cannon, J. Clayton, A. Dietz, N. Fotopoulos, L. M. Goggin, D. Keppel, C. Pankow, Larry R. Price, and R. Vaulin. Detecting transient gravitational waves in non-gaussian noise with partially redundant analysis methods. *Physical Review D*, 85:122009, Jun 2012.

[113] M. P. Wand and M. C. Jones. *Kernel smoothing*, volume 60. Chapman & Hall / CRC, Boca Raton, 1995.

[114] B. Abbott et al. Search for gravitational waves from binary black hole inspirals in LIGO data. *Physical Review D*, 73:062001, 2006.

[115] B. Abbott et al. Search for gravitational waves from galactic and extra-galactic binary neutron stars. *Physical Review D*, 72:082001, 2005.

[116] B. Abbott et al. Search of S3 LIGO data for gravitational wave signals from spinning black hole and neutron star binary inspirals. *Physical Review D*, 78:042002, 2008.

[117] B. Abbott et al. Search for gravitational waves from binary inspirals in S3 and S4 LIGO data. *Physical Review D*, 77:062002, 2008.

[118] B.P. Abbott et al. Search for gravitational waves from low mass compact binary coalescence in 186 days of LIGO's Fifth Science Run. *Physical Review D*, 80:047101, 2009.

[119] F. Acernese et al. Virgo status. *Classical and Quantum Gravity*, 25(18):184001, 2008.

[120] S. Klimenko, I. Yakushin, A. Mercer, and G. Mitselmakher. Coherent method for detection of gravitational wave bursts. *Classical and Quantum Gravity*, 25:114029, 2008.

[121] M. van der Sluys, I. Mandel, V. Raymond, V. Kalogera, C. Röver, and N. Christensen. Parameter estimation of spinning binary inspirals using Markov-chain Monte Carlo. *Classical and Quantum Gravity*, 25:184011, 2008.

[122] T. Cokelaer. Gravitational waves from inspiralling compact binaries: Hexagonal template placement and its efficiency in detecting physical signals. *Physical Review D*, 76:102004, 2007.

[123] S. Privitera, S. R. P. Mohapatra, P. Ajith, K. Cannon, N. Fotopoulos, M. A. Frei, C. Hanna, A. J. Weinstein, and J. T. Whelan. Improving the sensitivity of a search for coalescing binary black holes with nonprecessing spins in gravitational wave data. *Physical Review D*, 89(2):024003, 2014.

[124] B. Allen. A χ^2 time-frequency discriminator for gravitational wave detection. *Physical Review D*, 71: 062001, 2005.

[125] The LIGO Scientific Collaboration. Tuning matched filter searches for compact binary coalescence. *Internal LIGO document T070109-01*, 2007.

[126] P. R. Brady, J. D. E. Creighton, and A. G. Wiseman. Upper limits on gravitational-wave signals based on loudest events. *Classical and Quantum Gravity*, 21:S1775–S1781, 2004.

[127] R. Biswas, P. R. Brady, J. D. E. Creighton, and S. Fairhurst. The loudest event statistic: General formulation, properties and applications. *Classical and Quantum Gravity*, 26:175009, 2009.

[128] Chad Hanna. *Searching for gravitational waves from binary systems in non-stationary data*. PhD thesis, Louisiana State University, 2008.

[129] E. Poisson and C. M. Will. Gravitational waves from inspiraling compact binaries: Parameter estimation using second post-Newtonian waveforms. *Physical Review D*, 52:848–855, 1995.

[130] K. G. Arun, B. R. Iyer, B. S. Sathyaprakash, and P. A. Sundararajan. Parameter estimation of inspiralling compact binaries using 3.5 post-Newtonian gravitational wave phasing: The non-spinning case. *Physical Review D*, 71(8):084008, 2005.

[131] R. J. E. Smith, K. Cannon, C. Hanna, D. Keppel, and I. Mandel. Towards rapid parameter estimation on gravitational waves from compact binaries using interpolated waveforms. arxiv:1211.1254 [astro-ph.HE], 2012.

[132] Matt West. personal communication.

[133] B. Abbott et al. Search for gravitational wave ringdowns from perturbed black holes in LIGO S4 data. *Physical Review D*, 80:062001, 2009.

[134] J. Aasi et al. Search for gravitational radiation from intermediate mass black hole binaries in data from the second LIGO-Virgo joint science run. arXiv:1404.2199 [gr-qc], 2014.

[135] W. G. Anderson, P. R. Brady, J. D. E. Creighton, and E. E. Flanagan. An excess power statistic for detection of burst sources of gravitational radiation. *Physical Review D*, 63:042003, 2001.

[136] G. Mazzolo, F. Salemi, M. Drago, V. Necula, C. Pankow, G.A. Prodi, V. Re, V. Tewari, G. Vedovato, I. Yakushin, and S. Klimenko. Prospects for intermediate mass black hole binary searches with advanced gravitational-wave detectors. arXiv:1404.7757v2 [gr-qc].

[137] V. Mandic and A. Buonanno. Accessibility of the pre-big-bang models to LIGO. *Physical Review D*, 73(6):063008, 2006.